Mach Zehnder interferometry and coherent manipulation of the valley in a graphene PN junction

Paul Brasseur

université PARIS-SACLAY

Mach Zehnder interferometry and coherent manipulation of the valley in a graphene PN junction

Thèse de doctorat de l'université Paris-Saclay

École doctorale n°564, Physique de l'Île-de-France (PIF)
Spécialité de doctorat : Physique
Unité de recherche : Université Paris-Saclay, CEA, CNRS, SPEC, 91191, Gif-sur-Yvette, France.
Référent : Faculté des sciences d'Orsay

Thèse présentée et soutenue à Saint-Aubin, le 28/09/2020, par

Paul BRASSEUR

Composition du Jury

Mark Oliver GOERBIG Directeur de Recherche, UP-Saclay	Président
Dmitri EFETOV Professeur, ICFO	Rapporteur & Examinateur
Romain DANNEAU Chargé de Recherche, HDR, KIT	Rapporteur & Examinateur
Clément FAUGERAS Chargé de Recherche, LNCMI	Examinateur
Rebeca RIBEIRO-PALAU Chargée de Recherche, UP-Saclay	Examinatrice
Benoît HACKENS Professeur, UCLouvain	Examinateur
Patrice ROCHE Directeur de Recherche, CEA-Saclay	Directeur de thèse
Preden ROULLEAU Chargé de Recherche, CEA-Saclay	Co-Encadrant de thèse

Thèse de doctorat

NNT : 2020UPASP012

Contents

Introduction

The advent of quantum mechanics at the beginning of the 20^{th} century had implications in many fields of classical physics, and in particular optics. The main difference appears when dealing with interference : in classical optics we deal with interference in electric field amplitudes, whereas in a quantum mechanical treatment we have to consider interference in probability amplitudes. In many cases, there is no difference between those two frameworks. Observing experimentally features of quantum mechanics in optics is actually an entire research field called quantum optics. The development of this field from the beginning of the sixties lead to impressive fundamental results, and in particular the resolution of one of the major controversy of the 20^{th} century beyond physicists : the Einstein-Podolsky-Rosen paradox (EPR paradox). According to the EPR paradox, quantum mechanics theoretical description is not complete as it doesn't take into account some "elements of reality"; this lead to a hidden-variable theory to depict quantum mechanics. One of the milestones in quantum optics is Alain Aspect's experiment [7] exhibiting the Bell's inequality violation, which directly contradicts any hidden-variable theory.

Electron quantum optics is an emerging field whose goal is to mimic quantum optics experiments replacing photons by electrons. For this aim, physicists used a peculiar type of system, called two dimensional electron gas (2DEG), in which electrons are confined to a plane. 2DEG can be formed at the surface of liquid He, or at the interface of semiconducting heterostructures as the widely studied GaAs/AlGaAs. Interestingly, at very low temperature (typically below $100mK$ in GaAs/AlGaAs heterostructures), an analogue of fiber optics is obtained for electrons through the chiral edge states, formed in the quantum Hall regime appearing when a strong perpendicular magnetic field is applied on a 2DEG. This enables to guide electrons up to the electronic equivalent of a beam splitter, thanks to which one can recreate quantum optics experiments. Using these techniques, a team achieved a first electronic Mach Zehnder interferometer (MZI) in 2003 [37].

This pioneering experiment paved the way towards the generation of entangled states thanks to a double MZI structure, as proposed by Samuelsson et al. [74]. Entangled electronic states are of primary importance for theoretical and practical purposes. Indeed, theoretically, this double MZI experiment should enable to exhibit a Bell's inequality violation as in Alain Aspect's experiment, but with electrons replacing photons, which is fundamentally important as electrons are fermions, whereas photons are bosons. On the other hand, electronic entangled states are essential to envision quantum computing using the flying qubit approach. This approach was developed in electron quantum optics in analogy with the single photon qubits manipulated in quantum optics. The state of the flying qubit is encoded into the electron trajectory, and a superposition of two

trajectories can be obtained thanks to an electronic equivalent of a beam splitter (as a quantum point contact for instance), forming an Hadamard gate. In this framework, the double MZI geometry generating entangled states is an essential building block to achieve multi-qubits quantum gates.

Unfortunately, the coherence in GaAs/AlGaAs heterostructures is fragile, and the decoherence was too strong to observe experimentally a Bell's inequality violation [60]. Moreover, this weak coherence makes it difficult to envision quantum computation, thanks to a complex set of quantum gates, in semi-conducting heterostructures. The solution to these problems could come from a novel material with extraordinary properties, isolated by a team from Manchester University [65] in 2005 : the famous graphene. Graphene is a perfectly two-dimensional crystal of Carbon atoms arranged in a honeycomb lattice. Each Carbon atom has 4 Valence electrons : three forming co-valent bounds with other Carbon atoms, and an extra one above the sheet. The set of all the extra electrons forms a 2DEG, at the surface of the graphene sheet, and, as in GaAs/AlGaAs heterostructures, when a perpendicular magnetic field is applied on a graphene sheet, it also gives rise to a quantum Hall effect and chiral edge states are created. In addition, the coherence in graphene was predicted to be much steadier, making it an interesting potential candidate for electron quantum optics. In 2015, Morikawa et al. [58] achieved the first electronic Mach Zehnder interferometer in graphene using a pn junction, opening the way for the more complete study carried out in the Yacoby group in 2017 [84].

A striking feature of graphene is the existence of the valley degree of freedom, which adds up to the spin to generate a four fold spin and valley degeneracy. The degeneracy is lifted under strong perpendicular magnetic field, generating chiral edge channels polarized in valley and spin. Recently, the possibility to encode information into the valley degree of freedom in two-dimensional layered materials with broken spatial inversion symmetry has generated a lot of interest [10][75], as it could give rise to a new kind of electronics : the valleytronics. Valleytronics in monolayer graphene has been less studied [30] in experiments because of the difficulty to manipulate valley isospin by electrostatic means; the inversion symmetry cannot be broken by usual gate voltage that generates electrostatic potential smoothly changing on an atomic distance scale. Unlocking this issue is valuable, since it implies the robustness of the valley isospin, a crucial merit of valleytronics in monolayer graphene. Finally, for quantum computing, it opens interesting perspectives, as we could achieve a new type of steadier flying qubits, where the information is not encoded into the trajectory, but into the valley isospin.

During my PhD, the main goal was to demonstrate that the valley-isospin can be electrically controlled, in monolayer graphene, thanks to an electronic Mach Zehnder interferometer with tunable transmissions. For this aim, I used as Wei et al. [84] a pn junction acting as MZI, mixing occurs at the two ends of the junction which play the role of electronic beam splitters. In their experiment, they cannot tune directly the beam splitters transmissions, which is necessary to obtain an output state with a controlled valley polarization. In order to overcome this difficulty, our idea was to add local gates at the junction ends to be able to tune the transmissions, and thus to obtain a full electrical control over the valley polarization of the output state. Then, another important aim of my work was to study the steadiness of the coherence of these valley polarized states, as this is the stumbling block if one wants to achieve quantum computations using valley flying-qubits.

Hereafter, is detailed the outline of this thesis. **Chapter 1** is a reminder about electron quantum optics, where the previous experimental studies on MZI and entangled states in GaAs are detailed. In a second part, I tried to briefly summarize the essential properties of graphene, and to expose why it is a good candidate to carry out electron quantum optics experiments. Afterwards, in **chapter 2**, I present the sample geometry that we elaborated, and the fabrication procedure that we developed. The sample is composed of a home made graphene sheet encapsulated between two hexagonal Boron Nitride crystals (hBN). Using conventional electron beam nano-lithography techniques, we patterned gates, and ohmic contacts on top of the graphene stack. Finally is detailed the experimental measurement set-up, which was completely developed and installed during my PhD, as the fridge arrived a few months after me. **Chapter 3** describes the core experiment carried out during my PhD, in which we demonstrated, that thanks to our sample geometry, we have a full electrical control over the valley polarization of the output state. Then, in **chapter 4**, is exposed the experimental investigation of characteristic coherence energy scales of the valley polarized states. For this purpose, we studied the dependence of MZI interference on the energy of incoming electrons : first by applying a DC bias on a edge state incoming on the MZI, then by increasing the temperature of the whole system. **Chapter 5** is centered on the experimental determination of the coherence length thanks to our sample, which has never been done in graphene in the quantum Hall regime. The coherence length is a length scale characterizing the quantum coherence of a system, it represents the typical propagation length on which an excitation looses its phase coherence due to information exchange. To measure it, one needs to measure the temperature dependence of interferences in at least three MZIs of different lengths. Remarkably, we could achieve this measurement with one sample. Finally, in **chapter 6**, is presented a study of spin waves (or magnons) and their effect on the coherence of the system. Magnons correspond to magnetic excitations propagating through a magnetic system, and may be an important source of decoherence in quantum Hall systems which can present a ferromagnetic bulk. By studying the effects of magnons on interference in a MZI, we showed that the coherence is effectively limited in DC bias by these collective bulk excitations.

Chapter 1

Electron quantum optics and Graphene

1.1 Electron quantum optics

1.1.1 Principle

Electron quantum optics is an emerging field whose goal is to mimic quantum optics experiment replacing the photons by electrons. This has fundamental implications as it changes the nature of the particles from bosons to fermions. In order to carry out electron quantum optics experiments, electronic equivalents of the basic elements used in quantum optics are needed. Typically a quantum optic experiment requires the following components :

- Beam splitters to split the incident photon into a quantum supperposition of two trajectories
- A way to guide the photons : fiber optics, mirrors...
- A single photon source and a single photon detector

In the last decades, equivalent electronic structures have been developed in GaAs/AlGaAs semiconducting heterostructures, the state of the art for each electronic component is briefly presented hereafter.

Guiding the electrons with the quantum Hall effect

Interestingly, at the interface of GaAs/AlGaAs heterostructure, a quantum well confines electrons, creating a two dimensional electron gas (2DEG).The application of a strong magnetic field perpendicularly to the 2DEG gives rise to the quantum Hall effect discovered in 1980 [43]. As illustrated in figure 1.1a, the bulk of the 2DEG becomes insulating as the electrons are trapped due to their cyclotron motion induced by the magnetic field. The current is only flowing through one dimensional chiral wires at the edges of the 2DEG, also called edge channels, and which can be seen as electron beams. In the presence of strong magnetic field, the zero field continuum of electronic states becomes quantified in energy, giving rise to the so called Landau Levels. The number of edge

channels corresponds to the number of filled Landau levels given by the filling factor ν. This leads to a quantification of the Hall resistance $R_h = \frac{h}{ie^2}$ with i the number of edge channels. Measurement wise, the quantum Hall effect is characterized, as shown in figure 1.1b, by the appearance of plateaus of Hall resistance at the quantified values, associated with a zero longitudinal resistance.

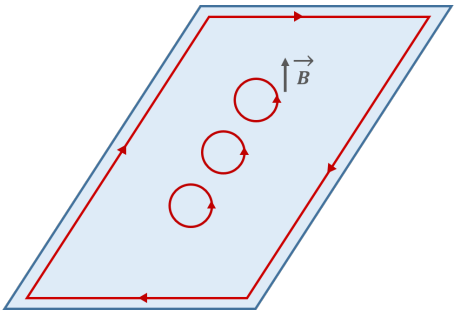

(a)

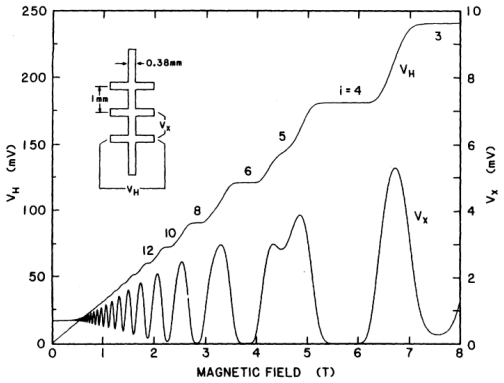

(b)

Figure 1.1: **Illustration of the quantum Hall effect.** (**a**) Illustration of the chiral edge channels (red) created in a 2DEG (light blue) when a strong magnetic field is applied. A few cyclotron orbits are traced to represent the trapping of the bulk electrons. (**b**) Hall resistance and longitudinal resistance measurements of a 2DEG while varying the magnetic field (from [15]).

The quantum point contact : an electronic beam splitter

A structure called quantum point contact (QPC) is a common way to obtain a beam splitter for electrons. As shown in figure 1.2a, it is composed of small metallic constriction deposited above the electron gas. By applying a voltage on the QPC, one can deplete the 2DEG below the gates thanks to the semiconductor gap. It is then possible to control the number of transmission channel through the QPC and even to tune the partial transmission of one channel continuously from 0 to 1, as shown in figure 1.2b.

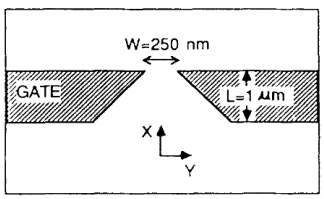

(a) QPC layout

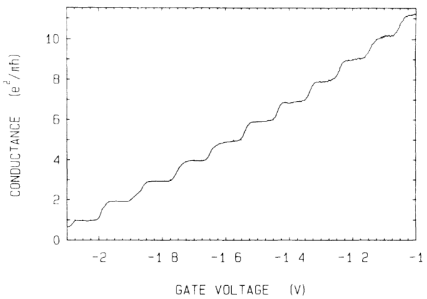

(b) QPC conductance

Figure 1.2: Historical measurement of the QPC conductance, extracted from [81]

Single electron sources :

Single electron sources are an essential building block to envision quantum computation with electrons. A first single electron source defined in energy was achieved in 2007 [24]. More recently a single electron source defined in time has been developed [21].

As shown in figure 1.3, the source defined in energy is composed of a quantum dot coupled to a conductor via a tunnel barrier (achieved thanks to a QPC). The idea is to apply a voltage step Δ on a gate capacitively coupled to the dot. When the highest energy level of the dot is driven above the Fermi sea, an electron can tunnel through the barrier at a rate $\frac{1}{\tau} = \frac{D\Delta}{h}$, with D the transmission of a single edge state through the QPC. One of the drawback of the single electron sources defined in energy is the lack of control on the escape time of the electron. In addition, it has been demonstrated [23] that the energy-resolved single electron excitations present a fast relaxation followed by a spin-charge separation, and thus modeling the electronic wave-function after a certain propagation time is difficult.

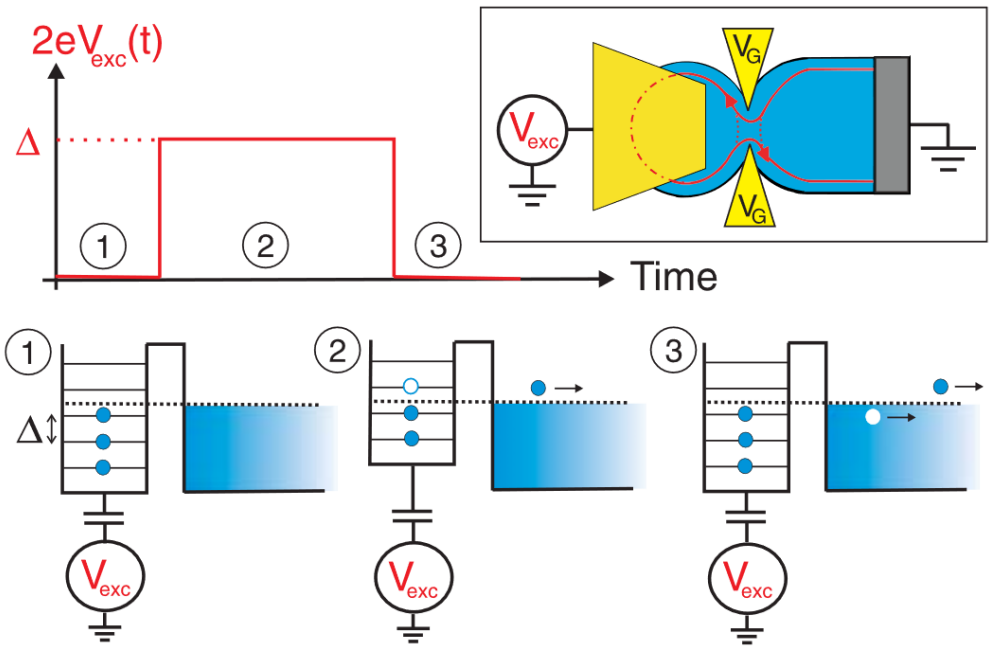

Figure 1.3: Layout of the on-demand energy defined single electron source, and the single electron injection scheme associated (extracted from [21]).

Another type of single electron source, called Leviton source, defined in time and not in energy was developed [21]. The idea is to directly apply a Lorentzian shape voltage pulse on an ohmic contact. A random voltage pulse affects all states below the Fermi energy, injecting a complex superposition of particle and hole excitations in the system. However, as shown theoretically by Levitov and co-workers [36][41][49], the application of a Lorentzian time-dependant potential should result in a minimal particle excitation free of holes. An experimental study [21], carried out in 2013, exhibited a minima of charge fluctuations (or shot noise) for a lorentzian wavefunction, the so called Leviton, injected

onto a tunnel barrier (QPC). This is in agreement with the picture of an excitation free of electron-hole pairs. Contrarily to the energy resolved electron source, the Leviton source does not exhibit a fast relaxation, but only a spin-charge separation [23] enabling a better understanding of the electron wave packet [20].

1.1.2 The electronic Mach Zehnder

Thanks to those building blocks it was possible to achieve the electronic equivalent of "Fabry-Pérot and Mach Zehnder interferometer (MZI), providing the necessary quantum gate for an all-linear quantum computation" [24]. The MZI is at the center of this PhD, so hereafter are presented a brief reminder of the principles of the optical MZI and a state of the art of its electronic version in GaAs/AlGaAs heterostructures.

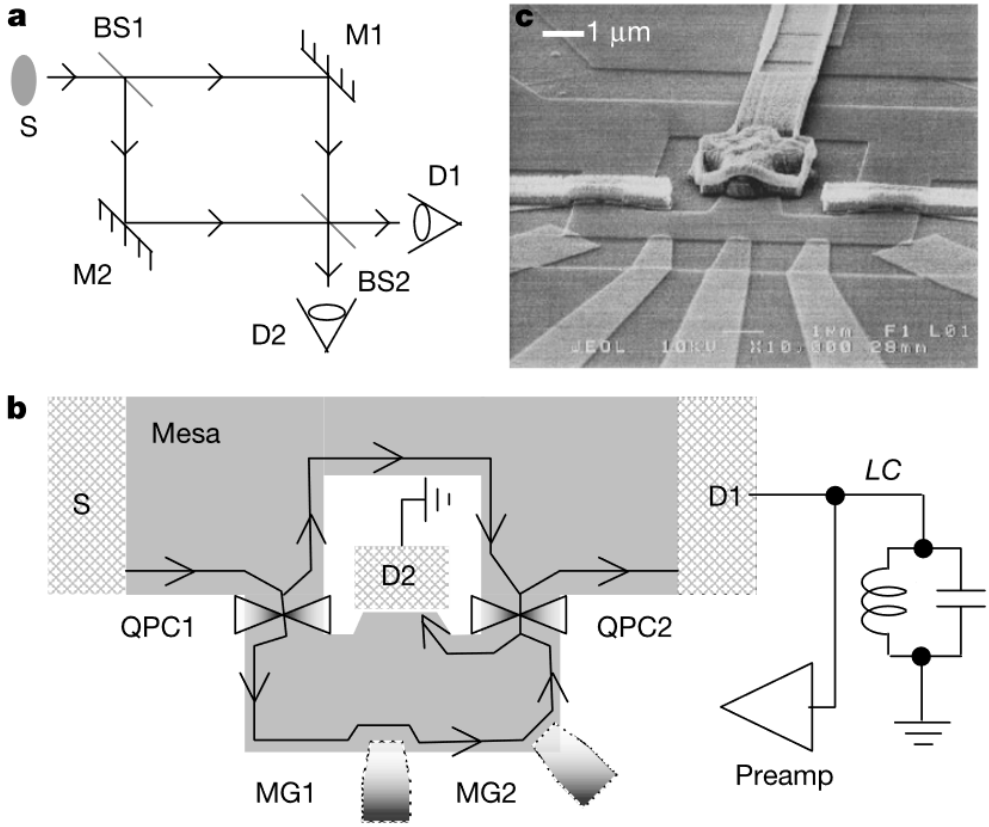

Figure 1.4: Optical MZI layout (a). Schematic of the first MZI achieved at the Weizman Institute (b), and SEM image of the actual sample (c). Figure extracted from [37].

In optics, the MZI is a simple set up composed of two mirrors and two beam splitters as shown in the (a) layout in figure 1.4. An incident light beam is separated in two on a first beam splitter with a transmission (reflection) amplitude t_1 (r_1). As the flux is conserved : $|t_1|^2 + |r_1|^2 = T_1 + R_1 = 1$. The two light beams are then recombined on a second beam splitter with a transmission (reflection) amplitude t_2 (r_2). If the coherence length of the photon is larger than the size of the MZI, the amplitude on the outputs,

t_{D1} and t_{D2}, correspond to the sum of the complex amplitudes from the upper path and the lower path. One can express t_{D1} and t_{D2} in the form of the equations 1.1 and 1.2 (as explained in [35]), where ϕ_{up} (ϕ_{down}) are the phase accumulated on the upper (lower) path.

$$t_{D1} = r_1 e^{i\phi_{down}} t_2 + t_1 e^{i(\phi_{up}+\pi)} r_2 \tag{1.1}$$

$$t_{D2} = r_1 e^{i\phi_{down}} r_2 + t_1 e^{i\phi_{up}} t_2 \tag{1.2}$$

A π shift appears in equation 1.1 because on the second beam splitter there are two incident beams of different direction [35]. From the transmission amplitudes, one can compute the probability transmissions in outputs D_1 and D_2 as shown in equations 1.3 and 1.4, where ϕ is a phase coming from $\arg(t_i)$ and $\arg(r_i)$.

$$T_{D1} = |r_1 t_2|^2 + |t_1 r_2|^2 - 2|r_1 t_1 r_2 t_2|\, cos(\phi_{down} - \phi_{up} + \phi) \tag{1.3}$$

$$T_{D2} = |r_1 r_2|^2 + |t_1 t_2|^2 + 2|r_1 t_1 r_2 t_2|\, cos(\phi_{down} - \phi_{up} + \phi) \tag{1.4}$$

Therefore, the two light intensities measured in D_1 and D_2 oscillate sinusoidally in phase opposition with the difference $\phi_{down} - \phi_{up}$. In the case where the two arms of the MZI have equal lengths, there is no phase difference : $\phi_{down} - \phi_{up} = 0$. A phase difference can be introduced by adding a transparent medium with a different optical index or by changing the length of one path. Finally, one can remark that $T_{D1} + T_{D2} = 1$, which means that no photon is lost.

In 2003, the first electronic MZI was achieved at the Weizmann Institute [37] in GaAs/AlGaAs heterostructure. As shown in the schematic of their sample in figure 1.4, two QPCs act as the two electronic beam splitters of a MZI, and ohmic contacts serve as electronic detectors. Thanks to the chiral edge channels created in the quantum Hall regime, they can guide the electrons injected from ohmic contact S to QPC_1, where the incoming edge current is splitted between the upper and the lower trajectories. Later on the two trajectories are recombined on QPC_2, the transmitted current is then measured through contact D_1. The reflected current at QPC_2 is collected thanks to the grounded ohmic contact D_2, avoiding the reinjection of the current inside the interferometer. Due to the Aharanov Bohm effect, the flux of the magnetic field B through the area enclosed A by the upper and the lower part generates a phase difference between the two trajectories $\phi = \frac{2\pi BA}{\Phi_0}$, with Φ_0 the quantum flux. The modulation gates MG_1 and MG_2 enables to tune the length of the lower path, thus to control the area enclosed and the phase shift between the two paths. As shown in figure 1.5a and 1.5b, sinusoidal oscillations of the current intensity in D_1 as a function of the magnetic field B and as function of the voltage MGs where obtained. Therefore this system is an electronic equivalent of the MZI, where the oscillations in light intensity are replaced by oscillations in current intensity.

The oscillations can be characterized thanks to a quantity called visibility V, defined as :

$$V = \frac{T_{max} - T_{min}}{T_{max} + T_{min}} \tag{1.5}$$

T_{max} (T_{min}) is the maximum (minimum) value of the oscillating current intensity. In other words, the visibility corresponds to the ratio between the amplitude of the sinusoidal oscillations and their offset. Using equations 1.3 and 1.4, one can determine the expected visibility of the current oscillations in D_1 (equation 1.6) and in D_2 (equation 1.7) as

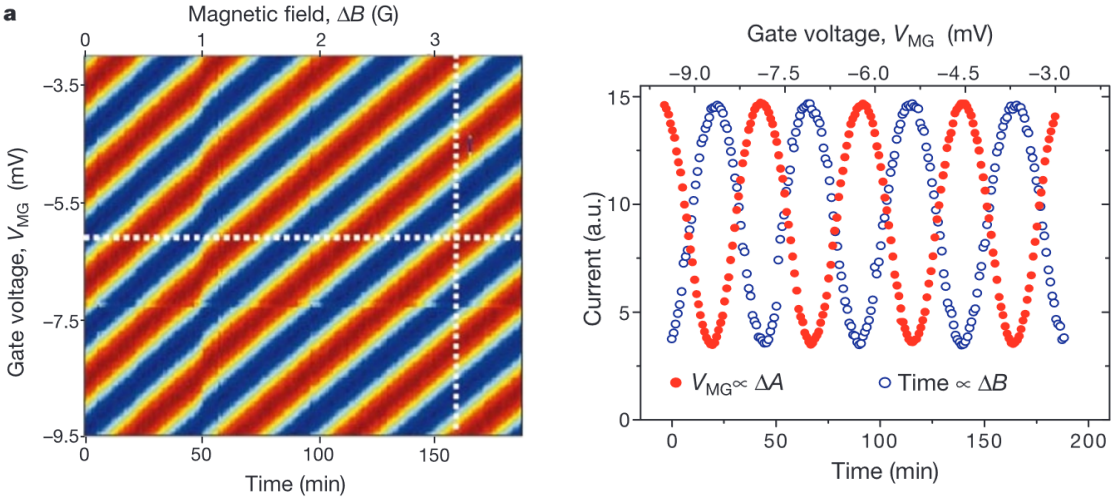

(a) (b)

Figure 1.5: Measurements of the first electronic MZI at $\nu = 1$, extracted from [37]. (**a**) Sinusoidal oscillations of the current collected in D_1 as a function of the magnetic field and the voltage applied on the MG gates, while the two QPCs are set to transmission $T_1 = T_2 = 0.5$. (**b**)Single traces (corresponding to the dotted line in the color map in (a)) of the current collected in D_1 as a function of the modulation gate voltage V_{MG} in blue, and as a function of the magnetic field B in red.

a function of the probability of transmission and reflection of both beam splitters T_1, $R_1 = 1 - T_1$, T_2, and $R_2 = 1 - T_2$.

$$V_{D1} = \frac{2\sqrt{R_1 T_1 R_2 T_2}}{R_1 T_2 + T_1 R_2} \tag{1.6}$$

$$V_{D2} = \frac{2\sqrt{R_1 T_1 R_2 T_2}}{R_1 R_2 + T_1 T_2} \tag{1.7}$$

The maximum visibility $V_{D1} = 1$ is obtained when both beam splitters are exactly half-transmitting ($T_1 = T_2 = 0.5$). In the experiment of the Weizmann institute [37], the maximum visibility in this configuration is 0.62, which means that some decoherence effects limit the maximum visibility. In following works in GaAs/AlGaAs heterostructures, visibilities as high as 0.9 have been found [62]. Finally in [37], they measured the visibility as function of the transmission probability T_1 of QPC_1, while the transmission probability of QPC_2 was fixed at $T_2 = 0.5$. In this configuration, equation 1.6 becomes $V_{D1} = 2\sqrt{T_1(1 - T_1)}$. As shown in figure 1.6, the experimental visibility dependence on T_1 is in good agreement with this law when adding a renormalization coefficient $\eta = 0.6$.

1.1.3 Entangled states and quantum computation

In electron quantum optics, a novel and appealing approach, the flying qubit [9][28], was developed in analogy with the single photon qubits manipulated in quantum optics. The state of the flying qubit is encoded into the electron trajectory, and a superposition of

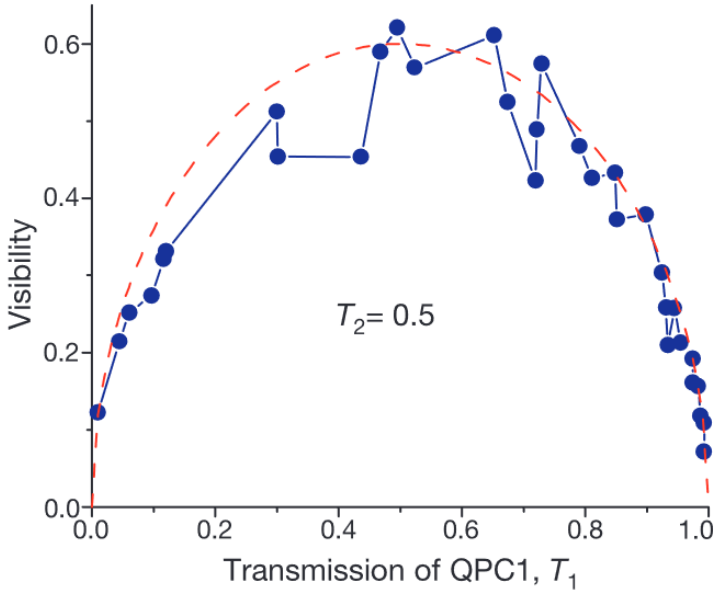

Figure 1.6: Visibility of the interference pattern (blue points) as a function of the transmission T_1 of QPC_1, while the transmission at QPC_2 is fixed at $T_2 = 0.5$. Red dashed line corresponds to $2\eta\sqrt{T_1(1-T_1)}$ with $\eta = 0.62$. Extracted from [37]

two trajectories can be obtained thanks to a QPC, forming an Hadamard gate. This allows to perform "quantum operations on qubits while there are coherently transferred" [9], thus generating a new paradigm for quantum information processing in which one can envision non-local architectures. The achievement of the electronic MZI paved the way towards the creation of quantum gates for flying qubits in electron quantum optics. Indeed, one of the building blocks to envision multi-qubits quantum gates is the possibility to generate entangled states.

In 2004, Samuelsson et al. [74] proposed an electronic implementation of the Hanbury Brown Twiss (HBT) experiment, based on a double MZI geometry as shown in figure 1.7, giving rise to a two-particle interference effect. Electrons streams are injected from ohmic contacts 2 and 3, and are respectively partitioned into two streams at QPC C and D. The electrons emitted in 3 (2) reflected at QPC D (C) interfere on QPC A (B) with the electrons emitted in 2 (3) and transmitted at QPC C (D). If one electron is detected in 5 and one in 8, two quantum mechanical probability amplitude contribute to this event : an electron going from 3 to 5 and one from 2 to 8, or an electron going from 2 to 5 and one from 3 to 8. As those two-particle scenarii are indistinguishable, they can interfere. One can demonstrate that the current cross correlations between 5 and 8 are given by $S_{58} = \frac{-e^3V}{4h}(1 + cos(\Phi_1 + \Phi_2 - \Phi_3 - \Phi_4))$, with Φ_i the phases accumulated on the different sections of the double MZI (as shown in figure 1.7). A magnetic field is applied creating an Aharanov Bohm flux through closed loops, therefore the total phase accumulated in the double MZI is : $\Phi_1 + \Phi_2 - \Phi_3 - \Phi_4 = \frac{2\pi BA}{\Phi_0}$, with B the magnetic field, A the area enclosed, and Φ_0 the flux quantum. Moreover, as ohmic contacts 1 and 7 are grounded, single particle trajectories never form a closed loop, thus the magnetic field

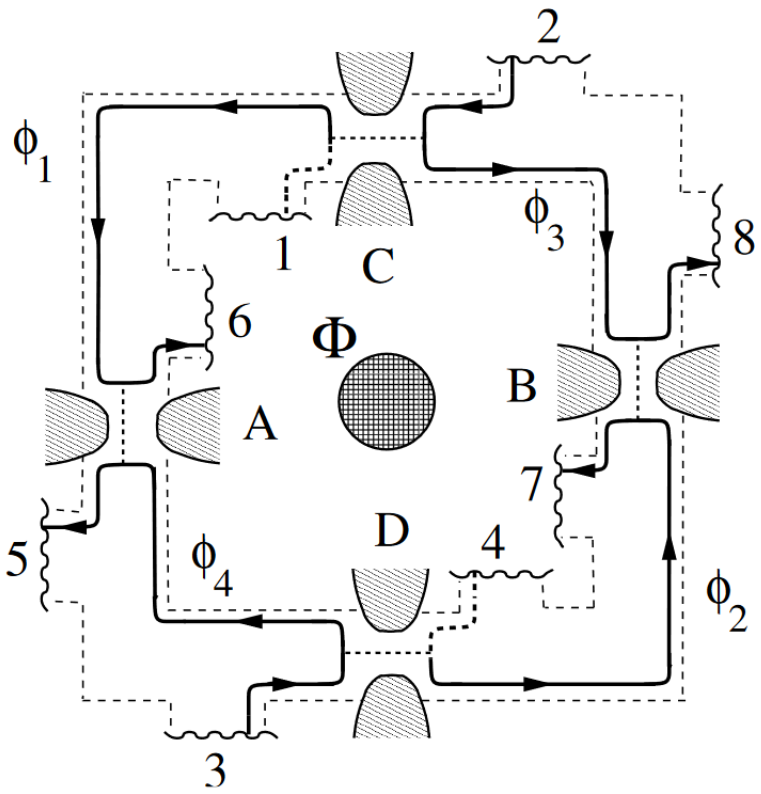

Figure 1.7: Schematic of the double MZI proposed by Samuelsson et al. [74]. It is composed of 4 QPCs A,B,C,D, and 8 ohmic contacts : 2 and 3 are the injection ohmic contacts, 4 and 1 are grounded, output current is measured through 5,6,7, and 8. An Aharanov Bohm flux is imposed at the center of the sample, but has no influence on the single particle properties.

has no influence on them. Finally, the two-particule interference effect should generate oscillations of the cross current correlator S_{58} with the magnetic field, while the single particle quantities (currents, autocorrelations) should be independent of the magnetic field. In addition, violation of Bell's inequality, accompanying the generation of entangled pairs, can be obtained for specific tuning of the beam splitters transmission in analogy with the optimal polarization in the Aspect experiment.

This proposal was experimentally implemented by Neder et al. [62] in a GaAs/AlGaAs sample. As shown in figure 1.8a, the sample used is composed of two symmetrical loops separated by the Middle Gate (MG), each one containing two QPCs. By opening the MDG, one can go from a configuration with two separated MZI to a two-particle interferometer as proposed by Samuelsson et al. [74]. In the latter configuration, auto-correlation measurement in D_2 and D_4 exhibited no dependence on magnetic field B or modulation gate voltage V_{MG} (which changes the area enclosed). However, the cross-correlation of currents in D_2 and D_4 exhibits oscillations directly visible in B and V_{MG} (figure 1.8c), and more clearly appearing in the FFT (figure 1.8b).This measurement is thus a clear signature of a two-particle interference. Nevertheless, the low visibility of the oscillations in the current cross correlations was not sufficient to observe a violation of Bell's inequality,

and thus to prove the presence of entangled states.

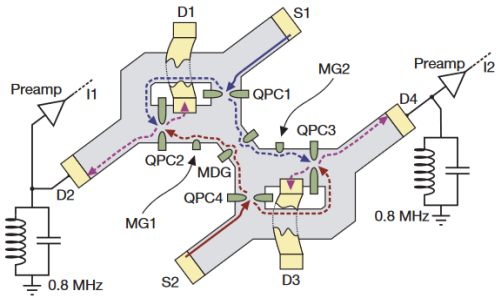

(a) Schematic of the two-particle interferometer. Electrons are injected from ohmic contacts S_1, S_2. Ohmic contacts D_1 and D_3 are grounded. Current fluctuations are measured in D_2 and D_4.

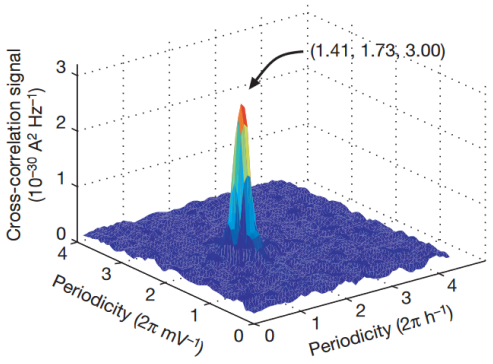

(b) FFT of current cross-correlations measured between D_2 and D_4.

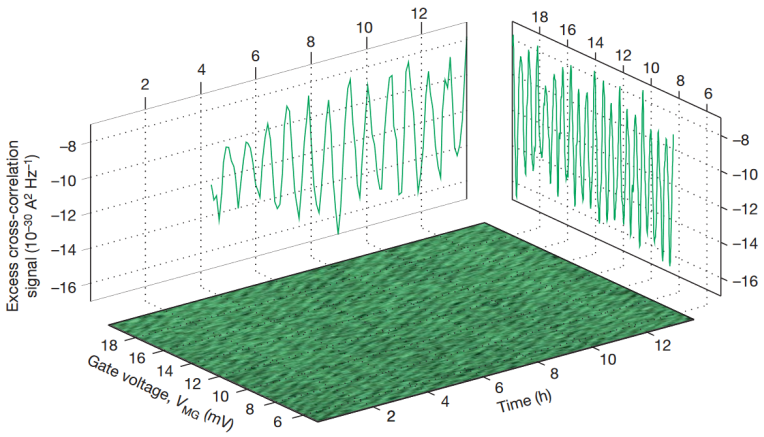

(c) Cross-correlation measured between D_2 and D_4.

Figure 1.8: Two-particle interferometer sample achieved by Neder et al. [62].

1.1.4 Limitations of GaAs/AlGaAs heterostructures and graphene perspectives

To observe interference effects in GaAs/AlGaAs heterostructures, experimental studies were typically carried out at very low temperature, around $20mK$, because the quantum coherence of the system is extremely fragile. Indeed, as shown in figure 1.9, the visibility of the MZI oscillations completely vanishes above $100mK$, and for applied DC voltages of a few tens of μV. In addition, most of the studies were actually achieved at filling factor $\nu = 2$ (steadier than $\nu = 1$) as the edge channel spectroscopy in the integer quantum Hall regime [4], the origin of decoherence [73], or the Hong Ou Mandel experiment [13]. Thanks to all these studies, it was understood that a strong capacitive coupling between the 2 co-propagating edge channels was at the origin of decoherence. As shown in [73], in these conditions the coherence length l_ϕ is around $20\mu m$ at $20mK$. Thus a MZI should

not exceed this size, which imposes an important constraint on sample fabrication. An interferometer of $0.1mm$, much bigger than l_ϕ, was recently achieved by Duprez et al. [22] thanks to a clever sample design limiting the coupling between co-propagating edge channels, however the sample fabrication is challenging as it requires a lot of gates. Therefore, it seems difficult to envision more advanced quantum operations in GaAs/AlGaAs heterostructures.

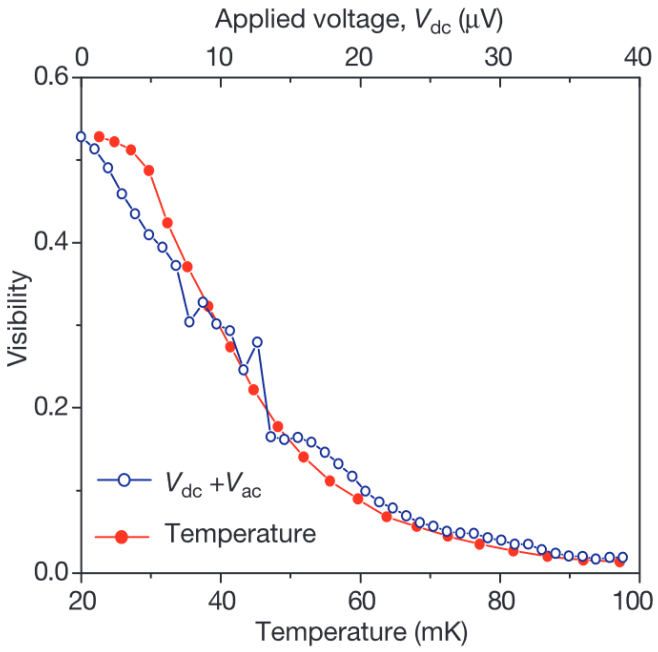

Figure 1.9: Measurement at filling factor $\nu = 2$ of the visibility of a MZI as a function of the DC bias applied, and of the temperature (extracted from [37]).

The discovery of graphene in 2004 [65], a monolayer of carbon atoms, opened countless research avenues. In particular the demonstration of its unconventional quantum Hall effect [66] [91] revealed that electrons in graphene are behaving as a two dimensional gas of massless Dirac fermions. But the existence of the quantum Hall effect also made graphene a potential candidate for electron quantum optics experiment. The main advantage of graphene compared to GaAs/AlGaAs heterostructures is that it exhibits steady quantum properties. For instance, the quantum Hall effect, which was never observed above 30K in any other materials, was obtained at room temperature [64] (at high magnetic field). This persistence is due to the large cyclotron gaps $\hbar\omega_c$ in graphene. Finally the width of the edge channels was estimated to be 4nm thanks to a measurement of edge magnetoplasmons [48], whereas it is much larger in GaAs/AlGaAs heterostructures around $2\mu m$ [92] [46]. Therefore the geometrical capacitance between edge channels should be much smaller in graphene than in GaAs, limiting the decoherence effects. Due to all this, graphene is a promising material for electron quantum optics.

1.2 Graphene a new material for electron quantum optics

1.2.1 Graphene a brief presentation

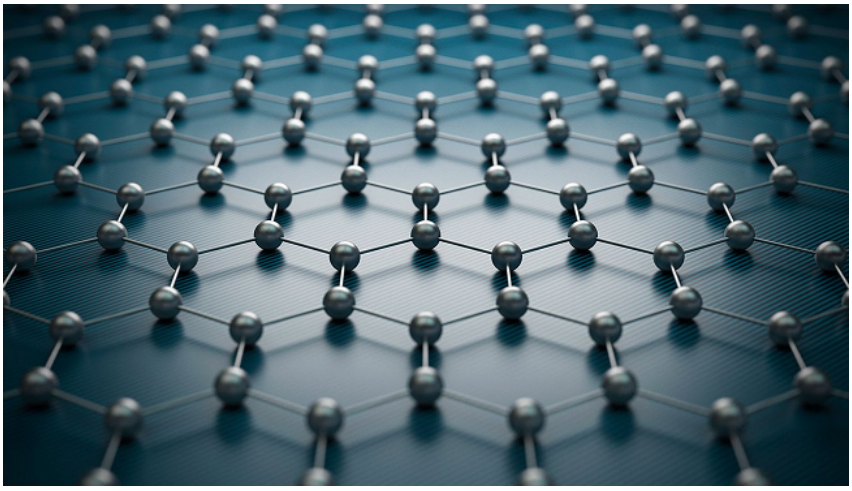

Figure 1.10: Artist view of a graphene layer.

Graphene is a monolayer of carbon atoms arranged in an honeycomb lattice, as shown in figure 1.10. It is the basic unit of graphite, which is a stack of graphene layers attached by van der Walls forces. For a long time, it was believed that graphene could not exist on its own, as it would be unstable according to some thermodynamical argument. However, as briefly evoked in the previous section, thanks to a simple scotch tape technique a team from Manchester University was able to isolate a graphite composed of few graphene layers in 2004 [65], and a single graphene layer in 2005 [67]. The principle of the scotch tape technique, or micromechanical exfoliation, is really simple. A small graphite crystal is deposited on scotch tape, which is then closed and opened several times. By doing so, one can overcome the Van der Walls forces, which glue together the graphene layers composing the graphite crystal. Thus the repetition of this process leads to the formation of thinner and thinner graphite crystals up to the monolayer. These crystals are then deposited on silicium chips with a $300nm$ thick oxyde on top, which enables to directly spot the graphene layers thanks to their color with an optical microscope [12] (see figure 1.11). This raised a lot of interest as it was the first observation of a perfectly bi-dimensional crystal, and A. Geim and K. Novoselov were awarded the Physics Nobel price in 2010 for this discovery.

But more than being just a perfectly bi-dimensional crystal, graphene has exceptional properties that caused the scientific effervescence after its discovery. In particular, in the first publication on graphene [65] an electric field effect was reported, which means that by simple application of a gate voltage one can control the carrier density in a graphene sheet. This property opens wide potential applications in electronics. Moreover, electrons in graphene show a relativistic behavior and the low-energy excitations can be described by a relativistic quantum mechanics equation, the so called Dirac equation [29]. This was demonstrated through transport measurements done in parallel by the Manchester group [66], and P. Kim's group at Columbia University [91]. Therefore

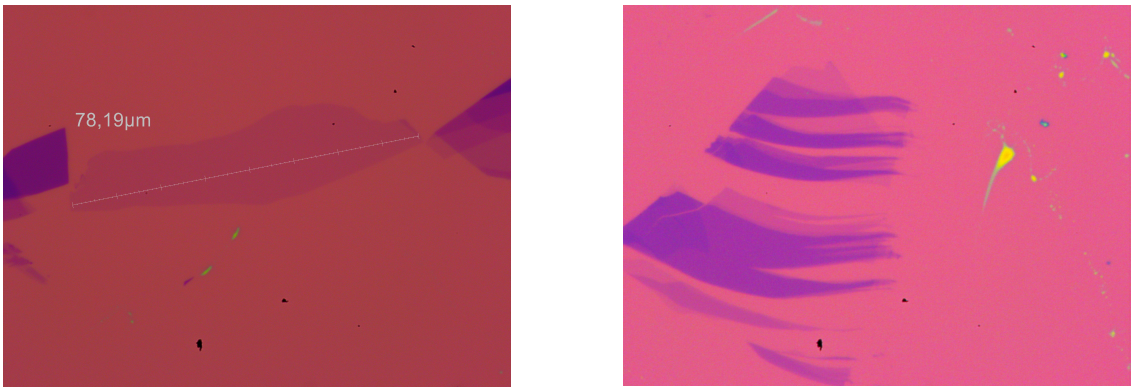

(a) (b)

Figure 1.11: **Optical microscope observations** of my exfoliation of graphene monolayer, and few layers graphite deposited on silicium chip with a $300nm$ thick $Si0_2$ oxyde. (**a**) Big monolayer graphene flake. (**b**) Crystal with graphene (light purple), bi-layer, and few layers graphite. The darker the more layer there are.

electrons in graphene may be viewed as massless charged fermions, whereas all existing massless elementary particles are charge neutral. This makes graphene a good candidate to test quantum electrodynamics properties, such as the Klein paradox or unusual Andreev reflection [10]. The Klein paradox predicted by the physicist of the same name in 1929 corresponds to the "the unimpeded penetration of particles through high and wide potential barriers" [40], this phenomenon was so far not observed with elementary particles. However, as predicted by Katsnelson et al. [40], the massless Dirac fermions in grahene confronted to an electrostatical barrier should give the possibility to test the Klein tunneling, this was experimentally observed in graphene pn junction in 2009 [79]. This phenomenon underlines the possible use of graphene as bridge between condensed matter and high energy physics.

Most of the striking properties of graphene described above are coming from its crystallographic structure and the resulting band structure, which will be described hereafter following M. Goerbig's review [29].

Crystal structure of graphene

A carbon atom has 6 electrons and its ground state is $1s^2 2s^2 2p^2$. Two of these are core electrons, close to the nucleus, and only the four outer electrons, or valence electrons, form chemical bounds. In the presence of other atoms, the four valence electrons spread in four equivalent quantum mechanical states, $|2s\rangle$, $|2p_x\rangle$, $|2p_y\rangle$, and $|2p_z\rangle$. In the case of graphene, we have a quantum mechanical superposition of states $|2s\rangle$, $|2p_x\rangle$, $|2p_y\rangle$, called the sp^2 hybridization, where the three hybridized orbitals are in the graphene plane with 120° between each of them (see figure 1.12b). The $|2p_z\rangle$ orbital is unhybridized and orthogonal to the plane. The three inplane orbitals form the covalent bounds generating graphene honeycomb lattice, whereas the delocalisation of all the $|2p_z\rangle$ electrons, called π electrons, create a 2DEG.

As shown in figure 1.12a, the graphene honeycomb lattice is composed of two nonequiv-

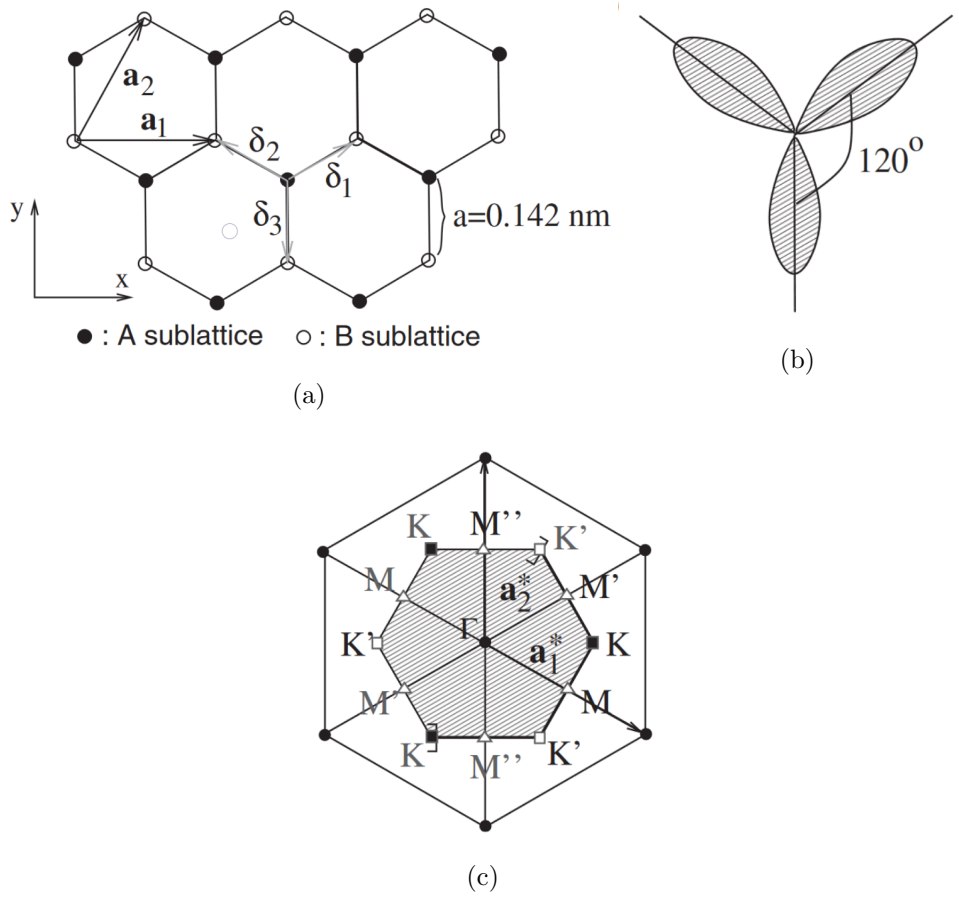

Figure 1.12: (a) Graphene honeycomb lattice. The carbon atoms are separated by a distance $a = 0.142nm$. The vectors $\mathbf{a_1}$ and $\mathbf{a_2}$ are the basis vector of the triangular lattice. (b) Schematic view of the sp^2 hybridization. The orbitals form an angle of 120°. (c) Reciprocal lattice of the triangular lattice with primitive vectors $\mathbf{a_1^*}$ and $\mathbf{a_2^*}$. The shaded region represent the first Brillouin Zone (BZ), with its center Γ and the two inequivalent corners K (black squares) and K' (white squares). The three inequivalent crystallographic points M, M', and M" are also represented (white triangles). Extracted from M. Goerbig's review [29]

alent crystallographic sites A and B, forming two sulattices. Consequently, it is not a Bravais lattice. However graphene can be described as a triangular Bravais lattice with a two-atom basis, with one atom from A sublattice and one atom from B sulattice. The basis vector $\mathbf{a_1}$ and $\mathbf{a_2}$ of this triangular lattice are represented in figure 1.12a. The distance between nearest neighbor C atoms is $a = 0.142nm$. The reciprocal Bravais lattice is also a triangular lattice with basis vectors $\mathbf{a_1^*}$ and $\mathbf{a_2^*}$, as represented in figure 1.12c. The first Brillouin zone (BZ) corresponds to the shaded hexagon, whose submits are composed of two inequivalent point K and K'. The low-energy excitations are centered around these points in the reciprocal space. Finally, these two inequivalent points are extremely important as they give rise to the valley degree of freedom in graphene (which will be detailed

in what follows).

Graphene band structure

A tight-binding computation of the energy bands for the π electrons, responsible for the low energy electronic properties of graphene, can be achieved as explained in [29]. The band structure obtained is shown in figure 1.13. It is composed of a valence band π (lower band) and a conduction band π^* (higher band) meeting at the so-called Dirac points D and D', which coincides with the points K and K' of the reciprocal lattice. Each C atom has one electron $|2p_z\rangle$, thus the valence band π is completely filled and the conduction band completely empty. In this configuration, the Fermi surface is only formed of the two Dirac points. Since we have a pair of Dirac points D and D', the low-energy excitations around these points are doubly degenerate, forming the so called twofold *valley degeneracy*. Moreover, two spin states are accessible to electrons, spin-up and spin-down, generating another twofold degeneracy. The combination of the valley and spin degeneracies give rise to a *fourfold degeneracy* in graphene. At the vicinity of

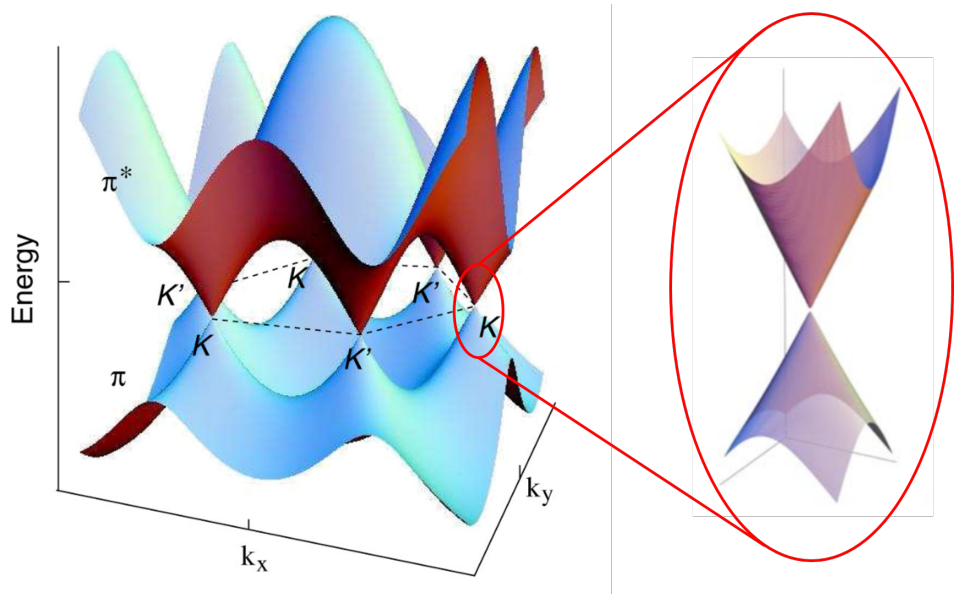

Figure 1.13: Energy dispersion as a function of the wave-vector components k_x and k_y, obtained within the tight-binding approximation. One distinguishes the valence band π from the conduction band $\pi*$. Right inset : zoom in on a Dirac cone structure, at the vicinity of K. Figure extracted from [29] (see review for precisions).

the Dirac points, as we consider low energy excitations, one can linearise the dispersion relation which can be expressed as follow (computation done in [29]) :

$$\epsilon^{\lambda}{}_{\mathbf{q},\zeta} = \lambda \hbar v_F |\mathbf{q}| \tag{1.8}$$

In equation 1.8, ζ represents the valley degree of freedom K or K', $\mathbf{q}$ the wave vector, and ϵ the energy. The band is labeled by $\lambda = \pm$: $\lambda = -$ corresponds to the valence band π, $\lambda = +$ denotes the conduction band π^*. The Fermi velocity v_F is approximately of

$10^6 ms^{-1}$ in graphene, and thus 300 times smaller than the speed of light c. Interestingly, the dispersion relation becomes linear as a function of the wave vector $\mathbf{q}$, forming locally around the points K and K' the Dirac cones. Another remarkable point is that energy dispersion is electron-hole symmetric : $\epsilon^{\lambda}{}_{\mathbf{q},\zeta} = -\epsilon^{-\lambda}{}_{\mathbf{q},\zeta}$.

The electric effect in graphene (measured by Novoselov et al. [65]), which is the possibility to tune the carrier density by simple application of a gate voltage, can be explained thanks to the Dirac cone picture. Indeed, as shown in figure 1.14, the graphene resistance is symmetrical with the gate voltage applied, and presents a peak at zero-bias. As shown in the cartoon, at zero-bias the Fermi level is exactly located at the Dirac point, where there is no charge carrier. For positive (negative) voltage, the Fermi level is moved in the conduction (valence) band inducing electrons (holes) charge carriers, and resistance decreases.

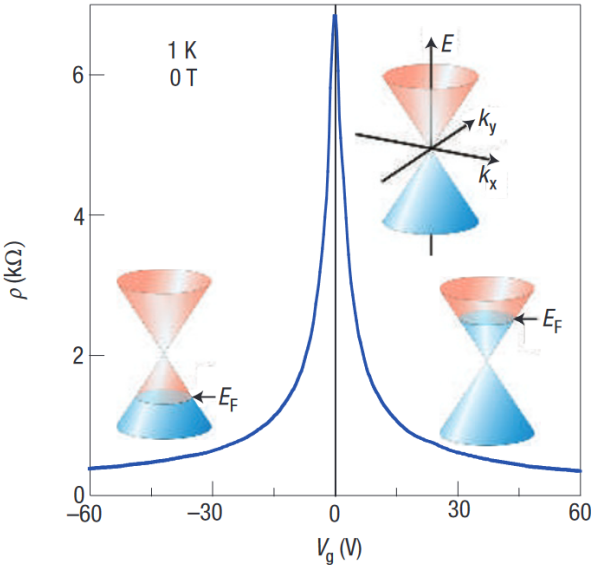

Figure 1.14: Resistance measurement through a graphene sheet as a function of the gate voltage applied. In the insets are shown cartoons of the low-energy excitation spectrum, or Dirac cones, with the different Fermi energy depending on gate voltage. Figure extracted from [26].

1.2.2 Quantum Hall effect in graphene

An unusual quantum Hall effect

The discovery of graphene and its electric field effect was followed one year later by experimental evidences of an unconventional quantum Hall effect, called relativistic quantum Hall effect (RQHE), through two studies one by the Manchester University group [66] and one by P. Kim's group at Colombia University [91]. As explained briefly at the beginning of this part (section 1.2.1), these were milestones experiments as it proved the relativistic nature of low energy excitations in graphene. As shown in M. Goerbig review of electronic properties of graphene in strong magnetic field [29], by solving the

Hamiltonian for charged particles in a magnetic field, one can obtain the energy spectrum for relativistic Landau Levels (LL) :

$$\epsilon_{\lambda,n} = \lambda \frac{\hbar v_F}{l_B} \sqrt{2n} \tag{1.9}$$

In equation 1.9, the quantum number $\lambda = \pm$ denotes the states of positive and negative energy. $l_B \approx 26nm/\sqrt{B[T]}$ is the magnetic length in graphene, and n is the LL index. As

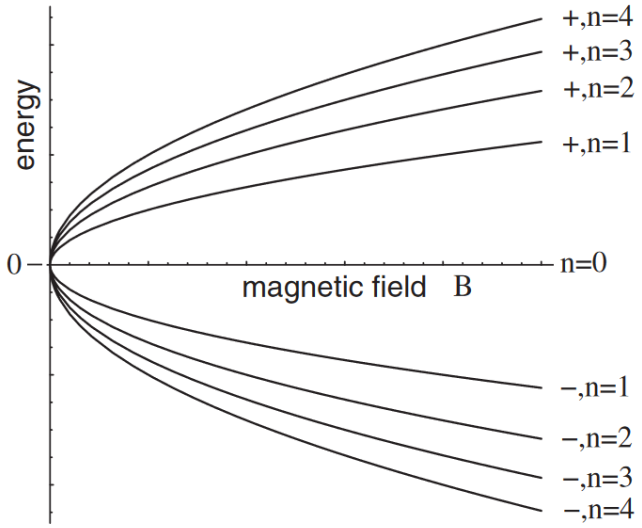

Figure 1.15: Relativistic Landau levels as a function of the magnetic field. Figure extracted from [29].

shown in figure 1.15, the LL energies are proportional to $\lambda\sqrt{Bn}$, with B the magnetic field. One can remark that this LL structure is quite different from the one observed in GaAs/AlGaAs heterostructures, where the LL spacing is constant at fixed magnetic field. Furthermore, LLs are highly degenerate states with the number of flux quanta. One usually quantify the filling of these levels thanks to the filling factor ν which corresponds to the ratio between the electronic density n_{el} and the flux density n_B :

$$\nu = \frac{n_{el}}{n_B} = \frac{h n_{el}}{eB} \tag{1.10}$$

As evoked in section 1.1.1, in GaAs/AlGaAs heterostructures the quantization of the LLs leads to the integer quantum Hall effect (IQHE), which is characterized by the quantization of the Hall resistance $R_H = \frac{h}{ie^2}$ with i the integer part of the filling factor ν. This IQHE is accompanied by a twofold spin degenaracy, which means that the Hall resistance quantization is achieved for even filling factors : $\nu = 2n$. This spin degeneracy can be lifted at high enough magnetic field through the Zeeman effect which generates an energy difference between the two spin branches given by $\Delta_Z = g\mu_B B$ (with g the g-factor of the material and μ_B the Bohr magneton). One of the main difference when

comparing the quantum Hall effect in graphene and in GaAs/AlGaAs heterostructures, is that there is, in addition to the usual twofold spin degeneracy, a twofold valley degeneracy due to the presence of Dirac cones at the inequivalent points K and K' of the first BZ. This generates the so called fourfold spin and valley degeneracy. One can show that the Hall resistance is thus quantized for the RQHE following the filling factor sequence given in equation 1.11.

$$\nu^{RQHE} = 2(2n+1) \tag{1.11}$$

Each plateau in the RQHE is separated by four in terms of filling factor, and not by two as in the IQHE in GaAs/AlGaAs heterostructures. Moreover, when $\nu = 0$, i.e. at the Dirac point, all the negative energy states ($\lambda = -$) are filled and all the positive ones are empty ($\lambda = +$). Therefore, $\nu = 0$ corresponds to a half filled $n = 0$ LL. The quantum Hall effects appears for completely filled (empty) $n = 0$ LL, i.e. $\nu = 2(-2)$, explaining equation 1.11 sequence of filling factor for the RQHE.

Experimentally, P. Kim group measured the Hall resistance and the longitudinal resistance of graphene sample under strong magnetic field $B = 9T$ as a function of a global gate voltage. By changing the gate voltage, one can tune the carrier density, and therefore control the filling of the different LLs. As shown in figure 1.16, the Hall resistance exhibits plateaus quantized following equation 1.11, thus proving the existence of the RQHE.

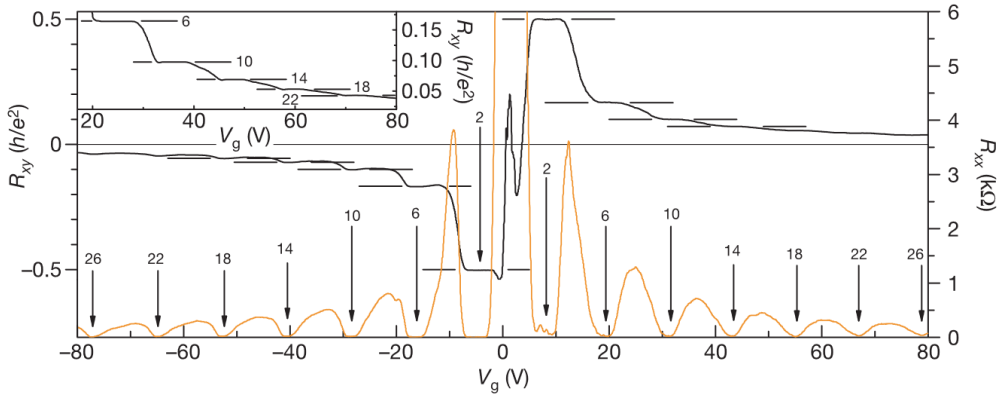

Figure 1.16: Hall resistance (black) and longitudinal resistance (orange) as a function of gate voltage at fixed magnetic field $B = 9T$ and at $20mK$. The inset in the upper left corner shows a detailed view for high filling factors plateaus. Figure extracted from [91]

Lifting the spin-valley fourfold degeneracy

Experimental observations : As explained in the previous section, each LL has a fourfold spin-valley degeneracy, which gives rise to the unusual sequence of the RQHE with Hall plateaus appearing at filling factors $\nu = \pm 2, \pm 6...$ However for high quality graphene samples, measurements in 2006 revealed intermediate plateaus of resistance for integer filling factors $\nu = \pm 1, \pm 4$ [90][38] in addition to the latter sequence, indicating a partial lifting of the degeneracy. Later on, a full lifting of the fourfold spin-valley degeneracy was observed by Dean et al. [16] thanks to extremely high quality graphene samples, obtained by the deposition of the graphene on top of a thin exfoliated Boron Nitride (BN) crystal.

This was the first step of the full encapsulation technique, developed by P. Kim's group, where graphene is placed in between of two BN crystals. The encapsulation technique group was a major advance for the achievement of high quality graphene samples; this is the procedure we used for our samples (detailed in chapter 2). An example of a longitudinal resistance measurement (Zimmermann et al. [94]) performed on a state of the art encapsulated graphene sample is displayed in figure 1.19. The longitudinal resistance is cancelled around each integer value of the filling factor ν for a magnetic field $B > 7T$, thus exhibiting the full degeneracy lifting.

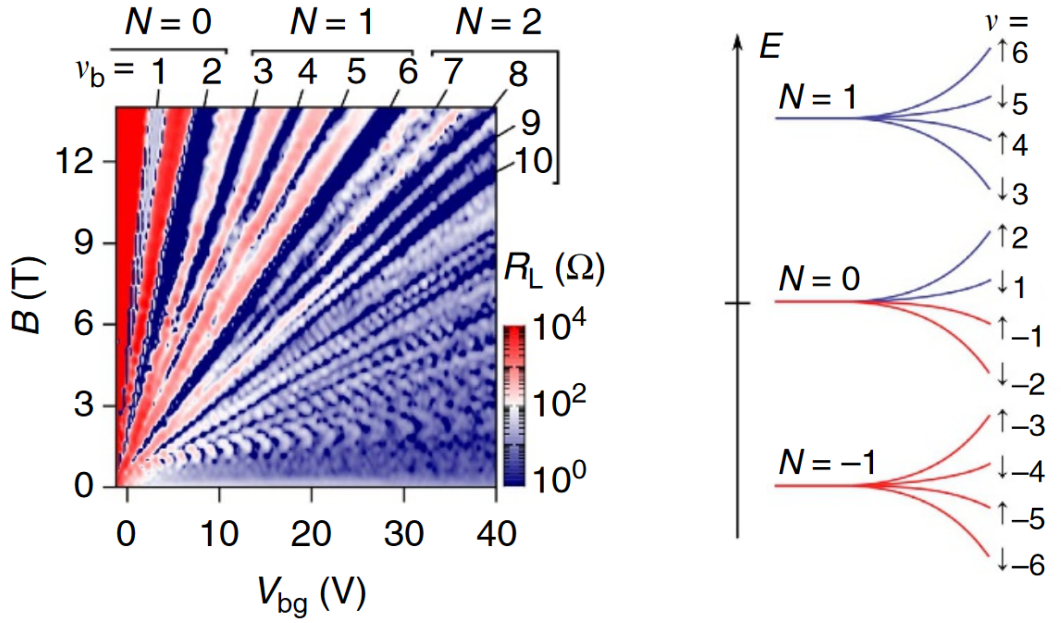

(a) $\Delta_Z > \Delta_{kek}$ (b)

Figure 1.17: (a) Fan diagram of longitudinal resistance R_L measured at $0.05K$ as a function of the back gate voltage V_{bg} and of the magnetic field B. The indexed blue strips indicate bulk quantum Hall states, and N is the LL index. (b) Energy diagram showing energy degeneracy lifting of $N = -1, 0, 1$ LLs into broken symmetry states. Arrows indicate the spin polarization of each electron (blue) and hole (red) level. Figure extracted from [94]

Concerning the fractional quantum Hall effect, which is a marker of strongly correlated two dimensional electron systems, it was first observed at $\nu = \frac{1}{3}$ in suspended graphene [14][19][27], and later on Dean et al. sample [16]. Recent studies (by R. Ribeiro-Palau et al. [69]) on fully encapsulated graphene with graphite back gate and top gate exhibited a rich variety of fractional states, as shown in figure 1.18.

How the degeneracy is lifted ? As in GaAs/AlGaAs heterostructures, the Zeeman effect can lift the spin degeneracy, thanks to the energy difference induced between the different spins $\Delta_Z = g\mu_B B$ (with $g \sim 2$ the g-factor of the material and μ_B the Bohr magneton). However, while the Zeeman effect breaks the spin symmetry, it does not

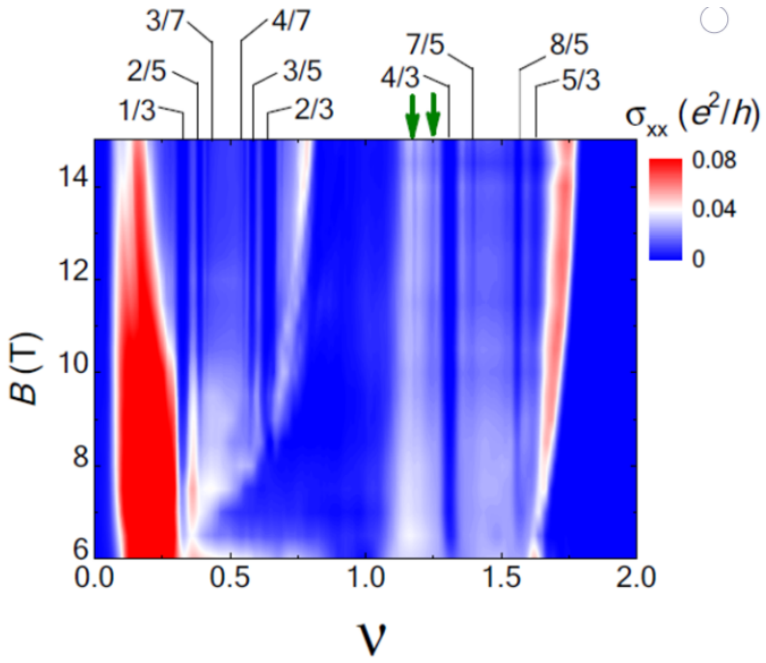

Figure 1.18: Longitudinal conductivity in the $n = 0$ LL as a function of the magnetic field and the filling factor, measurement done at $300mK$. Figure extracted from [69]

break the valley symmetry. Remarkably in the $n = 0$ LL, there is an equivalence between the valley isospin K or K' and the sublattice A or B. Therefore "a valley degeneracy lifting of the zero-energy LL $n = 0$ may be achieved through fields that couple to the sublattice index" [29]. As explained in M. Kharitonov's article [42] electron-electron and electron-phonon interactions can play the role of the valley symmetry breaking fields. The electron-phonon is generated by out of plane distortions of the lattice, or in plane distortions called Kekulé. In what follows the characteristic energy breaking the valley symmetry is noted Δ_{kek}. For $\Delta_Z > \Delta_{kek}$, the energy levels with lifted spin-valley of the $n = 0$ LL are ordered as shown in figure 1.19a. In this configuration, two of the LLs cross at the Fermi energy, which would generate at $\nu = 0$ an insulating graphene bulk associated with counter-propagating edge states. For $\Delta_Z < \Delta_{kek}$, as shown in figure 1.19b, there is no crossing of the lifted degeneracy levels of the $n = 0$ LL, thus generating an completely insulating state at $\nu = 0$ (with no edge channels). The two hole states are polarized in valley K', whereas the electron states are polarized in K.

Anyway, the essential point is that when the spin-valley degeneracy is lifted, each edge channel (created when the Fermi energy crosses the energy level) is carrying a different spin-valley couple $(K', \downarrow)$, $(K', \uparrow)$, $(K, \downarrow)$, or $(K, \uparrow)$. In reality the valley pseudospin of edge states is not necessarily K or K', but can be a superposition $\pm\overrightarrow{w}$ of those valleys (with $\pm$ noting two opposite valleys). The valley polarization is highly dependent on the nature of the physical edge (zigzag or armchair) [80].

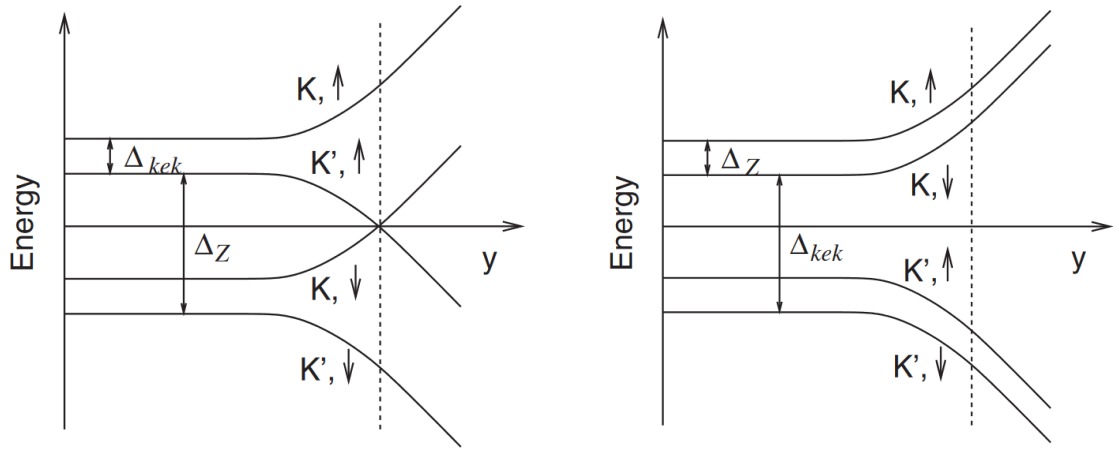

(a) $\Delta_Z > \Delta_{kek}$ (b) $\Delta_Z < \Delta_{kek}$

Figure 1.19: Possible scenarios for the lifted spin-valley degeneracy at $\nu = 0$. Figure extracted from [29]

1.2.3 Building blocks of electron quantum optics in graphene

With the existence of the quantum Hall effect in graphene, we find back one of the building block for electron quantum optics (see section 1.1.1). Indeed, thanks to the edge channels created at integer filling factors, one can guide the electrons in graphene as in GaAs/AlGaAs heterostructures.

The second essential element is the beam splitter, created through quantum point contacts (QPCs) in GaAs. The QPCs benefit from the semiconducting gap to create a constriction of the 2DEG, however the gapless structure of graphene makes it much more difficult to envision this kind of structures. Nevertheless, in a work by Zimmermann et al. [94], they developed a split gate structure in graphene analogous to QPCs structure in GaAs, which enabled them to control in a limited range of parameters the transmission of one edge channel in quantum Hall regime. However, the principle is quite different from a QPC as the transmission is based on local pn junctions formed below the split gates. In addition, a QPC analogue has been developed in bilayer graphene [45]. Anyway, the fabrication of these structures is complex and the range of tuning limited, making it difficult to envision electron quantum optics experiments, as Mach Zehnder interferometry (MZI), thanks to this structure.

Another original approach was explored in graphene using the possibility to create pn junctions thanks to the electric field effect. Indeed, by covering covering half of the graphene sheet by a top gate on top of an insulator and using global back gate (see figure 1.20), one can tune the carrier density to the p-doped regime in one half of the graphene sheet and to the n-doped regime in the other half. This generates a pn junction in the graphene sheet at the border of the top gate. The first experimental studies of graphene pn junction in the quantum Hall regime [85][53] revealed fractional plateaus of conductance in the bipolar regime (pn junction), whereas integer plateaus were present in

the unipolar regime. This was explained by the presence of quantum Hall edge channels along the pn junction, with electron and hole modes that can mix [1][54]. The presence of partitioning and mode mixing along the pn junction made it a potential candidate for a beam splitter in graphene. But for this, the mode mixing mechanism has to be elastic : shot noise measurements gave encouraging results in this direction [47].

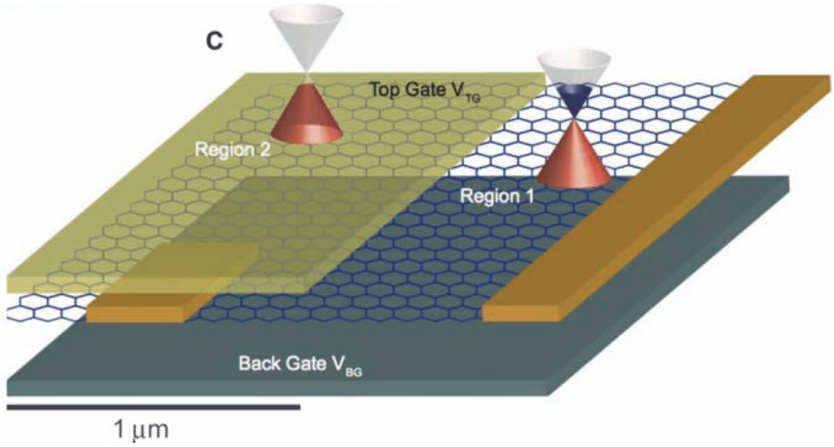

Figure 1.20: Schematic of a device used to create a pn junction in a graphene layer. A global graphite back gate enables to n-dope the graphene layer. A top gate covering half of the layer is tuned to p-dope the covered region. A picture of the Dirac cone configurations is presented for each region. Figure extracted from [85]

However, as we will see in the next section 1.2.4, this story is not complete, and the physics behind the pn junctions in graphene in the quantum Hall effect is even richer than what was thought, making it an essential block for electron quantum optics in graphene.

1.2.4 Mach Zehnder interferometry in graphene

In a pioneering work in 2015, Morikawa et al. [58] studied conductance oscillations over a pn junction in the quantum Hall regime as a function of the magnetic field and gate voltages. They interpreted their observations not as a simple beam splitter, but as a fully working Mach Zehnder interferometer (MZI). Indeed, they claimed that the mixing of the co-propagating edge channels formed along the pn junction was strongly suppressed for high quality encapsulated devices (as shown in [5]), except at the two ends of the pn junction where the junction encounters the physical edge of graphene. Therefore, those two mixing points act as the two beam splitters of a MZI, and the co-propagating edge channels as the two arms of the MZI. Their experiment was confirmed by studies carried out in Yacoby's group at Harvard [84], which enriched the picture by considering edge channels fully polarized in spin and valley i.e. a lifted fourfold degeneracy. Further discussion on the nature of the oscillations was achieved at the Schoenenberger's group in Basel [56].

I will now present the experimental results and analysis for MZI of the Yacoby group [84], which is the actual state of the art concerning graphene MZI. As shown in the schematic (see figure 1.21a), they used a pn junction defined thanks to a top gate and a bottom gate. The left part of the sample is n-doped and thus as a filling factor

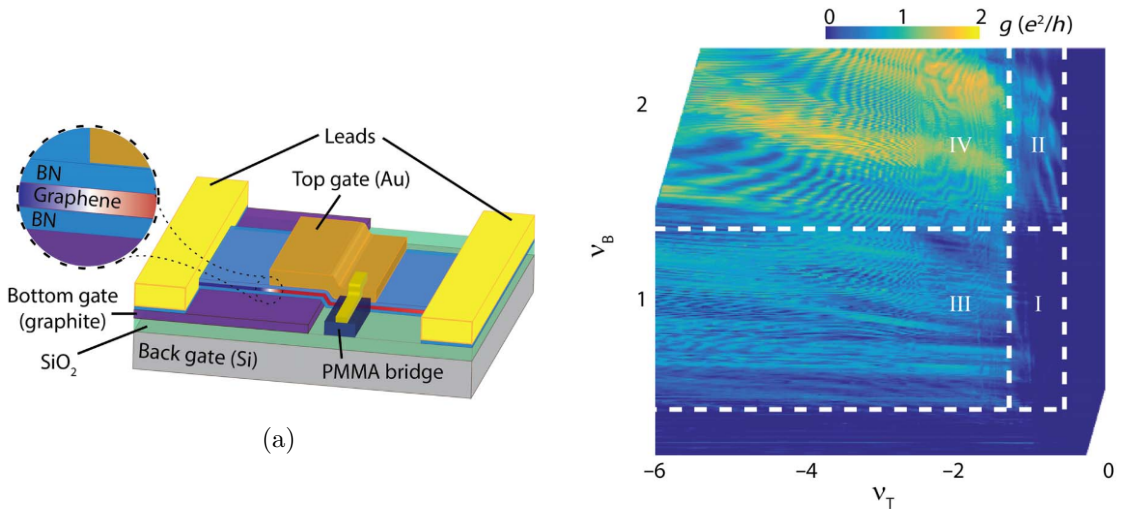

(a) (b)

Figure 1.21: (a) Schematic of the device used in [84] as spin- and valley-polarized MZI. An edge-contacted monolayer graphene flake encapsulated in BN. The top gate (Au) and the bottom gate (graphite) define the pn junction : p-doped region in red color with a filling factor ν_T; n-doped region in blue color with a filling factor ν_B. The back gate (Si) is used to strongly enhance the p-doping of the graphene leading up to the right lead and to reduce the contact resistance. (b) Two-terminal conductance measurement of the device in the pn regime at $B = 4T$. We distinguish four regions : I with $\nu_B = 1, \nu_T = -1$, II with $\nu_B \geq 2, \nu_T = -1$, III with $\nu_B = 1, \nu_T \leq -2$, and IV with $\nu_B \geq 2, \nu_T \leq -2$. Figure and legend extracted from [84]

$\nu_B > 0$, the right part is p-doped and thus as a filling factor $\nu_T < 0$. They achieved two-terminal conductance measurements in the pn junction at $B = 4T$ as a function of ν_B and ν_T, the result is depicted in figure 1.21b. Four different regions depending on the filling factors are visible :

- Region I : $\nu_B = 1$ and $\nu_T = -1$
  In this region, as illustrated in figure 1.22a, one n-type spin-down and one p-type spin-up edge channel copropagate along the junction. As the edge channels have opposite spin the scattering should be suppressed between them. Indeed, the conductance is almost zero in the whole area.

- Region II : $\nu_B \geq 2$ and $\nu_T = -1$
  As represented in the schematic 1.22c, two n-type (with opposite spins) and one p-type spin-up edge channels are copropagating along the pn junction. As the second n-type edge channel is also spin up, interchannel scattering is no longer forbidden. The observed conductance is not uniformly zero as in region I, it varies from 0 to $\frac{e^2}{h}$. This is consistent with a transmission occurring through one pair of edge channels.

- Region III : $\nu_B = 1$ and $\nu_T \leq -2$
  It's the same case as region II, but with two edge channels on the p side and one

on the n side.

- Region IV : $\nu_B \geq 2$ and $\nu_T \leq -2$
  The configuration is presented in figure 1.22b, this time two p-type (with opposite spins) and two n-type (with opposite spins) edge channels are copropagating along the pn junction. The p-type and n-type edge channels with the same spin can be mixed thanks to interchannel scattering, thus the transport through the pn junction should be mediated by two pairs of edge channels. In this region, the measured conductance is consistently fluctuating between 0 and $\frac{2e^2}{h}$.

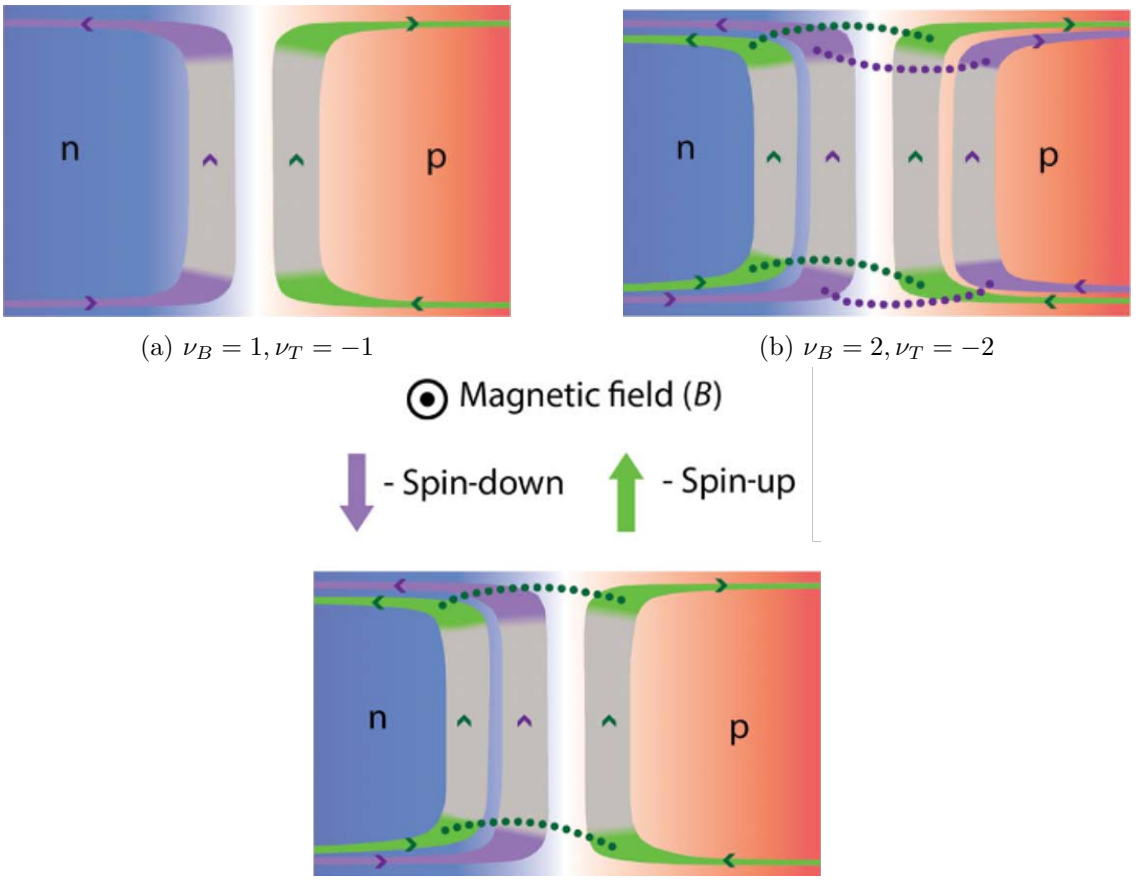

(a) $\nu_B = 1, \nu_T = -1$

(b) $\nu_B = 2, \nu_T = -2$

(c) $\nu_B = 2, \nu_T = -1$

Figure 1.22: Schematic illustration of the formation of MZIs at a graphene pn junction. Green and purple colors denote quantum Hall edge channels of opposite spins. Figure and legend extracted from [84]

According to Yacoby's interpretation, edge channels from higher LLs ($n \neq 0$) are not contributing to any transport mechanism as they are too far away from the junction, thus the trans-junction conductance is only mediated by the $n = 0$ LL. In addition, it is important to highlight that each MZI is formed by a pair of edge channels with the same spin, and therefore which belongs to different valleys. In the configuration $\nu_B = 1$ and $\nu_T = -2$, where only one pair of edge channels mediate the transmission (as in 1.22c),

they obtained sinusoidal conductance oscillation by sweeping the magnetic field from 8 to $9T$ with a periodicity $\Delta B = 66mT$. As displayed in figure 1.23, the amplitude of the oscillations goes from 0 to almost $\frac{e^2}{h}$, giving a 98% visibility. This is much higher than what was observed in GaAs/AlGaAs heterostructures; and it implies an almost perfect phase coherence along the pn junction, which is quite promising for the future use of graphene in electron quantum optics.

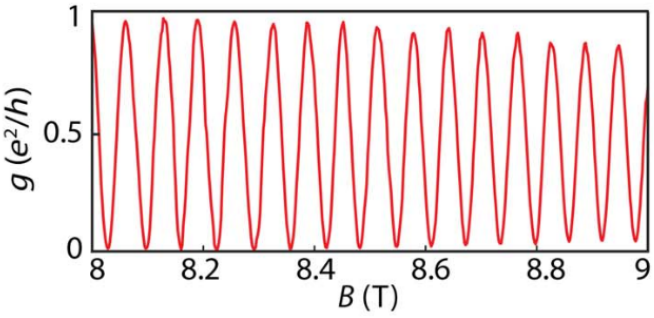

Figure 1.23: Mach Zehnder oscillations with the best visibility as a function of the magnetic field at filling factors $\nu_B = 1$ and $\nu_T = -2$. Figure extracted from [84]

The conductance oscillates sinusoidally with the Aharanov-Bohm phase Φ which is proportional to the flux of the magnetic field B through the area A enclosed by the two arms of the MZI : $\Phi = \frac{2\pi BA}{\Phi_0}$ with Φ_0 the flux quantum. Considering that the length of the pn junction corresponds to the length of the interferometer, one can deduce from the magnetic field periodicity ΔB an estimation of the edge channels separation across the junction. Numerically one obtains $52nm$.

In order to justify the length equality between the pn junction and the interferometer, Yacoby et al. claim that the intervalley scattering only occurs on the physical edge of graphene and is completely suppressed along a clean gate-defined edge. Thus they measured the trans-conductance through several pn junction with different lengths, the evolution of the magnetic field periodicity ΔB is in qualitative agreement with this hypothesis. Therefore all the data obtained at high field (around $8T$) seems quite consistent with the MZI picture.

However, P. Makk et al. [56] refined the analysis of the oscillations observed over a wide range of filling factors as in figure 1.21b. Indeed, they claim that at low filling factors $|\nu| \leq 2$ the oscillations observed corresponds to a MZI, but that at higher filling factors and intermediate field ($B \sim 5T$) the MZI oscillations can be mixed with oscillations coming from snake states along the junction.

1.2.5 Still a lot needs to be understood !

These first studies of MZI thanks to a pn junction in graphene are really promising, but they also raise numerous questions. First of all, the main issue is the control of the transmission of each beam splitter. Indeed, by tuning the top gate and bottom gate, oscillations can be obtained. However, there is no direct control on the transmission of each beam splitter. A clear demonstration of the MZI through a study of the oscillations

visibility dependence on the transmission can not be carried out as in GaAs (see figure 1.6). In addition, the underlying mechanism for the inter-channel mixing is still not clear.

In my PhD, the goal was to obtain a direct control over the transmissions of each beam splitter created at the ends of a pn junction in graphene in the quantum Hall regime. First this would enable us to check the consistency of the MZI picture as explained in the previous paragraph. But beyond this, it would lead to the possibility of coherently manipulating the valley degree of freedom in graphene. Indeed, as explained in section 1.2.4, the pair of edge channels forming a MZI along the junction have the same spin and opposite valleys. Therefore, the MZIs created are mixing the valley while being spin polarized. This implies that at the first beam splitter an incident electron is scattered between two states carrying different valleys and can be described thanks to a quantum mechanical superposition of them. Controlling the beam splitter transmission mean being able to tune the electronic valley, in other words it can act as a *valley splitter*. In addition, the fact that high visibility is observed in latter experiments shows that the underlying mechanism for the valley splitting is a coherent process. Finally, obtaining a tunable transmission could give us some insights on the physical nature of this mixing mechanism.

In order to obtain tunable valley splitter, we implemented local gates located at the two ends of the pn junction, i.e. where the mixing occurs. I will detail in the next part, our sample geometry, its principles, and also all the fabrication challenges that we overcame to achieve such a sample.

Chapter 2

Experimental set up and sample fabrication

As explained in section 1.2.5, the goal of my PhD is to coherently manipulate the valley degree of freedom in graphene by achieving a valley splitter. The purpose of this chapter is to present how it was experimentally implemented. First are described the valley splitter sample geometry and the its principles. Then the sample specifications and the fabrication procedure (in particular the encapsulation technique) are presented. And in a last part, I detail the experimental set up and techniques.

2.1 Design of the valley splitter sample

2.1.1 Sample geometry

The stumbling block of our study are the experiments of Mach Zehnder interferometry (MZI) carried out by a few teams [58][84][56] in graphene. All these studies are based on the same concept : a graphene pn junction in the quantum Hall regime act as an electronic MZI (as detailed in section 1.2.4).

Therefore, the building block of our sample geometry, presented in figure 2.1, is also a pn junction created by electric field effect in graphene. The p-doped region is colored in red, and the n-doped one in blue. In the presence of a magnetic field, counter-propagating edge channels are formed in the n and p regions. These edge channels meet at the pn junction, where they form co-propagating edge states along it, acting as the arms of the MZI. The inter-channel mixing occurs at the two points where the pn junction meets the physical edge of graphene; these points play the role of the beam splitters. If the magnetic field is strong enough (typically $\geq 7T$), the fourfold spin-valley degeneracy is lifted (see section 1.2.2). In this regime the edge channels are polarized in spin and valley pseudospin, and by changing the filling factors in each region one can directly control the number of edge channels on the p side and on the n side. Let's now consider the configuration represented in figure 2.1, with :

- In the n-doped region : $\nu_n = 2$, with a spin up edge state $|\uparrow, T_R\rangle$ (blue) and a spin down one $|\downarrow, T_R\rangle$ (yellow), where T_R denotes an edge channel incoming on the pn junction from the top right part of the sample.

- In the p-doped region : $\nu_p = -1$, with a spin down edge state $|\downarrow, T_L\rangle$ (red), where T_L denotes an edge channel incoming on the pn junction from the top left part of the sample.

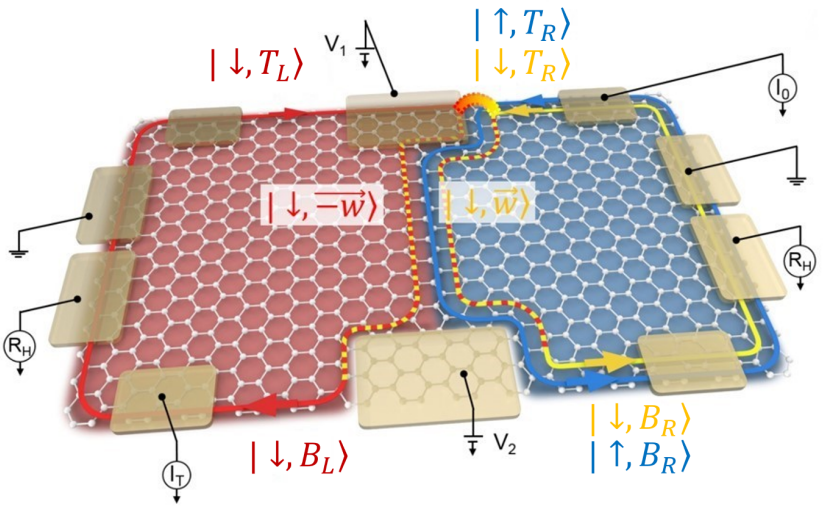

Figure 2.1: Schematic representation of the pn junction. n region is depicted in blue, p region in red. Electrons are injected from the upper right ohmic contact (defining an injected current I_0), and transmitted current I_T is measured on the lower left ohmic contact. Buried ohmic contacts enable to simultaneously tune the filling factor by measuring the two-points Hall resistance on both sides of the junction (noted R_H on the figure).

$|\downarrow, T_L\rangle$ encounters $|\downarrow, T_R\rangle$ and $|\uparrow, T_R\rangle$ at the intersection between the top graphene edge and the pn junction. Concerning the same spin states $|\downarrow, T_L\rangle$ and $|\downarrow, T_R\rangle$, they can be polarized in identical or different valleys depending on the nature of the physical border (zigzag or armchair). However, along the junction those incident spin down states form interface states with opposite valley pseudospins $\pm\vec{\omega}$: $|\downarrow, \vec{w}\rangle$ in the n-doped region and $|\downarrow, -\vec{w}\rangle$ in the p-doped one. On his part, the edge state $|\uparrow, T_R\rangle$ is preserved all along its trajectory, staying in the n-doped region, as the exchange energy to flip a spin is too large. An electron injected in the state $|\downarrow, T_R\rangle$ is splitted between the spin down interface states along the junction, where it can be described by the quantum mechanical state $|\Psi_{\text{initial}}\rangle$ superposition of $|\downarrow, -\vec{w}\rangle$ and $|\downarrow, \vec{w}\rangle$. If one notes t_1 (r_1) the transmission (reflection) coefficient from $|\downarrow, T_R\rangle$ to $|\downarrow, -\vec{w}\rangle$ ($|\downarrow, \vec{w}\rangle$), the state $|\Psi_{\text{initial}}\rangle$ can be expressed in the following way :

$$|\Psi_{\text{initial}}\rangle = r_1|\downarrow, \vec{w}\rangle + t_1|\downarrow, -\vec{w}\rangle \tag{2.1}$$

For the current conservation, the transmission probability $T_1 = |t_1|^2$ and the reflection probability $R_1 = |r_1|^2$ must verify : $T_1 + R_1 = 1$. In addition, whatever the valley polarization of $|\downarrow, T_R\rangle$, all the valley polarization of $|\Psi_{\text{initial}}\rangle$ are accessible, provided that scattering on the physical edge can supply the large momentum transfer from one valley to the other [80].

In order to develop a valley splitter we need to control the valley polarization of the output state $|\Psi_{\text{initial}}\rangle$ through electrical means. In other words, we want to tune the valley

polarization via an electrical bias, so that we can , in the ideal case, continuously go from a state fully polarized in valley $\overrightarrow{w}$ to a state polarized in the opposite valley $-\overrightarrow{w}$. For this aim, we fabricated two small side gates above the intersection between the graphene physical edge and the pn junction, i.e. where the mixing occurs between edge states with same spin. Biases on the side gates modify the profile of the electrostatic potential at both ends of the pn junction and, therefore the degree of the valley isospin mixing. When the filling factor below a side gate is set to $\nu \leq -1$, situation of the top side gate (or side gate 1) in figure 2.1, the pn junction intersects the physical edge; there the sharp potential change facilitates the isospin mixing. On the other hand, when the filling factor is set to $\nu = 0$, situation of the bottom side gate (or side gate 2), the pn junction ends on the edge electrically defined by the side gate; the potential change is gentle and the isospin does not mix.

2.1.2 Experimental measured quantities

As shown in figure 2.1, in addition to the complex gate structure, four ohmic contacts are located on both sides of the sample. Electrons are injected on the n-side from the upper right ohmic contact, defining the injected current I_0. This current is carried by the two T_R edge channels on the top graphene border up to the pn junction. Here, the half of the current having a spin up is completely reflected, as it cannot flow to the P region, because of large energy cost for spin flip. The other half $I_0/2$ of spin down, on which we focus hereafter, is partitioned on the first valley splitter (top side gate), propagates along the junction through the copropagating edge states, and finally is recombined on the second valley splitter (bottom side gate). The transmitted current I_T through the junction is measured on the lower left ohmic contact on the p-side. Moreover, the two-points Hall resistance (noted R_H in figure 2.1) is measured on the n-doped region and p-doped region simultaneously, as depicted in the schematic. In order to carry out this measurement, the ohmic contacts used for the two-points measurements are followed by a grounded ohmic contact, which also avoids looping currents.

2.2 Sample fabrication

In order to experimentally implement valley splitters, we fabricated a sample in a stack made of graphene encapsulated in hexagonal Boron Nitride (hBN) with a global graphite back gate. During my PhD, we developed the stacking procedures, solved several fabrication challenges (the achievement of edge contacts), and tested different geometries. The final sample used in this study was fabricated by Myunglae JO, and is the outcome of all these preliminary works. Hereafter are presented the characteristics of the valley splitter sample and important fabrication processes.

2.2.1 The samples specifications

The stack used

An optical micrograph of the stack used for the valley splitter sample (before nanofabrication) is presented in figure 2.2a. It is composed of (from bottom to top) : a $9nm$-thick graphite back gate, a bottom hBN of $33nm$, a monolayer graphene sheet, and a top hBN

of $27nm$. On the picture, the graphene is delimitated thanks to the green dashed line, the hBN flakes appear in green, end the graphite back gate in purple. Graphene, hBN, and graphite flakes were mechanically exfoliated onto the surface of SiO_2/Si using the conventional scotch tape method (from NGS Naturgraphit GmbH for graphene, and from NIMS crystals for hBN). By optical microscope, single-layer graphene was chosen. The monolayer nature of the graphene sheet has been further confirmed with Raman spectroscopy after successful encapsulation with hBNs (see figure 2.2b). By doing this we can avoid any spurious signature in the Raman spectrum of graphene [68]. All the crystals were carefully checked with optical microscopy and noncontact mode AFM to detect any defects, contamination and in-homogeneities in thickness before stacking. Using the van der Waals (vdW) dry transfer method (see section 2.2.2), graphene was encapsulated in hBNs [82]. Then this BN/graphene/BN stack was transferred on a flake of graphite ($9nm$), which is used as a back gate. The finished stack was annealed in vacuum at approximately $350°C$ to enhance the quality of the sample and finally it was checked with non-contact mode AFM to locate bubbles and defects.

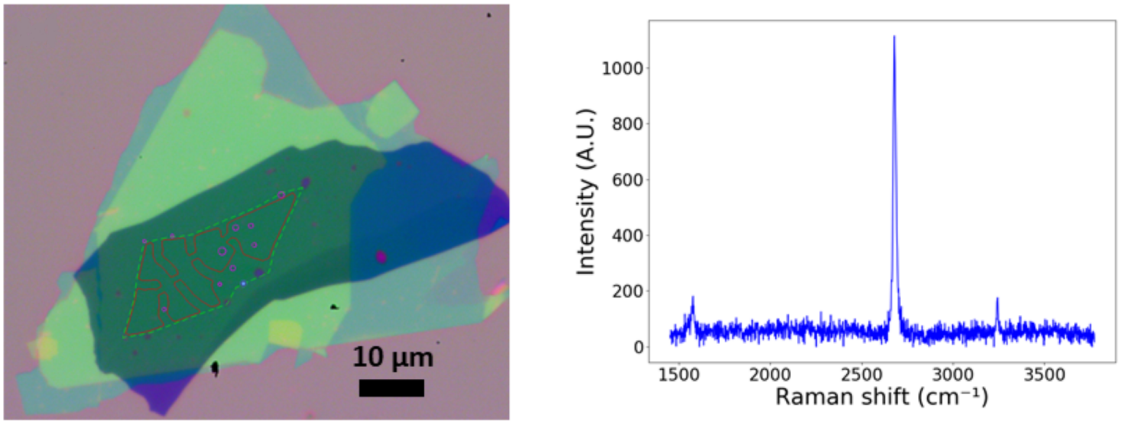

(a) (b)

Figure 2.2: (a) Optical image of BN/graphene/BN/graphite stack. The green dashed line indicates the edge of graphene. Red line indicates graphene mesa which would be defined by subsequent RIE etch. Purple circles indicate bubbles in the stack which later would be eliminated by ohmic contacts fabrication or mesa etching. (b) Raman spectroscopy of encapsulated single-layer graphene. This data was taken after successful encapsulation of graphene with top and bottom hBN but before adding additional graphite. We could minimize the spurious substrate effect and also avoid overlapping with the spectrum of graphite underneath.

Nanofabrication

After obtaining the stack, we used nano-fabrication techniques to achieve top gates, side gates, to contact graphene and graphite, to etch the graphene... Starting from the bare stack, the different steps of this complex fabrication process are the following :

- Realization of the ohmic contacts
  For this aim, a poly-methyl-methacrylate (PMMA) pattern defined by e-beam

lithography was used as a mask for O_2/CHF_3 reactive ion etch (RIE) to expose the 1D edge of graphene. And using the same PMMA layer as a lift off mask, edge contacts were defined by evaporating Cr/Au=10/30nm while rotating the sample using a tilted rotation stage (see section 2.2.2)

- Etching of the mesa
  We etched the graphene channel into desired mesa geometry by using the same RIE procedure with PMMA resist mask. PMMA resist was cleanly removed in hot Acetone later.

- Deposition of a hBN flake on top
  To prevent any possible leakage between the exposed graphene edge and additional gates, 10nm hBN was picked up and dry transferred on top of the sample. When removing PPC, annealing was not used this time to avoid any possible degradation of ohmic contacts. Melted PPC was cleaned with hot Acetone.

- Evaporation of side gates
  Side gates were defined by evaporating Cr/Au=10/30nm.

- Deposition of a hBN flake on top
  An additional 15nm BN was picked up and dry transferred on top of the sample like described before.

- Definition of the top gates
  Then finally top gates were defined by evaporating Cr/Au=10/40nm.

.

Sample description

An optical micrograph of the sample after nano-fabrication is presented in figure 2.3.a. There are actually two top gates, which correspond to the two main golden plates visible on the picture. In this study, we only used the right part of the sample, centered on one of the top gates, and delimited by the red dashed line in the sample picture. A layout of the used part of the sample is presented in figure 2.3.c. The region below the top gate is doped n, whereas the rest of the graphene is p-doped thanks to the graphite back gate. Therefore we have a pnp junction : the right pn junction has no side gates and it was just used as a test sample, whereas the left one has side gates and corresponds to the valley splitter sample as depicted in section 2.1.1. Burried ohmic contacts are placed below the top gate enabling to completely isolate the two junctions from each other thanks to cold grounds. Therefore, it is possible to measure, at the same time and independently, the transmission through both junctions and the two-point Hall resistance below the top gate (noted $R_{H,tg}$ on the schematic). The precise dimensions of the sample, as the width of the pn junction or side gates size, are summarized in figure 2.3.b. The length of the rigth pn junction corresponds to the width of the graphene ribbon $\approx 1.0\mu m$. The left pn junction length depends on the side gates tuning, when the pn junction follows the side gates border, its length is $\approx 1.5\mu m$. One can notice that the side gates size is non negligible compared to the junction length. Indeed, half of the junction is covered by the

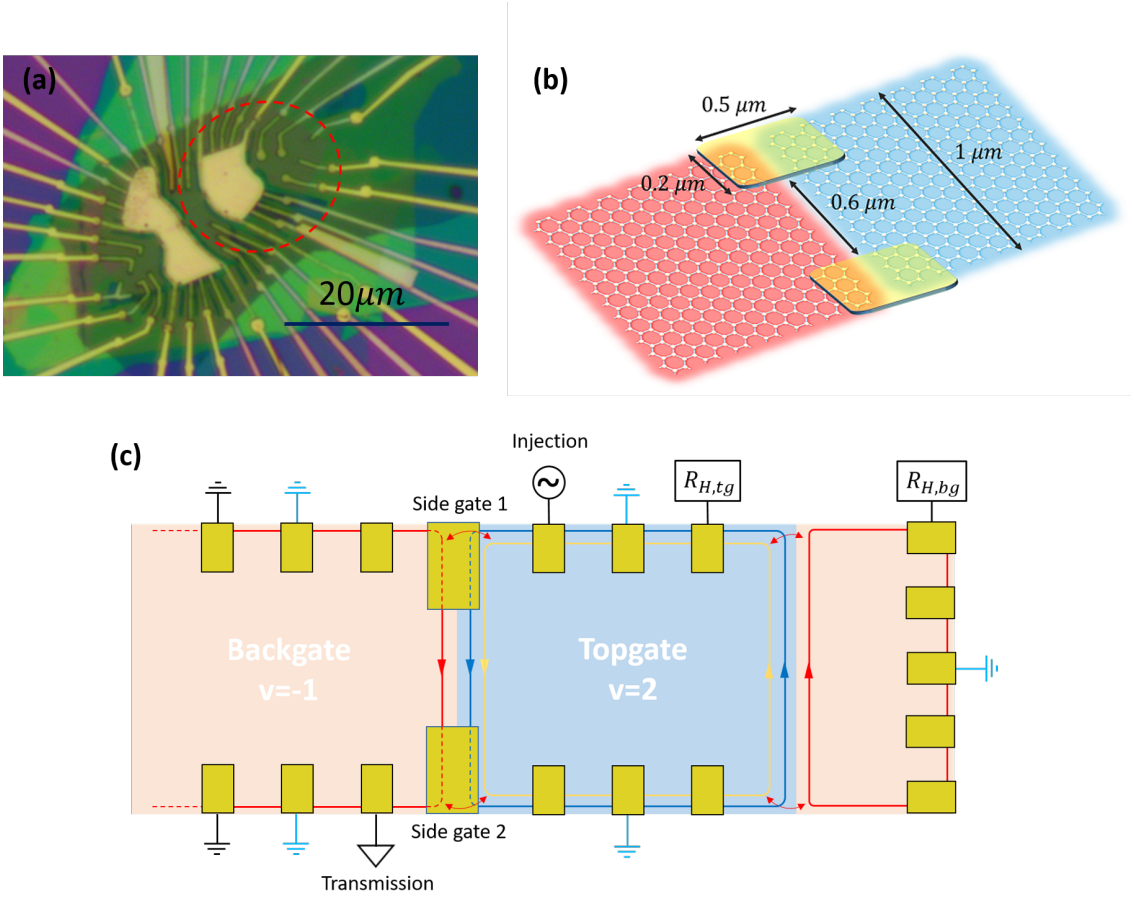

Figure 2.3: (**a**) Optical micrograph of the finalized device. The dashed red line indicates the pnp-junction actually used in our study, it is defined by applying gate voltages of opposite sign from the graphite back gate and the metallic top gate. (**b**) Characteristic dimensions of the valley splitter sample : the sample width $1.0\mu m$, the distance between the side gates $0.6\mu m$, a side gate width of $0.5\mu m$, and a side gate length of $0.2\mu m$. (**c**) Schematic representation of the real sample used in the pnp configuration (circled by the red dashed line in (a)) : n region is depicted in blue, p region in red. The light blue grounds correspond to cold grounds.

side gates. This is the results of several tests that we carried out on samples with different widths. For longer junctions without side gates, the visibility MZI oscillations was always quite low; it is only when we reduced the length of the junction that we could obtain high visibilities as in Wei et al. work [84].

In order to visualize the arrangement of the different elements (gates, ohmic contacts...), a vertical cut of the sample is drawn in figure 2.4. As one can understand from the layout, by applying a negative bias on the graphite back gate, it is possible to p-dope the full graphene layer. The application of a positive bias on the top gate can compensate in the graphene underneath the effect of the back gate, and even enable to n-dope the top gate covered region. Considering the side gates, they are isolated from the top gate

thanks to one layer of hBN (which is insulating). One half of the side gate is below the top gate whose potential is screened. Finally, the buried edge contact are also covered by hBN to isolate it electrically from the top gate.

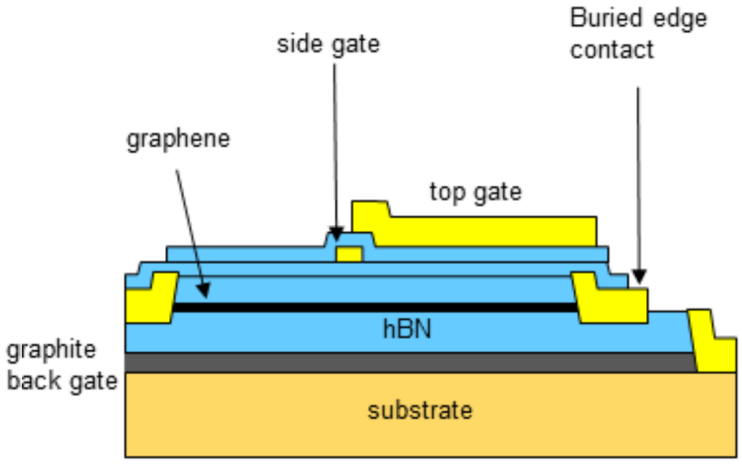

Figure 2.4: Schematic cut view of the sample layers.

2.2.2 Fabrication procedures

In this section, I will detail the main fabrication procedures used and developed at the laboratory. First of all, the encapsulation technique, which enabled us to fabricate the graphene and hBN stacks, is presented. Then is depicted one of the main challenges in the nanofabrication of encapsulated graphene stacks : contacting the graphene thanks to edge contacts.

Encapsulating graphene

The use of a simple scotch tape technique, by the Manchester team, to isolate graphene was mind blowing. Moreover, as shown in [66], this scotch tape technique is also applicable to a lot of different crystals as BN, MoS_2, $NbSe_2$... Rapidly, an idea emerged from this possibility to isolate different two-dimensional crystals : What if we stack those crystals to form heterostructures ? This simple idea gave rise to the rich field of Van der Walls heterostructures [25] where one can stack graphene, 2D chalcogenides, 2D oxides in the desired sequence. The inplane stability of the crystals is maintained through strong covalent bounds, whereas the different layers are hold together thanks to the weak Van der Walls forces. An important advent in this field was the high quality graphene devices obtained thanks to encapsulation in hBN [16]. Nowadays, a lot of intriguing phenomena have been observed in many different types of heterostrustures, and I would like to underline in particular a recent achievement : the twisted bilayer graphene encapsulated in hBN which exhibited superconducting properties [87]. The emergence of this entire research field is based on the development of transfer techniques which enabled to achieve the stacking of the crystals. The first wet transfer techniques were developed in Colombia university by C.R. Dean et al. [17]. After a few years of developments the technique was

improved and gave rise to the state of the art dry transfer technique [82], which is detailed hereafter as it is the one we used.

The encapsulation procedure : Prior to any transfer, one has to carry out micromechanical exfoliation of graphene and hBN crystals on $Si/Si0_2$ ($290nm$) chips thanks to the scotch tape technique. The clean crystals with the good thicknesses are found by optical microscopy, and can eventually be checked by atomic force microscope (AFM) imaging. Then the transfer process can start thanks to a transfer station (see figure 2.5a) composed of : a microscope, a heated copper stage, and a micromanipulator where a glass slide can be fixed.

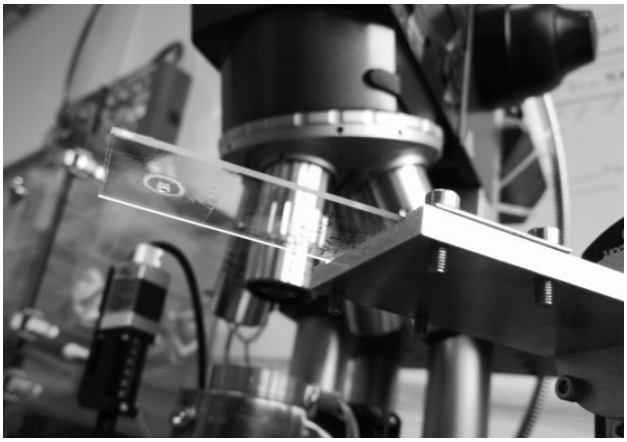

(a)

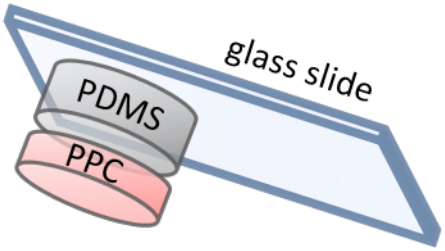

(b)

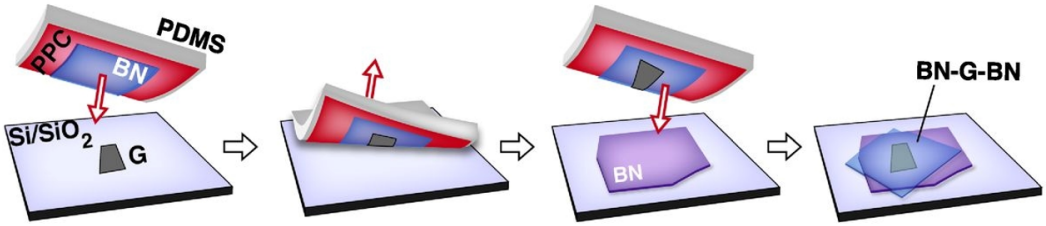

(c)

Figure 2.5: (a) Picture of the transfer station composed of a microscope, an heated copper stage, and a micromanipulator where the glass slide is fixed. (b) Schematic of the glass slide used for the transfer procedure. At the end of the glass, a sticky polymer (PPC) is placed on top of a PDMS cylinder. (c) Schematic of the van der Waals technique for polymer-free assembly of layered materials (extracted from [82]).

The exfoliation chips are placed on the copper stage. Glass slides (figure 2.5b) are prepared upstream with a sticky polymer, the poly-propylene carbonate (PPC), placed on top of a transparent elastomer stamp in poly dimethyl siloxane (PDMS). For the transfer, a glass slide is placed on the micromanipulator, and the copper stage is heated at 40°. By putting the stamp in contact with a BN crystal on the $Si/Si0_2$ chip, one can detach it from the substrate as the adhesion to the PPC is stronger. Afterwards, as depicted in the schematic 2.5c, one can stack the graphene layer on the BN attached, as again the

adhesion of graphene to BN is stronger than to the substrate. The procedure is repeated for the bottom BN, and other layers could be added using the same technique. During the procedure the crystals are aligned thanks to the optical microscope. Once the stack is done, one can deposit it on a clean Si/SiO_2 chip by putting the stamped stack in contact with the substrate and raising the temperature up to 130°. Indeed, at high temperature PPC is melting, thus releasing the stack. In order to remove all PPC residues the sample is finally annealed at 350° for 30min.

Why is the encapsulation so important ? As I briefly mentioned before, encapsulating graphene in BN was a key element in order to obtain high quality samples. Historically the first graphene samples studied were graphene flakes on top of SiO_2, their mobility was quite low due to the defects and charge puddles induced by the substrate. Therefore, in order to obtain higher mobility, suspended graphene was developed, but the the fabrication process was extremely challenging. However, thanks to encapsulation, it is now possible to obtain mobilities as high as in suspended graphene, but with much easier fabrication processes.

Microscopically the effect of encapsulation is astonishing as shown in this nice scanning tunneling microscopy (STM) study [18]. Indeed, on the obtained topograph and charge density map for graphene/SiO_2 important puddles and defects are visible (figure 2.6.b and d), whereas an extraordinarily flat graphene layer with almost no puddle is displayed when it is placed on top of BN (figure 2.6.a and c). The suppression of puddles gives rise to the high mobilities observed in encapsulated graphene. Actually, all the state of the art studies on fragile effects such as the MZI [58][84][56] or FQHE [69] have been achieved in encapsulated samples.

Nowadays, people are even going further by using a global graphite back gate (in addition to the BN encapsulation) which is supposed to screen any charge inhomegeneity from the substrate. In addition, a recent scanning nanothermometry study [32] enabled to visualize atomic-scale defects in graphene. As clearly visible in their measurement (see figure 2.7) defects are mainly located on the graphene physical edges. This is why, recently, R. Ribeiro-Palau et al. [69] developed an encapsulated graphene sample with a global graphite back gate but also a graphite top gate, which enables, thanks to the $\nu = 0$ band gap, to electrostatically define the edges of the graphene layer in the presence of a magnetic field.

Edge contacts

Van der Walls heterostructures made of two-dimensional crystals assembled together were predicted to have exceptional properties; however to benefit from those properties several technical challenges had to be overcome, and in particular obtaining high-quality electrical contact for 2D materials using 3D metallic electrodes. For graphene the first approach was to metalize 2D surfaces, but this leads to high contact resistance due to the lack of surface bounding sites. In 2013, Wang et al. [82] developed an innovative approach, the so-called edge contacts. As depicted in figure 2.8, the idea is to etch graphene following a mask designed by electron beam lithography. The exposed graphene edge is then metalize thanks to the same mask. As shown in the STEM images of their ohmic contatcs (figure 2.8.B), the etched border forms a 45° angle with the plane of the

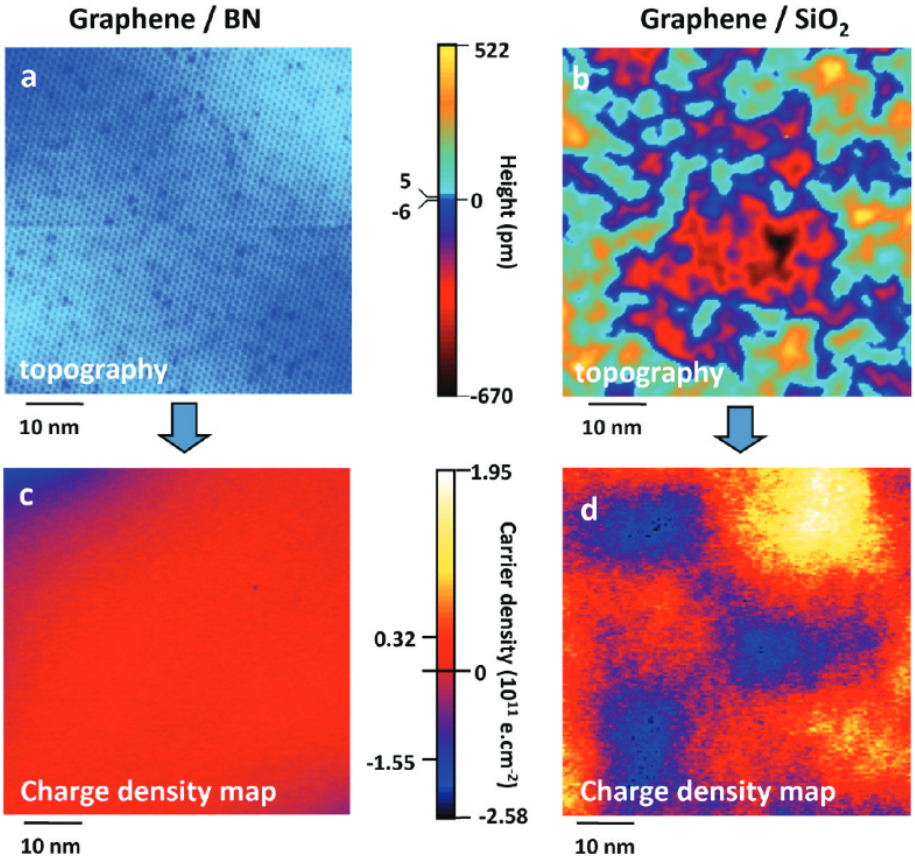

Figure 2.6: Comparing topography and charge density for graphene/BN vs graphene/$Si0_2$. (a,b) The 60nm x 60nm STM topographs of (a) graphene/BN and (b) graphene/SiO_2. (c,d) Charge density maps obtained from conductance maps taken in the same area simultaneously are shown for (c) graphene/BN, and (d) graphene/SiO_2. Figure extracted from [18].

stack. Thus, only one or two lines of C atoms are exposed, creating a real edge contact.

During my PhD, the obtention of high-quality edge contacts was an important challenge, which required a lot of developments. The final recipe we used is based on a PMMA mask which is designed by electron beam lithography. Before spin-coating the PMMA, the stack was etched with a 0_2 plasma for a short time (between 5 to 10s). Indeed, we noticed that, without this step the PMMA mask tend to crack after the electron beam lithography. Then the stack is etched following the mask design thanks to $CHF_3/0_2$ reactive ion etching (RIE). Controlling the etching rate is essential as we want to fully etch the stack bellow the graphene layer, but we should not make a shortcut to the graphite back gate by fully etching the bottom BN (see figure 2.4). Afterwards, we have an evaporation step of Cr/Au=10nm/40nm. The conditions of evaporation are extremely important for the contact quality.
After many tests we obtain the following set of conditions :

1. Low vacuum : $\sim 10^{-8} mbar$

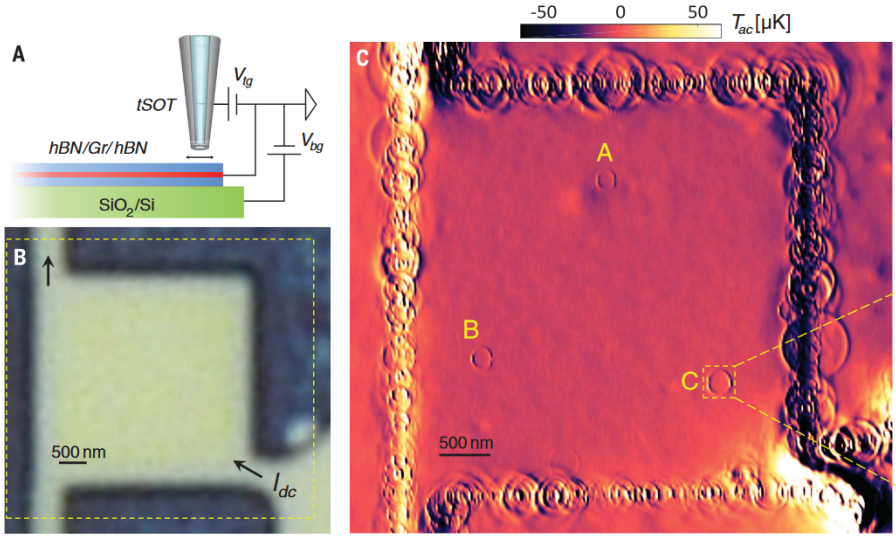

Figure 2.7: **Observing individual dissipation sources in a graphene heterostructure.** (**A**) Schematic side view of the measurement setup with the hBN-graphene-hBN heterostructure and SQUID-on-tipnanothermometer. (**B**) Optical image of the device patterned into a square chamber (bright; $4\mu m$ x $4\mu m$). (**C**) Scanning ac nanothermometry $T_{ac}(x, y)$ the area outlined in (B). Figure extracted from [32].

2. Deposition with a tilt 15° and a rotation $18°/s$ of the stage

3. Low deposition rates : $0.05nm/s$ for Cr, $0.1nm/s$ for Au

Thanks to this process we were able to obtain reliable contact resistance of few hundred ohms per micron.

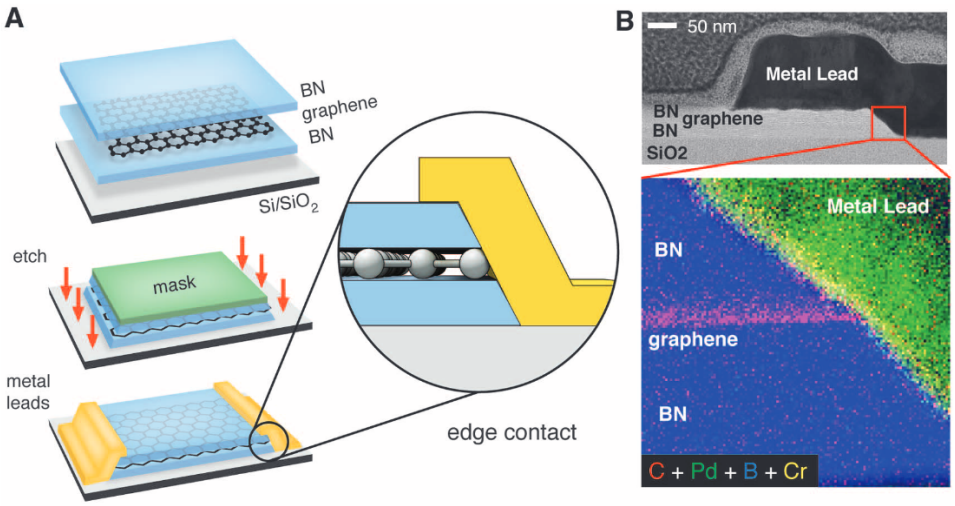

Figure 2.8: **Edge-contact**.(**A**) Schematic of the edge-contact fabrication process. (**B**) High-resolution bright-field STEM image showing details of the edge-contact geometry. Figure extracted from [82].

2.3 Experimental set up

All the measurements were achieved at very low temperature thanks to a cryoconcept dilution fridge with a base temperature of 15mK. Inside the fridge, a superconducting coil can produce magnetic field up to 14T perpendicularly to the sample plane. When I arrived in the team, the fridge hasn't been delivered yet, therefore I participated to the set up of the fridge, and in particular to the installation of DC lines and noise measurement lines.

During all this study, we achieved differential conductance measurements through the ohmic contacts thanks to Lock-in amplifiers with low noise preamplifiers. AC excitations 1nA-5nA with different frequencies (70Hz-300Hz) were used. Buried ohmic contacts underneath top gates enabled us the direct determination of filling factors from regions of interest. In order to inject small signal and to protect the sample, we added dividers, capacitors, and big resistances on the DC lines going to the sample. The different circuit used are briefly presented hereafter :

- For AC injection on ohmic contacts : as depicted in figure 2.9a, after the Lock-in amplifier output we placed a divider followed by a big resistance to polarize in current the sample.
- For AC and DC injection on an ohmic contact : it is the same circuit as in the previous case, but with an additional Yokogawa DC source in serie with a resistor (see figure 2.9b).
- For DC injection on the gates (figure 2.9c) : we used a divider in parallel with a small capacitor. The time constant of the RC circuit was tuned to be short enough (around $50\mu s$) compared to the time constant of the Lock-in and to the wait time between two measured points.

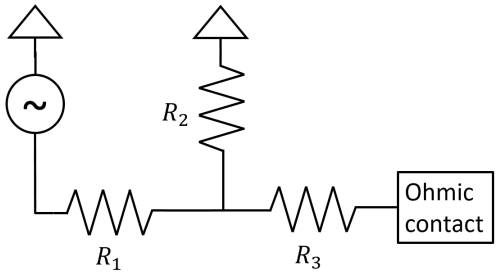

(a) AC injection circuit on ohmic contacts

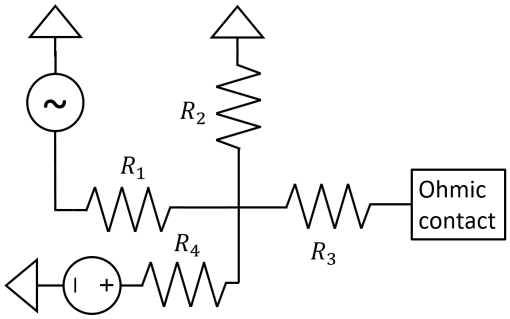

(b) AC and DC injection circuit on ohmic contacts

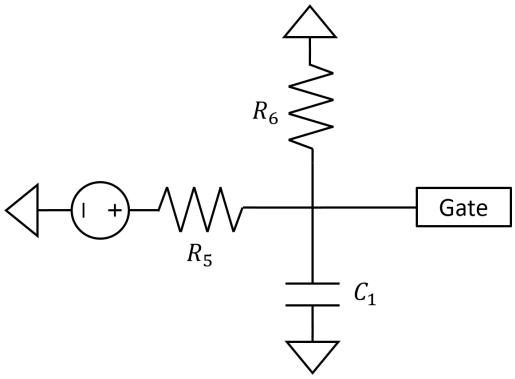

(c) DC injection circuit for gates

Figure 2.9: Schematics of the different electrical circuits used for signal injection on the sample. $R_1 = 100k\Omega$, $R_2 = 1k\Omega$, $R_3 = 1M\Omega$, $R_4 = 10k\Omega$, $R_5 = 10k\Omega$, $R_6 = 1k\Omega$, and $C_1 = 10\mu F$.

Chapter 3

Coherent manipulation of the valley

In this chapter, I will present how, by using the valley splitter sample, we implemented the coherent manipulation of the valley isospin. First, I will show how we can fully tune the valley polarization of the output state of our system, by controlling the transmission between the incoming and outgoing states below each side gate, and present simulations corroborating those results. Then the coherence of the mixing process is investigated thanks to Mach Zehnder interferometry. Finally, the prospects for valleytronics of the coherent valley manipulation are discussed.

3.1 A full control of the valley polarization

3.1.1 Experimental tuning of the valley thanks to the side gates

The principles of the valley splitter sample are described in details in section 2.1.1. For this study, a bipolar quantum Hall state is obtained by tuning, in the presence of a strong magnetic field ($B \approx 9T$), the back and top gates in order to juxtapose : a n-doped region with $\nu_n = 2$, and p-doped region with $\nu_p = -1$. Counter-propagating edge states formed in the n and p regions co-propagate along the pn junction (figure 3.1a). The valley isospin mixing only occurs at the two points where the pn junction meets the graphene physical edge. In order to control the mixing, we implemented side gates which can change locally the filling factor at the ends of the junction : for $\nu_{sgi} = 0$ ($i = 1, 2$ denoting the side gate 1 or 2) no valley mixing should occur as the junction ends on a gate defined border (figure 3.1a), whereas for $\nu_{sgi} \leq -1$ (figure 3.1b) or $\nu_{sgi} \geq 2$ (figure 3.1c) the mixing should be preserved. As shown in figure 3.1a, experimentally we injected a current I_0 from the contact at the top right of the junction, and measured the current transmitted I_T on the bottom left contact. Half of I_0 is injected into the spin down state $|\downarrow, T_R\rangle$, at the junction it is split between the same spin co-propagating interface states formed along the junction : $|\downarrow, \overrightarrow{w}\rangle$ in the n-doped region, and $|\downarrow, -\overrightarrow{w}\rangle$ in the p-doped one. The other half of I_0 is injected into the spin up state $|\uparrow, T_R\rangle$. Due to its opposite spin this current is preserved all along the junction and fully transmitted to the $|\uparrow, B_R\rangle$ state. Therefore, the maximum value of the transmitted current is $I_T = I_0/2$, and in all the following measurements I_T is normalized in units of transmission $D = I_T/(I_0/2)$.

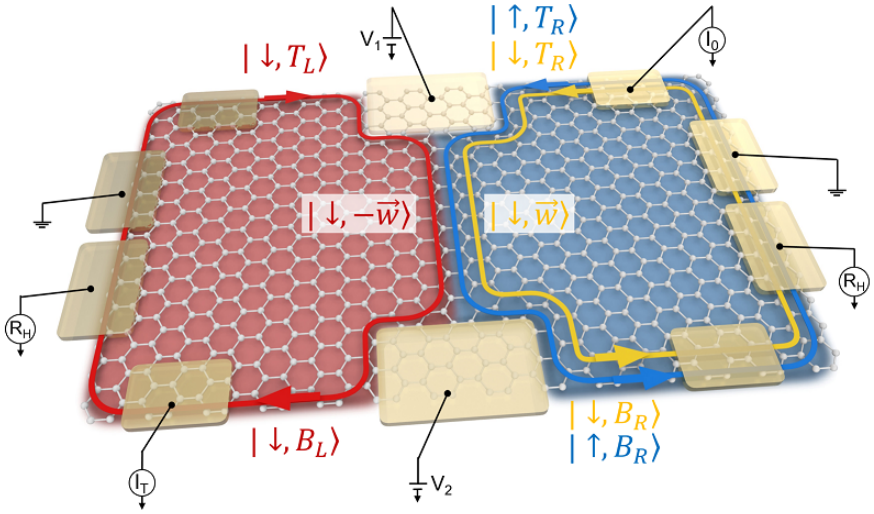

(a) Fully reflecting configuration : $\nu_{sg1} = \nu_{sg2} = 0$

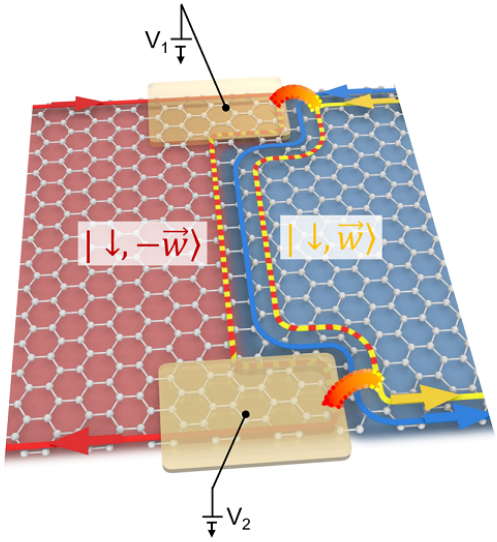

(b) Zoom transmitting configuration : $\nu_{sg1} = \nu_{sg2} = -1$.

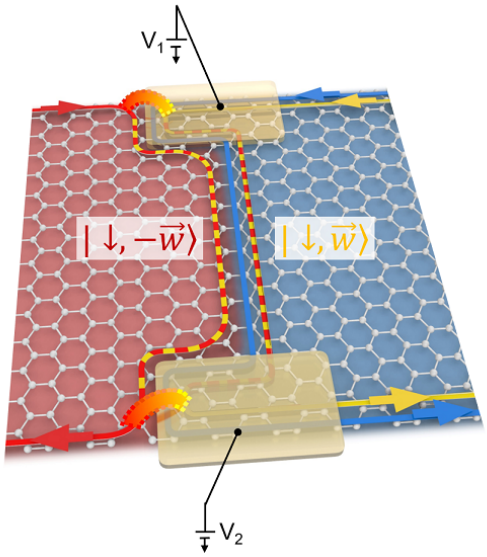

(c) Zoom transmitting configuration : $\nu_{sg1} = \nu_{sg2} = 2$.

Figure 3.1: Schematic representation of the valley splitter sample in the fully reflecting and the transmitting configurations. n region is depicted in blue, p region in red. Electrons are injected from the upper right ohmic contact (defining an injected current I_0), and transmitted current I_T is measured on the lower left ohmic contact. Buried ohmic contacts enable to simultaneously probe the filling factor on both sides of the junction by measuring the two-points Hall resistance (noted R_H on the figure).

Suppression of the valley mixing

The first step was to check that a full suppression of the valley mixing was achievable, i.e. a zero-transmission $D = 0$ can be obtained for some tuning of the voltages on the side gates. In what follows, we call V_1 the voltage applied on side gate 1 (top one), and V_2 the one on side gate 2 (bottom side gate). As depicted in figure 3.1a, when $\nu_{sg1} = \nu_{sg2} = 0$, the valley mixing should be suppressed, generating a fully reflecting configuration in which all the current flows to the ground on the n side. To check the existence of such a regime, we applied an identical voltage on both side gates $V_1 = V_2$, and measured the transmission D as a function of this bias. The curve obtained is plotted in figure 3.2. For a certain range of voltage, between 0 and 1 V, no current is transmitted giving rise to a full reflection of the current. Outside of this fully reflecting region, the transmission fluctuates and can reach high values, up to 0.8 (indicating that most of the current is transmitted).

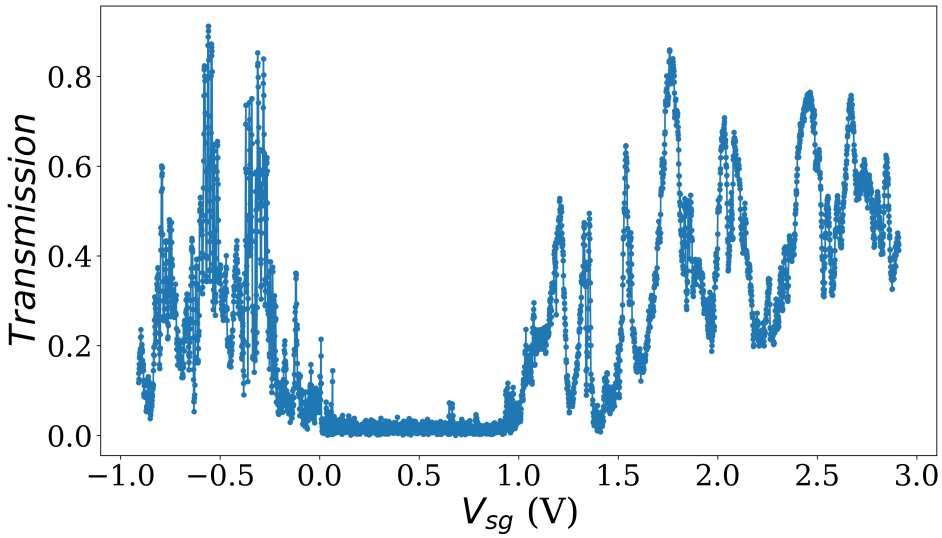

Figure 3.2: Transmission as a function of gate voltages $V_1 = V_2$, noted V_{sg}, applied on the side gates for a magnetic field of 13.5T.

When decreasing the voltage applied on the side gates, the filling factor below them ν_{sgi} (with $i = 1, 2$ denoting the side gate) is diminished. At some point ν_{sgi} reaches -1, implying that the $|\downarrow, T_L\rangle$ (red) edge channel propagates below the side gates as depicted in figure 3.1b. Therefore, the pn junction ends on the physical edge of graphene, enabling valley mixing at its extremities. In the latter configuration, an electron injected from $|\downarrow, T_R\rangle$ or $|\downarrow, T_L\rangle$ can be scattered on the physical edge in $|\downarrow, \overrightarrow{w}\rangle$, $|\downarrow, -\overrightarrow{w}\rangle$, or any superposition of them depending on the momentum transfer conferred by the scattering. The interface states cannot mix along the junction because it is defined in the clean graphene bulk which prevents the presence of any scatterer. At the bottom end of the pn junction, interface states encounter again graphene physical edge, where the valley mixing is enabled, and are splitted between the output states $|\downarrow, B_L\rangle$ and $|\downarrow, B_R\rangle$. Valley mixing, occurring at the two ends of the pn junction for $\nu_{sgi} \leq -1$, enables the transmission of the current carried by the $|\downarrow, T_R\rangle$ to $|\downarrow, B_L\rangle$. As we inject from the n-doped region at filling factor $\nu_n = 2$, a full transmission $D = 1$ would give a transmitted current $I_T = I_0/2$,

because the spin up current is fully reflected. All intermediate transmission values can be generated depending on the transmission at each mixing point. The increase of the transmission for negative voltages can be explained thanks to this picture. Finally, the transmitted current observed above 1V can be explained in an analogue way : when $\nu_{sgi} \geq 2$, the $|\downarrow, T_L\rangle$ (yellow) edge state propagate below the side gates, creating a configuration equivalent to the previous case (figure 3.1c).

Tuning the valley mixing

In the previous section, I showed that, by changing the bias applied on both side gates, we can set the valley splitter sample in a transmitting configuration (figure 3.1b and 3.1c) or in a fully reflecting configuration (figure 3.1a) where the mixing is suppressed at the ends of the junction. If now we tune each side gate independently, as depicted in figure 3.3, we can set the bottom side gate at a bias V_2 suppressing the mixing between incoming edge states (i.e. $\nu_{sg2} = 0$), and sweep the bias V_1 applied on the top side gate. In that configuration, the measurement of the transmitted current I_T gives us a direct access to the transmission T_1 of the top valley splitter (side gate 1) as a function of the bias V_1 applied on it.

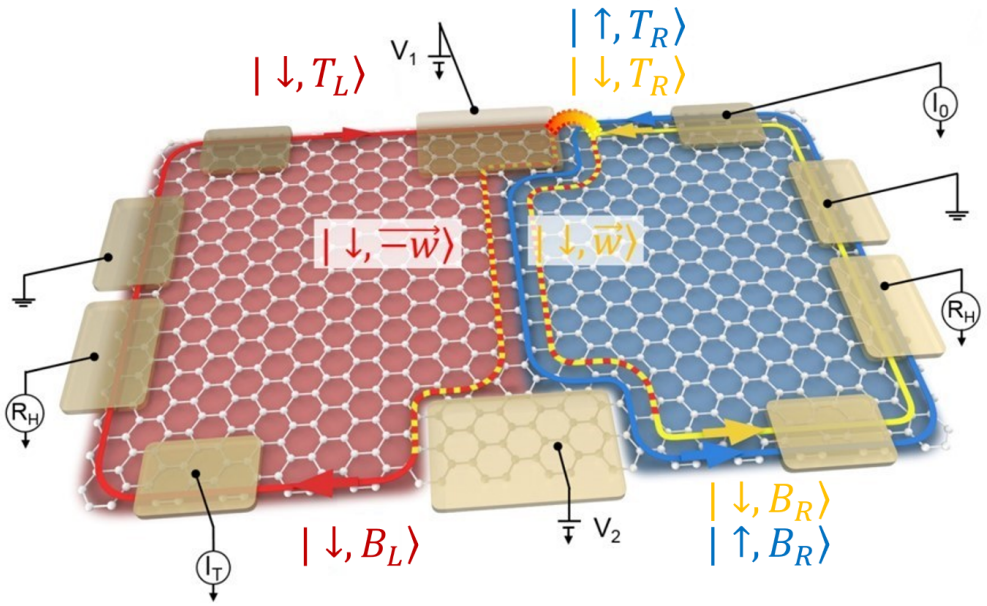

Figure 3.3: Schematic representation of the valley splitter sample with the bottom side gate fully reflecting : $\nu_{sg1} = -1$, $\nu_{sg2} = 0$.

Experimentally, T_1 was measured as a function of the bias V_1 on side gate 1 and of the magnetic field. The resulting measurement is presented in the form of a color map in figure 3.4.a. We observe irregular oscillations of the transmission with the mangetic field and the side gate voltage V_1. The average period in V_1 is roughly $\Delta V_1 \sim 100$ mV. In magnetic field it is approximately : $\Delta B_1 \sim 300$ mT. The single trace in red representing T_1 oscillations as a function of the voltage V_1 at a fixed magnetic field in figure 3.4.b, exhibits that T_1 can be continuously tuned from 0 to 0.89 electrostatically, through the

bias V_1. Therefore, by killing the mixing at the bottom side gate and by playing on the bias on the top side gate, we are able to continuously go from an output state fully polarized in valley $\overrightarrow{w}$ ($T_1 = 0$) to an output state in valley $-\overrightarrow{w}$ ($T_1 \sim 1$). In other words we control the degree of valley mixing, and our sample acts as a valley splitter.

Similarly, one can suppress the mixing at the top side gate by fixing V_1 so that $\nu_{sg1} = 0$. In this configuration the same study can be carried out by this time sweeping the bias V_2 applied on the bottom side gate (see black trace in figure 3.4.b). The transmission T_2 of the bottom valley splitter presents a dependence, similar to T_1, on the magnetic field and V_2.

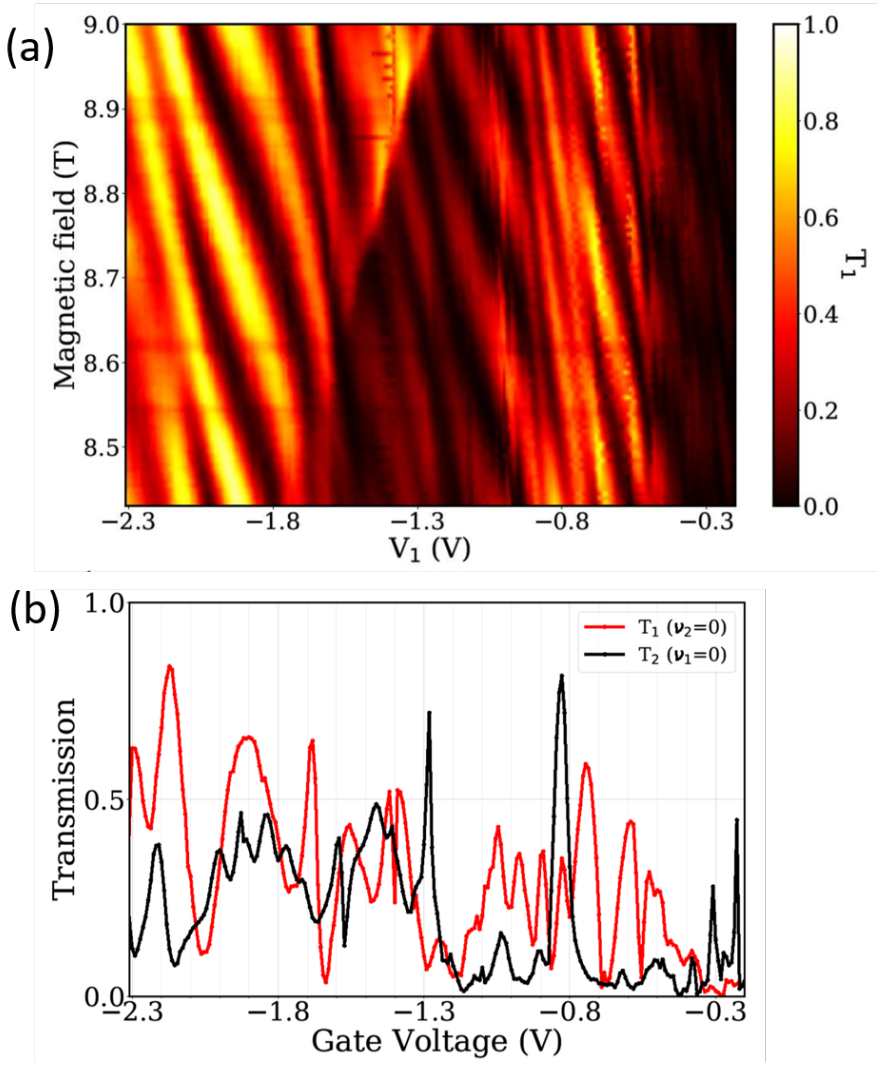

Figure 3.4: (**a**) Measured T_1 as a function of V_1 and the magnetic field with V_2 tuned so that $\nu_{sg2} = 0$. (**b**) Measured transmission as a function of side gate voltage for different configurations: in red T_1 as a function of V_1 for filling factor $\nu_1 \leq -1$ and $\nu_2 = 0$ at $B = 9.23$ T. In black T_2 as a function of V_2 for $\nu_1 = 0$, $\nu_2 \leq -1$ at $B = 8.96$ T.

3.1.2 Origin of the tunability

As shown previously, we can experimentally tune by electrical means the valley degree of freedom. Indeed, the valley mixing can be completely suppressed by imposing a filling factor $\nu_{sgi} = 0$ below the side gates. This can easily be understood, because we push the ends of the pn junction inside the graphene bulk where no scatterer can provide the large momentum transfer necessary to go from one valley to another. In addition, the transmission T_1 of the top valley splitter can be tuned continuously from 0 to 0.89, by electrical means. This fine control obtained on the valley isospin raises fundamental questions about the underlying physical mechanism. Theoretically, we still don't have a clear picture for it, however simulations carried out by our collegue from SPEC, G. Fleury, seems to corroborate the experimental behaviors observed. In this section, I will first detail a few elements of theoretical description of our system, followed by a discussion of G. Fleury's numerical simulations.

Elements of theoretical description

In this paragraph, I will present how one can theoretically describe our system. First, as explained before, we call interface states, states that propagate along the pn junction. In the configuration depicted in figure 3.3, they have a spin down and are noted : $|\downarrow, \overrightarrow{w}\rangle$ in the n region, $|\downarrow, -\overrightarrow{w}\rangle$ in the p region. Splitting of the incoming edge channel $|\downarrow, T_{\mathrm{R}}\rangle$ into the two interface states implies that the interface scattering state is a superposition defined as follows :

$$|\Psi_{initial}\rangle = t_1|\downarrow, -\overrightarrow{w}\rangle + r_1|\downarrow, \overrightarrow{w}\rangle \tag{3.1}$$

r_1 and t_1 in equation 3.1 satisfy $|r_1|^2+|t_1|^2=1$. However, we still don't have a clear theoretical framework to explain how by changing V_1, one can change t_1.

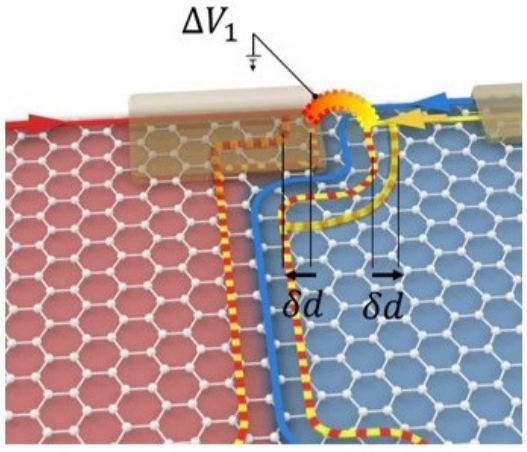

(a)

Figure 3.5: (**a**) Schematic of the δd displacement of the pn junction interface along the top side gate induced by a change ΔV_1 of the applied bias.

Simulations

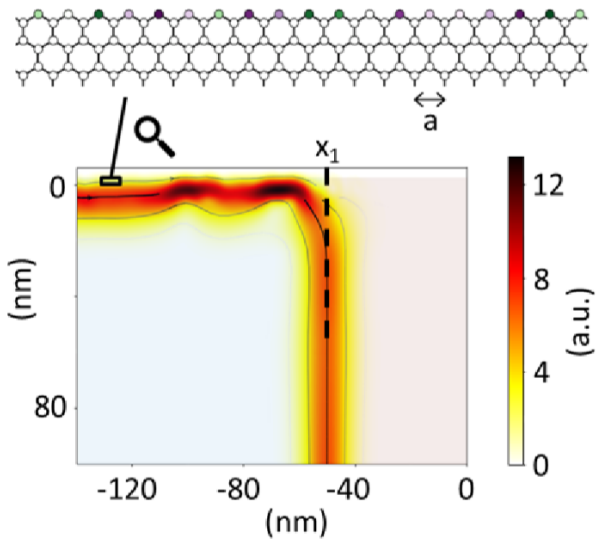

Figure 3.6: Simulations done by G. Fleury. Local current of spin down electrons injected from the upper left contact, in the vicinity of the pn interface and of the top sample edge. The latter is modeled as a disordered zigzag edge in KWANT simulations. The two interface states are superimposed within the considered non-interacting model.

Valley splitting relies on the atomic defect of the upper physical edge and therefore depends both on the edge configuration (zigzag or armchair) and the disorder. We numerically calculate T_1 with KWANT [31] considering a local current of spin down electrons injected from the upper left contact in a pn junction (see Appendix A for detailed explanations). Position x_0 of the bottom interface is fixed while position x_1 where the np interface and the sample edge intercept is varied (see layout in figure 3.6). Note that experimentally the position of x_1 is set by V_1. We first consider the ideal case in the absence of disorder for a zigzag edge configuration. In figure 3.7.a, T_1 is plotted as a function of x_1, and oscillates with a period a (a being the lattice constant). In the physical case, we have no control on the edge configuration (random mix between zigzag and armchair) and the disorder. In figure 3.7.b, we add roughness at the zigzag physical boundary and on-site disordered potential. Oscillations are robust to edge disorder, though the amplitude and the period of the oscillations (well defined locally) vary with x_1. In particular, this period is found to fluctuate roughly between a and 2a. Since the comparison between experimental measurement (figure 3.4.b) and numerical simulation with disorder (figure 3.7.b) are in good qualitative agreement, we interpret the oscillations of $T_1(V_1)$ as the hallmark of the manipulation of $|\Psi_{\text{initial}}\rangle$ valley polarization with side gate voltage. This also means that applying 100meV on the side gate typically shifts the interface state by 1nm.

If now we consider the Bloch sphere, with $|\overrightarrow{w}\rangle$ as North pole and $|-\overrightarrow{w}\rangle$ as South pole, to represent the valley mixing process, by changing the transmission T_1 (thanks to the bias V_1), we can directly tune the azimutal angle of a valley-isospin qubit. When the azimutal angle is chosen to be $\pi/2$ (the top valley splitter is half-open as $T_1 = |t_1|^2 = 0.5$), the valley isospin of the initial state $|\Psi_{\text{initial}}\rangle = (|\downarrow, \vec{w}\rangle + e^{i\theta}|\downarrow, -\vec{w}\rangle)/\sqrt{2}$ (θ being an irrelevant phase

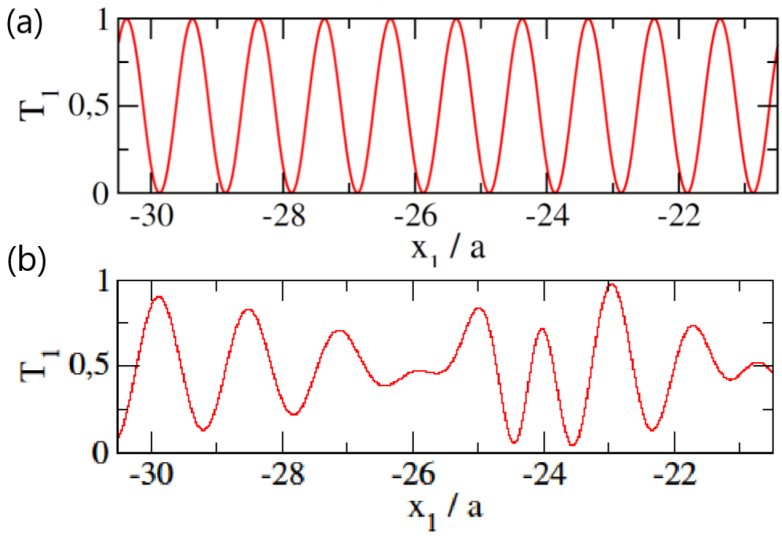

Figure 3.7: Simulations done by G. Fleury. (**a**) Transmission T_1 of the configuration depicted in figure 3.6, calculated with KWANT as a function of the N-P interface position x_1 in the absence of disorder. $T_1(x_1)$ oscillates between 0 and 1 with period a (lattice spacing). (**b**) Same as (a) when roughness and disorder are added at the upper zigzag edge.

set to 0 here) at the entrance of the PN interface lies on the equator. However, without taking into account the magnetic field, the manipulation of the state in the equatorial plane is not possible.

3.2 Probing coherence of valley polarized state by MZI

The electrical control over the splitting of the incoming states between the interfacial states $|\downarrow, -\overrightarrow{w}\rangle$ and $|\downarrow, \overrightarrow{w}\rangle$ thanks to the bias V_1 gives us a completely tunable valley polarization of the $|\psi_{initial}\rangle$ state, i.e. we directly manipulate the valley degree of freedom. The observed experimental results are in agreement with numerical simulations, indicating that we have a fine control over the interface position with the electrical gating. However, in order to envision electron quantum optics experiments with the valley polarized states propagating along the junction, the valley mixing process has to be coherent. We used Mach Zehnder interferometry (MZI) to probe the coherence of the valley polarized state. In this section, I will first present how we carried out a MZI experiment, a theoretical framework describing the experiment, and the results obtained. Then a quantitative study of MZI oscillations depending on the side gates transmissions is developed.

3.2.1 MZI in the valley splitter sample

Principle and theoretical description

By tuning the filling factor below both side gates to $\nu_{sgi} \leq -1$, pseudo spin can mix at the top and bottom corners defining a closed loop or "valley" interferometer (as depicted

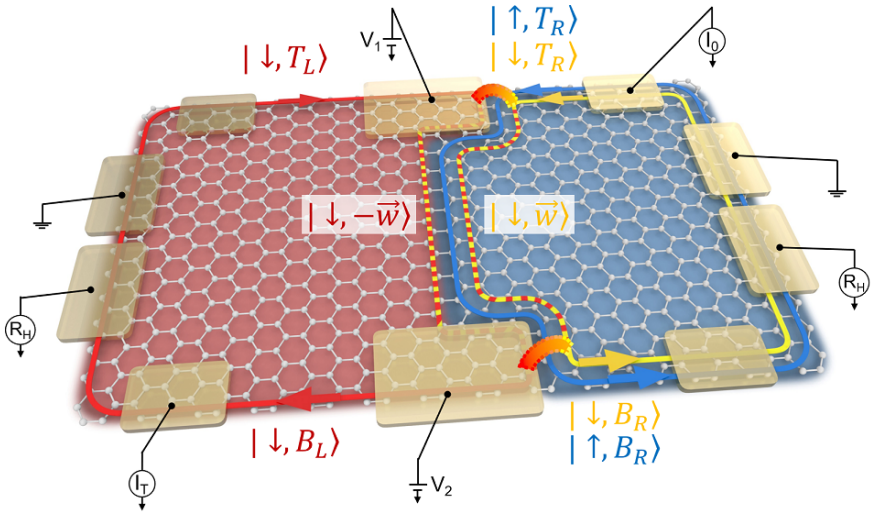

Figure 3.8: Schematic representation of the valley splitter sample in the MZI configuration, i.e. each side gate tuned in a transmitting configuration, here : $\nu_{sg1} = \nu_{sg2} = -1$.

in figure 3.8). The two arms of the interferometer are formed by the two spin down interface states propagating along the pn junction, which are split in space as a result of electron-electron interactions (not included in numerical simulations discussed above). Electrons propagate on each side of the pn interface and accumulate an Aharanov-Bohm phase which is at the bottom end of the junction $\Phi_{\mathrm{AB}}/2$ $(-\Phi_{\mathrm{AB}}/2)$ for electrons coming from the left (right) arm. Φ_{AB} is expressed in equation 3.2 as a function of B the applied magnetic field, A the area enclosed by the two arms of the interferometer and $\Phi_0 = h/e$ the flux quantum.

$$\Phi_{\mathrm{AB}} = 2\pi \frac{\mathrm{BA}}{\Phi_0} \tag{3.2}$$

Taking into account this Aharanov-Bohm phase, the state $|\Psi_{initial}\rangle$ after propagating along the junction gives rise to the state $|\Psi_{final}\rangle$ as expressed in equation 3.3. As shown in figure 3.9, this corresponds in the Bloch sphere representation to a rotation of the $|\Psi_{initial}\rangle$ state of an angle Φ_{AB} around the z-axis.

$$|\Psi_{final}\rangle = r_1|\downarrow, \vec{w}\rangle + t_1 e^{-i\Phi_{AB}}|\downarrow, -\vec{w}\rangle \tag{3.3}$$

Bottom end of the pn junction being a physical edge, it facilitates valley mixing. For the top mixing point, we introduced a scattering process converting $|\downarrow, T_{\mathrm{R}}\rangle \rightarrow |\Psi_{initial}\rangle$, we can introduce a similar process at the bottom end by considering an interface "eigen"-state $|\widetilde{\Psi}\rangle$ that perfectly goes to the left. In other words, at the bottom mixing point, we have a scattering process such that $|\widetilde{\Psi}\rangle \rightarrow |\downarrow, B_L\rangle$. $|\widetilde{\Psi}\rangle$ can be expressed in the following way :

$$|\widetilde{\Psi}\rangle = r_2|\downarrow, -\vec{w}\rangle + t_2|\downarrow, \vec{w}\rangle \tag{3.4}$$

Again, r_2 and t_2 satisfy $|r_2|^2+|t_2|^2=1$. Note that the state orthogonal to $|\widetilde{\Psi}\rangle$, perfectly goes to the right, i.e. to $|\downarrow, B_R\rangle$. The valley interferometer transmission $\mathrm{T_{VI}}$ is given by

the following equation :

$$T_{\mathrm{VI}} = |\langle\widetilde{\Psi}|\Psi_{final}\rangle|^2 = |r_1t_2|^2 + |r_2t_1|^2 + 2|r_1t_1r_2t_2|\cos(\Phi_{\mathrm{AB}} + \phi) \tag{3.5}$$

where $\phi = \arg(t_1t_2r_1^*r_2^*)$. We recognize the standard form of the Mach Zehnder interference.

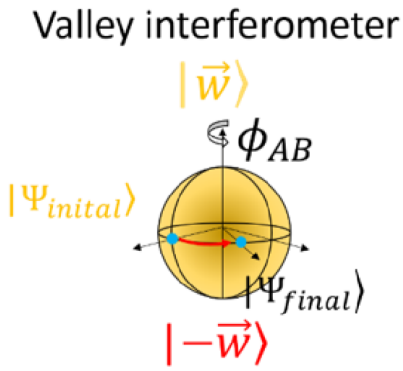

Figure 3.9: Formal equivalence of the interferometer in the Bloch representation, where the poles stand for the interface states $|\overrightarrow{\omega}\rangle$ and $|-\overrightarrow{\omega}\rangle$. If the first valley splitter is half-open ($T_1 = |t_1|^2 = 0.5$), the vector representing the scattering state $(|\overrightarrow{\omega}\rangle + e^{i\theta}|-\overrightarrow{\omega}\rangle)/\sqrt{2}$ (θ being an irrelevant phase set to 0 here) at the entrance of the junction lies in the equator and subsequently rotates around the z-axis when it accumulates an AB phase upon propagation.

Experimental measurements

To measure the transmission of the top side gate T_1, we swept the voltage V_1 applied on it and the magnetic field B, while keeping a constant bias V_2 on the bottom side gate so that $\nu_{sg2} = 0$ (i.e. $T_2 = 0$). In order to experimentally investigate the MZI regime, we achieved the same experiment but with a different fixed bias V_2 so that $T_2 \sim 1/2$. In figure 3.10, the valley interferometer transmission $T_{VI} = I_T/(I_0/2)$ is plotted on the same magnetic field and V_1 range as in figure 3.4 but for $T_2 \sim 1/2$. A clear interference pattern is observed. To change the Aharanov-Bohm phase Φ_{AB}, we can either sweep the magnetic field (B) or change the enclosed area (A) defined by the two arms using side gates. This is why in figure 3.10 the interference fringes depend on the magnetic field and on V_1.

Afterwards, we concentrated on a small $B-V_1$ window in which T_1 was almost constant and around 1/2, while keeping V_2 fixed so that $T_2 \sim 1/2$. The resulting oscillations, presented in figure 3.11a, have a magnetic field periodicity of $\Delta B = 25mT$. These smaller period oscillations are naturally interpreted as interference fringes of a Mach-Zehnder interferometer. From the Aharanov-Bohm phase (equation 3.2), we get the valley interferometer area $A = \Phi_0/\Delta B = 0.15\mu m^2$, and a spatial separation of $110nm$ between the two interface channels, given a $1.5\mu m$ long pn junction. The separation results from electron-electron interactions [84].

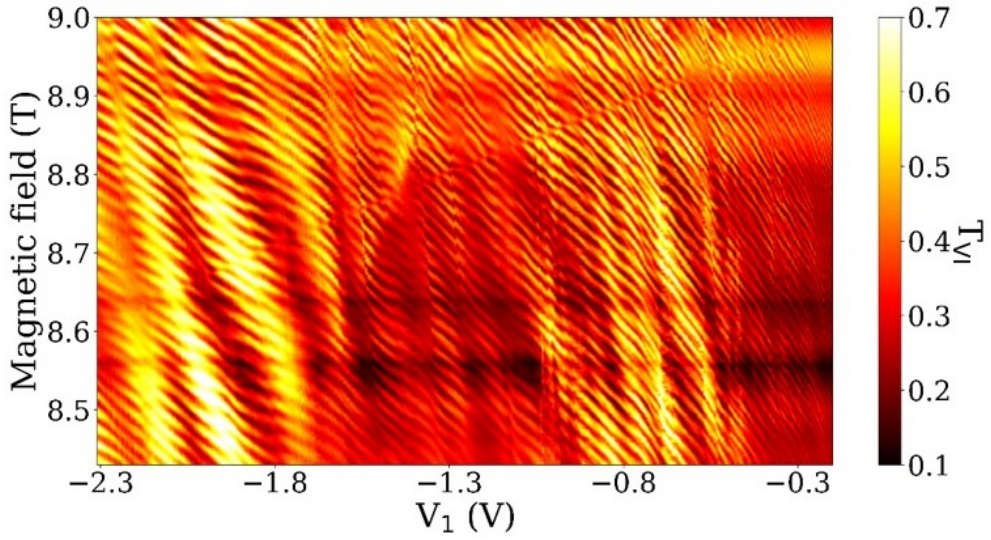

Figure 3.10: Valley interferometer transmission T_{VI} as a function of the magnetic field B and V_1 for $T_2 \sim 1/2$ (same $B - V_1$ range as in figure 3.4).

The period $\Delta V_1 = 50meV$ indicates that the interferometer area A is tuned by V_1. The gate voltage V_1 generates potential to the p side and the n side asymmetrically, resulting in change δs of the spatial separation between the interface channels and shift $\delta d \sim \delta s/2$ of the pn interface below the top side gate (as depicted in figure 3.11b). When changing the voltage V_1 by ΔV_1, the Aharanov-Bohm phase undergoes a 2π rotation generated by a $\delta s L_s$ change of the area enclosed by the interferometer arms, with the side-gate length $L_s = 450$ nm. From this, we estimate $\delta s \sim 1$ nm, hence $\delta d \sim 0.5$ nm (considering $B = 9.2T$). This implies that $\Delta V_1 = 100$ meV applied on the top side gate voltage V_1 enables to shift the pn interface by a distance of $\delta d \sim 1$ nm, supporting that the dependence of T_1 on V_1 in figure 3.4 is related with the valley isospin. The two measurements in figure 3.4 and 3.10 are perfectly consistent and confirm our interpretation. We remark that independent control of the two valley splitters is crucial for characterization of the valley splitters and the Mach-Zehnder interferometers, as there are the multiple periodicities of different origin : oscillations of T_1 and MZI oscillations T_{VI}. This was not achieved previously [84][33]. Moreover, using the MZI configuration we checked that the reflection and transmission through the pn junction are oscillating in phase opposition, and that their sum is equal to the injected current, i.e. the current is conserved (see appendix A.2 for details).

The visibility of the MZI oscillations is an essential tool to study the coherence in the system. As explained in the introductive section about MZI (section 1.2.4), the visibility V can be computed thanks to the maximum MZI transmission value $T_{VI,max}$ and the minimum one $T_{VI,min}$ (equation 3.6). In order to determine the experimental visibility, we fitted the MZI oscillations by a sinusoidal function. Indeed, as shown in equation 3.6, the visibility of the oscillation is directly given by the ratio between the amplitude A_{osc} and the offset B_{osc} of the sinusoidal fit function.

$$V = \frac{T_{VI,max} - T_{VI,min}}{T_{VI,max} + T_{VI,min}} = \frac{A_{osc}}{B_{osc}} \tag{3.6}$$

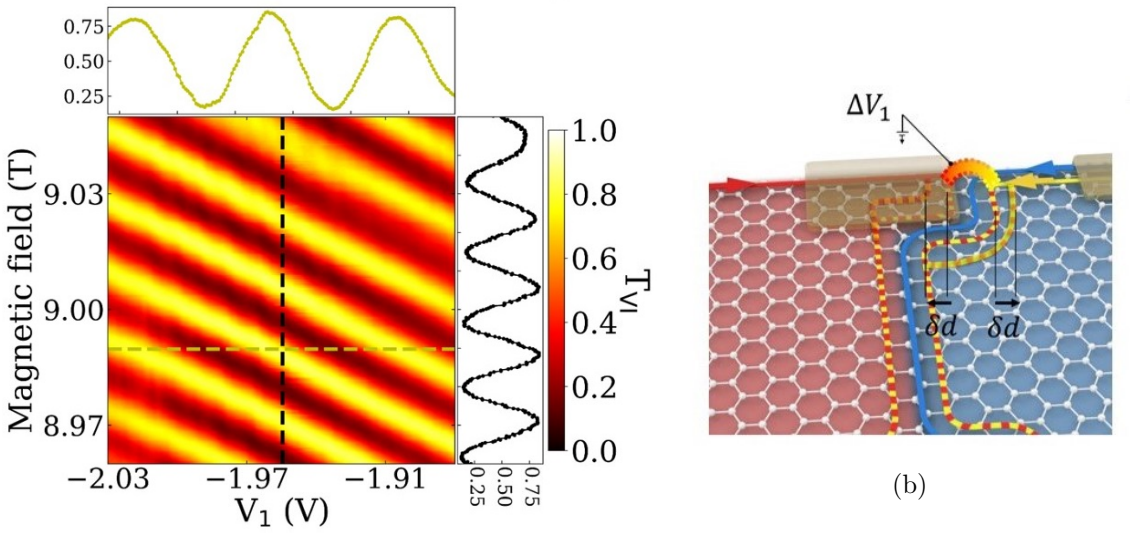

(a) (b)

Figure 3.11: (**a**)Valley interferometer transmission T_{VI} as a function of the magnetic field and V_1 with $T_1 \sim T_2 \sim 1/2$. (b) Schematic of the δd displacement of the pn junction interface along the top side gate induced by a change ΔV_1 of the applied bias.

An example of a sinusoidal fit is presented in figure 3.12. One can note the good agreement between the fit function and the experimental data. Thanks to this procedure, a visibility of 70% was extracted from data presented in figure 3.11a.

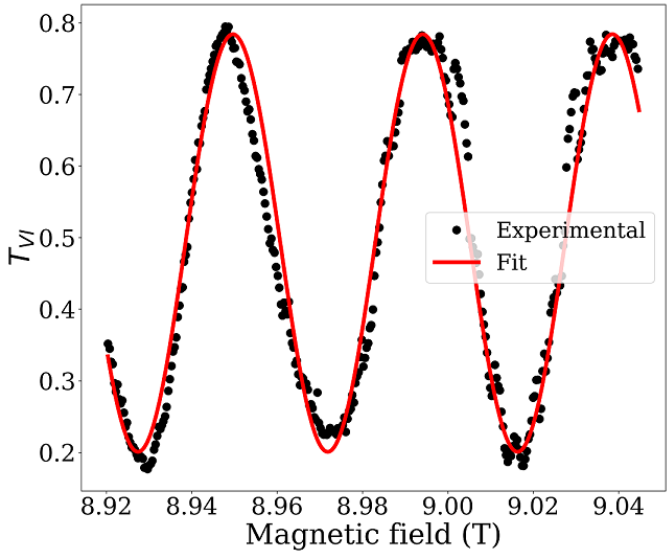

Figure 3.12: Sinusoidal fit (red) of T_{VI} oscillations as a function of the magnetic field.

Similarly to the side gates, back and top gates can change the area A enclosed by the two arms of the interferometer. Thus, we also obtained oscillations of the valley interferometer transmission T_{VI} by sweeping the bias applied on the back and top gates.

Nevertheless, the periodicities obtained are different for each gate as the lengths on which they act are not the same.

Finally, I would like to underline that our study represents the first experimental realization of a fully tunable valley-MZI in graphene, i.e. a MZI with tunable transmissions T_1 and T_2. Thanks to this tunability we could carry a quantitative study of the visibility dependence on the transmissions of the valley splitters, as will be detailed in the following section.

3.2.2 Quantitative study of the visibility dependence on transmission

In the brief recap of chapter 1 about MZI in GaAs/AlGaAs heterostructures (see section 1.2.4), I underlined an important feature of MZI : the dependence on T_1 of the visibility $\upsilon = 2\sqrt{T_1(1-T_1)}$ when $T_2 = 1/2$. Similar measurements were not achievable in graphene MZI up to now, as in the previously implemented interferometers, there was no control over the transmission at each mixing point. Thanks to our tunable valley splitters, we are able in our sample to tune independently the transmissions T_1 and T_2. Therefore, we can carry out an experimental study of the visibility dependence on the valley splitters transmissions, and check the consistency of the results obtained with theoretical predictions. This would further confirm the MZI picture along graphene pn junction with tunable valley splitters at its extremities. First, I will present a theoretical framework for the graphene MZI predicting the visibility dependence on the transmission T_1 when $T_2 = 1/2$. Then the experimental results are described and compared to the theoretical prediction.

Theoretical dependence of the visibility

As explained previously, the visibility υ of the oscillations can be computed thanks to the following formula :

$$\upsilon = (T_{VI,max} - T_{VI,min})/(T_{VI,max} + T_{VI,min}) \tag{3.7}$$

with $T_{VI,min}$ ($T_{VI,max}$) the minimum (maximum) transmission T_{VI} through the valley interferometer. In addition, we obtained the following expression for our graphene MZI :

$$T_{\mathrm{VI}} = |\langle\widetilde{\Psi}|\Psi_{final}\rangle|^2 = |r_1t_2|^2 + |r_2t_1|^2 + 2|r_1t_1r_2t_2|\cos(\Phi_{\mathrm{AB}} + \phi) \tag{3.8}$$

Considering $|t_2|^2 = |r_2|^2 = 1/2$ and $T_1 = |t_1|^2$, using equations 3.7 and 3.8, one gets :

$$\upsilon = 2\sqrt{T_1(1-T_1)} \tag{3.9}$$

We recover a standard transmission dependence of the visibility in a Mach-Zehnder.

Experimental result

As underlined by equation 3.9, the visibility of the MZI transmission T_{VI} oscillations is directly related to the transmission of the top valley splitter T_1, when the bottom one is tuned at a transmission $T_2 \sim 1/2$. Our goal was to experimentally measure the visibility (V) dependence on T_1, in order to compare it to theoretical predictions and see the degree of control obtained in our MZI.

For this aim, the starting point was to find a region where T_1 could be continuously tuned, thanks to the bias V_1, on the biggest span as possible between 0 and 1. As clearly visible in figure 3.4.a of section 3.1, T_1 oscillates while sweeping V_1, and in some spots the span covered by T_1 is effectively large. The transmission also depends on the magnetic field B and oscillates with a big periodicity $\delta B \sim 0.3T$. Since we want to compute the oscillations visibility for a fixed T_1, this latter needs to be constant with the magnetic field. A constant transmission while sweeping the magnetic field can be obtained by adding, for each magnetic field value B, a linear correction to the gate voltage $V_{1,\text{corr}}(B) = aB + b$ (with a and b the computed coefficients). In figure 3.13a, the gate voltage $V_1(B)$ was swept around the corrected value $V_{1,\text{corr}}(B)$ following formula : $V_1(B) = V_{1,\text{corr}}(B) + \delta V_1$ with δV_1 going from -110 to 80mV. Thanks to this, an almost B-independent T_1, going from 0.018 to 0.812, is achieved as a function of the relative bias δV_1. Since T_1 does not reach neither 1 nor 0, we introduce $\bar{T_1} = (T_1 - T_{1,\text{min}})/(T_{1,\text{max}} - T_{1,\text{min}})$ (figure 3.13b). This normalization procedure is based on the assumption that a part of the current is reflected at another point, and does not flow through the interferometer, explaining the lower value of the maximum transmission. An analogue assumption can be made to explain the slightly above zero minimum of the T_1.

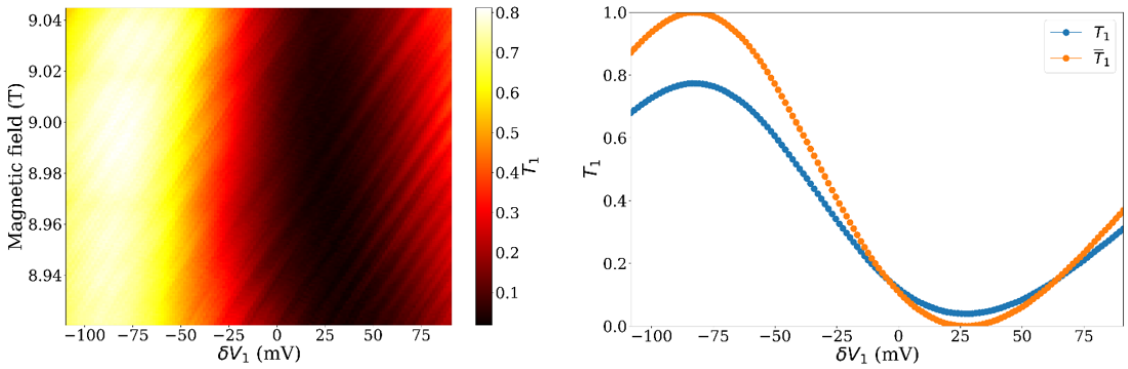

(a) (b)

Figure 3.13: (**a**) Transmission T_1 of the top valley splitter as a function of the magnetic field and the bias δV_1 applied on it (with $\nu_{sg2} = 0$). (**b**) Transmission T_1 averaged over the magnetic field span as a function of δV_1. $\overline{T_1}$ is the normalized value of T_1 defined by $\overline{T_1} = (T_1 - T_{1,min})/T_{1,max}$ with $T_{1,max}$ the maximum value of T_1 and $T_{1,min}$ its minimum.

Then, we tuned $T_2 \sim 1/2$ in the same B-range. As seen on figure 3.14, one can obtain a relatively stable value of T_2, roughly around 1/2, with the magnetic field B by following the brown line in the $B - V_2$ space.

By combining the tuning of T_1 and T_2, we were able to achieve a map showing the evolution of the oscillations with the magnetic field as a function of T_1, while $T_2 \sim 1/2$. The T_{VI} map obtained is shown in figure 3.15. Qualitatively, one can observe that the oscillation amplitude is maximal when $T_1 \sim 1/2$, whereas for $T_1 \sim 1$ and $T_1 \sim 0$ the oscillations are completely washed out.

Quantitatively, for each value of δV_1, corresponding to a fixed value of T_1, we computed the experimental visibility thanks to sinusoidal fits (method explained in section 3.2.1). The experimental visibility as a function of T_1 is plotted in figure 3.16. It is compared

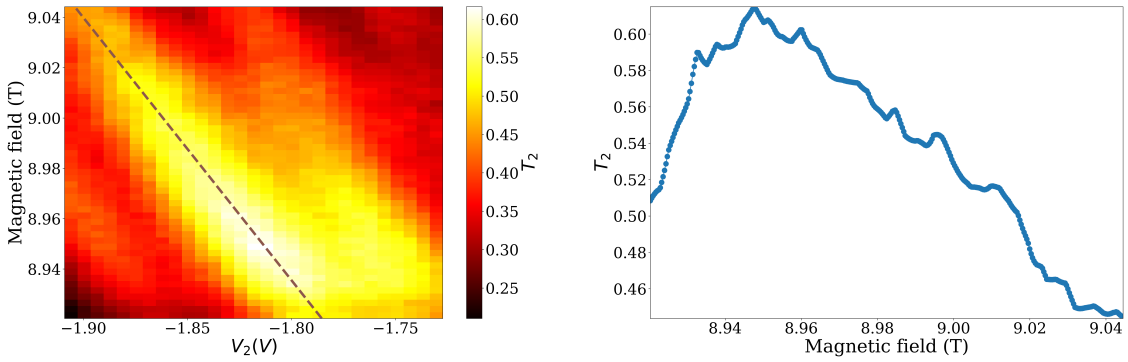

(a) (b)

Figure 3.14: (**a**) Transmission T_2 of the bottom valley splitter as a function of the magnetic field and the bias V_2 applied on it (while $\nu_{sg1} = 0$). (**b**) Transmission T_2 as a function of V_2 following the brown line in (**a**).

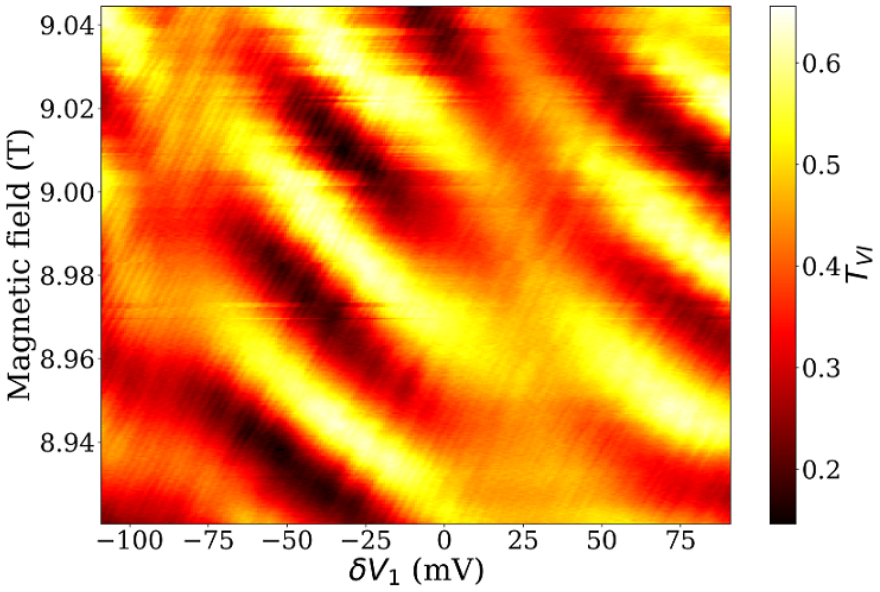

Figure 3.15: (**a**) Transmission T_{VI} of the valley interferometer as a function of the magnetic field B and the bias δV_1 on the top valley splitter, same $B - \delta V_1$ window as in T_1 measurement (figure 3.13) with $T_2 \sim 1/2$ (figure 3.14).

to the theoretical dependence (black line) for $T_2 \sim 1/2$ derived previously in equation 3.9 with the addition of a decoherence prefactor z, giving the following equation :

$$V = 2z\sqrt{\bar{T}_1(1-\bar{T}_1)} \tag{3.10}$$

z was fixed at 0.59 using the maximum experimental visibility. The averaged value of T_2 over the magnetic field range is 0.53 (confirming the assumption $T_2 \sim 1/2$). The good agreement between the experimental visibility and the theoretical law support the formation of the Mach-Zhender valley interferometer and confirms the coherence of the

valley superposition in equation 3.1.

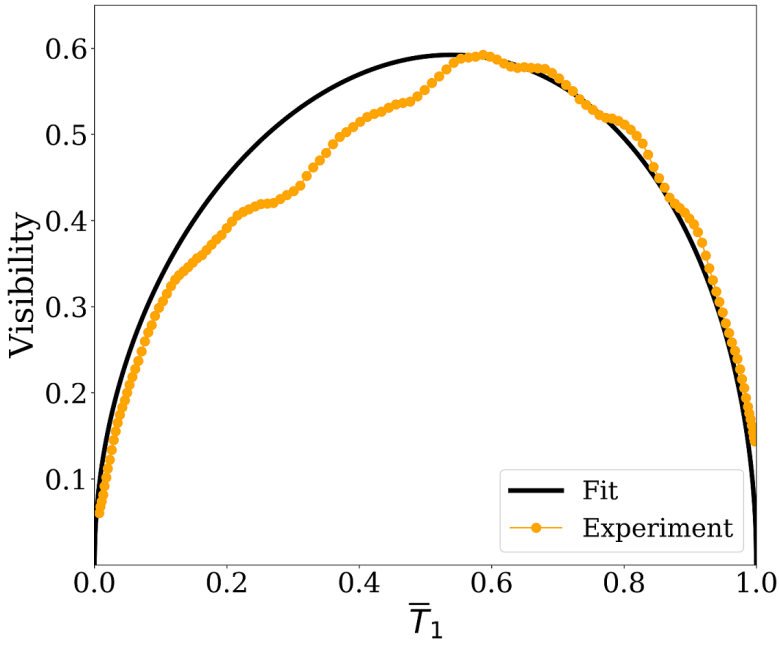

Figure 3.16: Orange dots : experimental visibility measured as a function of the normalized $\bar{T}_1$ with T_2=0.5. Black solid line : Computed visibility $V = 2z\sqrt{\bar{T}_1(1-\bar{T}_1)}$ with $z = 0.59$.

3.2.3 Phase shift

Experimental observations

A closer look at the interference pattern of T_{VI} at fixed V_2 reveals unusual phase shifts. They are highlighted in figure 3.17b and analyzed in view of data for T_1 in the same range of V_1 and B parameters (see figure 3.17a). In both panels, black dashed lines are added to indicate trajectories in the (B, V_1) plane along which T_1 shows a local maximum. By comparing the oscillation pattern of T_{VI} along those two (adjacent) trajectories for each value of B (vertical green grid in figure 3.17b), we observe a sudden change $\sim \pi$ of the phase of the oscillations within the magnetic-field change of $\leq 30mT$ at certain parameter regions (see the third and fourth vertical lines). The change $\sim 30mT$ is much smaller than the period ($\Delta B \sim 300mT$) of the top and bottom valley splitters, so it is unlikely that the phase shift originates from the phase change of the valley-splitter amplitudes $t_{i=1,2}$ and $r_{i=1,2}$ by the magnetic field; such nontrivial phase shifts have not been found in Mach-Zehnder interferometers in GaAs.

Theoretical leads

We attribute the sudden change ($\sim \pi$) of the phase shift to the valley-isospin rotation at the top valley splitter. It was theoretically predicted [80] that the valley isospin of the

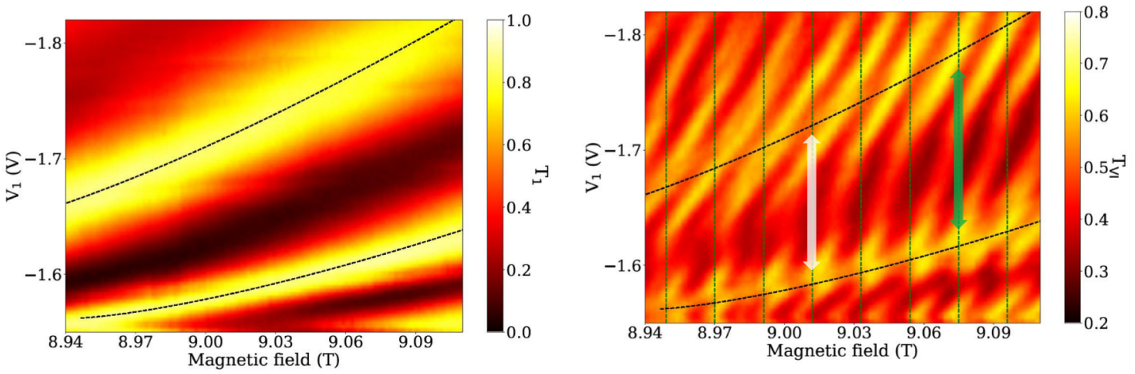

(a) (b)

Figure 3.17: (**a**) T_1 as a function of the magnetic field B and V_1. In this interesting region, local maximum of T_1 has been highlighted with a black dashed curve. (**b**) T_{VI} in the same magnetic field and V_1 range as in figure 3.17a with now $\nu_2 \leq$ -1 set at the bottom side gate. We note phase shift of T_{VI} between two adjacent values of maximum T_1 at a fixed magnetic field (vertical dashed lines). The phase shift shows sudden change $\sim \pi$ around the third and fourth vertical lines (the area with phase shift π is framed with a dashed white line).

interface states rotates by a large angle $\Theta_{ww'} \sim \pi$ when a PN interface is parallel shifted on the top edge by the period of the atomic structure while fixed on the bottom edge (by tuning V_1 for instance). Before a parallel interface shift, the initial interface state $|\Psi_{initial}\rangle$ and the junction transmission probability T_{VI} are described by equations (3.1) and (3.8). After the parallel interface shift, the valley isospin rotates from $\pm\vec{w}$ to $\pm\vec{w'}$, and the initial state becomes :

$$|\Psi'_{initial}\rangle = r'_1|\downarrow, \overrightarrow{w'}\rangle + t'_1|\downarrow, -\overrightarrow{w'}\rangle \tag{3.11}$$

with $\Theta_{ww'}$ the valley-isospin rotation angle from $\vec{w}$ to $\vec{w'}$. After propagating along the pn junction, an Aharanov-Bohm phase Φ_{AB} is accumulated, and $|\Psi'_{initial}\rangle$ gives rise to the state :

$$|\Psi'_{final}\rangle = r'_1|\downarrow, \overrightarrow{w'}\rangle + t'_1 e^{-i\Phi_{AB}}|\downarrow, -\overrightarrow{w'}\rangle \tag{3.12}$$

However, the expression of the state going to the left at the bottom $|\widetilde{\Psi}\rangle$ is unchanged, and one has :

$$|\widetilde{\Psi}\rangle = r_2|\downarrow, -\overrightarrow{w}\rangle + t_2|\downarrow, \overrightarrow{w}\rangle \tag{3.13}$$

Therefore, when $|\Psi_{initial}\rangle$ is modified into $|\Psi'_{initial}\rangle$, the valley interferometer transmission becomes :

$$\begin{aligned} T'_{VI} &= |\langle\widetilde{\Psi}|\Psi'_{final}\rangle|^2 = |r'_1\widetilde{t^*_2} + t'_1\widetilde{r^*_2}e^{-i\Phi_{AB}}|^2 \\ &= |r'_1\widetilde{t^*_2}|^2 + |\widetilde{r^*_2}t'_1|^2 + 2|r'_1t'_1\widetilde{r^*_2}\widetilde{t^*_2}|\cos(\phi_{\mathrm{AB}} + \phi') \end{aligned} \tag{3.14}$$

where $\phi' = \arg(t'_1\widetilde{t_2}r'^*_1\widetilde{r^*_2})$. As shown in equation 3.15, $\widetilde{t^*_2}$ and $\widetilde{r^*_2}$ are related to t^*_2 and r^*_2 by the unitary matrix U representing the change of basis from $(|\downarrow, \overrightarrow{w}\rangle, |\downarrow, -\overrightarrow{w}\rangle)$ to

$(|\downarrow, \overrightarrow{w'}\rangle, |\downarrow, -\overrightarrow{w'}\rangle)$.

$$\begin{pmatrix} \widetilde{t_2^*} \\ \widetilde{r_2^*} \end{pmatrix} = U \begin{pmatrix} t_2^* \\ r_2^* \end{pmatrix} \tag{3.15}$$

Matrix U can be expressed as a function of the rotation angle of the valley $\Theta_{ww'}$:

$$U = \begin{pmatrix} cos(\frac{\Theta_{ww'}}{2}) & sin(\frac{\Theta_{ww'}}{2}) \\ -sin(\frac{\Theta_{ww'}}{2}) & cos(\frac{\Theta_{ww'}}{2}) \end{pmatrix} \tag{3.16}$$

The oscillation phase shift between T_{VI} and T'_{VI} is the difference between $\phi = \arg(t_1 r_1^* t_2 r_2^*)$ and $\phi' = \arg(t'_1 {r'_1}^* \tilde{t}_2 \tilde{r}_2^*)$. Using the parametrization of $t_2 = e^{i\varphi}\sin(\gamma/2)$ and $r_2 = \cos(\gamma/2)$ with $\gamma \in [0, \pi]$ and $\varphi \in [0, 2\pi]$, we find :

$$\begin{cases} 2t_1 r_1^* t_2 r_2^* = t_1 r_1^* e^{i\varphi} \sin\gamma \\ 2t'_1 {r'_1}^* \tilde{t}_2 \tilde{r}_2^* = t'_1 {r'_1}^* (\sin\Theta_{ww'}\cos\gamma + \sin\gamma\cos\varphi\cos\Theta_{ww'} + i\sin\gamma\sin\varphi) \end{cases} \tag{3.17}$$

So, the rotation angle $\Theta_{ww'}$ can affect the interference pattern, which may explain the unusual abrupt $\sim \pi$ jump as a function of the magnetic field in certain parameter regions.

3.3 Towards valleytronics in monolayer graphene

Recently, the possibility to encode the information into the valley degree of freedom in two-dimensional layered materials has generated a lot of interest [10][75]. For example, optical control of the valley isospin has already been demonstrated in monolayer MoS_2 [55], and the pure valley current [78] and the domain wall effects [39] have been observed in a biased bilayer graphene. Valleytronics in monolayer graphene has been less studied [30] in experiments because of the difficulty in manipulating valley isospin by electrostatic means — the inversion symmetry cannot be broken by usual gate voltage that generates electrostatic potential smoothly changing on an atomic distance scale. Unlocking this issue is valuable, since it implies the robustness of the valley isospin, a crucial merit of valleytronics in monolayer graphene.

In order to achieve valleytronics devices in monolayer graphene, a full electrical control of the valley isospin is necessary. Being able to tune the valley isospin scattering at graphene edge is a way of resolving the difficulty. Indeed, the analysis achieved in the previous section (3.2.2) indicates that, thanks to the side gates, the valley isospin direction of the superposition $|\Psi_{\mathrm{final}}\rangle$ can be tuned over the range of $|t_1|^2 = 0.03$ - 0.89 and $\phi_{\mathrm{AB}} = 0$ - 2π by changing V_1 and B. As shown in figure 3.18, this implies that we can cover almost all the states in the Bloch sphere representation of the valley qubit. Hence the valley splitters would enable the basic operations of a valley-isospin qubit.

However, if we want to use valley-isospin qubits for quantum operation they have to be sufficiently sturdy. In the next chapter, I will study the characteristic energies of the decoherence of the system in order to investigate the steadiness of the coherent valley mixing process.

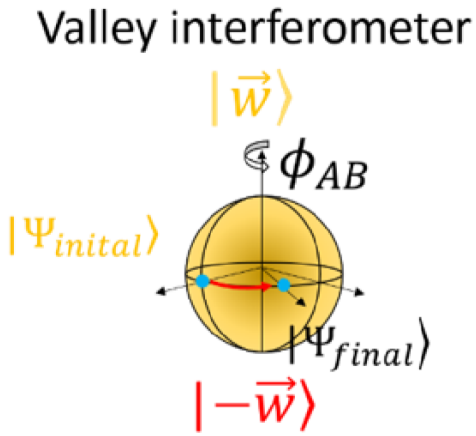

Figure 3.18: Equivalence of the interference and the rotation of a valley-isospin qubit on the Bloch sphere, where the poles stand for the valley isospin $\pm\vec{w}$ of the copropagating PN interface channels. The azimutal angle of the valley-isospin qubit is tuned by V_1. When the azimutal angle is chosen to be $\pi/2$ (the top valley splitter is half-open as $T_1 = |t_1|^2 = 0.5$), the valley isospin of the initial state $|\Psi_{\text{initial}}\rangle = (|\downarrow, \vec{w}\rangle + e^{i\theta}|\downarrow, -\vec{w}\rangle)/\sqrt{2}$ (θ being an irrelevant phase set to 0 here) at the entrance of the PN interface lies on the equator and subsequently further rotates around the z-axis by the polar angle ϕ_{AB} while the qubit evolves to $|\Psi_{\text{final}}\rangle$ while accumulating an Aharonov-Bohm phase ϕ_{AB} upon propagation.

Chapter 4

Characteristic energies of the coherence

Thanks to the side gates, we obtained a coherent control over the valley degree of freedom. Indeed, by adjusting the transmission below the side gates and inducing an Aharanov-Bohm phase via the magnetic field, one can tune the valley isospin direction of the output state over the almost whole parameter range in a Bloch sphere representation for a valley-isospin qubit. However, in order to envision quantum operations via the valley encoding, the coherence of the system has to be steady. In this chapter, we investigate the characteristic energy scales of the coherence, by studying the MZ interferences visibility dependence on the energy of incoming electrons. Two different techniques are commonly used to tune the energy of incoming electrons : applying a DC bias on the arms of the interferometer, and increasing the temperature of the whole system. This chapter begins with a reminder of the visibility dependences observed experimentally, in temperature and in DC bias, in GaAs/AlGaAs MZIs, followed by the presentation of different theoretical frameworks developed to explain these results. Then, I will expose the experimental study that we carried out in our graphene valley splitter sample in order to investigate the visibility dependence on the electrons energy and the associated characteristic energy scales. Finally, is discussed how the theoretical frameworks, enabling to model the behaviors observed in GaAs/AlGaAs, can be adapted to graphene MZIs, taking into account the peculiarities of this new material.

4.1 Reminder of GaAs case

In order to understand the coherence properties in quantum Hall edge channels in GaAs/AlGaAs heterostructures, extensive studies have been carried out in MZIs to investigate the visibility dependence on the temperature and the DC bias. In this section, I briefly summarize the results obtained in these studies, and in particular the characteristic energy scales extracted. First is described the case of the DC bias studies, followed by the temperature studies. In a second time, I detail two theoretical frameworks that have been developed in order to understand the decoherence experimentally observed in both cases.

4.1.1 Finite bias visibility in GaAs MZIs

The basic idea of DC bias studies is to superimpose a finite bias to the injected AC signal on the input channel of the MZI, and then to measure the evolution of the MZ interferences visibility with the applied bias. Experimentally in GaAs MZIs, as detailed hereafter, an intriguing and unexpected finite bias visibility dependence was observed. Furthermore, at $\nu = 2$, the decay of the visibility with the DC bias was shown to present different characteristics depending on the number of incoming edge channels biased : two or one. In particular, in the case of one edge channel biased an intriguing lobe structure was observed. The different experimental observations obtained in those two configurations are detailed sequentially hereafter.

Configuration with one biased edge-channel

In an experiment carried out in 2006 [59] at the Weizmann institute, they studied an electronic MZI defined thanks to two QPCs (noted QPC1 and 2 in figure 4.1), with the addition of an extra QPC (named QPC0) before the MZI. This QPC enables to reflect back one of the incoming edge channels on the MZI. After QPC0, the outer edge state (OES) is at the bias imposed by the source S2, while the inner edge state (IES) is fixed at the ground potential; therefore, they are in a configuration where only one of the edge channels incoming on the MZI is biased.

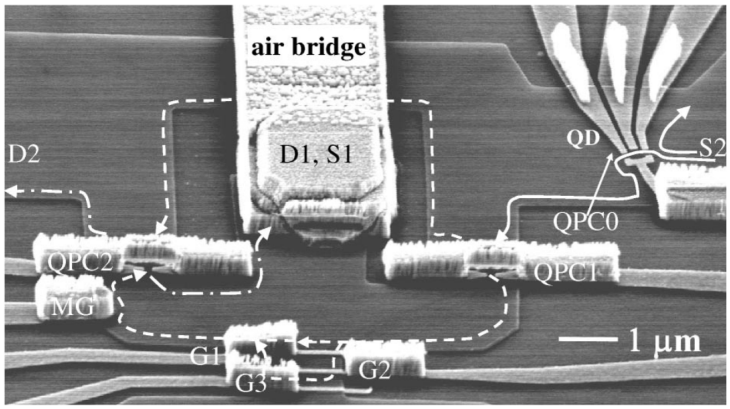

Figure 4.1: Sample used by Neder et al. [59]. A top scanning electron microscope micrograph of the MZI. QPC 1 and 2 correspond to the two beam splitters of the interferometer, while QPC 0 is used to reflect back the desired edge channel.

In this configuration, they obtained a surprising result when measuring the MZI oscillations as a function of the DC bias : a beating appeared in the oscillation contrast as the DC bias was increased, as clearly visible in figure 4.2a. In order to quantitatively study this, they computed the visibility of the oscillations for each DC bias value and observed an intriguing lobe structures varying with the filling factor :

- at $\nu = 1$: a central lobe is surrounded by two side lobes (see figure 4.2c).
- at $\nu = 2$: five major lobes are visible, each $\sim 14\mu V$ wide (see figure 4.2b).

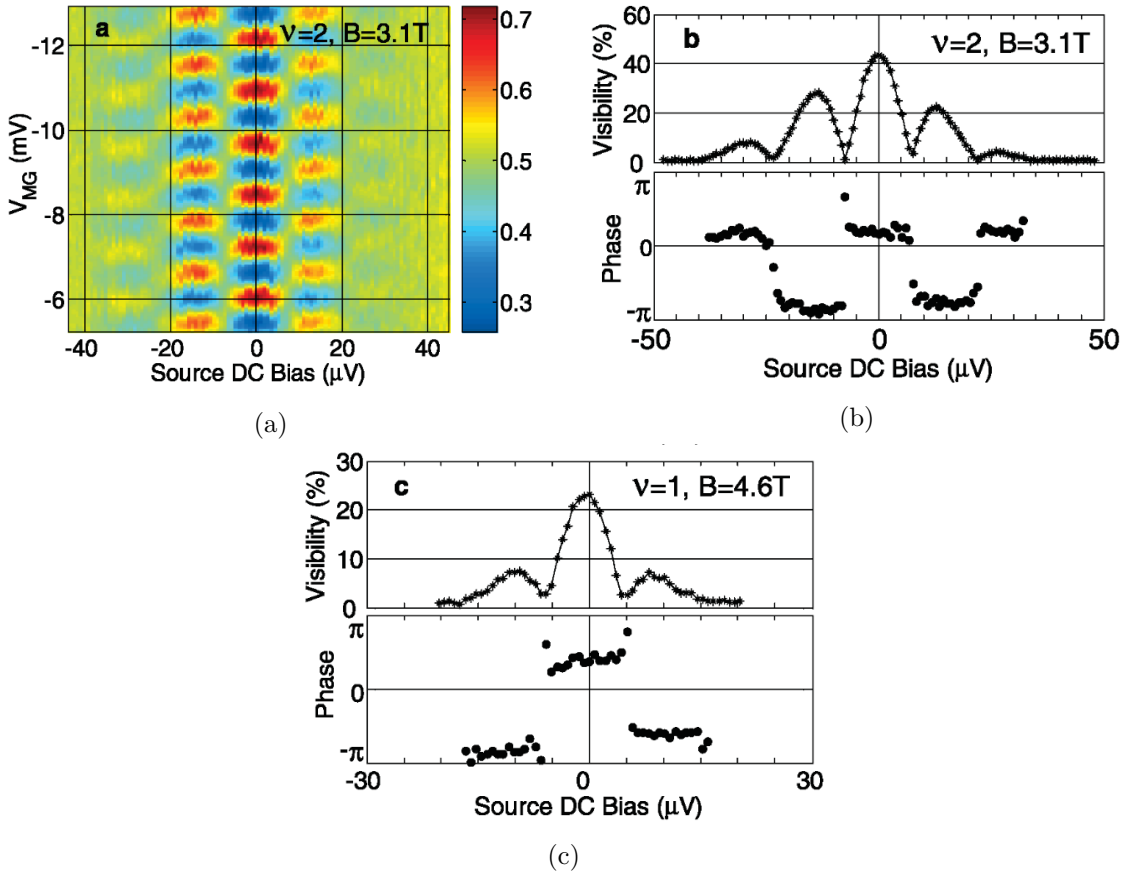

Figure 4.2: Measurement by Neder et al. [59] of the interference oscillations and visibilities. (**a**) Two-dimensional color plot of the differential transmission as a function of the applied DC bias, at filling factor $\nu = 2$. (**b**) Visibility and phase interference pattern at $\nu = 2$ as a function of the applied DC bias. Five major lobes are visible, each $\sim 14\mu V$ wide. The phase at each lobe is constant and slips abruptly by π at each node. (**c**) Similar measurement at $\nu = 1$ exhibiting only three major lobes with the same stick-slip phase behavior.

Remarkably, in this configuration, the central lobe and the side lobes have the same width.

In figure 4.2b and 4.2c, the phase associated with the MZ interferences is plotted in parallel of the visibility. Interestingly, the phase at each lobe is constant and slips abruptly by π at each node. The existence of a one side lobe structure was confirmed by the measurements of Roulleau et al. [72] one year later, however they did not observe the multiple side lobe structure. A transition between one side lobe to several side lobes depending on the filling factor was reported later on by Litvin et al. [51].

Configuration with two edge channels biased

In the case of a bias applied on both of the incoming edge channels, the visibility dependence on DC bias, although decaying, presents different characteristics. This configuration and the resulting visibility dependence on DC bias were first studied in the

pioneering work by Ji et al. [37]. They observed a monotonous decay of the visibility with the temperature and the DC bias, as shown in figure 4.3.

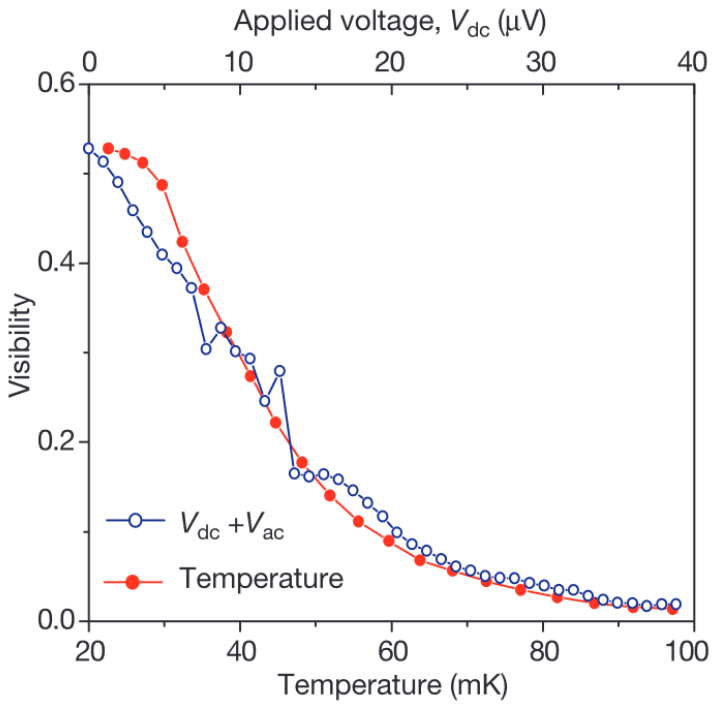

Figure 4.3: Ji et al. measurement [37] in GaAs of the visibility of a MZI, at filling factor $\nu = 2$, as a function of the DC bias applied, and of the temperature.

The decay of the visibility, observed in this configuration (with a bias applied on two edge channels), was studied in more details by Bieri et al. [11], who measured its evolution with the transmission of the first beam splitter, and in particular in the weak back-scattering (WB) and in the weak-tunneling (WT) regimes. As shown in figure 4.4, in the WT regime, they observed a lobe-type structure, but with a central lobe two times wider than the side lobes. In the WB regime, no lobe structure is visible, the visibility still decays with DC bias but non-monotonously. Indeed, one can notice an unexpected enhancement of the visibility, compared to its zero-bias value, when the DC bias is moved away from zero.

To summarize, when the two incoming edge channels are biased the visibility evolution with the DC bias presents a strong dependence on the transmission of the first beam splitter forming the MZI. In addition, in this configuration, no phase rigidity is observed, contrarily to the case where one edge channel is biased.

The energy scales involved

Finally, I would like to stress the energy scale of coherence in the case of GaAs/AlGaAs heterostructures revealed by the measurements of the visibility dependence on the DC bias. Typically the MZ oscillations completely vanish for $|V_{DC}| \sim 40\mu V$, and in the case of a lobe structure, the main lobe width is approximately $20\mu V$, as one can see in

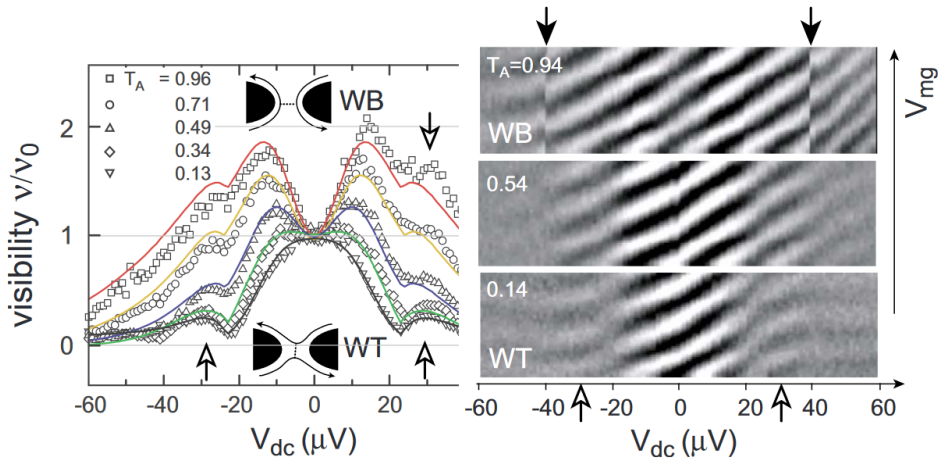

Figure 4.4: **Bieri et al. experimental results in [11].** (**a**) The dependence of the visibility on the DC bias voltage V_{DC} scaled to the zero-bias value for five different T_A (transmission of the first QPC) values $T_A = 0.96$, 0.71, 0.49, 0.34, and 0.13 and QPCB (second QPC) fixed. In the weak back-scattering (WB) limit, the visibility first grows with increasing V_{DC}, whereas it decays in the opposite case of weak-tunneling (WT). (**b**) The phase evolution is visible in the measured differential transmission through the MZI as function of V_{DC} in the WB, WT, and an intermediate regime.

figure 4.2. Therefore, the oscillations are really fragile, electrons injected with an energy of a few tens of μV are sufficient to destroy the coherence along the interferometer.

4.1.2 Temperature dependence of the visibility in GaAs MZIs

The second technique to increase the energy of the incoming electrons is to enhance the temperature of the system. As shown in the pioneering work by Ji et al. [37], the visibility of Aharanov-Bohm oscillations in GaAs MZIs decreases rapidly with the temperature, and completely disappears around $100mK$ (see figure 4.3). Therefore, the coherence in MZI formed in GaAs/AlGaAs heterostructures is really fragile considering temperature increase of the system, consistently with the dependency observed in DC bias. These very low temperatures, necessary to avoid decoherence in these systems, represent an important experimental constraint as it requires state of the art He^3/He^4 dilution fridges.

The temperature dependence of the visibility was investigated further by later studies [73][51], which exhibited an exponential decay of the visibility with the temperature at filling factor $\nu = 2$. As shown in figure 4.5a, in P. Roulleau et al. measurement [73], the visibility follows an exponential decay even at the lowest temperatures ($\sim 20mK$). In comparison, the measurement of Litvin et al. [51], displayed in figure 4.5b, exhibits a deviation from the exponential decay below roughly $40mK$. This deviation may be due to a thermal saturation in their sample, i.e. their electronic temperature never goes below $40mK$.

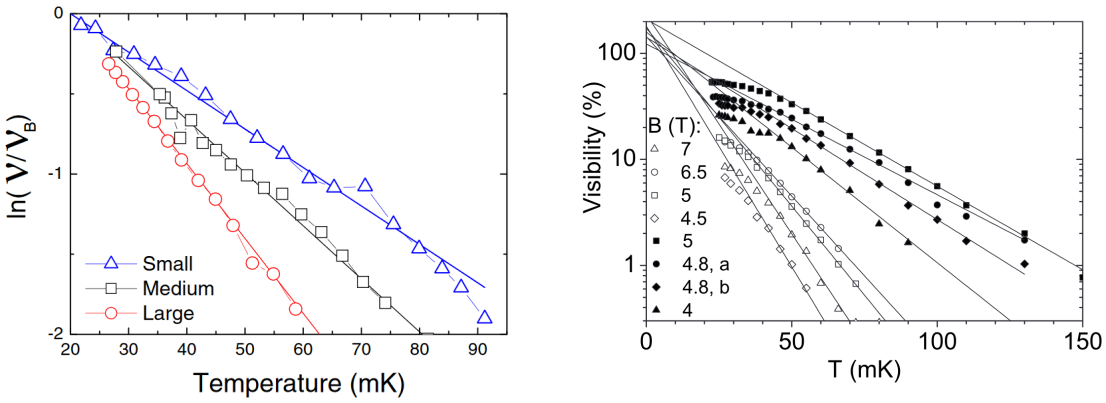

(a) (b)

Figure 4.5: **Exponential decay of the visibility with the temperature.** (**a**) P. Roulleau et al. [73] measurement of the logarithm of the visibility normalized by the visibility at $20mK$. The measurement has been done for three samples of different sizes, at the magnetic field for which the visibility decay is the smallest. (**b**) Litvin et al. [51] measurement of the temperature dependence of visibilities for large (open symbols) and small (full symbols) MZIs at different magnetic fields. The curves "a" and "b" for B=4.8 T correspond to different QPC half transmission points.

4.1.3 Existence of a capacitive coupling between edge channels

In order to apprehend the temperature and DC bias dependence of the visibility, one has to understand the decoherence processes. Interestingly, in GaAs/AlGaAs heterostructures the highest visibility was not observed at filling factor $\nu = 1$, as one could expect, but at $\nu = 2$. As claimed in [70], this may be due to decoherence induced by collective spin excitations, typically the skyrmions described in [8], which enables spin flip processes. Hence, most of the experiments have been carried out at $\nu = 2$. In this regime, one of the source of decoherence could be related to the coupling between the co-propagating edge channels, as will be detailed in the next section 4.1.4. Hereafter, I will just give some experimental evidences of the existence of a capacitive coupling.

For probing this coupling, P. Roulleau et al. [70] used the same sample as in their previous study [73]. As depicted on the layout in figure 4.6.a, the inner edge state (in red), linked to the voltage source V_2, is completely reflected by the QPC G_0, while the outer edge state (in blue) is fully transmitted. By sweeping the voltage applied on the side gate, noted SG on the schematic, they change the area enclosed by the two arms of the interferometer, and thus the Aharanov-Bohm phase. The oscillations of the current transmitted through the outer edge state as a function of the voltage V_{SG} on SG are presented in figure 4.6.b. As shown in figure 4.6.c, the phase oscillations of the transmitted current can also be obtained via the application of a bias V_2 on the inner edge channel. This implies that the inner edge channel is acting as a local gate thanks to its capacitive coupling to the outer one. Indeed, the interfering part $I_\sim$ of the transmitted current in the presence of a capacitive coupling was computed in [71], and its expression is the

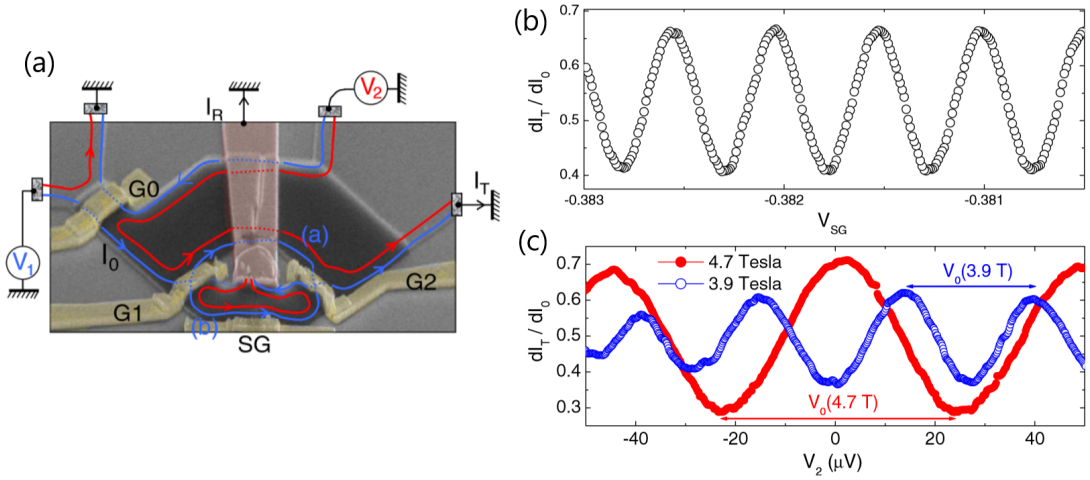

Figure 4.6: Figure extracted from [70]. (**a**) Tilted SEM view of their device, with schematic representation of the edge states. G1 and G2 are Quantum Point Contact (QPC) which define the two beam splitters of the MZ interferometer. They are set to transmission $T_1 \sim T_2 \sim 1/2$ for the outer edge state (OES), while fully reflecting the inner edge state (IES). SG is a side gate. G_0 is an additional beam splitter which makes it possible to bias the IES by V_2, while the other is biased by V_1. G_0 is tuned such that the OES is fully reflected, while the IES is transmitted with a probability T_0. (**b**) Phase sweeping by varying the side gate voltage V_{SG}. (**c**) Phase sweeping by varying V_2 with $T_0 = 1$ for two different magnetic fields. The periodicity V_0 depends on the magnetic field.

following :

$$I_\sim = I_D e^{-{V_1}^2/(2{V_{lob}}^2)} \times cos(\phi - 2\pi \frac{V_2}{V_0}) \tag{4.1}$$

where $I_D = \frac{e^2}{h} V_{DC} \sqrt{T_1 R_2 T_2 R_1}$, V_1 (V_2) is the bias applied on the OES (IES), and V_{lob} is a fitting parameter. Finally, the differential conductance of the current transmitted through the OES $dI_\sim/dV_1$ is proportional to $cos(\phi - 2\pi V_2/V_0)$, explaining the appearance of conductance oscillations with V_2.

4.1.4 Theoretical description of decoherence in GaAs/AlGaAs heterostructures

The simple single particle picture of edge states, where the electronic edge excitations propagate as plane waves with the group velocity v_F at the Fermi level, fails to explain the experimental observations for MZIs. Indeed, within this framework, the visibility of the interferences does not depend on the DC bias applied on the interferometer arms, while experimentally the dependence is quite strong and associated with peculiar behaviors such as lobe structures. The physical origin of the dependence of the visibility has been the subject of intense theoretical debates. A phenomenological approach, detailed in the first part of this section, was developed by Roulleau et al. to describe the lobe structures they obtained in DC bias when only the interfering edge channel was biased.

In a second time, I will detail another framework which considers the dephasing, induced on the interfering edge channel, by the noise on the capacitively coupled non-interfering edge channel; this enabled to fit experimental dephasing observed when increasing the temperature or injecting shot noise on the inner edge state (IES). Finally, is described a model of dephasing based on the spin-charge separation induced by the coupling between edge states, which can describe most of the experimental features in DC bias of interferences.

A first phenomenological explanation

P. Roulleau et al. in [70], by applying a bias V on the interfering IES while the OES is grounded, observed as in [59] a lobe structure in visibility. Interestingly, they found an almost perfect fit for the lobe structure by assuming a gaussian phase averaging. The model used, presented hereafter, is detailed in the PhD of P. Roulleau [71].

Considering a stochastic distribution of the phase Φ during the measurement, the interfering part of the current $I_\sim$ at a bias V is given by the following equation :

$$I_\sim = \frac{e^2}{h} V \sqrt{T_1 R_2 T_2 R_1} \langle sin(\phi) \rangle \tag{4.2}$$

where T_1 (T_2), R_1 (R_2) are the transmission and reflection coefficient at the top (bottom) side gate, and $\langle\rangle$ denotes the average over the phase distribution. By supposing that the number of electronic excitations participating to the dephasing is large, we have a gaussian phase distribution, which leads to :

$$\langle sin(\phi) \rangle = sin(\langle \phi \rangle) e^{-\langle \delta\phi^2 \rangle / 2} \tag{4.3}$$

Moreover, by assuming a variance to be of the form $\langle \delta\phi^2 \rangle = V^2/{V_0}^2$, with V_0 a fitting parameter and V the applied bias, one obtains :

$$I_\sim = \frac{e^2}{h} V \sqrt{T_1 R_2 T_2 R_1} sin(\langle \phi \rangle) e^{-\frac{V^2}{2{V_0}^2}} \tag{4.4}$$

Finally, the differential conductance $G_\sim$ can be expressed as :

$$G_\sim = \frac{dI_\sim}{dV} = \frac{e^2}{h} V \sqrt{T_1 R_2 T_2 R_1} sin(\langle \phi \rangle) e^{-\frac{V^2}{2{V_0}^2}} (1 - V^2/{V_0}^2) \tag{4.5}$$

When V is swept around a value $V_{DC,0}$ such that ${V_{DC,0}}^2/{V_0}^2 = 1$, equation 4.5 implies that $G_\sim$ crosses zero and changes its sign, causing a π shift of the phase. The visibility υ, directly proportional to the difference $(G_{\sim,max} - G_{\sim,min})$, can be expressed by equation 4.6, where υ_0 corresponds to the visibility at zero bias.

$$\upsilon = \upsilon_0 e^{-V^2/({2V_0}^2)} \left| 1 - \frac{V}{{V_0}^2} \right| \tag{4.6}$$

As one can deduce from equation 4.6, the $V_{DC,0}$ values correspond to the visibility nodes. Consistently with the experimental measurements these visibility nodes are associated with a π shift of the oscillations. Using V_0 as a fit parameter, they could fit with a good accuracy the experimental lobe structure obtained for one edge channel biased with equation 4.6. In order to explain, in this framework, the results obtained by Bieri et al. [11] in the case of two biased edge channels, according to [71], one has to take into account the gating effect of the IES on the OES.

Decoherence induced by the capacitive coupling to a noisy environment

In the previous experimental reminder, I detailed evidences of the existence of a capacitive coupling between the interfering OES and the non-interfering IES. This capacitive coupling has also been considered as a source of decoherence in MZIs at filling factor $\nu = 2$. In this section, I will detail a first theoretical approach that have been developed in order to model the dephasing effect induced by this coupling, and in particular to predict the experimentally observed decay of the visibility with the temperature and the injection of shot noise in the IES.

The idea of the model developed here is to take into account the dephasing effect of the noise generated in the non-interfering edge channel. Indeed, due to the capacitive coupling, noise on the inner edge state (IES) generates dephasing on the outer one (OES). Hence, a noisy IES will induce decoherence, characterized by a decrease in the visibility of Aharanov-Bohm oscillations occurring in the OES. The characteristic energy scale of the electronic excitations in the IES can be represented by $E_C = max(2k_BT, eV_2)$, with V_2 the bias in the IES, and T the temperature. In addition, one can define the frequency $\nu = 1/\tau$, with $\tau = v_D/L$, v_D being the drift velocity and L the interferometer arm length. τ represents the characteristic residency time of an electron in the MZI. If $h\nu \ll E_C = max(2k_BT, eV_2)$, the number of electronic excitations is large, inducing a gaussian phase distribution on the OES. In this configuration the IES can be described as a gaussian noise source. When $h\nu \gg E_C = max(2k_BT, eV_2)$, a few electronic excitations are coupled with the OES, inducing a non-gaussian noise.

The gaussian regime : The starting point is again the expression of the interfering part of the current given in equation 4.2, while assuming a gaussian phase distribution, due to the large number of electronic excitations, giving rise to equation 4.3. However, here, the phase variance is directly linked to the noise power spectrum S_{22} in the IES through a coupling constant V_0 and the unknown bandwidth $\Delta\nu$:

$$\langle \delta\varphi^2 \rangle = (2\pi)^2 S_{22} \Delta\nu / {V_0}^2 \tag{4.7}$$

When $eV_2 \ll k_BT$, the noise is dominated by the Johnson-Nyquist noise, thus $S_{22} = 4k_BTR_Q$ with $R_Q = h/e^2$. Finally, one can express the visibility in the following way :

$$\upsilon = \upsilon_0 e^{-T/T_\varphi} \tag{4.8}$$

where ${T_\varphi}^{-1} = 16\pi^2 k_B R_Q \Delta\nu / {V_0}^2$. From equation 4.19, we directly recover the exponential decay of the visibility with the temperature observed experimentally.

In [70], they also apply this theory to the case were S_{22} is dominated by the shot noise due to partitioning on the QPC G_0. In this case the visibility can be expressed by :

$$\upsilon = \upsilon_0 e^{-T_0(1-T_0)(V_2 - 2k_BT/e)/V_\varphi} \tag{4.9}$$

where ${V_\varphi}^{-1} = 4\pi^2 e R_Q \Delta\nu / {V_0}^2$. Interestingly, they could fit with a really good accuracy the experimental visibility dependence on the transmission T_0 (of the partitioning QPC G0) for different values of V_2, as shown in figure 4.7. This validates the assumption of a gaussian phase distribution in the case of shot noise in the IES created by partitioning on G_0.

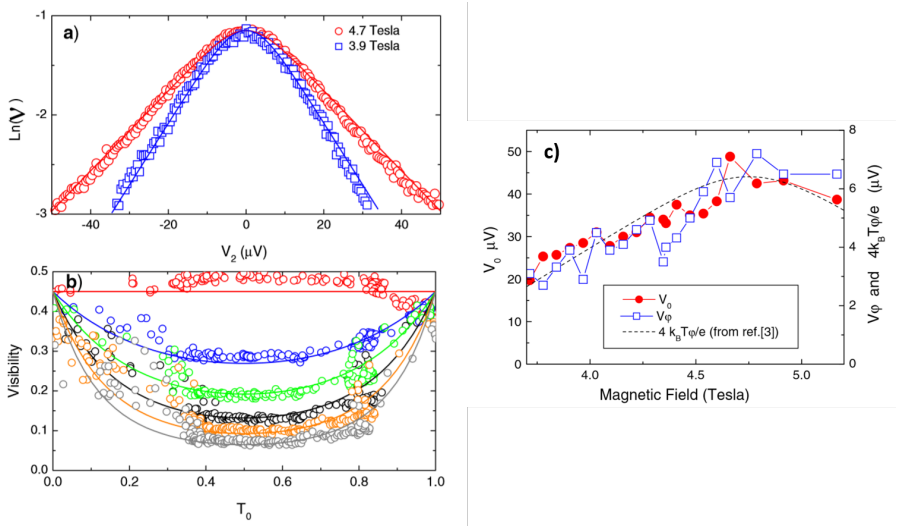

Figure 4.7: Figure extracted from [70]. (**a**) Visibility of the interferometer as a function of V_2 at $T_0 = 1/2$ for two different magnetic field 4.7 and $3.9T$. The solid lines are fit to the data $\upsilon = \upsilon_0 \times exp(-2\pi^2 \Delta S_{22} \Delta\nu / {V_0}^2)$ with an electronic temperature of $25mK$ and $T_0 \sim 1/2$. The V_φ parameter is determined thanks to high bias fit of the exponential decrease $\upsilon = \upsilon_0 \times exp(-T_0(1-T_0)V_2/V_\varphi)$. (**b**) Visibility decrease of the interferometer as a function of T_0 for $V_2 = 0, 21, 31, 42, 53$, and $63\mu V$ from top to bottom. The solid lines are fit to the data using equation 4.9 with $\upsilon_0 = 0.45$, $V_\varphi = 7.2\mu V$, and $T = 25mK$. (**c**) V_0 and V_φ as a function of the magnetic field. The dashed line is the general behavior of $4k_B T_\varphi/e$ measured in reference [73], on the same sample.

In addition, thanks to the fits they extracted the parameter V_φ for different magnetic field. The result is plotted in 4.7.c. Similarly from fits of temperature measurements, they extracted the parameter T_φ on the same magnetic field range. From previous equations, one can directly express V_φ as a function of T_φ : $eV_\varphi = 4k_B T_\varphi$. In figure 4.7.c, the V_φ computed from the measured T_φ is plotted, it agrees almost perfectly with the measured V_φ. This indicates that the assumption of gaussian phase averaging is also valid to describe the dephasing effect of temperature.

The non-gaussian regime : The non-gaussian regime was studied by Neder et al. [61] in 2007 in a sample with a similar geometry than the one used by Roulleau et al. (see schematic in figure 4.6.a) with a close experimental set up : $\nu = 2$, OES fully transmitted under G_0, bias V_{det} ($\equiv V_2$) is applied on the IES. They measured the differential conductance of the interfering current propagating in the OES, while inducing shot noise on IES. The shot noise is controlled by the transmission T_{QPC0} of the IES.

As shown in figure 4.8, they studied the visibility of the Aharanov-Bohm oscillations as a function of T_{QPC0} for different values of V_{det}. Interestingly, for low values of V_{det}, they could fit the experimental data by assuming a gaussian phase averaging. However, for $V_{det} = 15\mu V$ (figure 4.8.b), their experimental data has a V-shape which notably deviates from the gaussian model. They could fit this V-shaped dependency by assuming that the dephasing in the interfering current in the OES was caused by a single electron in the

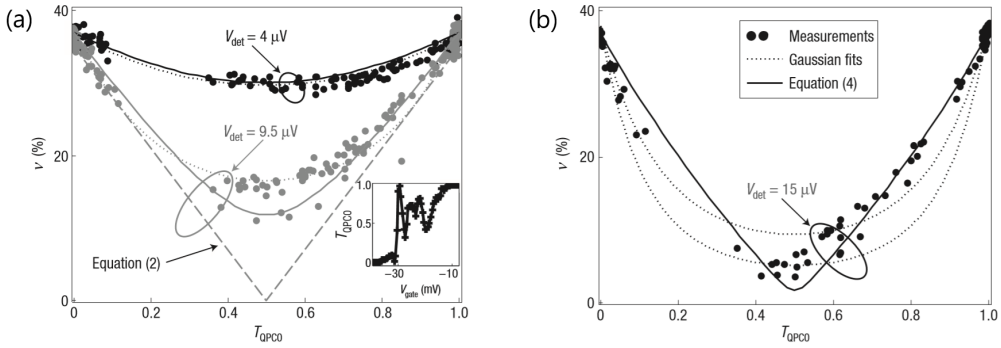

Figure 4.8: **The effect of partitioning the detector channel (thanks to QPC0) on the visibility of the interfering signal, at three different detector bias values. Figure extracted from [61].** Dotted lines show the best fitted gaussian model; solid lines show the 'microscopic' non-gaussian predictions. As V_{det} increases, the dependence of the visibility on T_{QPC0} turns from a smooth one to a sharp V-shape (at $V_{det} = 15\mu V$). (**a**) Data points and theoretical predictions for $V_{det} = 4\mu V$ and $9.5\mu V$. The gaussian model (dotted lines) is adequate at low bias ($4\mu V$) and gives a reasonable fit at intermediate bias ($9.5\mu V$). The dashed line is the V-shaped prediction of a single-detector-electron model (equation) for $V_{det} = 9.5\mu V$. (**b**) Data points and theoretical predictions for $V_{det} = 15\mu V$ (data from [60]). The V-shape is observed experimentally, as predicted by the 'microscopic' non-gaussian model. The gaussian model fails for the arbitrary fitting parameter; the best fit (upper curve) strongly overestimates the visibility at $T_{QPC0} = 0.5$ and underestimates the visibility for $0.7 < T_{QPC0} < 0.9$.

IES. Therefore, they analysed this measurement as a direct evidence of a non-gaussian regime, in which the dephasing is caused by a few electrons implying a peculiar phase distribution.

A decoherence induced by spin-charge separation

In 2008, two theoreticians, Levkivskyi and Sukhorukov, developed in [50] a different theoretical framework to explain decoherence in electronic MZ experiments in GaAs/AlGaAs heterostructures at filling factor $\nu = 2$. Starting from the observation that a theoretical description of the system thanks to a single-particle model of the edge states cannot explain the peculiar properties observed, the idea of Levkivskyi and Sukhorukov is to consider that the "two chiral channels at the edge of $\nu = 2$ electron systems interact via the long-range Coulomb potential". In their model, the strong "Coulomb interaction at the $\nu = 2$ edge leads to the separation of the spectrum of edge excitations in a fast (charged) mode with the speed u and slow (dipole) mode with the speed v" [50]. They considered interactions only between the two co-propagating edge channels, and neglected the coupling to edge channels located on another border of the 2DEG. In addition, due to the difficulty to find a general framework, they limited their investigations to the cases of weak tunneling (WT) and weak back-scattering (WB) under the first QPC. This leads to the configurations depicted in figure 4.9 for one biased edge channel and in figure 4.11 for two biased edge channels. Hereafter, the results of their simulations achieved in the

two different configurations for the WB and WT regimes are presented.

One edge channel is biased : First, I will detail the case where only one of the incoming edge channels is biased at the potential $\Delta\mu$. The chemical potential distribution between the MZI arms is represented in figure 4.9 : the left panel corresponds to the WT regime, while the right one depicts the WB regime. Interestingly, in this configuration, the WT regime and the WB regime are symmetrical. Indeed, to go from one configuration to another, one simply needs to vertically flip the interferometer. This symmetry implies that the WT and WB regimes are equivalent when one edge channel is biased, given that the length L_U of the upper arm is equal to the length L_D of the lower one.

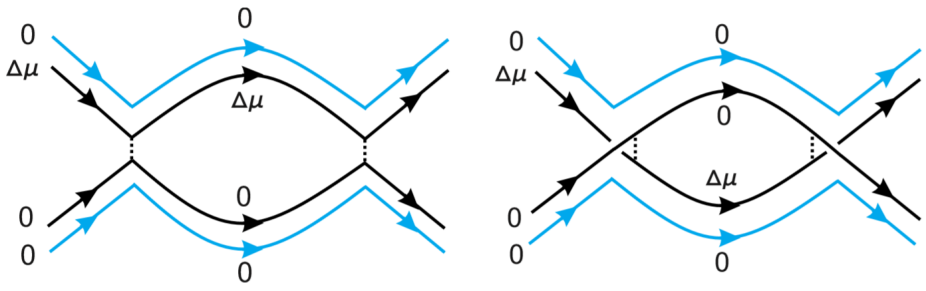

Figure 4.9: Schematic representation of a MZI with a voltage $\Delta\mu$ applied on one of the incoming edge channels. The left panel represents the weak-tunneling (WT) regime where the outer edge state is almost fully reflected at the first QPC. The right panel depicts the weak back-scattering (WB) regime where the outer edge state is completely transmitted through the first QPC. Figure extracted from [50].

Figure 4.10 presents the visibility and phase dependence computed by Levkivskyi and Sukhorukov in this configuration while considering slight asymmetries of the MZI arms. As shown in the upper panel of figure 4.10, the visibility oscillates with the potential $\Delta\mu$, and the central lobe has the same width as the lateral ones. Furthermore, the computed phase, depicted in the lower panel of figure 4.10, appears to be almost constant on the lobes width, while it abruptly shifts by π at the points where the visibility vanishes. Interestingly, the configuration presented here with one of the incoming edge channels biased directly corresponds to the experiment carried out by Neder et al. [59], and their experimental results, plotted in figure 4.2, are in good agreement with all the theoretical predictions detailed previously.

Two edge channels are biased : Let's see now if their model can explain the experimental observations obtained when two of the incoming edge channels are biased. The chemical potential distribution in this configuration is presented in figure 4.11 for the WT regime (left panel) and for the WB regime (right panel). One should notice an important difference compared to the previous case : the WT and WB regimes are asymmetrical, implying that they present different visibility and phase dependence on the potential $\Delta\mu$. The visibility dependence on the potential $\Delta\mu$, computed thanks to their model, is shown in figure 4.12 : the black line corresponds to the WT regime, and the blue one to the WB regime. In the WT regime, a lobe structure appears in the visibility, however this

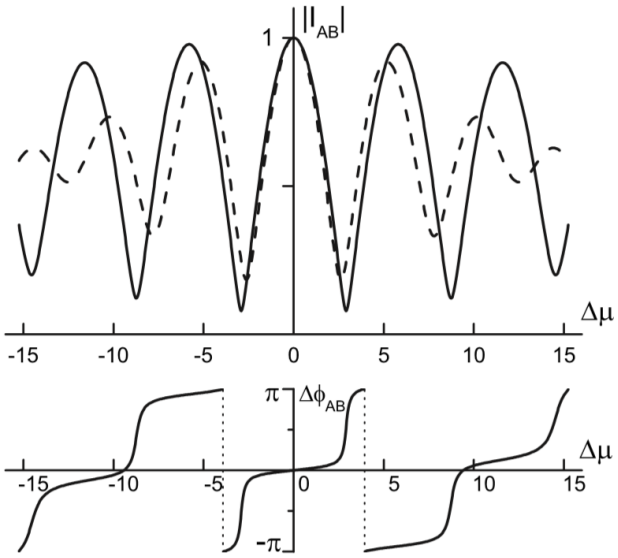

Figure 4.10: **Simulations in the case of one biased edge channel extracted from [50]. The top panel :** Intrinsic visibility of Aharanov-Bohm (AB) oscillations $|I_{\mathrm{AB}}|$ plotted as a function of the bias $\Delta\mu$ in units v/L_U for $L_D = 1.15L_U$ (solid line) and for $L_D = 1.35L_U$ (dashed line), with L_U (L_D) the length of the upper (lower) arm of the MZI. **The bottom panel :** AB phase shift, corresponding to $Arg(I_{\mathrm{AB}})$, plotted for $L_D = 1.15L_U$.

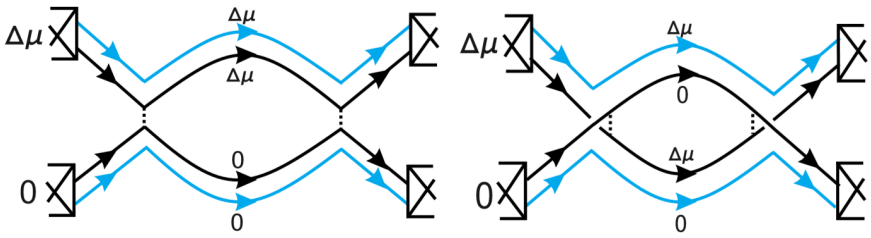

Figure 4.11: Schematic representation of a MZI with a voltage $\Delta\mu$ applied on two of the incoming (co-propagating) edge channels. The left panel represents the weak-tunneling (WT) regime. The right panel depicts the weak back-scattering (WB) regime. Figure extracted from [50].

time the central lobe is two times wider than the lateral ones. Furthermore, in the WB an intriguing evolution of the visibility is observed. Indeed, on the blue curve, one can note that unexpectedly the visibility is not maximum when $\Delta\mu = 0$, in other words the application of a potential can increase the visibility. In order to obtain this dependency, Levkivskyi and Sukhorukov considered an important asymmetry between the arms of the MZI : $L_D = 1.8L_U$. However, they claim that a similar result can be obtained by considering the coupling with the opposite arm of the MZI. Once again the theoretical results obtained via their model are in good agreement with the experimental observations in

this configuration and in particular with Bieri et al. [11] work (see figure 4.4).

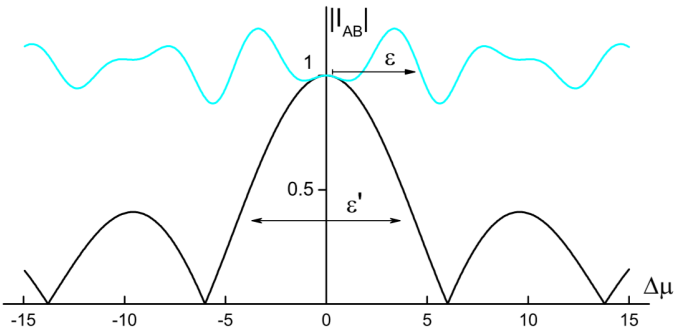

Figure 4.12: **Simulations in the case of two biased co-propagating edge channel extracted from [50].** The intrinsic visibility of Aharanov-Bohm (AB) oscillations $|I_{\mathrm{AB}}|$ is plotted as a function of the bias $\Delta\mu$ in units v/L_U for a strongly asymmetric interferometer $L_D = 1.8L_U$, with L_U (L_D) the length of the upper (lower) arm of the MZI. The WT regime is represented by the solid black line, while the WB is depicted by the blue line.

Remark on the temperature dependence : Finally, I would like to stress that the spin-charge separation model developed by Sukhorukov can also explain the exponential decay of the visibility with the temperature observed experimentally [73].

4.2 DC bias dependence of the coherence in graphene

I presented in the previous section, the essential characteristics of the visibility dependence on the DC bias observed in MZIs in GaAs/AlGaAs heterostructures, and two theoretical frameworks developed to explain them. These measurements indicates that in GaAs/AlGaAs heterostructures the coherence is really fragile : the application of a $40\mu V$ bias is sufficient to completely suppress Aharanov-Bohm oscillations. In graphene, the quantum properties are supposed to be much steadier, making it a good candidate for electron quantum optics experiments and quantum computations. The results of the first DC bias measurements carried out in graphene MZIs seems to comfort the previous statement, as detailed in the first part of this section. In the second part, are detailed the DC bias measurements that we achieved in our valley splitter sample.

4.2.1 Previous DC bias studies in graphene MZIs

In graphene, the first MZI experiment was carried out by Morikawa et al. [58] in 2015. They studied the DC bias dependence of their magnetoconductance oscillations. As shown in figure 4.13, the oscillations vanish at a certain DC bias, and appear again at higher DC bias voltages with a π shift, forming a check board pattern characteristic of a lobe structure in visibility. Strikingly, the oscillations are still clearly visible at $8mV$, which is 200 times bigger than the observed $40\mu V$ in GaAs/AlGaAs heterostructures. However, as will be underlined afterwards, two parameters in their experimental conditions are

essential to understand their result : the magnetic field is quite low $B \sim 5T$, the filling factors on both sides of the pn junction are high.

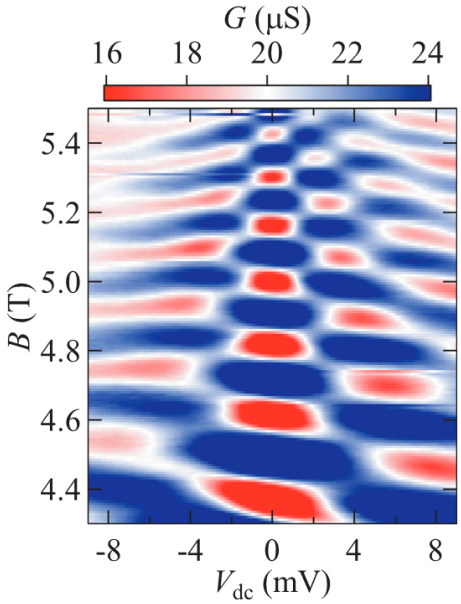

Figure 4.13: Color plot of differential conductance $G = dI/dV_{DC}$ as a function of DC bias voltage V_{DC} and magnetic field B. Extracted from [58]

In the study carried out two years later in the Yacoby group [84], they observed a much smaller energy scale for the decoherence. Indeed, as clearly visible in figure 4.14, the Aharanov-Bohm oscillations completely vanish for an applied DC bias $V_{DC} \sim 1.5mV$, which is still 40 times higher than in GaAs/AlGaAs heterostructures. Interestingly, the visibility as a function of the DC bias (figure 4.14.B) presents a single main lobe, but no side lobes. Contrarily to Morikawa et al. study, in Yacoby's measurement, the magnetic field is quite high $B \sim 8T$, and the filling factors are fixed at $\nu_p = -2$ and $\nu_n = 1$. The DC bias is applied on the two edge channels incoming on the junction in the p side. Along the junction in the p side, the outer edge channel is not interfering due to its opposite spin, whereas the inner one interferes with the edge channel on the n side, forming the two arms of the MZI. The monotonous decay of the visibility observed by Wei et al. in this configuration reminds the dependency measured in GaAs/AlGaAs heterostructures when two incoming edge channels are biased.

More recently, P. Makk et al. [56] reported the existence of different sets of oscillations in graphene pn junction in the quantum Hall regime which they associated to different physical origins. In their study, they designated each set by a color (red, orange, cyan, green) and measured for each one the DC bias dependence, the experimental measurements are presented in figure 4.15. I will now quickly summarize the features of each set of oscillation with their analysis :

- The red set corresponds to big oscillations observed at low field $B \sim 3T$ and at filling factors $|\nu|$ going from 3 to 6, whose periodicity decreases with the magnetic field, as shown in figure 4.15.a. In DC bias this set present a check board pattern similar

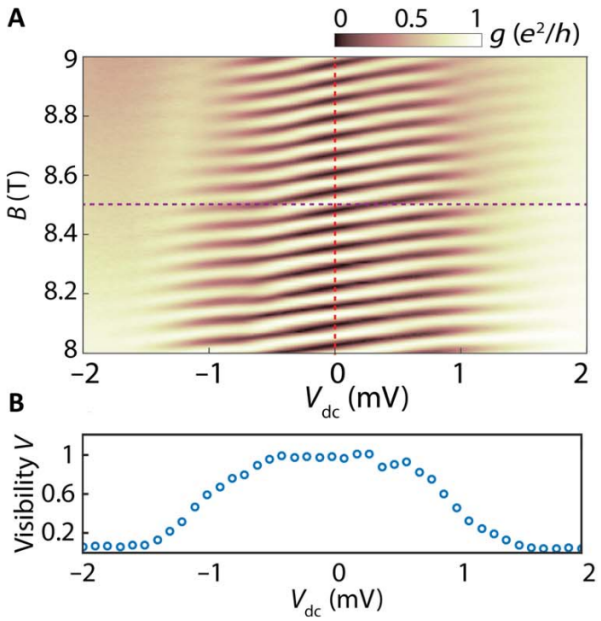

Figure 4.14: **Mach-Zehnder oscillations as a function of magnetic field and dc voltage bias.** (**A**) Two-terminal differential conductance as a function of magnetic field B and DC voltage bias V_{DC} at filling factors (ν_n,ν_p)=(1,-2), for which only one interferometer is formed at the pn interface. (**B**) Visibility of the conductance oscillations shown in (**A**) as a function of DC bias. Extracted from [84]

to Morikawa et al. study, and persists to DC voltages as high as $|V_{DC}| \sim 10mV$. Interestingly they associated this set, not with Aharanov-Bohm oscillations, but with snake states along the junction.

- The orange set regroups oscillations occurring at filling factors $|\nu|$ going from 6 to 20, and at low magntic field between $3.0 - 4.0T$. As visible in the DC bias dependence, presented in figure 4.15.b, the orange oscillations also persists up to high energies up to $|V_{DC}| \sim 10mV$. P. Makk et al. associated this set with Aharanov Bohm oscillations.

- The cyan set appears at for magnetic fields $B \geq 4T$, and persists up to low filling factors $|\nu| \sim 2$. They also associated the cyan set with Aharanov-Bohm oscillations. As shown in figure 4.15.c, this set is more fragile and disappear for DC biases $V_{DC} \sim 1.5mV$, similarly to the oscillations observed by Wei et al. [84].

- Finally the green set also presented in figure 4.15.c was associated to dots.

I would like to underline that in this study, as in previous MZI experiments in graphene, oscillations coming from a displacement of the pn junction at one of its ends, in other word the mechanism behind the valley splitters described in chapter 3 , was not considered. One of the oscillation set observed by P. Makk could also be created by this kind of mechanism.

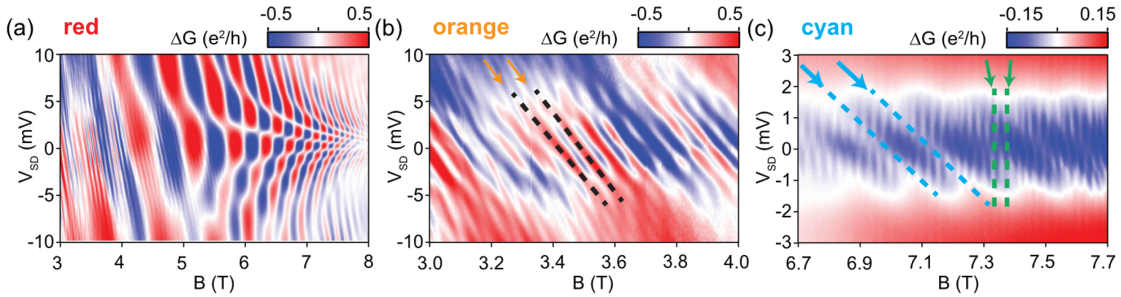

Figure 4.15: Bias spectroscopy (extracted from [56]). (**a**)–(**c**) Measurement of different sets of magnetoconductance oscillations as a function of bias and magnetic field where a smooth background was subtracted. Gate voltages remain fixed at high filling factors on both sides of the junction.

The comparison between this study and the previous experiments can give us some insights on the origin of the different energy scales observed by Morikawa et al. (oscillations still clearly present at $V_{DC} \sim 8mV$) and Wei et al. (oscillations killed at $V_{DC} \sim 1.5mV$). Indeed, the red oscillation set was observed in the same magnetic field range and filling factor range than in Morikawa's experiment. In addition, the DC bias dependence is similar in both cases and oscillations persist up to identically high values. Therefore, I think that the red set and the oscillations used in the DC bias analysis by Morikawa et al. are of the same physical origin and are not Aharanov-Bohm oscillations (P. Makk associated them to snake states).

On the other hand, the cyan set appears in the same conditions than the oscillations studied by the Yacoby group. Remarkably, those two experiments have identical DC bias energy scales : the oscillations disappear at $V_{DC} \sim 1.5mV$. Therefore, I think that those two have the same origin : Aharanov-Bohm oscillations. The persistence of these oscillations up to $V_{DC} \sim 1.5mV$ is remarkable, it is 40 times higher than in equivalent samples in GaAs/AlGaAs heterostructures. We carried out similar experiment with our sample, and obtained complementary results to those previous studies.

4.2.2 Visibility dependence on DC bias in the valley splitter sample

In our valley splitter sample, we investigated the coherence of the valley polarized output state using MZI, and similarly to previous studies in graphene we checked, for this aim, the DC bias dependence of the visibility. Remarkably, thanks to the control over the transmissions, one can distinguish, in our sample, Aharanov-Bohm oscillation in the MZI configuration from oscillations due to the displacement of the intersection between the pn junction and the graphene physical edge. I will start by presenting the DC bias measurements that we carried out on our valley splitter sample, in which we observed a lobe structure in visibility similar to the case of MZIs in GaAs/AlGaAs. Afterwards, the dependence of this lobe structure on other parameters such as the transmission T_1 is discussed.

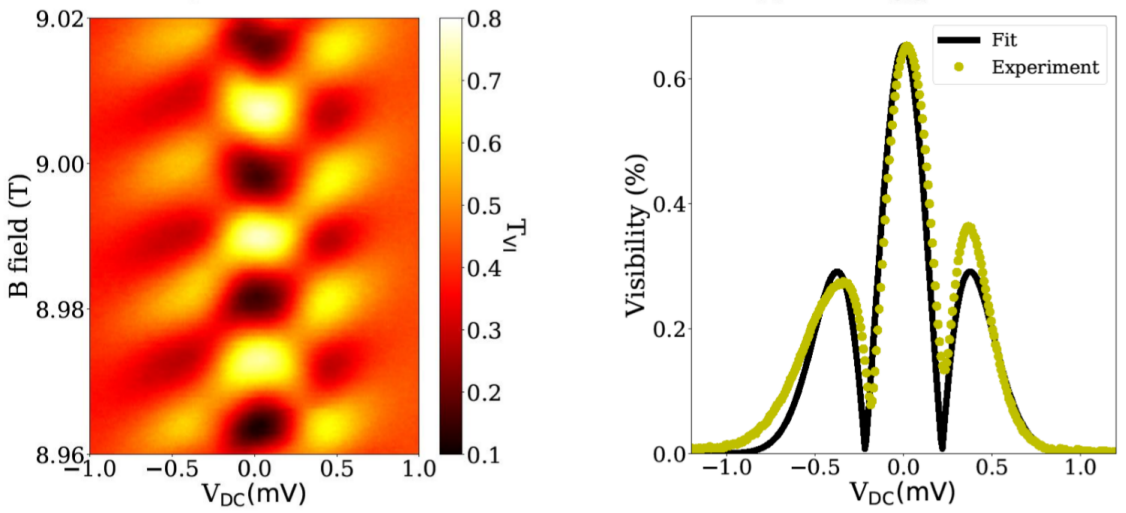

(a) (b)

Figure 4.16: (**a**) T_{VI} as a function of the applied DC bias V_{DC} and the magnetic field at $\nu_n = +2$,$\nu_p = -1$. (**b**) Measured visibility (yellow dots) as a function of V_{DC}. Computed visibility (black solid line) based on gaussian phase fluctuations is in agreement with the experimental data.

Observation of a lobe structure

In order to carry out this study, we set our sample in the MZI configuration depicted in chapter 3, i.e. we have a pn junction in the quantum Hall regime with $\nu_n = 2$ and $\nu_p = -1$. Moreover, the top and bottom side gates are tuned at filling factor $\nu_{sgi} \leq -1$ to have mixing at the two ends of the pn junction. A DC bias was superimposed to the Lock-in AC oscillation applied on the top right contact (see layout in figure 3.8). In figure 4.16a, the transmission through the valley Mach Zehnder T_{VI} is plotted as a function of the bias V_{DC} applied. As expected, for $V_{DC} = 0$, we have Aharanov-Bohm oscillations of T_{VI} as a function of the magnetic field with a maximum visibility around 65%. When $|V_{DC}|$ is increased the oscillations amplitude diminishes symmetrically for positive and negative voltages. At $V_{DC} \approx \pm 0.25mV$ the oscillations vanishes, however when $|V_{DC}|$ exceeds this value the oscillations appear again with a π shift, forming the so-called check board pattern. Finally, the oscillations amplitude seems to approach zero for biases around $1mV$. More quantitatively the visibility was computed for each value of V_{DC} thanks to sinusoidal fits, the result is displayed in figure 4.16b. As one can see, the visibility is maximal at 0 bias, and decreases at higher biases following a peculiar lobe structure : a main lobe, centered at $V_{DC} = 0$ and limited by two minima in visibility at $V_{DC} = \pm 0.25mV$, is surrounded by two slightly asymmetrical side lobes which are completely washed out around $|V_{DC}| \approx 0.8mV$. The width at half height of the main lobe is similar to the one of the side lobes. And finally, the minima in visibility coincide with the π-shift point.

Interestingly, we observed, as Morikawa et al. [58], a check board pattern for the MZI oscillations dependence over the DC bias. However, the oscillations in our experiment vanish at $V_{DC} \sim 0.8mV$, whereas in Morikawa's work they are still well defined at

$V_{DC} \sim 8mV$. As discussed previously, P. Makk's study might give us an insight on the origin of this difference. Indeed, they carried out a similar experiment, but they identify different sets of oscillations, and in particular : one with the same energy scale as ours, and one similar with Morikawa's experiment. And they claimed that this second one does not correspond to Aharanov-Bohm oscillations, contrarily to the first one. In addition, the oscillation set that they associated with Aharanov-Bohm oscillations has a dependence on DC bias really close to the one observed by Wei et al. [84]. In both cases, the oscillations vanish around $V_{DC} \sim 1.5mV$, which is much closer to the $0.8mV$ obtained in our measurement. However, they both reported a monotonous decay of the visibility with the DC bias, similarly with what was observed in the case of two biased edge channels by Ji et al. [37] in GaAs/AlGaAs heterostructures.

But in our experiment a clear lobe structure with lobes of same width appears, which is closer to what was observed in the configuration where only one edge channel is biased in GaAs/AlGaAs heterostructures, although here we apply the bias on two edge channels. Therefore, we fitted the data using the formula derived by Roulleau et al. in [72] for the case of one biased edge channel by assuming a gaussian phase averaging. In figure 4.16b, the visibility fit, represented by the thick dark line, is in good agreement with the experimental measurement (yellow dots). The fact that a model, used when only the interfering edge state is biased in GaAs MZIs, works well to explain our experimental data when both edge states are biased could indicate that the coupling between the co-propagating edge states at $\nu = 2$ in graphene is small. However, the physical origin of the different behaviors observed in our experiment and in Wei et al. work remains unclear at the moment.

Anyway, this measurement indicates that the coherence of the valley polarized states propagating along the pn junction is impressively steady. Indeed, in GaAs MZI, the visibility is completely washed out around $40\mu V$ (figure 4.2b), whereas in our valley splitter graphene sample the visibility goes to zero around $0.8mV$. In other words, the coherence persists in graphene at energies 20 times larger than in GaAs/AlGaAs heterostructures. This is a promising result for quantum computations based on information encoded in the valley isospin thanks to our valley splitter set up.

Dependence of the lobe structure on other parameters

In this sections, I present two experiments that we conducted in order to investigate the origin of the lobe structure observed.

In a first experiment, we studied the effect of the transmission T_1 of the first beam splitter on the lobe structure. Indeed, in GaAs/AlGaAs heterostructures, in the configuration with two edge channels biased, the visibility evolution with the DC bias experimentally exhibited a strong dependence on the transmission T_1, as shown by Bieri et al. (see figure 4.4). In our sample, we measured the visibility dependence on DC bias for the following values of transmission $T_1 = 0.09, 0.29$ and 0.85. The results are presented in figure 4.17a. Interestingly here we observe almost identical lobe structures in the weak back-scattering regime ($T_1 = 0.85$), and in the weak tunneling regime ($T_1 = 0.09$), which clearly differs from the case of two edge channels biased in GaAs/AlGaAs.

Moreover, all the previous measurements were achieved by applying a DC bias voltage from the top right ohmic contact on the n side where the filling factore is $\nu_n = 2$. There-

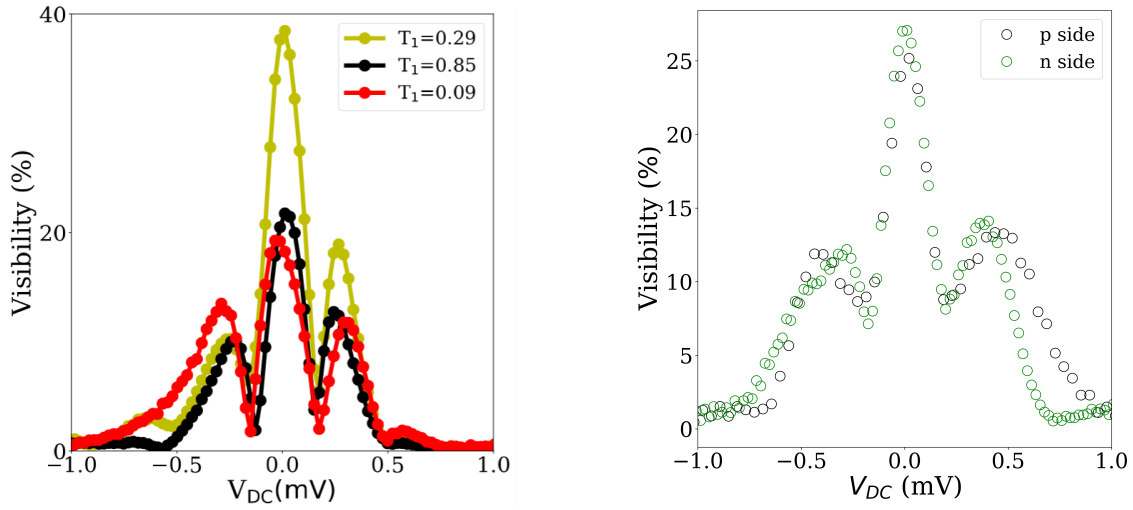

(a) (b)

Figure 4.17: **Transmission dependence.** (**a**) Measured visibility as a function of V_{DC} for three different transmissions of the first valley splitter T_1. (**b**) Measured visibility for a DC bias injection on the n side (from the top right contact), or on the p side (from the top left contact).

fore, we had two co-propagating biased edge channels on the n side of the junction. If now, we inject the DC bias on the top left ohmic contact from the p doped region where the filling factor is $\nu_p = -1$, only one of the incoming edge channels is biased. As detailed previously, in GaAs/AlGaAs heterostructures, really different behaviors were observed in the configuration with one biased edge channel, and in the configuration with two. This why, we decided to measure the visibility dependence on DC bias for an injection on the p and n side, the resulting curves are plotted in figure 4.17b. Here, no noticeable difference is visible. Once again, this seems to indicate that the non-interfering edge state is less coupled to the interfering one than in GaAs/AlGaAs MZIs.

Origin of the asymmetries in the lobe structure

Asymmetries in the lobe structure are clearly visible in figure 4.17, which is surprising as we would expect the dephasing to be symmetrical in DC bias. One possible origin for this asymmetry could be a non constant value with the DC bias of the transmissions T_1 under the top side gate, and T_2 under the bottom side gate.

In the previous measurements of the DC bias dependence of the visibility, we applied a fixed voltages V_1 on the top side gate and V_2 on the bottom side gate. The corresponding transmissions T_1 and T_2 were supposed to be constant and equal to their value at zero DC bias. In figure 4.18b, an experimental measurement of a visibility lobe structure is shown. By fixing V_2 so that $\nu_{sg2} = 0$ and V_1 at the same value than in the lobe structure measurement, we could measure the evolution of the transmission T_1 with the DC bias. Similarly, we measured the T_2 dependence on DC bias. Experimental dependence of T_1 and T_2 are presented in figure 4.18a, important changes of the two transmissions are visible with DC bias. In particular, T_1 goes from 0.2 to approximately 0.7. Such big fluctuations

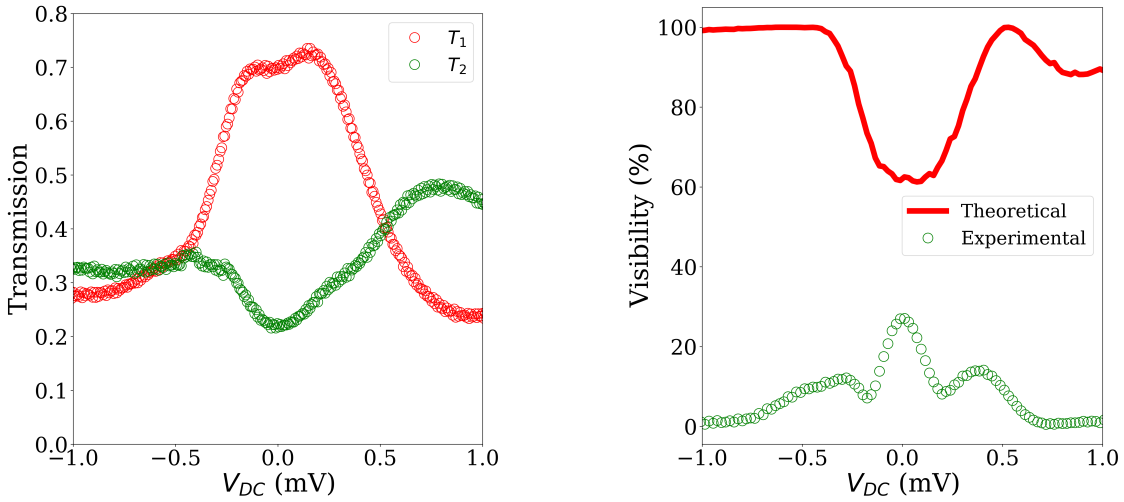

(a) (b)

Figure 4.18: **Transmission dependence.** (**a**) Evolution of the transmission T_1 (T_2) of the top (bottom) valley splitter as a function of the applied DC bias on the top right contact on the n side. (**b**) Measured visibility with the same voltage applied on the top (bottom) side gate as in the measurement of T_1 (T_2) in (a). The theoretical visibility is computed theoretically from the measured value of T_1 and T_2 for each DC bias. Note that no gaussian phase averaging is taken into account here, explaining the absence of decay observed in the theoretical visibility.

will have a clear impact on the visibility dependence on DC bias. Using the formula 1.7 derived in chapter 1, we plotted, in figure 4.18b, the theoretical visibility expected from the values of transmissions T_1 and T_2 for each DC bias. The resulting red curve exhibits an almost 100% visibility for the negative DC biases up to $-0.5mV$, where it drops and reaches almost 60% at $V_{DC} = 0$. One should note that in this visibility computation, we don't take into account any dephasing with DC bias, which explains why the visibility does not vanish when the DC bias is increased. Qualitatively, the lower theoretical visibility at $V_{DC} = 0$ tends to damp the height of the main lobe compared to the side lobes one. Moreover, the theoretical visibility is not exactly symmetrical in DC bias. Indeed, from the almost 100% visibility reached at $V_{DC} = 0.5mV$, the visibility starts to decrease for increasing DC bias reaching a minimum value of 85%. This asymmetry could explain the asymmetry observed in the lobe structure.

To summarize, if one wants to fully understand the visibility dependence, it is essential to measure the transmissions T_1 and T_2 dependence. However, we have noticed in our measurements that the lobe structure could not be explained by the T_1 and T_2 fluctuations. Indeed, most of the time, the transmissions changes by $\pm 10\%$ around an initial $T_1 \sim 0.5$, inducing only slight changes in the visibility, which can not explain the lobe structure.

4.3 Temperature dependence of the coherence in graphene

In the previous part, we have studied how steady the oscillations are with the DC bias applied on the input channels of the MZI formed in our valley splitter sample. Interestingly, the coherence is preserved up to energies 20 times larger than in MZI formed in GaAs/AlGaAs heterostructures. Another important energy scale for the coherence is the temperature, studied in this section. First, is presented the only preliminary temperature measurement achieved in graphene MZI. Then, is exposed the detailed study carried out in our valley splitter sample, which exhibited an exponential decay as in GaAs, but also the co-existence in the same sample of two different regimes of decoherence.

4.3.1 Previous study in graphene samples

In graphene MZI, surprisingly, only P. Makk et al. studied (in [56] supplementary) the temperature dependence of their magneto-conductance oscillations. Their measurement, presented in figure 4.19, exhibits a decrease of the oscillations amplitude with the temperature. But they have not computed the visibility to check if its decay was exponential as in GaAs case, maybe because of the slope and high base temperature in their measurement. However, what is striking in this measurement is the temperature energy scale : the oscillations are still clearly visible at $2K$, which is again 20 times larger than in GaAs experiments. The existence of Aharanov-Bohm oscillations at this range of temperatures would enable to achieve MZI experiments, and more generally electron quantum optics, in graphene without using an He^3/He^4 dilution fridge. Indeed, a simple liquid Helium fridge with a Helium pumping can reach this range of temperature.

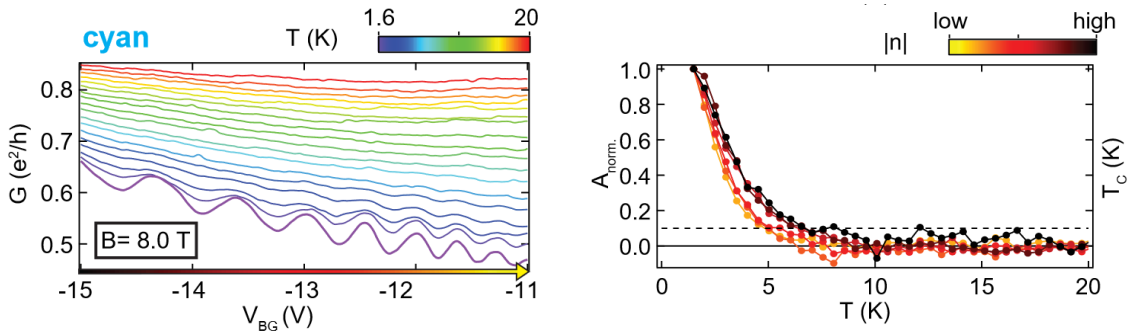

(a) (b)

Figure 4.19: **Temperature dependence of oscillations in graphene (extracted from [56]).** (**a**) Conductance as a function of the global back gate and temperature. (**b**) Normalized area below a given oscillation as a function of temperature at a series of densities, the colors corresponding to the x axes of the plots of (a).

4.3.2 Measurements in the valley splitter sample

I will now present the study of the temperature dependence of Aharanov-Bohm oscillations in the valley splitter sample. In order to carry out this experiment, we set our sample in the MZI configuration as depicted in the DC bias study, i.e. we have a pn

junction in the quantum Hall regime with $\nu_n = 2$ and $\nu_p = -1$. Moreover, the top and bottom side gates are tuned at filling factor $\nu_{sgi} \leq -1$ to have mixing at the two ends of the pn junction. In this configuration, we have Aharanov-Bohm oscillations of the transmission T_{VI} through the valley interferometer as a function of the magnetic field. This is a direct consequence of the Aharanov-Bohm phase proportionality to the flux of the magnetic field through the area enclosed. Identically, oscillations can be obtained by changing the area enclosed thanks to the side gates, the top gate, or the back gate. In figure 4.20, we measured the oscillations of T_{VI} as a function of the top gate voltage starting from the base temperature of the fridge ($20mK$) up to $1.65K$. Interestingly, at $1.2K$ the oscillations are still well defined, whereas in GaAs they completely vanish at $100mK$.

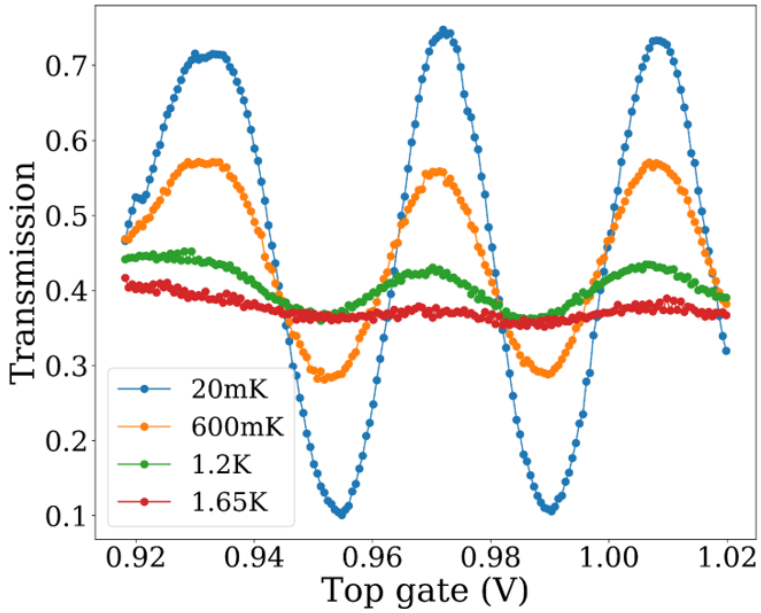

Figure 4.20: **Temperature dependence of the Aharanov-Bohm oscillations in the valley splitter sample.** (**a**) Aharanov-Bohm oscillations of the transmission T_{VI} of the valley interferometer as a function of the top gate voltage, for four different temperatures $T = 0.02,\ 0.6,\ 1.2,$ and $1.65K$.

More quantitatively, we computed the visibility of the oscillations for temperatures up to $1.65K$. In figure 4.21, the visibility is plotted in logarithmic scale as a function of the temperature. Below a certain temperature (indicated by the dashed line), temperature dependence is linear, i.e. there is an exponential decay of the visibility with the temperature, and thermal dephasing is weak. Above the threshold temperature, thermal dephasing is strong, but the temperature dependence is still linear.

A first explanation for the existence of two regimes could be a simple thermal saturation of the electronic temperature in our sample. However, the threshold temperature is around $400mK$, which seems too high compared to the electronic temperature expected with our set up. Interestingly, the co-existence of two regimes can be explained within the two theoretical frameworks that are detailed in the last section of this chapter. For instance, when considering a model where the dephasing arises from the capacitive cou-

pling of an interferometer arm to a noisy edge channel, two decoherence regimes are predicted : a gaussian regime where a lot of electrons are present in the environment creating a gaussian phase distribution, and a non-gaussian regime where there are only a few electronic excitations. The non-gaussian regime could correspond to the regime observed at low temperature, while the gaussian regime would be associated to the regime at high temperature. In the framework of dephasing induced by spin-charge separation, it is also possible to recover the observed dependency under certain conditions. The adequation of those models to the experimental data are discussed in more details in section 4.4.

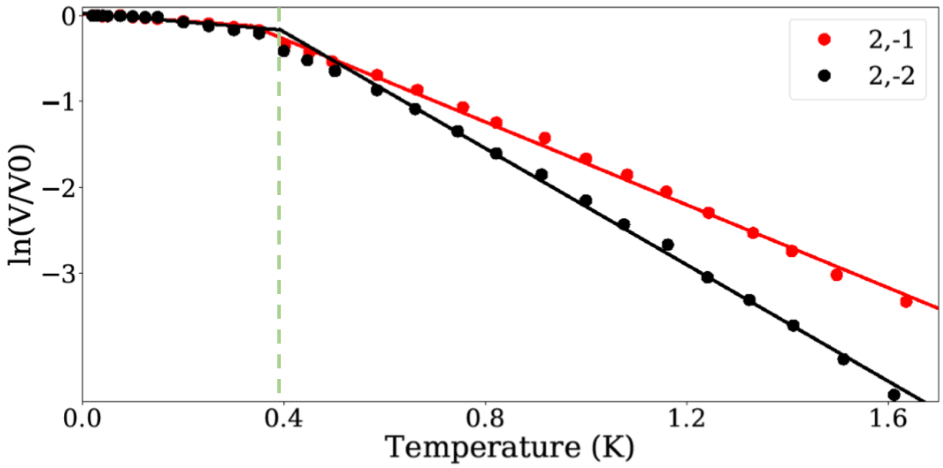

Figure 4.21: Temperature dependence in log scale of the visibility of the Aharanov-Bohm oscillations, divided by its maximum, in the valley splitter sample for two configuration of the pn junction: (ν_n=+2,ν_p=-1) in red and (ν_n=+2,ν_p=-2) in black. Below a certain temperature, the temperature dependence is linear and thermal dephasing is weak. Above a threshold temperature, a different dephasing regime is present : a linear dependence is still visible, but with a much faster decay.

Finally, we measured temperature dependence of oscillations obtained when the filling factors are set to $\nu_n = 2$ and $\nu_p = -2$, black curve in figure 4.21. At ν_n=2 and ν_p=-1 there is only one edge channel coupled to the MZI, whereas at ν_n=2 and ν_p=-2 there are two. Below the threshold temperature, temperature dependence of the visibility is the same for both setting. If the slope is larger for ν_n=2 and ν_p=-2 above the threshold temperature, we do not find a factor 2, as could be expected, naively, from the addition of a second noisy edge channel coupled to the MZI.

4.4 Theoretical description of decoherence in graphene

Graphene MZIs are quite different from their GaAs/AlGaAs counterpart. Indeed, in graphene the MZI is formed along a pn junction in the quantum Hall regime : the same spin edge channels propagating on both sides of the junction represent the arms of the interferometer, and the two points of intersection between the junction and the graphene physical edge act as beam splitters. The physics of the pn junction and the proximity of the interferometer arms ($\sim 100nm$) may generate important differences

in the description of the decoherence processes compared to the case of GaAs/AlGaAs heterostructures. Furthermore, in our study, we used different filling factors on both sides of the pn junction : $\nu_p = -1$ and $\nu_n = 2$. This implies that, contrarily to MZIs in GaAs/AlGaAs heterostuctures, the MZI we studied is asymmetric with one arm composed of two edge channel on the n-side, while the arm on the p-side is composed of only one edge channel. Finally, in our graphene MZI, we cannot, as in GaAs MZIs, impose the bias only on the interfering edge channel due to the lack of QPC.

In the first part of this section, I will discuss the relevance for the graphene MZI of the phenomenological model developed by Roulleau et al. in order to explain the lobe structure in GaAs/AlGaAs heterostructures at $\nu = 2$ when one edge channel is biased. Then, is detailed and discussed the application to our system of the model of a capacitive coupling to a noisy environment in order to explain the temperature dependence observed experimentally. Afterwards, the main lines of a spin-charge separation model applied to the graphene case are sketched, followed by a discussion of its relevance.

4.4.1 A phenomelogical explanation of the lobe strucuture

In our graphene valley interferometer, the transmission probability is given by the following formula :

$$\begin{aligned} T_{VI} &= |\langle\downarrow, B_L|\Psi_{final}\rangle|^2 = |r_1 t_2^* + t_1 r_2^* e^{i\phi_{\mathrm{AB}}}|^2 \\ &= |r_1 t_2|^2 + |r_2 t_1|^2 + 2|r_1 t_1 r_2 t_2|\cos(\phi_{\mathrm{AB}} + \phi), \end{aligned} \tag{4.10}$$

where $\phi = \arg(t_1 t_2 r_1^* r_2^*)$, and ϕ_{AB} is the Aharanov-Bohm phase. This has the standard form of the Mach-Zehnder interference, but now includes the effect of the valley isospin. Therefore, in order to understand the dephasing effect of a bias V applied on the interfering edge channel, one can follow the phenomenological approach developed by Roulleau et al. and detailed in section 4.1.4. The idea is to consider that the phase has a gaussian distribution, with a variance of the form $\langle\delta\phi^2\rangle = V^2/{V_0}^2$ (V_0 being a fitting parameter). This leads to :

$$\langle cos(\phi)\rangle = cos(\langle\phi\rangle) e^{-\langle\delta\phi^2\rangle/2} \tag{4.11}$$

From this, one can extract the following expression for the visibility υ :

$$\upsilon = \upsilon_0 e^{-V^2/(2{V_0}^2)} \left| 1 - \frac{V}{{V_0}^2} \right| \tag{4.12}$$

In the case of GaAs/AlGaAs MZIs, the latter formula for the visibility can only describe the case when only the interfering OES is biased and not the non-interfering IES. Indeed, to model the case of a bias applied on the IES and on the OES, one has to take into account the gating effect of the IES, due to the capacitive coupling between IES and OES (see P. Roulleau thesis [71]).

In our graphene MZI, the bias is applied on the n-side at $\nu_n = 2$, which implies that both the interfering IES and non-interfering OES are biased. One should note that in the graphene MZI, the interfering and non-interfering edge states on the n-side are interverted compared to MZIs in GaAs/AlGaAs heterostructures. Experimentally, the lobe structures observed in our graphene MZI can be directly fitted by the formula 4.12, without adding any gating effect. An explanation for this, could be that the actual coupling between the

IES and the OES is much smaller in graphene than in GaAs. Comforting this assumption, when we injected the bias from the other side (p-side) at $\nu_p = -1$, we observed an almost identical lobe structure with the DC bias. This seems to indicate that whether or not we apply a bias on the non-interfering edge channel it does not affect the decoherence. Finally, in GaAs, when the OES and IES are biased, a strong dependence on the transmission T_1 of the first QPC was observed, which is not the case here.

All this comforts the hypothesis than in graphene MZIs the coupling between the OES and IES is much smaller than in GaAs/AlGaAs MZIs.

4.4.2 Capacitive coupling to a noisy environment

I would like to introduce now a detailed theoretical framework describing the dephasing effect induced in the graphene MZI by a capacitive coupling to a noisy environment (for instance a noisy edge channel). In particular, I will describe two limit cases :

- the gaussian regime, where numerous electronic excitations are coupled to the interfering edge state, generating a gaussian phase distribution
- the non-gaussian regime, where a few electronic excitations are present

The Gaussian limit

In the Gaussian limit [70], where many detection electrons are involved, using the same approach than the one developed in section 4.1.4, one can explain in an analogue way the temperature dependence of the oscillations. The dephasing effect of temperature was modeled, by taking into account a capacitive coupling to the noisy non-interfering and co-propagating spin up edge channel, called detector edge channel in what follows, which scrambles the phase of the interfering electrons in $|\downarrow, \overrightarrow{\omega}\rangle$ and results in an additional dephasing term $z_2 = e^{-i\delta\varphi_2}$ in the interferometer transmission:

$$T_{\mathrm{VI}} = |r_1 t_2|^2 + |r_2 t_1|^2 + 2z_2|r_1 t_1 r_2 t_2|\cos(\phi_{\mathrm{AB}} + \phi) \tag{4.13}$$

In the gaussian regime, the averaged dephasing term becomes :

$$\langle z_2 \rangle = \langle e^{-i\delta\varphi_2} \rangle = e^{-\langle \delta\varphi_2^2 \rangle/2} \tag{4.14}$$

with $\langle \delta\varphi_2^2 \rangle$=$\mathrm{S}_{\varphi_2\varphi_2}(\omega)\Delta\nu$ and $\Delta\nu$=v/L. Internal potential of the interfering $|\downarrow, \overrightarrow{\omega}\rangle$ edge state is noted U_2, and U_2 fluctuations give rise to phase fluctuations through :

$$\varphi_2(\tau) = \int_0^\tau \frac{eU_2(t)}{\hbar} dt \tag{4.15}$$

with τ=L/v. We can relate phase noise to internal potential noise :

$$S_{\varphi_2\varphi_2}(\omega) = 4\frac{e^2}{\hbar} S_{U_2U_2}(\omega) \frac{sin(\frac{\omega\tau}{2})^2}{\omega^2} \tag{4.16}$$

To express U_2 as a function of the electrochemical potential of non-interfering detector edge state, noted V_D, we need to introduce the admittance between the detector spin

up edge state and $|\downarrow, \overrightarrow{\omega}\rangle$: $G_{2,D} = \frac{dI_2(\omega)}{dV_D(\omega)}$ [76]. Calculations of the admittance (see in appendix A.3) leads to :

$$S_{U_2,U_2} = |\frac{C}{2C + \frac{i}{\omega}\frac{e^2}{h}(1 - e^{i\omega\tau})}|^2 S_{V_D,V_D} \tag{4.17}$$

When $eV_D \ll k_BT$, the noise is dominated by the Johnson-Nyquist noise, thus S_{V_D,V_D}=$4k_BTR_Q\Delta\nu$ with $R_Q = h/e^2$. This leads to the following equation for z_2 :

$$\langle z_2\rangle = e^{-T/T_{\varphi,G}} \text{ with } \begin{cases} 1/T_{\varphi,G} = \frac{4k_B}{\hbar}\tau I(\gamma) = \frac{4k_BT}{\hbar}\frac{R_QC}{\gamma}I(\gamma) \\ I(\gamma) = \int_0^\infty \frac{sin^2(x)\gamma^2 dx}{sin^2(x)+2\gamma sin(2x)+4\gamma^2x^2} \end{cases} \tag{4.18}$$

Finally, following the procedure detailed in section 4.1.4, one recovers a similar expression than in GaAs/AlGaAs heterostructures for the visibility dependence on temperature in the gaussian regime :

$$\upsilon = \upsilon_0 e^{-T/T_{\varphi,G}} \tag{4.19}$$

This framework gives us an exponential decay of the visibility with the temperature when a large number of electrons are involved in the dephasing.

The non-Gaussian limit

In the non-Gaussian limit [61], less than one electron will scramble the phase of the interferometer. Probability that a thermal electron is present in the edge coupled to the interferometer is noted η. Visibility is reduced by the following factor :

$$z_2 = |(1 - \eta) + \eta e^{i2\pi V_D/V_0}| \tag{4.20}$$

In the limit $V_D/V_0 \ll 1$ and $\eta \ll 1$, we can extend z_2 to the second order:

$$z_2 = e^{-\eta(\frac{2\pi V_D}{V_0})^2} \tag{4.21}$$

A rough assumption would be : $V_D^2 \sim S_{V_D,V_D}\Delta\nu$, with $\Delta\nu$ the bandwidth given by $\Delta\nu$=$1/\tau$. Following this, one obtains as previously an exponential decay of the visibility with the temperature with a different constant :

$$\frac{1}{T_{\varphi,NG}} = \frac{4k_BT}{\hbar}\frac{R_QC}{\gamma}\frac{\pi\eta(1-\eta)}{(2+1/\gamma)^2} \tag{4.22}$$

In addition, within this rough description, at very low temperature $\eta \ll$1, phase scrambling induced by the detector edge state is suppressed. Finally, one should note that :

$$T_{\varphi,G}/T_{\varphi,NG} = \frac{\pi\eta(1-\eta)}{I(\gamma)(2+1/\gamma)^2} \tag{4.23}$$

The assumptions achieved here to describe the non-gaussian limit are rough, and further theoretical developments have to be carried out to have a proper description of this regime.

Discussion of this approach

The exponential decay of the visibility with the temperature, and the existence of two regimes are also consistent with this framework : the regime observed at low temperature could be associated to a non-gaussian configuration, while the regime at high temperature would correspond to a gaussian configuration. Indeed, an exponential decay is predicted for the gaussian regime in this framework, however further theoretical developments are needed to see if the exponential decay in the non-gaussian regime can be explained within a more complete theoretical model.

4.4.3 The spin-charge separation in graphene

Our Korean collaborator, HS Sim, worked on the adaptation of a spin-charge separation model in order to explain the results observed in our graphene MZI, and in particular the existence of a lobe structure in DC bias, and the presence of two different regimes of decoherence in temperature.

In a first model, represented in figure 4.22, only the coupling between edge states on the same side of the junction was considered. Describing this model in a spin-charge separation framework, they could fit the two different slopes obtained in temperature at ($\nu_p = -2$,$\nu_n = 2$) and at ($\nu_p = -1$,$\nu_n = 2$). For this aim, they used the ratio u/v_0 as a fitting parameter, with u representing the interaction between the edges and v_0 the velocity in absence of interaction. Unfortunately, the ratio u/v_0 extracted is too small to reproduce within this framework the lobe structures observed in DC bias.

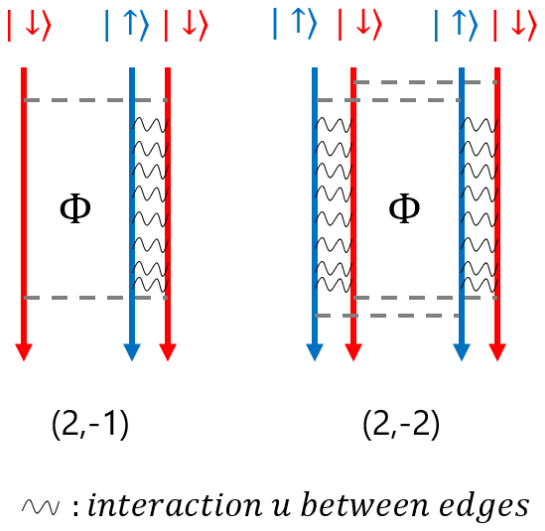

Figure 4.22: Schematic representation of the first coupling model considered by H. Sim to simulate the experimental results in temperature and DC bias thanks to a spin-charge separation model. Here are represented in red the spin down edge states and in blue the spin up ones existing along the pn junction for two MZI configurations used in our measurements : ($\nu_p = -1$,$\nu_n = 2$) and ($\nu_p = -2$,$\nu_n = 2$). In this first model, only the coupling between edge states on the same side of the junction, i.e. p or n side, is considered.

This is why, they considered a second model for the coupling, represented in figure 4.23, where the outer edge state is this time coupled to the inner edge state on the same side of the junction, but also to the closest edge state on the other side. Thanks to this model, they could fit again the two different slopes obtained at ($\nu_p = -1$,$\nu_n = 2$) and at ($\nu_p = -2$,$\nu_n = 2$), but the corresponding u/v_0 ratio is larger than previously. In this framework, they obtained a velocity $\sim 0.66 \times 10^4 m/s$ for the slow mode, and $\sim 4.9 \times 10^4 m/s$ for the bare velocity v_0. The value of v_0 is low compared to the velocity measured on the graphene edges $\sim 10^6 m/s$ [48], however one should note that here v_0 corresponds to the velocity along a pn junction created thanks to electrostatic gates, and thus where the potential is much smoother than along the graphene physical edge. Furthermore, using these values for u and v_0, they could predict lobe structures but with multiple side lobes, and not one as experimentally observed. However, this could be explained by the existence at higher bias of another decoherence source that would erase all interferences. For me, the main weakness of this approach is that it considers an identical coupling of the outer edge state to the inner edge state on the same side of the junction than to the closest edge state on the other side of the junction. Indeed, due to the existence of a $\nu = 0$ region in the center of the pn junction, I would expect the coupling to be much stronger between edge states on the same side of the junction.

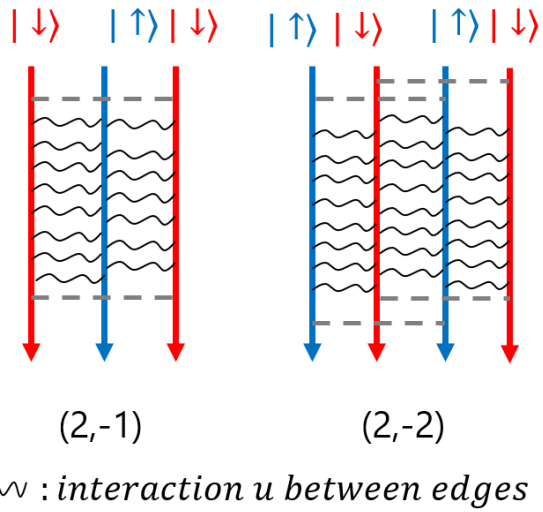

Figure 4.23: Schematic representation of the second coupling model considered by H. Sim to simulate the experimental results in temperature and DC bias thanks to a spin-charge separation model. Here are represented in red the spin down edge states and in blue the spin up ones existing along the pn junction for two MZI configurations used in our measurements : ($\nu_p = -1$,$\nu_n = 2$) and ($\nu_p = -2$,$\nu_n = 2$). In this second model, only the outer edge state is coupled, as previously, to the inner edge state on the side of the junction, but also to the closest edge states on the other side.

The models of decoherence presented previously can predict some of the features observed experimentally, however further investigations are needed to have a more comprehensive understanding of the underlying physics.

4.5 Partial conclusion

In chapter 3, we have shown that thanks to our side gates, we obtained a full electrical control over the valley isospin. Indeed, the valley isospin direction of the output state of the system, noted $|\psi_{final}\rangle$, can cover almost all the accessible states in a valley Bloch sphere representation. In order to achieve, quantum operations via these valley polarized states (valleytronics), their coherence needs to be steady. In this chapter, we studied the typical energy scales, in DC bias and temperature, of the coherence of the system using MZI. In particular, our valley splitter sample exhibited the persistance of Aharanov-Bohm oscillations up to a DC bias voltage as high as $0.8mV$, and a temperature of $1.5K$. These values are almost 20 times larger than the one observed in GaAs MZI. The DC bias study also exhibited a lobe structure, similar to the one observed in GaAs MZI, but which has never been reported in previous studies in graphene at this energy scale. Finally, for the temperature dependence, a comprehensive study for graphene MZI was lacking; our measurement showed an exponential decay of the visibility with the temperature as in GaAs, but with the coexistence of two different regimes of decoherence. On the theoretical point, the two frameworks that I detailed give some clues to understand the decoherence in the system. To conclude, the coherence properties of valley isospin largely surpass the state of the art values of charge state reported in high-mobility semiconductors, making it an interesting platform to achieve quantum computations thanks to valley-polarized states, and valleytronics devices.

Chapter 5

Coherence length in graphene

As exhibited in chapter 4, the coherence properties in graphene quantum Hall edge states, formed along a pn junction, are much steadier than in their GaAs counterpart. Indeed, Aharanov Bohm oscillations persist at energies 20 times higher in DC bias and in temperature. In the physics of quantum conductors, an essential physical scale to characterize the coherence of the system is the quantum coherence length, noted l_φ. It represents the typical propagation length on which an excitation loses its phase coherence due to information exchange with the environment. In 2001, the coherence length was measured for the first time in a 2DEG formed in a GaAs/AlGaAs heterostructure without magnetic field, thanks to a ring shaped sample [34]. The achievement of an electronic MZI by Ji et al. [37] paved the way towards the measurement of l_φ in the quantum Hall edge channels. Indeed, in 2007, Roulleau et al. [73] directly measured it at filling factor $\nu = 2$, by checking the temperature dependence of the Aharanov-Bohm oscillations in MZIs of different sizes. We used a similar procedure to evaluate the coherence length in the quantum Hall edge channels formed along a pn junction in graphene. Therefore, I will first present the experimental procedure followed by Roulleau et al., to measure the coherence length in GaAs. Then, is detailed how we achieved MZIs of different lengths in graphene thanks to our valley splitter sample. Afterwards, I will describe our experimental study of the coherence length l_φ in the quantum Hall edge channels formed along a pn junction in graphene. Finally, is detailed the quantum dots behavior that we observed experimentally and their possible link with the record coherence length measured in our sample.

5.1 Measurement of the coherence length in GaAs

In order to directly measure the coherence length l_φ in the quantum Hall edge states formed in a GaAs/AlGaAs heterostructures at filling factor $\nu = 2$, Roulleau et al. [73] used three different samples, having a MZI geometry as depicted in figure 4.6.a, with different arm lengths : $L = 5.6,\ 8,$ and $11.3\mu m$ (noted respectively small, medium and large in what follows). As shown in figure 5.1a, they measured the evolution of the Aharanov-Bohm oscillations visibility V with the temperature for each sample. The plotted quantity $ln(V/V_B)$, where V_B is the visibility at the base temperature $T_B = 20mK$, exhibits a clear linear dependence on the temperature for the three samples, indicating an

exponential decay of the visibility. Interestingly, the longer the arm, the faster the decay. More quantitatively, they plotted in figure 5.1b the slope ${T_\varphi}^{-1} = ln(V/V_B)/(T - T_B)$ of each curve in figure 5.1a as a function of the arm length. ${T_\varphi}^{-1}$ appears to be directly proportional to the arm length. This result was interpreted thanks to the introduction of a coherence length $l_\varphi(T)$ verifying the following expression :

$$V = V_0 e^{-2L/l_\varphi(T)} \tag{5.1}$$

where V_0 contains the temperature independent part of the visibility. The scaling of the slope ${T_\varphi}^{-1}$ with the arm length L implies that :

$$\left\{ {T_\varphi}^{-1} = \frac{\ln(V/V_B)}{(T - T_B)} = aL \right\} \Rightarrow \left\{ \ln(V) = A + aLT \right\} \tag{5.2}$$

with a a constant corresponding to the slope in figure 5.1b, and A a temperature independent constant corresponding to $\ln(V_0)$. From equations 5.1 and 5.2, one obtains the following formula for $l_\varphi(T)$:

$$l_\varphi(T) = \frac{-2}{aT} \tag{5.3}$$

Following this procedure, Roulleau et al. extracted a coherence length of $20\mu m$ at $20mK$.

Finally, the spurious effect of thermal smearing could be ruled out as the length difference between the two arms required to explain the dephasing in this framework is too big. Consistently, the locked phase with the DC bias implies energy independent excitations, which also excludes the appearance of thermal smearing [73].

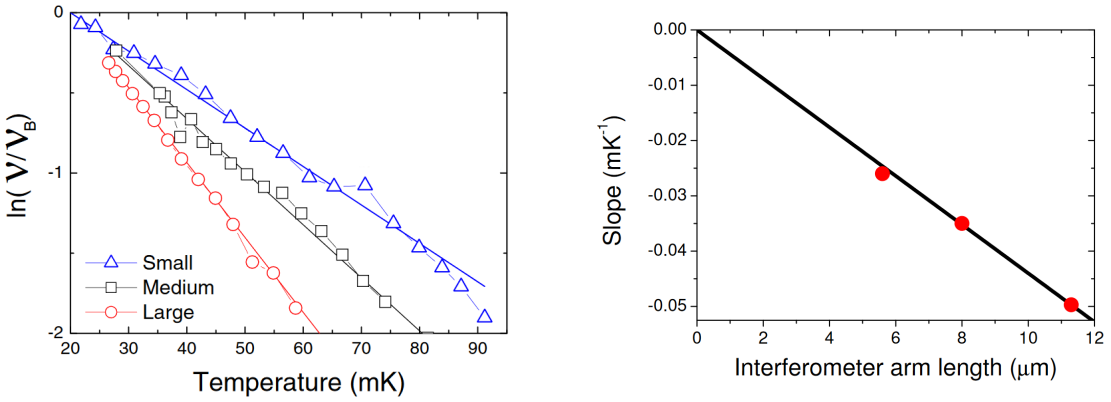

(a) (b)

Figure 5.1: **Coherence length measurement in GaAs (extracted from [73]).** (**a**) $ln(V/V_B)$ versus temperature for the three samples, V_B is the visibility measured at $T_B = 20mK$. The measurement has been done at the magnetic field for which the visibility decay is the smallest. (**b**) Slope measured for the three curves in (a) as a function of the interferometer length.

5.2 On chip interferometers with different sizes

The essential point, to measure the coherence length in the edge states of the quantum Hall effect, is to have interferometers of different lengths. The fabrication of MZI in graphene is tedious, making this study experimentally challenging. Moreover, we noticed in our preliminary samples presenting longer pn junctions that the visibility of Aharanov-Bohm oscillations was always much lower. However, an unexpected experimental observation enabled us to carry out the coherence length measurement with a single sample ! Indeed, as is detailed in this section, with our valley splitter sample, by tuning the side, top, and back gates in a peculiar regime, we can obtain three MZIs of different lengths going from 1.5 to $0.5\mu m$.

5.2.1 Introduction : going from the MZI to the full reflection

(a) Zoom transmitting configuration : $\nu_{sg1} = \nu_{sg2} = -1$.

(b) Zoom reflecting configuration : $\nu_{sg1} = \nu_{sg2} = 0$.

Figure 5.2: Schematic representation of the valley splitter sample in the fully reflecting and the transmitting configurations. n region is depicted in blue, p region in red.

As explained in chapter 3, when the pn junction is in a quantum Hall bipolar regime with $\nu_p = -1$ and $\nu_n = 2$ (see figure 5.2), by tuning the voltage applied on the side gates, one can go from a configuration where the pn junction ends on the graphene physical edge to a configuration where it ends on a gate defined edge. Indeed, in the case $\nu_{sgi} \leq -1$ (identically $\nu_{sgi} \geq 2$) with $i = 1, 2$ denoting the top (respectively bottom) side gate, as shown in the schematic 5.2a, the pn junction ends on the graphene physical edge which can supply the large momentum transfer necessary to go from one valley to another, enabling the mixing between the red and yellow edge channels. In this configuration, the system acts as a valley MZI with the two mixing points playing the role of the beam splitters, and the co-propagating edge states along the junction representing the two arms. Contrarily, when $\nu_{sgi} = 0$, situation depicted in figure 5.2b, the pn junction ends on the

side gate edge inside the graphene bulk. The potential there is much smoother, and no mixing should occur between the edge states with different valleys (the red and yellow).

In figure 5.3, the transmission $T_{VI} = I_T/(I_0/2)$ through the pn junction (with I_0 the injected current and I_T the transmitted one) is plotted as a function of the voltage V_1 on the top side gate and V_2 on the bottom one for a fixed magnetic field, and, fixed top and back gates voltages. For negative gate voltages V_1 ($\nu_{sg1} < 0$) and V_2 ($\nu_{sg2} < 0$), T_{VI} oscillates. For positive V_1 ($\nu_{sg1} \geq 0$) and V_2 ($\nu_{sg2} \geq 0$), the interference pattern is completely washed out and T_{VI}=0. This illustrates the two regimes described previously.

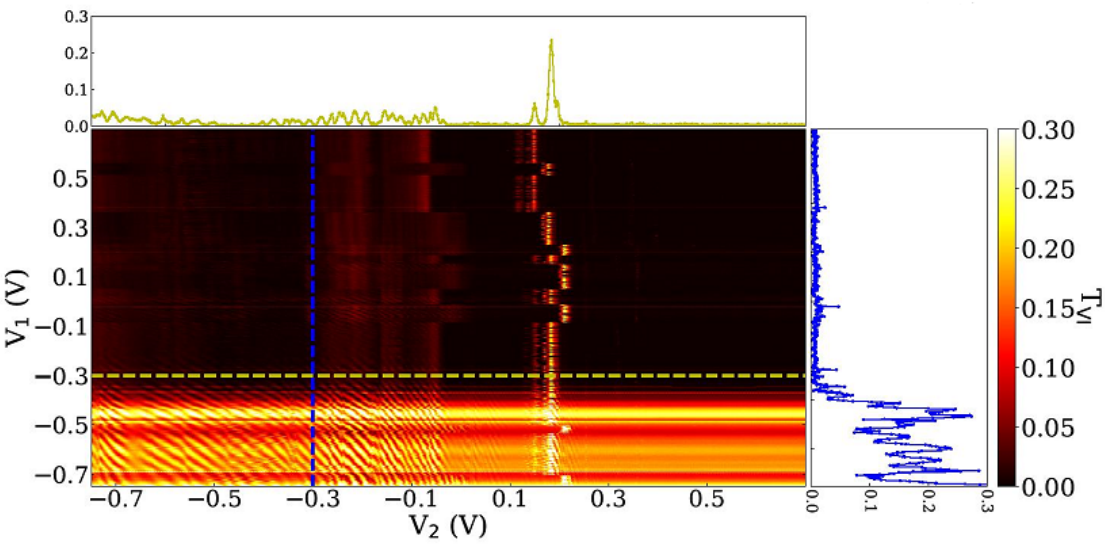

Figure 5.3: Valley-interferometer transmission T_{VI} as a function of V_2 and V_1 (voltage on the top and bottom side gates). Transition between $\nu_1 = \nu_2 = -1$ and $\nu_1 = \nu_2 = 0$ occurs for $V_1 \sim V_2 \sim 0$.

In the MZI configuration with $\nu_{sgi} \leq -1$, the flux of the magnetic field B through the area A enclosed by the two arms of the interferometer imposes a dephasing between them given by the Aharanov-Bohm phase $\phi_{\mathrm{AB}} = 2\pi BA/\Phi_0$, $\Phi_0 = h/e$ being the flux quantum. To change this phase, we can either sweep the magnetic field or the area enclosed A thanks to V_1, which explains the inclined oscillations observed in figure 5.4 corresponding to a magnetic field periodicity of $\Delta B = 25mT$. From the Aharonov-Bohm phase, we get the interferometer area $A = \Phi_0/\Delta B = 0.165\,\mu\mathrm{m}^2$ and the spatial separation of 110 nm between the two interface channels, given the length 1.5 μm of the PN interface.

5.2.2 Mixing along a gate defined edge

As explained previously, when the side gates are set at filling factor $\nu_{sgi} = 0$, no mixing should occur between the edge states propagating along the pn junction, as only the graphene physical edge can provide the large momentum transfer necessary to go from one valley to another. However, in this paragraph, I will show that surprisingly in our experiments we observed valley splitting in this configuration for some peculiar tuning of

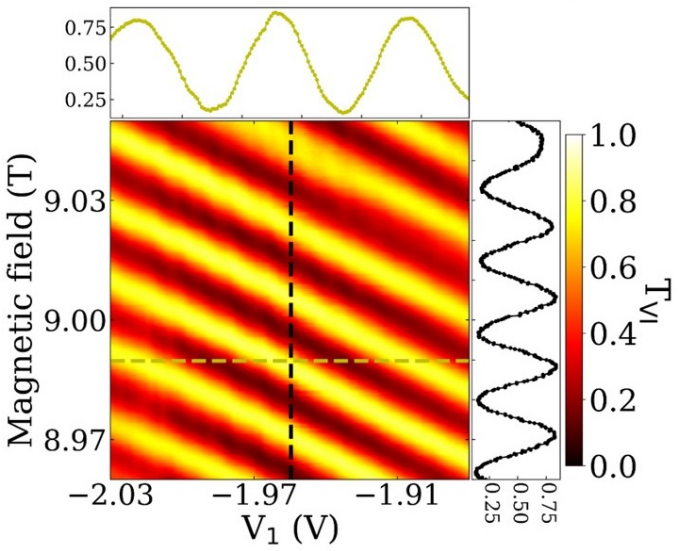

Figure 5.4: Valley-interferometer transmission $T_{\rm VI}$ for $\nu_{sg1} \leq -1$ and $\nu_{sg2} \leq -1$ as a function of B and V_1 with $T_1 = T_2 \sim 1/2$.

the system, enabling us to achieve MZIs with three different lengths.

An intermediate MZI

We slightly changed the top gate and back gate voltages compared to the one used in figures 5.3 and 5.4. In this new configuration, we measured T_{VI} as a function of the magnetic field and the voltage V_2 with $\nu_{sg1} = -1$. The resulting color plot, presented in figure 5.5.a, is intriguing. As expected, at $\nu_{sg2} \leq -1$ (i.e. $V_2 \leq 0.15V$), there are $T_{\rm VI}$ oscillations with B and with a small periodicity in V_2 indicating that the area A enclosed by the interferometer is tuned by the bias applied on the bottom side gate. However, on top of these fast oscillations in V_2, we observe oscillations in magnetic field which hardly depend on the bias V_2 and persists in the $\nu_{sg2} = 0$ region ($V_2 \geq 0.3V$). And, as visible in the black single trace in figure 5.5.a taken at at $V_2 = 0.55V$, the periodicity in magnetic field $\Delta B \sim 34.5mT$ is much larger than the $25mT$ periodicity observed in the normal MZI configuration (see figure 5.4).

Furthermore, we checked the V_1 periodicity of these steady V_2-independent oscillations. For this aim, we fixed $V_2 = 0.55V$ (spot of the black dashed line in figure 5.5.a), corresponding to a region where $\nu_{sg2} = 0$ and where we have only V_2-independent oscillations. Then, we measured T_{VI} as a function of the magnetic field and the voltage V_1 this time. As shown in figure 5.5.b, for $\nu_{sg1} \leq -1$ (i.e. $V_1 \leq 0.15V$), we observe oscillations, corresponding to the V_2-independent oscillations in figure 5.5.a, with a periodicity $\Delta B \sim 34.5mT$ in magnetic field and a small periodicity in V_1. This indicates that V_1 directly tunes the area A enclosed in this configuration. When ν_{sg1} reaches zero (i.e. $V_1 \geq 0.3V$), the oscillations are completely washed out.

We attribute these robust V_2-independent oscillations to the formation of a smaller interferometer where the top mixing point is defined at the intersection between the top side gate and the graphene physical edge, and the bottom one is at the intersection

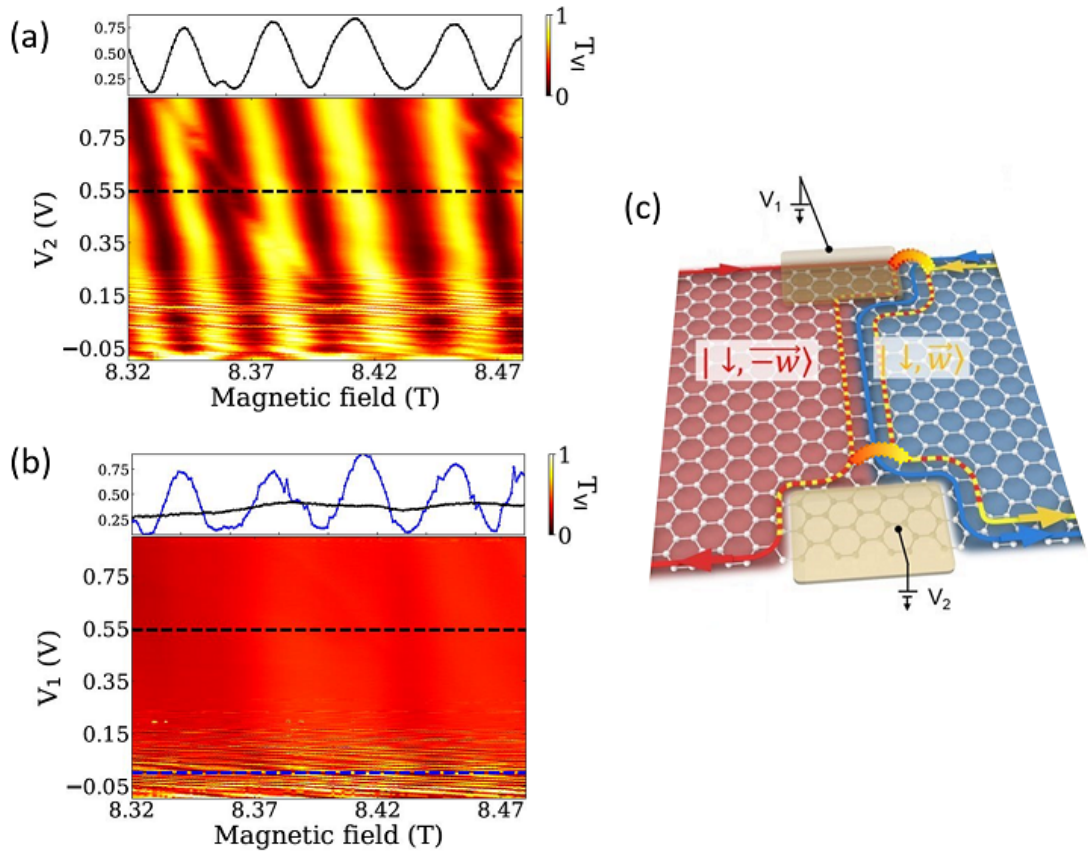

Figure 5.5: **Intermediate length interferometer.** (**a**) Valley-interferometer transmission T_{VI} as a function of magnetic field B and V_2 for ν_{sg1}=-1. For $\nu_{sg2} \leq$ -1 ($V_2 \leq 0.15V$), T_{VI} oscillates in B with $\Delta B \sim 34.5mT$, and in V_2 with a small period ΔV_2 indicating that the interferometer area A is directly tuned by V_2. On top of these oscillations, we note oscillations that hardly depend on V_2. For ν_{sg2}=0 highlighted by a black dashed line ($V_2 = 0.55V$), fast oscillations in V_2 are washed out but V_2-independent oscillations persist. We interpret them as originating from an intermediate size interferometer. (**b**) Valley-interferometer transmission T_{VI} as a function of B and V_1 for fixed $V_2 = 0.55V$ (black dashed line in figure 5.5.a), corresponding to the region where $\nu_{sg2} = 0$ and only V_2-independent oscillations persist. For $\nu_{sg1} = -1$ highlighted by a blue dashed line, T_{VI} oscillates in B with $\Delta B \sim 34.5mT$, and in V_1 with a small period ΔV_1. This means that the V_2-independent oscillations are modulated by V_1, indicating that the interferometer area A is tuned by V_1. For ν_{sg1}=0 highlighted by a black dashed line, oscillations are washed out. (**c**) Schematic representation of the intermediate size interferometer.

between the pn interface and the upper edge of the bottom side gate (i.e. along $\nu = 0$), as depicted in figure 5.5.c. This implies a smaller enclosed area consistently with the larger pariodicity observed : $\Delta B \sim 34.5mT$ while $\Delta B \sim 25mT$ for a normal MZI configuration (i.e. $\nu_{sgi} \leq -1$). Moreover, as the mixing point is at the top edge of side gate 2 (i.e. the bottom one), changing the bias V_2 on it should have no impact on the oscillations. Contrarily, for the top side gate, V_1 should directly tune the are enclosed A. Therefore, our

picture qualitatively explains our experimental observations. Finally, from the Aharonov-Bohm phase, we get the interferometer area $A = 0.12\mu m^2$ and the spatial separation of $114nm$ between the two interface channels, given the length $1.05\mu m$ of the pn interface.

We can also form a $1.05\mu m$-long interferometer where the top mixing point is defined along $\nu = 0$ in the bulk and the bottom one at the intersection between the graphene physical edge and the pn junction; in other words using a reverse configuration compared to the one depicted in figure 5.5.c.

A small MZI

Following the same reasoning, we can find another set of gate voltages where both mixing points are along $\nu = 0$ in the bulk, giving rise to a small MZI as depicted in figure 5.6.c.

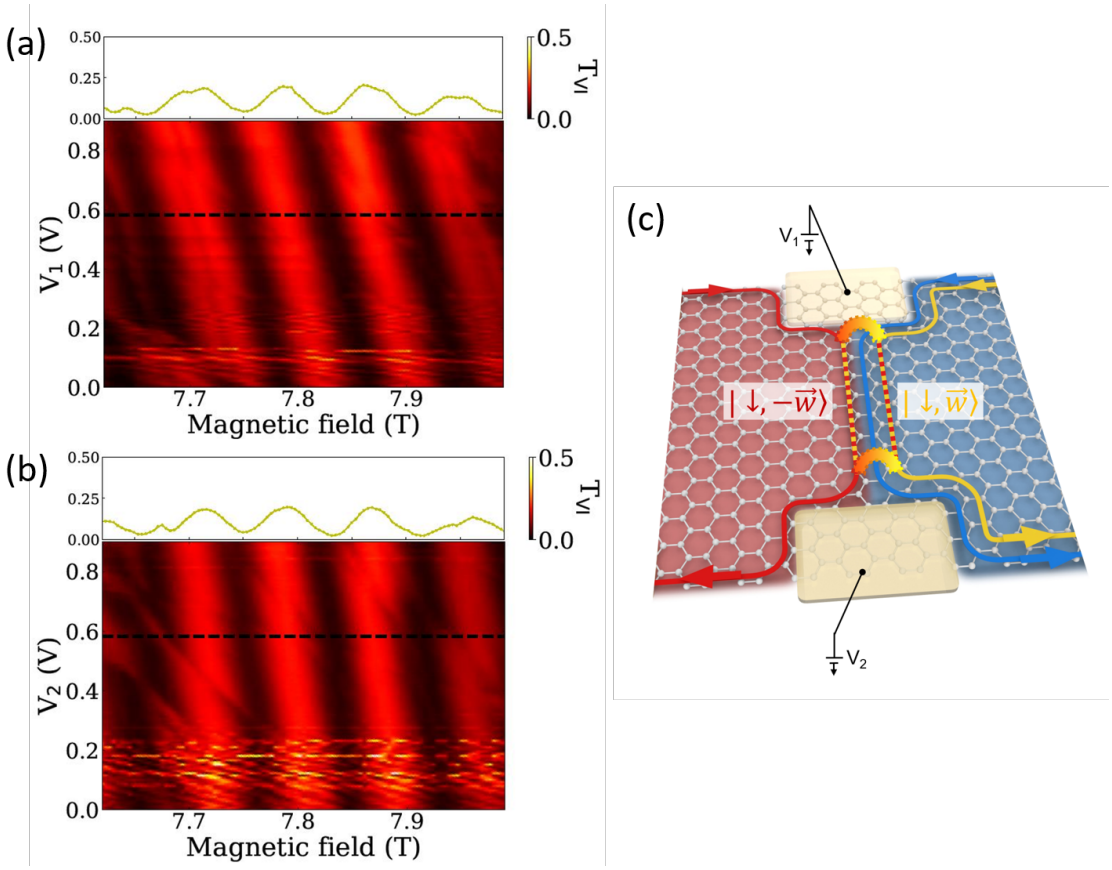

Figure 5.6: **Small length interferometer.** (**a**) Valley-interferometer transmission T_{VI} as a function of B and V_1 for ν_{sg2}=0. T_{VI} oscillates in B with $\Delta B \sim 83$ mT for ν_{sg1}=0 (black dashed line). (**b**) Valley-interferometer transmission T_{VI} as a function of B and V_2 for ν_{sg1}=0. T_{VI} oscillates in B with $\Delta B \sim 83$ mT for ν_{sg2}=0 (black dashed line). We interpret these ocillations to originate from a small size interferometer. (**c**) Schematic representation of the small size interferometer.

In figure 5.6.a, ν_{sg2} is fixed at 0, and T_{VI} is measured as a function of the magnetic field

and V_1. Interestingly, when $\nu_{sg1} = 0$ (region around the black dotted line), T_{VI} oscillates with B with period $\Delta B \sim 83mT$ and hardly depend on V_1. Similarly, in figure 5.6.b, we fix $\nu_{sg1} = 0$ and we sweep the magnetic field and the voltage V_2. When $\nu_{sg2} = 0$ (region around the black dotted line), we observe oscillations with the same magnetic field periodicity of $\sim 83mT$ hardly depending on V_2. To summarize, for $\nu_{sg1} = \nu_{sg2} = 0$, we have big oscillations in magnetic field not depending on either V_1 or V_2, indicating a small MZI as depicted in figure 5.6.c. From the Aharonov-Bohm phase, we get the interferometer area $A = 0.05\mu\text{m}^2$ and the spatial separation of 82.7 nm between the two interface channels, given the length 0.6 μm of the PN interface. This is the smallest electronic Mach Zehnder ever reported.

Conclusion

We have shown that by playing on the back and top gate voltages, we can obtain mixing of the valley inside the graphene bulk along the edge of the side gates under which the filling factor is fixed at $\nu = 0$. Therefore, with our valley splitter sample, three MZI of different lengths $L = 0.6,\ 1.05,$ and $1.5\mu m$ can be measured, enabling us to carry out an experimental study of the coherence length in graphene. This unexpected mixing of edge states meeting on a gate defined border for some peculiar tuning might be due to the coupling between edge states and the $\nu = 0$ phase below the side gates. Indeed, at Landau level filling factor ν= 0, different phases are in competitions with distinct symmetry-breaking properties, and very little is known about interactions between propagating edge state and ν= 0 in the bulk. Among these phases, one can cite the ferromagnet (F) state, the antiferromagnet (AF) state, or canted antiferromagnetic (CAF) state that can be addressed by changing the ratio between the Zeeman energy and the Coulomb energy [42].

5.3 Measurement of the coherence length in graphene

Following Roulleau et al. method [73], to evaluate the coherence length l_φ, one needs to measure the dependence of Aharanov-Bohm oscillations visibility on temperature for at least three interferometers of different size. Unexpectedly, we experimentally observed that, thanks to our valley splitter samples, we can achieve by playing on the back and top gates three configurations corresponding to MZIs of different length, respectively $L =$ 0.6, 1.05, and $1.5\mu m$. This enabled us to carry out the first experimental measurement of the coherence length in the quantum Hall edge channels formed along a graphene pn junction. Moreover, in our valley splitter sample, we observed two different regimes of decoherence (described in chapter 4) presenting exponential decays of the visibility with the temperature : one at low temperature (below $\sim 400mK$), and one at high temperature. Therefore, we should obtain two different coherence lengths corresponding to the two regimes. In this section, I will first present the temperature measurement corresponding to those three configurations, then the extraction of the coherence length from these measurements for the low temperature and high temperature regimes. Finally is discussed the visibility dependence on the DC bias for the different sizes of MZI.

5.3.1 Temperature dependence and coherence length

In figure 5.7.a, visibility is plotted as a function of the temperature in log scale for the long ($1.5\mu m$), intermediate ($1.05\mu m$) and small size ($0.6\mu m$) interferometers. Below a threshold value (indicated by a dashed line in figure 5.7.a), the temperature dependence of the visibility is weak and linear with the temperature confirming an exponential decay of the visibility with the temperature. Above this threshold value, temperature dependence of the visibility is more pronounced and still linear. If we interpret this threshold temperature as the crossover between a gaussian regime (at high temperature) and a non-gaussian regime (at low temperature), the threshold temperature will verify $k_B T = h\nu$. The frequency ν can be expressed thanks to the drift velocity v along the pn junction and the length L of the interferometer arm : $\nu = v/L$. In figure 5.7.b, the threshold temperature is plotted as a function of the arm length what gives, in this framework, a drift velocity $v \sim 0.98 \times 10^4 m.s^{-1}$. Note that this velocity is smaller than reported values along sample edges in GaAs/AlGaAs heterostructures (typically 2-5 $10^4 m.s^{-1}$) probably due to the gentle potential profile of the PN junction. Below or above this threshold, the trend is clear : the longer the interferometer, the faster the decay of the visibility.

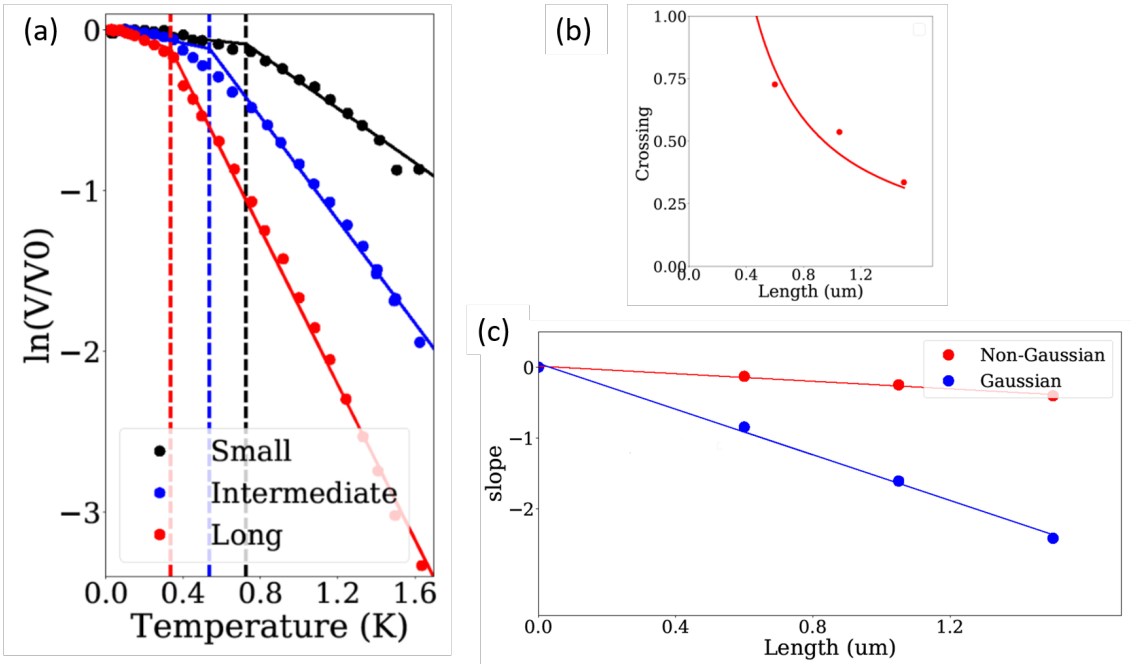

Figure 5.7: (**a**) Temperature dependence in log scale of the visibility divided by its maximum value for the three interferometer sizes. Below a size-dependent temperature (indicated by the dashed line), temperature dependence is linear and thermal dephasing is weak. Above the threshold temperature, thermal dephasing is strong. (**b**) Threshold temperature for the three interferometer sizes (red dots). Expected length dependence (red solid line). (**c**) Slope $\ln(V/V_0)/T$ as a function of the arm length in the high temperature (blue dots) and low temperature (red dots) regimes.

For each size, we extract the slopes $T^{-1}_{\varphi,low}$ ($T^{-1}_{\varphi,up}$) below (above) the threshold temperature and plot it as a function of the arm length (figure 5.7.c). The slope scales with

the length of the interferometer arm defining a coherence length $l_\varphi(T)$ such that :

$$V = V_0 e^{-2L/l_\varphi(T)} \tag{5.4}$$

Below the threshold temperature, we get $l_\varphi = 0.37mm$ at $20mK$, a record value in 2D material. Above it, we have : $l_\varphi = 1.2\mu m$ at $1K$.

From the two slopes, $1/T_{\varphi,up}$ at high temperature and $1/T_{\varphi,low}$ at low temperature, we extracted a ratio $T_{\varphi,up}/T_{\varphi,low} \simeq 0.16$. Considering the theoretical framework of gaussian and non-gaussian regimes to analyse the temperature dependence of the visibility (see section 4.4.2), we can attribute to the previous ratio a physical meaning. Indeed, in the non gaussian regime, we introduced the probability η that a thermal electron is present in the edge coupled to the interferometer. Considering the rough assumptions made in section 4.4.2, η can be directly determined from the ratio $T_{\varphi,up}/T_{\varphi,low}$, here we obtain : $\eta \simeq 0.11$.

5.3.2 Lobe structure and interferometer size

Finally, we will compare the DC bias dependence of the visibility for the small MZI (mixing inside the bulk along the side gates edges) and long MZI (mixing at the graphene physical edge). The measured visibility dependence on the DC bias for the two configurations are presented in figures 5.8.A and B.

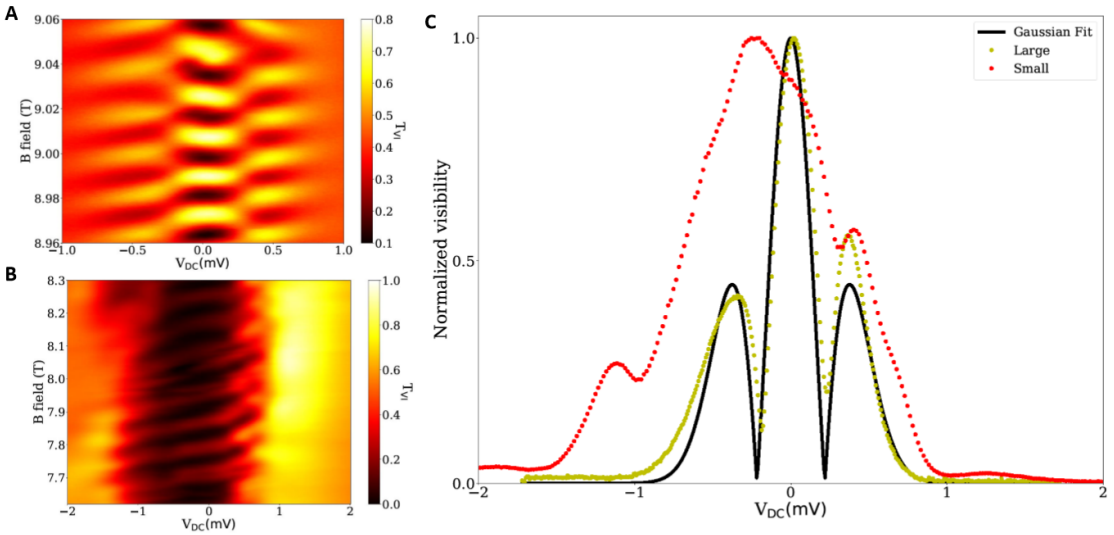

Figure 5.8: **Valley Splitter.** (**A**) $T_{\rm VI}$ as a function of the applied DC bias $V_{\rm DC}$ and the magnetic field for the long interferometer size. (**B**) $T_{\rm VI}$ as a function of the applied DC bias $V_{\rm DC}$ and the magnetic field for the small interferometer size. (**C**) Measured visibility as a function of $V_{\rm DC}$ for the long (yellow dots) and small (red) interferometer size. Computed visibility (black solid line) based on Gaussian phase fluctuations.

It has been demonstrated, as detailed in section 4.4.1, that a Gaussian distribution of phase at finite energy leads to a visibility $\propto e^{-\mathrm{V}^2/\mathrm{V}_{\rm lob}^2}|1 - V^2/V_{\rm lob}^2|$ (black solid line in figure 5.8.C) with $V_{\rm lob}$ an adjustable parameter [72]. In this model, the gaussian

distribution of phase is induced by the presence of an important number of electronic excitations. In the case of an applied DC bias, if the lobe structure originates from this, it should disappear at the crossover between gaussian and non-gaussian limit corresponding to $eV_{lob} = h\nu$. In figure 5.8.C $V_{lob} = 217\mu$V implying eV_{lob}/hν= 8.74 for the long size interferometer and 3.49 for the small one. If the crossover is not reached, the lobe structure is less pronounced for the small size interferometer.

5.4 Quantum dots and coherence length

Thanks to our valley splitter sample, we were able to measure for the first time the coherence length l_φ in graphene quantum Hall edge states. Impressively, in the low temperature regime, we obtained an exceptionally long coherence length : $l_\varphi \sim 370\mu m$ at $20mK$, which is 40 times higher than in GaAs/AlGaAs heterostructures. This opens the way to numerous applications of graphene for electron quantum optics and long-lived flying qubits, however it also raises fundamental question about the physical origin of this long coherence length. Interestingly, in the valley splitter sample, we observed some quantum dots behavior, characterized by the existence of Coulomb diamonds in DC bias measurements, which might explain our result for l_φ. Indeed, as detailed in the first part of this section, a recent study in GaAs/AlGaAs heterostructures by Duprez et al. [22] exhibited a strong enhancement of the coherence length, by engineering the adjacent edge states into closed loops. The quantum dots behavior that we measured in our sample, and which is presented in the second part of this section, may act as naturally formed closed loops, thus enhancing the coherence length, via the same mechanism.

5.4.1 Enhancing the coherence length in GaAs/AlGaAs heterostructures

For MZI in GaAs/AlGaAs heterostructures, the best Aharanov-Bohm oscillations visibilities were obtained at filling factor $\nu = 2$, and not $\nu = 1$ where the stronger decoherence is still not clearly understood. Therefore, most of MZIs experiments in GaAs/AlGaAs heterostructures were carried out at $\nu = 2$; configuration in which an unusual lobe structure in the DC bias dependence of the visibility [72][11][59] and an exponential decay of the visibility with the temperature [73][51] were reported. As detailed in chapter 4, a probable source of decoherence in this configuration, explaining those observations, is the long range Coulomb interaction, which generates a capacitive coupling between co-propagating edge states.

In [22], Duprez et al. followed a novel approach in order to enhance the coherence length in a MZI at $\nu = 2$ in a GaAs/AlGaAs heterostructure. The idea is to limit the dephasing effect of the capacitive coupling between the co-propagating edge channels. For this aim, they added to the classic MZI geometry a small gate depicted in light gray in figure 5.9.a. By tuning the bias applied on the gate, one can reach a configuration in which the outer interfering edge state trajectory, depicted by the black line on the schematic, is almost not affected by the presence of the gate, while the inner edge state (in gray) is strongly modified. Indeed, as depicted on the layout in figure 5.9.a, the inner edge channel is "closed in micron-scale loops of frozen internal degree of freedom combined with a loop-closing strategy providing an essential isolation from the environment". For

their experimental study, they achieved two samples using this geometry one with a $24\mu m$-long arm (figure 5.9.b), and one with a $0.1mm$-long arm (figure 5.9.c).

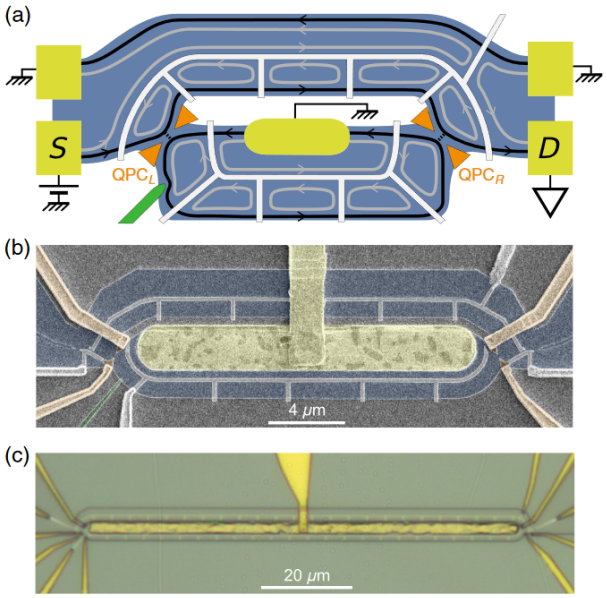

Figure 5.9: **Nanocircuit engineering of electronic coherence, extracted from [22].** (**a**) Sample schematic. Two chiral edge channels (black and gray lines with arrows) propagate along a 2D electron gas (blue) set in the integer quantum Hall regime at filling factor $\nu = 2$. The outer channel (black) follows two separate paths between tunable beam splitters implemented by quantum point contacts (orange),thereby forming a Mach-Zehnder interferometer. The inner edge channel (gray) can be closed into well-separated loops with specific comb-shaped gates (light gray) voltage biased to reflect only this channel. Sweeping the voltage on a lateral plunger gate(green) results in MZI oscillations of the current transmitted from source (S) to detector (D). (**b**) Colored scanning electron micro-graph of the sample with MZI arms of symmetric length $L \approx 24\mu m$. (**c**) Optical image of the $L \approx 0.1mm$ MZI. The inner edge channel loops have nominally identical perimeters of $9\mu m$, except one of $5\mu m$ for the lower left loop of each sample.

Experimentally, the results are striking. In figure 5.10, are presented the transmission through the MZI τ_{MZI} : in the normal MZI configuration without gate voltage (red curve), and in the closed loops configuration depicted in figure 5.9.a (blue curves). For the $24\mu m$ sample, as visible in figure 5.10.d, the blue oscillations are strongly enhanced compared to the red one, giving a visibility of 80%. Considering the $0.1mm$ long sample, no interference should be visible as its length is much longer than the coherence length, and consistently the red curve in figure 5.10.e exhibits no oscillations. However, the blue trace clearly oscillates, with a visibility estimated to 40%. From these measurements, they evaluated that the corresponding coherence length was around $l_\varphi \approx 0.25mm$ at 20mK in the closed loops configuration, which is 10 times higher than the coherence length measured using a normal MZI geometry at $\nu = 2$.

To summarize, by engineering the inner edge state in micron-scale loops combined to a loop closing strategy, Duprez at al. could strongly enhance the coherence length, which

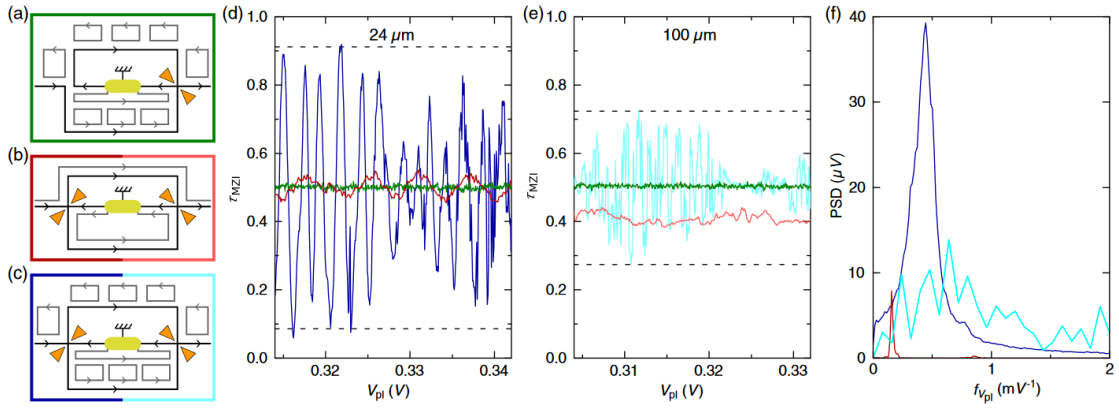

Figure 5.10: **Measurement of quantum oscillations while engineering the electronic coherence, extracted from [22].** (**a**)–(**c**) Schematics of the different configurations. (**d**),(**e**) Continuous lines show, versus plunger gate voltage V_{pl}, the measured fraction τ_{MZI} of current transmitted from S to D along the outer channel of the $L \approx 24\mu m$ (d) and 0.1 mm (e) MZI [same color as the box enclosing the corresponding schematic in panels (a), (b), or (c); darker shade for the shorter device].Horizontal dashed lines display the predicted τ_{MZI} extrema for the same $l_\varphi \approx 0.25mm$ in both MZIs. (**f**) Continuous lines show the power spectral density of $\tau_{MZI}(V_{pl})$ determined along large V_{pl} sweeps (extending between 50 and 80 mV) measured several times[same color code as in panels (d),(e)]. For the challenging case of $L \approx 0.1mm$ in configuration (c) (light blue line), the Fourier analysis is restricted to plunger gate-voltage windows exhibiting oscillations larger than 66% of their maximum amplitude.

means that they effectively reduced the dephasing effect of the capacitive coupling between the inner and the outer edge state. In what follows, I will show that a similar mechanism may naturally occur in our sample, explaining the long coherence length observed in the quantum Hall edge channels formed along a pn junction in graphene.

5.4.2 Quantum dots in graphene pn junction

In our valley splitter sample tuned in the bipolar quantum Hall regime we observed a surprising quantum dot behavior, which may play the role of the micron-scale loops in Duprez et al. work. In this section, I will first expose the experimental evidences of a quantum dot behavior. Then, is presented the mechanism that we proposed to explain the appearance of this quantum dot. Finally, is discussed the reduction of the capacitive coupling between co-propagating edge channels thanks to the presence of a quantum dot.

Experimental evidence for quantum dot behaviors

For this study, we first used the right pn junction (without side gates) in a configuration depicted in figure 5.11.A. In the n region the Landau-level filling factor is $\nu_n = 2$ and two channels of the opposite spin ($\uparrow$, $\downarrow$) counterclockwise circulate along the boundary. In the p region the filling factor is $\nu_p = -2$ and two channels of the opposite spin circulate clockwise. Along the bottom edge, the injected current I_0 is carried by the two edge

channels of the n region. Transmitted I_T and reflected I_R currents are represented in figure 5.11.B; their sum in black is constant and equal to I_0. We observe interference fringes of a Mach-Zehnder interferometer. Scattering of the valley isospin occurs at the bottom end and top end of the pn junction due to the atomic structure at the intersection between the interface of the pn junction and the physical edge.

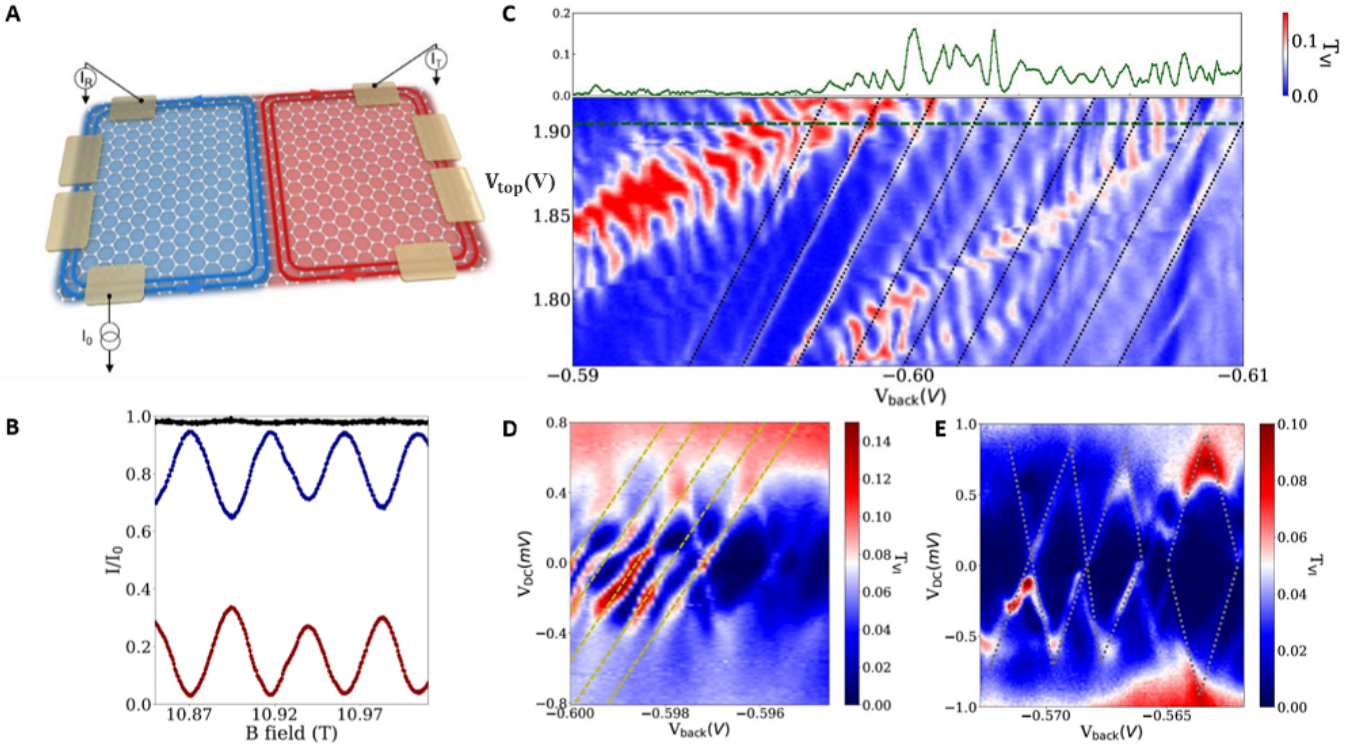

Figure 5.11: **Aharonov-Bohm and Coulomb blockade regime.** (**A**) Schematic representation of the pn junction. n region is depicted in blue, the p one in pink. Electrons are injected from the bottom left ohmic contact (defining an injected current I_0), transmitted I_T and reflected I_R currents are measured at the upper right and left contact. (**B**) Valley-interferometer transmission T_{VI} (in blue), reflection R_{VI} (in red), and their sum (in black) as a function of the magnetic field. (**C**) Valley-interferometer transmission T_{VI} as a function of back gate voltage V_{back} and top gate voltage V_{top}. On top of Aharonov Bohm oscillations, we note regularly spaced transmission peaks (black dotted lines). (**D**) Valley-interferometer transmission T_{VI} as a function of V_{back} and V_{DC}. V_{back} range is chosen to get both Aharonov-Bohm oscillations (yellow dashed lines) and transmission peaks. (**E**) Same as (D) with a V_{back} range that suppressed Aharonov Bohm oscillations.

In figure 5.11.C, the transmission probability $T_{VI} = I_T/I_0$ of the pn junction is plotted as a function of the global back gate voltage V_{back} and the top gate voltage V_{top}. On top of the expected Aharonov-Bohm oscillations, we note sharp transmission peaks highlighted by black dotted lines. The sign of the slope of Aharonov-Bohm oscillations with the top gate V_{top} is opposite to the one of the transmission peaks, indicating that the underlying physical mechanism is different. In figure 5.11.D, we tune V_{back} in a range where both

oscillations coexist and plot it as a function of the applied bias voltage V_{DC}. If Aharonov-Bohm oscillations (yellow dashed lines) disappear above 0.4 meV, one can also distinguish Coulomb blockade diamonds. To confirm this observation, we tune V_{back} in a range where Aharonov-Bohm oscillations are completely washed out while Coulomb blockade peaks are still there. The bias dependence measurement shows Coulomb blockade diamonds and confirms a Coulomb-blockade effect along the pn junction (in figure 5.11.E). Comparing with graphene/BN quantum anti-dot measured in the quantum hall regime [57], we roughly estimate the dot area to be $A \sim 0.3\mu m^2$ for a charging energy $\Delta E_C \sim 0.75meV$. pn junction length being equal to $1\mu m$, we get an island width of $300nm$. When V_{back} is tuned to obtain Aharonov-Bohm oscillations, we get a periodicity of $15mT$ what gives a distance between co-propagating edge states equal to $276nm$. Sizes of the Coulomb island and the valley inteferometer are comparable.

In a mere pn junction, valley-isospin tunneling between the two co-propagating states can not be tuned. In the following, we consider the left pn junction in our sample on which two valley splitters are located at its ends, enabling us to control the transmissions at those two points, and, therefore, to study separately the Aharonov-Bohm regime from the Coulomb Blockade regime. As depicted in figure 5.12.A, we used when studying a pn junction with valley splitters, the normal MZI configuration : $\nu_n = 2$ and $\nu_p = -1$. Therefore, in the n region, two channels of opposite spins circulate counter-clockwise along the boundary, while in the p region one spin down edge channel circulates clockwise.

When the filling factors below the top and bottom side gates verify $\nu_{sg1} \leq -1$ and $\nu_{sg2} \leq -1$, valley scattering occurs at the two intersection points of the junction with the graphene physical edge and we observe Aharanov-Bohm oscillations. For filling factors $\nu_{sg1} = \nu_{sg2} = 0$, valley scattering is suppressed and $T_{VI} = 0$ (see in figure 5.12.B). For intermediate regime, when filling factor below the side gates goes from -1 to 0, we observe sharp peaks that we interpret as Coulomb blockade peaks. In figures 5.12.C to F, we plot valley-interferometer transmission T_{VI} as a function of the magnetic field and V_{DC} for the Aharonov-Bohm regime (figure 5.12.C and D) and Coulomb blockade regime (figure 5.12.E and F). In figure 5.12.C, $\nu_{sg1} \leq -1$ and $\nu_{sg2} \leq -1$, valley scattering occurs at the top and bottom intersection. From the Aharonov-Bohm phase $\phi_{AB} = 2\pi BA/\Phi_0$, $\Phi_0 = h/e$ being the flux quantum, we get the interferometer area $A \sim 0.15\mu m^2$ (taking $\Delta B_{VI} = 17.6mT$) and the spatial separation of $157nm$ between the two interface channels, given the length $1.5\mu m$ of the pn interface. In figure 5.12.E, $\nu_{sg1} \leq 0$ and $\nu_{sg1} \leq 0$, weak valley tunneling occurs at the top and bottom intersection. We observe Coulomb blockade diamonds, with charging energy $\Delta E_C \sim 1meV$. From ΔE_C, we extract an island size $A \sim 0.169\mu m^2$. pn junction length being equal to $1.5\mu m$, we get an island width of $113nm$. In figure 5.12.D, $\nu_{sg1} \leq -1$ and $\nu_{sg2} = 0$, the larger magnetic field periodicity of the Aharanov-Bohm oscillations compared to figure 5.12.C indicates that the interferometer length is shorter; we are in the intermediate length MZI configuration. In figure 5.12.F, we are also in the intermediate-length MZI configuration (i.e. $\nu_{sg1} \leq -1$ and $\nu_{sg2} = 0$), and we observe Coulomb blockade diamonds, with charging energy $\Delta E_C \sim 1meV$. pn junction length being equal to $1.05\mu m$, we get an island width of $160nm$.

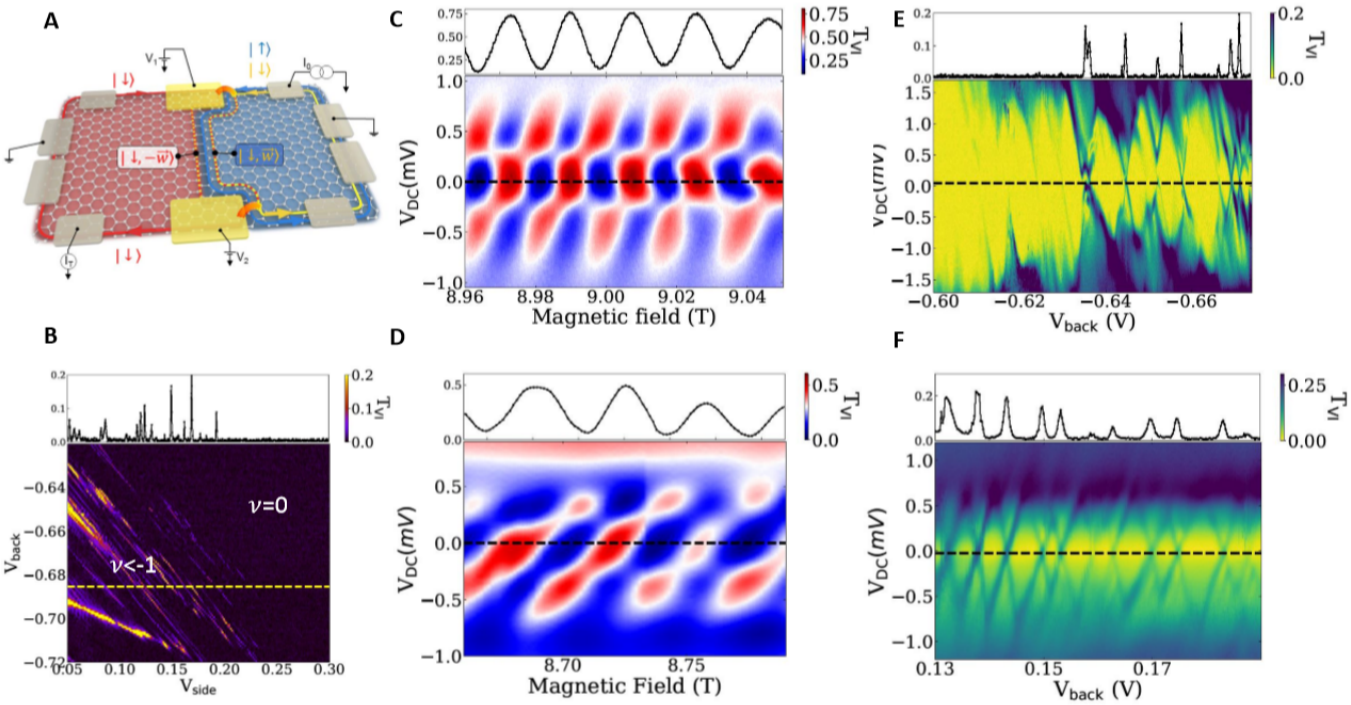

Figure 5.12: **Aharonov-Bohm and Coulomb blockade regime.** (**A**) Schematic representation of the pn junction with the two valley splitters on the top and bottom end of the pn junction. (**B**) Valley-interferometer transmission T_{VI} as a function of V_{side} (both sides gates are at the same voltage) and V_{back}. At the transition between between $\nu \leq -1$ and $\nu = 0$ filling factor below the side gates, we observe Coulomb blockade peaks. (**C**) T_{VI} as a function of magnetic field and V_{DC} for the long length interferometer. (**D**) T_{VI} as a function of the magnetic field and V_{DC} for the intermediate length interferometer. (**E**) Coulomb diamonds for the long length closed loop. (**F**) Coulomb diamonds for the intermediate length closed loop.

Origin of the quantum dots

In this section, I detail an underlying physical mechanism that can account for the observed Coulomb blockade regime. Graphene ground state at $\nu = 0$ is a degenerate SU(4) ferromagnetic multiplet. In the presence of symmetry breaking terms, different type of spin-isospin phases in the bulk but also along the edges can be obtained : among them are a ferromagnatic state (F), a canted antiferromagnetic state (CAF), a Kekule distorted state (K), and a charge density wave state (CDW). Main contributions of the Hamiltonian are the kinetic energy E_{kin} and the Coulomb energy which have full SU(4) symmetry. To break the SU(4) symmetry, Zeeman energy E_Z has to be considered together with lattice-scale effect that includes short range Coulomb electron interactions and electron-phonon couplings which are encoded into anisotropics terms u_z and $u_\perp$, following Kharitonov's terminology [42]. Note that energy difference between two kinetic Landau levels energy is larger than Zeeman energy by two orders of magnitude. In [42], Kharitonov derives the

following analytic expression for the single particle energy spectra ε :

$$\varepsilon = E_Z \sqrt{\left(\frac{E_{kin}(p)}{E_Z} - (1 - \frac{\Delta_{0z}}{E_Z})\right)^2 + \left(\frac{\Delta_{zx}}{E_Z}\right)^2} \tag{5.5}$$

with : $\begin{cases} \Delta_{0z} = -\frac{cos(\theta)}{2}(u_z + 2u_\perp) \\ \Delta_{zx} = -\frac{sin(\theta)}{2}(u_z - 2u_\perp) \end{cases}$, and θ describes the angle between the spin and the isospin.

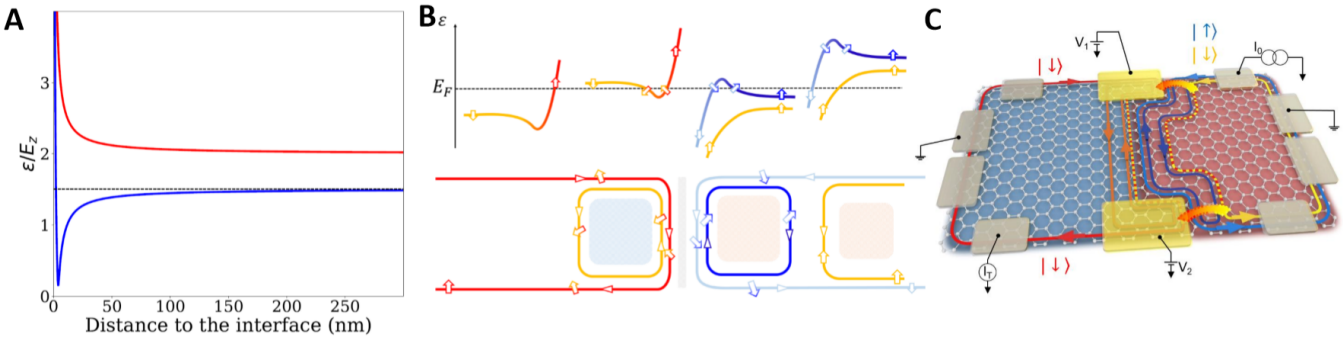

Figure 5.13: **Single particle energy spectrum.** (**A**) Energy spectrum of the single particle ground state in the CAF phase as a function of the distance to the pn junction interface at $\nu = 1$ (blue) and $\nu = 2$ (red). (**B**) Top part: energy spectrum of the single particle ground state in the CAF phase for $\nu_p = -2$ and $\nu_n = 1$. Bottom part: edge state configuration. Close to the pn junction interface, two closed loops are formed. (**C**) Schematic representation of the pn junction with the two closed loops.

In figure 5.13.A, the single particle energy spectrum is plotted as a function of the distance to the interface state of the pn junction for anisotropic terms $u_z = 5E_Z$ and $u_\perp = -E_Z$ corresponding to the CAF state in the bulk ground state phase diagram. To account for the Coulomb blockade regime, energy spectra are represented on both sides of the pn junction interface (see in figure 5.13.B). The top part of the figure describes the intersection of the Fermi energy E_F with the different Landau levels as a function of the distance to the interface. For $\nu = -2$ bulk, E_F crosses two Landau levels leading to two co-propagating edge states. For $\nu = -2$ close to the interface, E_F crosses a single Landau level twice leading to two counter-propagating edge states (see the bottom part of figure 5.13.B) and the formation of a large quantum dot. For the used parameters in figure 5.13.A, width of the dot is $\sim 200nm$. One should note also the presence of a second quantum dot in the $\nu = +1$ region. In figure 5.13.B, spin states are depicted and propagating electrons inside quantum dots have canted spins and isospins. It has been proposed that spin and isospin degree of freedom do not remain independent, separable variables, but can become entangled [44].

Considering this picture, quantum dots should appear as depicted in the layout in figure 5.13.C. Along the graphene pn junction interface, the interfering edge channel is naturally protected from the adjacent edge state by a closed loop. This may explain the macroscopic coherence length l_φ of $370\mu m$ observed at 20mK in our graphene valley splitter sample.

A dephasing protection

Finally, I will discuss some DC bias measurements in this configuration that corroborates the existence of a dephasing protection. Indeed, at finite DC bias, dephasing in GaAs/AlGaAs MZIs at $\nu = 2$, and in particular the lobe structure, can be described by taking into account the capacitive coupling between co-propagating edge channels. When a single edge channel is biased, oscillations visibility as a function of the applied bias voltage shows a lobe-type structure with almost equal widths of lobes. When the two edge states are biased, the central lobe should be approximately two times wider than side lobes [50].

In figure 5.14.A, T_{VI} is shown as a function of the magnetic field and the bias voltage applied on the upper left ohmic contact for the injection, which implies that only a single edge channel is biased. On the other hand, figure 5.14.B represents a similar measurement, but with this time a bias voltage applied on the upper right ohmic contact, and therefore with two biased edge channels. Strikingly, the lobe width is equal for both configurations, as visible in figure 5.14.C. This contradicts the expected larger lobe structure predicted for two biased edge channels, considering a capacitive coupling. This seems to indicate the absence of coupling between adjacent edge states, inducing a similar response for a bias applied on the right side or on the left side. These results are consistent with our picture of quantum dots formed by closed loops, and limiting the capacitive coupling between adjacent edge states.

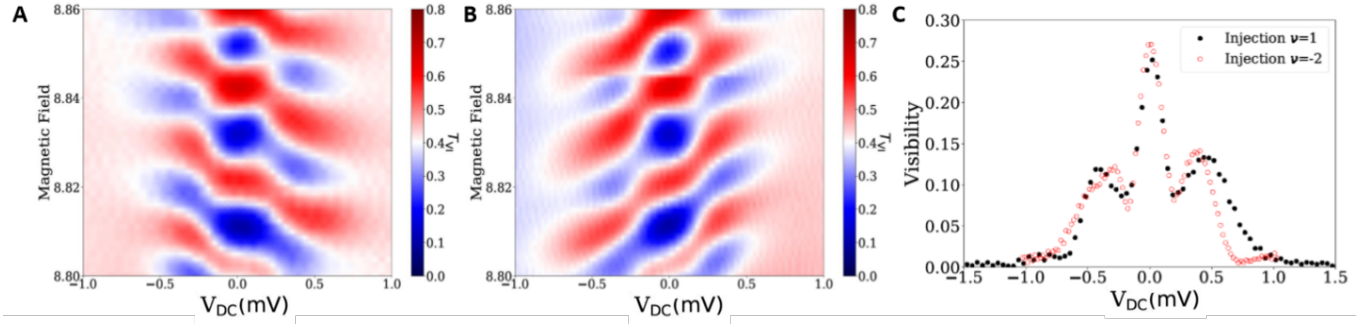

Figure 5.14: **Dephasing protection.** (**A**) T_{VI} as a function of the applied DC bias V_{DC} and the magnetic field for two biased edge channels. (**B**) T_{VI} as a function of the applied DC bias V_{DC} and the magnetic field for a single biased edge channel. (**C**) Measured visibility as a function of V_{DC} for both configurations.

Chapter 6

Spin waves and decoherence

In chapter 4, the DC bias and temperature measurements exhibited the exceptional coherence obtained in our graphene pn junction, with Aharanov Bohm oscillations persisting at energies up to twenty times larger than in GaAs/AlGaAs heterostructures. Consistently, as detailed in the previous chapter, the measured coherence length is also much longer, making graphene pn junction a good building block to achieve valleytronic devices, and quantum operations via valley-polarized states. On the way towards the new field of valleytronics, understanding the decoherence processes is a key point. A recent work by Wei et al. [83] made a step forward considering the comprehension of one of the main decoherence process, the so called magnons. Magnons are spin waves propagating through the bulk of a 2DEG in the quantum Hall regime, their absorption is a direct source of decoherence. Wei et al. managed to directly generate and detect magnons in an encapsulated graphene device in the quantum Hall regime. Hereafter, I will first present how they could experimentally control the magnons, then is detailed the study that we carried out about the decoherence, induced by magnons, using MZI.

6.1 Introduction to spin waves in graphene

6.1.1 Spin waves and ferromagnetic phases in graphene

Spin waves, or magnons, corresponds to collective excitations propagating through a magnetic system. Interestingly, in 2DEG in the quantum Hall regime, the interaction of electrons within the Landau levels gives rise to quantum Hall ferromagnetism, characterized by the appearance of peculiar magnetic phases. In graphene, the ground states of the $N = 0$ Landau level at one quarter filling ($\nu = -1$) and three-quarters filling ($\nu = 1$) correspond to a fully spin polarized quantum Hall ferromagnet [3][86][63][29] with an insulating bulk and spin polarized edge states. The nature of the ground state at filling factor $\nu = 0$ remains a matter of theoretical debate, according to Kharitonov's paper [42] different phases, represented in figure 6.1b, are possible : a Kékulé distorsion (KD) order, a ferromagnetic (F) order, a charge density wave order (CDW), and an anti-ferromagnetic order (AF). Those phases are competing following the phase diagram in figure 6.1a. The experimental study by Young et al. [89] ruled out the ferromagnetic order in their sample. Moreover, a few years later, A.F. Young [88] showed the existence of a quantum spin Hall state at $\nu = 0$, in the presence of a strong in plane magnetic field, exhibiting a transition

to a canted antiferromagnetic phase. Finally, when the Landau level is completely filled ($\nu = 2$) or completely empty ($\nu = -2$), the bulk is spin unpolarized and the magnons cannot propagate through it.

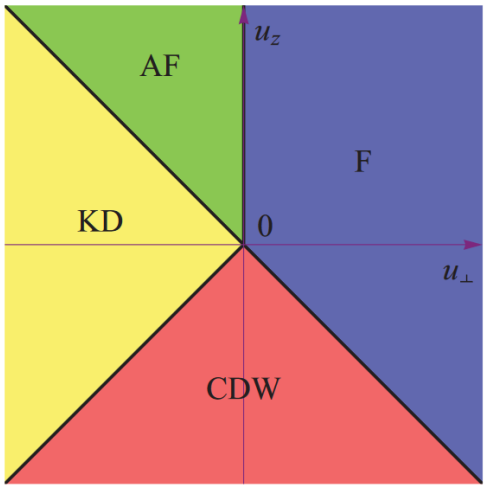

(a)

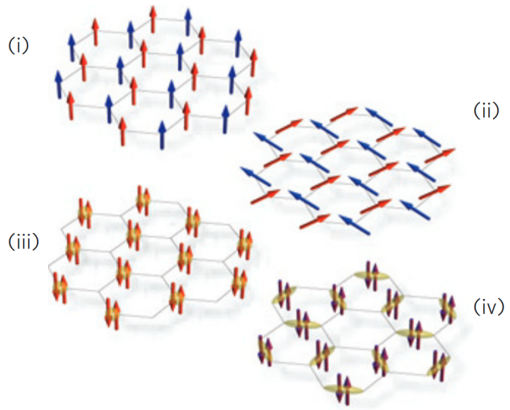

(b)

Figure 6.1: **Competing magnetic phases at $\nu = 0$ in graphene.** (**a**) Phase diagram of the $\nu = 0$ of the quantum Hall states minimizing the isospin anisotropy energy in the space of the anisotropy energies ($u_\perp$,u_z). Figure extracted from [42]. (**b**) Candidate quantum Hall ferromagnetic states at $\nu = 0$: the spin ferromagnet (i), the canted antiferromagnet (ii), the charge density wave order (iii), or Kékulé distorsion order (iv). Figure extracted from [89].

To conclude, the ferromagnetic phases present at filling factor $\nu = \pm 1$ in graphene constitute an ideal platform to investigate the propagation of spin waves, and are the building blocks of the experimental study of magnons in graphene carried out by Wei et al. [83], presented hereafter.

6.1.2 Experimental observation of spin waves in graphene

Wei et al. [83], in their pioneering experiment, achieved a direct electrical control of the generation and detection of spin waves in a graphene quantum Hall ferromagnet by imposing an imbalance in chemical potential between edge states of opposite spins. An optical micrograph of the sample used in their study is presented in figure 6.2.E. A graphene sheet connected to two leads is deposited on top of a global back gate. The central part of the sample is covered by a top gate, enabling to locally tune the filling factor in this region. In their study, they fixed the filling factor below the top gate at $\nu = 1$, i.e. a three-quarter filled N=0 Landau level corresponding to a fully spin-polarized quantum Hall ferromagnet. The surrounding regions are tuned to the non-magnetic fully filled Landau level $\nu = 2$, as depicted in the layouts of figure 6.2.A-C. As the spin degeneracy is lifted, the co-propagating edge channels have opposite spins : the inner one is spin down, whereas the outer one is spin up. A DC bias voltage is applied on the left ohmic contact,

imposing a chemical potential μ to the two outgoing channels, whereas the edge channels originating from the right ohmic contact are fixed at zero bias.

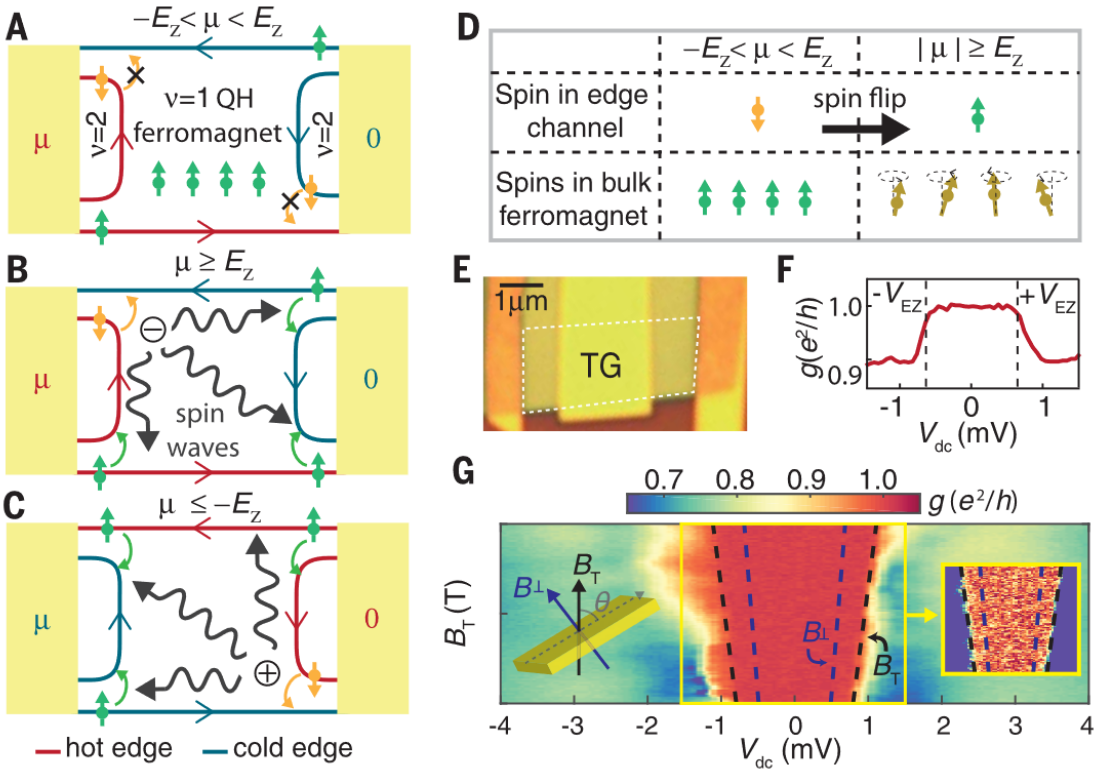

Figure 6.2: **Magnons in a quantum Hall ferromagnet. Figure extracted from [83].** (**A** to **C**) A chemical potential difference (μ) is applied between the left and right leads. Spin-up and spin-down polarization are denoted by the green and orange arrows, respectively. The central region is tuned to $\nu = 1$ and the adjacent regions to $\nu = 2$. (A) The chemical potential difference between the spin-up and spin-down edge channel is less than the Zeeman energy (E_Z) and scattering is suppressed. (B) $\mu \geq E_Z$: Electrons have enough energy to flip their spins and transfer spin angular momentum (magnons) into the bulk (at the encircled minus sign). (C) $\mu \leq -E_Z$: Magnons are generated at the location denoted by the encircled plus sign. (**D**) Bulk spin polarization before and after magnon creation, conserving the total spin angular momentum. (**E**) Optical micrograph of the device, graphene is outlined in white. TG, top gate. (**F**) Differential conductance as a function of the dc bias. (**G**) differential conductance as a function of bias and magnetic field. Blue dashed line: Zeeman energy calculated from the perpendicular magnetic field $B_\perp$. Black dashed line: Zeeman energy computed from the total magentic field B_T

In figure 6.2.F, the conductance through the sample is plotted as a function of the applied DC bias voltage V_{dc}. As expected, when $V_{dc} = 0$, the conductance is quantified and equal to e^2/h. However, when $|V_{dc}|$ reaches a threshold value $\sim 0.7mV$, the conductance deviates notably from the quantized value. They interpreted this limit value as a magnon

emission threshold corresponding to the Zeeman energy E_Z, i.e. the energy necessary to flip a spin. When the potential imbalance between a spin up and a spin down edge channel exceeds E_Z, at hot spots where the high-energy state (red on the layouts) meet the low-energy one (blue) electrons can be scattered by emitting magnons. As the bulk is a spin up ferromagnet, only magnons with a spin down angular momentum can propagate through it. No spin flip is possible in the absence of magnons, as it is the only way to conserve the angular momentum. This gives rise to three possible configurations for the system :

- In the case $-E_Z \leq \mu \leq E_Z$ (figure 6.2.A) : Spin flips are not allowed, therefore the scattering between the edge channels is suppressed.
- In the case $\mu \geq E_Z$ (figure 6.2.B) : The potential imbalance between the high-energy spin down edge channel (red) and the low energy spin up one (blue) exceeds the Zeeman energy. Therefore at the spot, denoted by the circled minus sign, where those two edge channels meet, spin-down electrons from the red state can flip their spin and relax into the blue state while emitting spin down magnons.
- In the case $\mu \leq -E_Z$ (figure 6.2.C): Same case as previously but inverting the high-energy and low-energy states, generating a magnon emission site at the circled plus sign location.

After propagating through the bulk, magnons can be absorbed via the reverse process of their emission. It is this magnon absorption that generates the deviations of the conductance from the quantized value above the Zeeman energy E_Z. Indeed, the emission processes at the plus or minus circled signs do not change the total potential incoming on the contacts.

In addition, Wei et al. noticed that when the filling factor of the whole graphene sheet is tuned to $\nu = 1$, the same deviations of the conductance are present as when the $\nu = 1$ region below the top gate is surrounded by two $\nu = 2$ regions. They interpreted this as a consequence of the local doping around the ohmic contacts, which creates a local $\nu = 2$ region around the contacts, emitting magnons via the same mechanisms as previously described.

Finally, they studied the magnon absorption signature via non-local voltage measurement using the sample sketched in figure 6.5.A. For this aim, a DC bias V_{dc} is applied between L_2 and L_3, and thanks to a superimposed AC voltage V_{ac} they can measure the resulting differential conductance dI/dV (with $V = V_{ac} + V_{dc}$). At the same time, the non local voltage signal $S_{NL} = dV_{NL}/dV$ induced by the magnon absorption, where V_{NL} is the voltage between L_4 and L_5, is recorded. In figure 6.5.B, the differential conductance g (in green) and the non-local signal S_{NL} (in purple) are plotted as a function of V_{dc}. Interestingly, at the same threshold value, corresponding to the Zeeman energy, a clear magnon signal appears on both curves. This indicates that magnons propagate through the whole sample, i.e. over a few microns.

6.2 Study of the decoherence induced by spin waves

The physical processes behind decoherence are usually difficult to explore experimentally, as a direct way to tune them is most of the time not accessible. One phenomenon

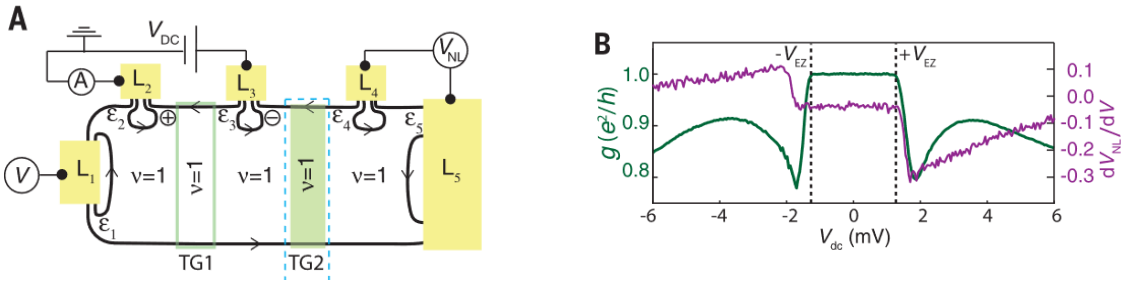

Figure 6.3: **Non-local voltage signal due to magnon absorption. Figure extracted from [83].** (**A**) Schematic circuit configuration for measuring a non-local voltage. The filling factor is fixed at $\nu = 1$. (**B**) Non-local signal $S_{NL} = dV_{NL}/dV$ (with $V = V_{ac} + V_{dc}$) in purple, superimposed to the differential conductance dI/dV between L_2 and L_3 in green. The sample is tuned at $\nu = 1$, the local doping around the contacts can generate magnons.

that may explain the decoherence observed at high DC bias, indicated for instance by the finite bias visibility in MZI experiments, is the emission of spin waves (or magnons). Interestingly, in a recent experiment, Wei et al. [83] presented a technique which enables to control the emission and detection of spin waves by electrical means using a quantum Hall ferromagnet formed in graphene at filling factor $\nu = 1$. In our valley splitter sample, the same quantum Hall ferromagnet regime is achievable, thus we can use the same process as Wei et al. to obtain a controlled emission of magnons. Thanks to this, our idea was to study the decoherence induced by magnons using a MZI as a quantum sensor. Hereafter, I will first show that we can emit magnons in our valley splitter sample using the same technique, based on the contact doping, as in [83]. Then is detailed a new magnon emission technique that we developed based on a chemical potential imbalance between edge states along a pn junction. Finally, is exposed the effect of the injected magnons on the coherence, using the visibility of Aharanov Bohm oscillations in a MZI, formed along a pn junction, as an indicator.

6.2.1 Spin waves in our valley splitter sample

Spin waves emission thanks to contact doping

The first step to study the effect of magnons on coherence in a MZI is to control the spin wave emission. As Wei et al., by tuning our valley splitter sample to $\nu = 1$ and imposing a DC bias on the contact, we can control the spin wave emission due to the local doping around the contact. I will detail hereafter how we implemented in practice this controlled emission technique.
The full schematic of the sample is shown in figure 6.4.a, the filling factors are fixed at $\nu_T = \nu_B = 1$. Experimentally, we directly have access, by two points resistance measurements, to the Hall resistance in the region covered by the top gate and in the region outside of it, as shown in figure 6.4.b. In our study, we fix the top gate and focus on a back gate voltage range where the filling factors ν_B and ν_T are well defined (and equal to one). At filling factor $\nu = 1$, spin wave emission occurs through locally doped regions in the vicinity of the metallic contacts where the filling factor is increased to $\nu = 2$.

This is depicted in the layout (figure 6.4.a) by localized edge states on each contacts. In order to generate spin waves, one has to apply a finite bias on one ohmic contact. This creates a chemical potential imbalance between edge channels incoming on a contact at two different locations : the contact where the DC bias is applied (e- location) and the following contact (e+ location). The emission takes place when the chemical potential imbalance reaches a threshold value, and its location depends on the sign of the voltage as shown in [83]. For positive (negative) voltage the emission occurs at the e+ ((e-)) site. After propagation in the insulating bulk, the magnon absorption leads to a change in chemical potential of the edge states which is detected with a lockin as a non local voltage signal dV_{nl}/dV where dV is the AC excitation applied at the same location as the DC bias. The net DC voltage V_{nl} due to spin waves absorption can be computed from :

$$V_{nl} = \frac{1}{e}\int_0^{eV_{DC,nl}} \frac{dV_{nl}}{dV}(\epsilon)d\epsilon$$

where $V_{DC,nl}$ is the DC bias used to generate spin waves.

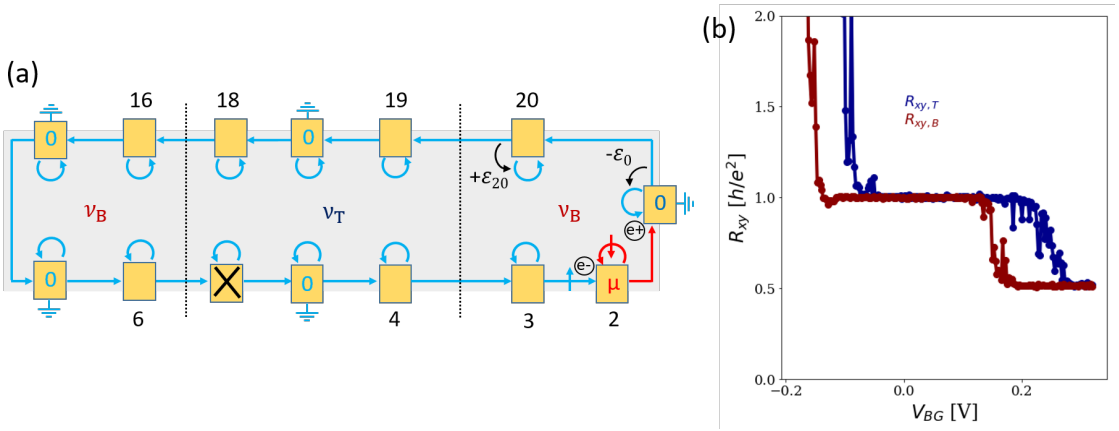

Figure 6.4: **Spin wave emission configuration of the valley splitter sample.** (**a**) Schematic representation of the device at $\nu_B = \nu_T = 1$, creating a spin up edge state. Doping near the metallic contacts increase locally the filling factor to $\nu = 2$ and is represented by a localized spin down edge state on each contact. The black cross denotes a non-working contact. A back gate covers all the sample and is used to tune both ν_B and ν_T, while the top gate covers only the middle part shown by the vertical dotted black lines and is used to adjust ν_T only. For positive (negative) voltage the spin wave emission site is represented by the encircled sign e+ (e-). Spin waves absorption lead to a change in chemical potential of the inner edge state ε_{20} and outer edge state ε_0. (**b**) Determination of the filling factors ν_T and ν_B by two points measurement as a function of back gate voltage.

In figures 6.5a and 6.5b, we show, at $\nu_B = 1$, the non local voltage $dV_{nl,20}/dV$ and $dV_{nl,18}/dV$ measured in contacts 20 and 18 as a function of the DC bias $V_{DC,nl}$ applied on contact 2. Ohmic contacts 20 and 18 are decoupled from 2 by a ground sink. At low voltage $V_{DC,nl}$, the non local signals are zero which confirms that there is no direct coupling between contacts 20 or 18 and the biased edge channel. However, a clear non local

voltage develops when $eV_{DC,nl} > E_Z + \delta$, where δ is a phenomenological density dependent term which is tuned by the back gate voltage. We interpret this signal as a non local voltage induced by spin wave absorption. Considering the magnon emission/absorption framework, the current conservation at ohmic contact 20 implies the following expression for the chemical potential μ_{20} :

$$\mu_{20} = \varepsilon_{20} + \mu_0 - \varepsilon_0 \tag{6.1}$$

where ε_0 (ε_{20}) is due to spin waves absorption at the ground (contact 20), and μ_0 corresponds to the chemical potential imposed by the ground sink. The absorption site ε_0 is closer to ohmic contact 2 than the second absorption site on ohmic contact 20 (see layout in figure 6.4.a). Therefore, we have $\varepsilon_0 > \varepsilon_{20}$, leading to a decrease of chemical potential, i.e. an increase of voltage.

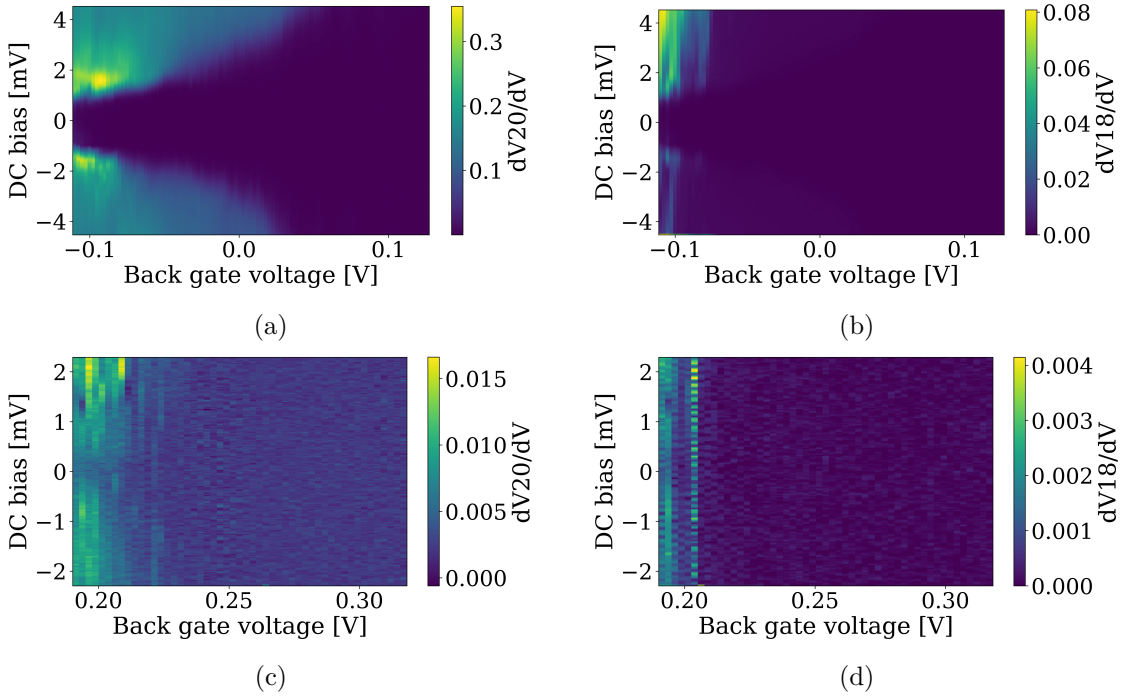

Figure 6.5: **Electrical emission of spin waves.** (**a**) Non local voltage signal in 20 as a function of DC bias $V_{DC,nl}$ in 2, when $\nu_B = 1$ is well defined. The magnons are propagating over the $5\mu m$ distance between 20 and 2. The voltage threshold for spin waves emission is $eV_{DC,nl} > E_Z + \delta$ where δ is density dependent and can be tuned with the backgate voltage. (**b**) Non local voltage signal in 18 as a function of DC bias $V_{DC,nl}$ in 2, when $\nu_B = 1$. This implies that spin waves can propagate over at least $10\mu m$. (**c**) Non local voltage signal in 20 as a function of DC bias $V_{DC,nl}$ in 2, when $\nu_B = 2$. The signal is much weaker. The remaining signal might be due to density fluctuations in the border of the $\nu_B = 2$ plateau which enable spin waves emission by locally decreasing the filling factor. (**d**) Non local voltage signal in 18 as a function of DC bias $V_{DC,nl}$ in 2, when $\nu_B = 2$.

Interestingly, contact 20 is located at $5\mu m$ from contact 2, while contact 18 is at $10\mu m$.

Therefore, our interpretation, of a non-local signal created in 18 and 20 by the absorption of magnons emitted from 2, implies that magnons can propagate over a distance of at least $10\mu m$ in the graphene bulk at $\nu = 1$. Comforting this interpretation, when the filling factor ν_B is tuned to 2, giving rise to a non-magnetic phase where magnons should not propagate, we observe an important decrease of the non local signal in 20 and 18, as shown in figures 6.5c and 6.5d. The very weak non local voltages detected are probably due to density fluctuations on the border of the $\nu_B = 2$ plateau, enabling spin waves emission and detection by locally decreasing the filling factor to $\nu_B = 1$.

To summarize, we showed here that by tuning the filling factor to $\nu = 1$, we can control the spin wave emission in our valley splitter sample. Applying a DC bias on a contact allows us to manage the magnons emitted thanks to the natural contact doping. Analogue experiments were carried out in the hole regime, i.e. at filling factor $\nu = -1$, exhibiting the absence of spin wave absorption in this regime, as detailed in the appendix A.4. In the following, I will present an experimental study of the magnon propagation depending on the filling factor.

Study of spin wave propagation depending on the filling factor

Our goal here is to study the magnon propagation depending on the filling factor. For this aim, we use a similar set up as previously (see figure 6.6.a) : the filling factor outside of the top gate is $\nu_B = 1$, magnons are emitted by applying a DC bias $V_{DC,nl}$ on contact 2, and we measure the non local voltage in 18 and 19. However, this time, we fix the back gate voltage at $V_{BG} = -0.1V$, while we modulate the filling factor under the top gate ν_T through the voltage V_{TG} applied on it. The two point Hall resistance measurements, under the top gate and outside of it, as a function of top gate voltage are presented in figure 6.6.b. Consistently, the filling factor outside of the top gate ν_B does not depend on the top gate voltage and is equal to one. On the other hand, ν_T varies a lot with the top gate voltage : the green dashed lines delimit the top gate range for which $\nu_T = 1$, the region after the blue dashed line corresponds to $\nu_T = 2$.

Let's now study, on the same top gate range, the non local voltage in contact 19 as a function of $V_{DC,nl}$. The resulting color map is plotted in figure 6.6.c. A ground sink between 2 and 19 insures that no charge current directly flows from 2 to 19, and indeed experimentally there is no signal in 19 at $V_{DC,nl} = 0$. At finite bias, above a threshold value, we observe a signal that we interpret within the framework of spin wave absorption, as detailed now. At $\nu_T = \nu_B = 1$, the current conservation on contact 19 implies that its chemical potential μ_{19} verifies :

$$\mu_{19} - \mu_0 = \varepsilon_{19} - \varepsilon_{0,19} \tag{6.2}$$

where $\varepsilon_{0,19}$ (ε_{19}) is due to spin waves absorption at the ground (contact 19), and μ_0 is the chemical potential imposed by the ground sink. As the ground is closer to the spin wave emission site (contact 2) than contact 19, the absorption coefficients verify $\varepsilon_{0,19} > \varepsilon_{19}$, leading to a decrease of chemical potential and thus an increase of voltage.

In the $\nu_\mathrm{T} = 2$ region the situation is different due to the reflection of one of the two edge states below the top gate at the right top gate border, therefore, we have:

$$\mu_{19} - \mu_0 = (-\varepsilon_{0,19} + \varepsilon_c)/2 \tag{6.3}$$

where ε_c is due to spin wave absorption at the site denoted by the circled C in figure 6.6.a, corresponding to the intersection between the lower graphene edge and the top gate. A net absorption voltage is observed.

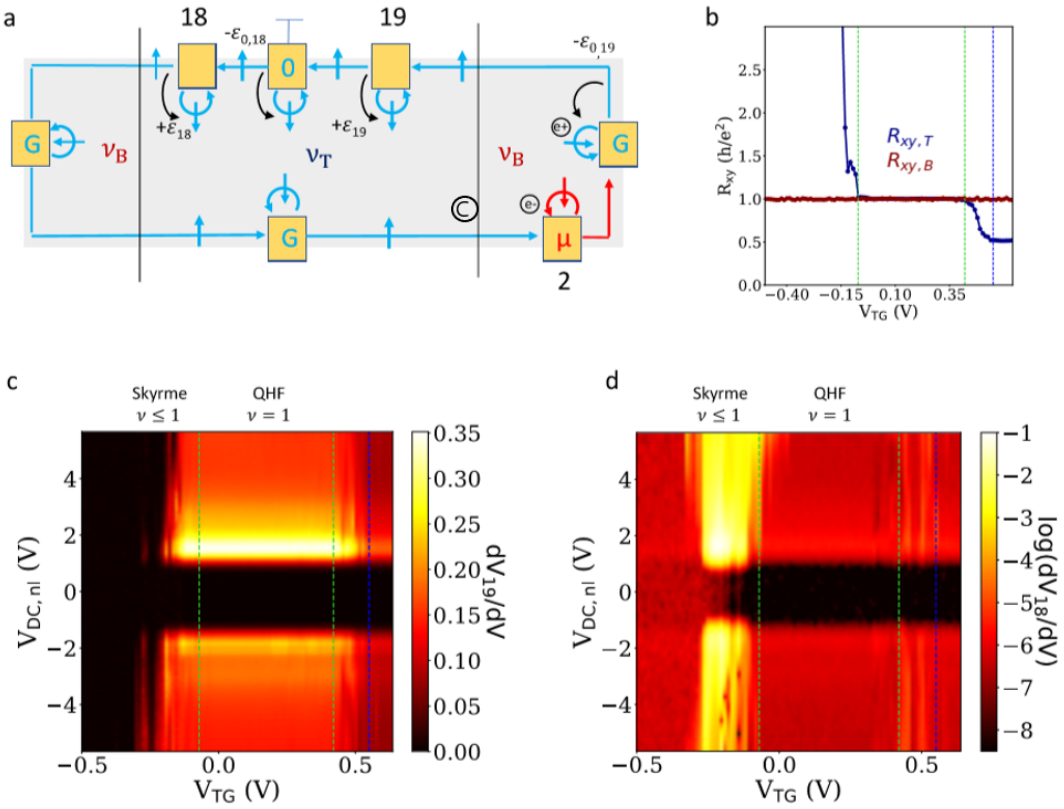

Figure 6.6: **Spin wave propagation in the fully spin polarized QHF and in the Skyrme ground state.** (**a**) Schematic representation of the device at $\nu_B = \nu_T = 1$. The DC voltage $V_{DC,nl}$ is applied on contact 2. For positive (negative) voltage the spin wave emission site is represented by the encircled e+ (e-) sign. Spin wave absorption leads to a change of the chemical potential of the edge states ε. The circled C denotes another magnon absorption site that appears when $\nu_T = 2$. (**b**) Determination of the filling factors ν_T and $\nu_B = 1$ by two points measurement as a function of top gate. Green vertical dotted lines delimit $\nu_T = 1$, and the blue dotted line the beginning of $\nu_T = 2$. (**c**) Non local voltage signal on contact 19, $\frac{dV_{19}}{dV}$, as a function of DC bias $V_{DC,nl}$. Spin waves are emitted when $eV_{DC,nl} > E_z + \delta$. The detection signal is high for $\nu_T = 1$ and low for $\nu_T \leq 1$. (**d**) Non local voltage signal in 18 as a function of DC bias. Here the situation is reversed, the detection signal is high for $\nu_T \leq 1$ and low for $\nu_T = 1$. Spin waves are deviated from 19 to 18 when the ground state of the system changes from the fully spin polarized QHF to the Skyrme ground state at filling factors $\nu_T \leq 1$.

For $\nu_T \geq 1$, we expect and observe experimentally the same trend for the non local voltage in 18, as visible in figure 6.6.d. However, for $\nu_T \leq 1$ we observe in 19 a decrease of the non local voltage compared to the $\nu_T = 1$ region, whereas, on the contrary, in contact

18 the non local voltage is larger for $\nu_T \leq 1$ than for $\nu_T = 1$. This could be explained by the peculiar spin order at $\nu_T \leq 1$. Indeed, due to the usually large ratio between the exchange $E_X = \frac{e^2}{\epsilon l_B}$ and the Zeeman energy $E_Z = g\mu_B B$ in quantum Hall systems, the ground state at $\nu = 1 \pm \varepsilon$, can consist in smooth spin texture which involves many spin flips to minimize the exchange interaction rather than a single spin flip. These topological defects in the spin orientation are known as skyrmions. A recent experiment [93] reported in graphene the existence at filling $\nu \leq 1$ of solids of quantum Hall skyrmions, also called Skyrme ground state. The phenomenon that we observed at $\nu_T \leq 1$ seems to indicate that the Skyrme ground state deviates spin waves.

A new way to emit spin waves using a biased pn junction

In the previous sections, I showed that we can control, in our valley splitter sample, the emission of magnons, thanks to an unintentional local doping due to the metallic contact as in [83]. This emission mechanism cannot be used in samples with electrostatically doped contacts [69], where the graphene region along the contact is set at high filling factor. These samples are of outmost importance to probe the spin physics of the fractional quantum Hall effect. Hereafter I will detail another approach that we developed to emit spin wave thanks to a pn junction, which enables to overcome the limitations due to the use of the contact doping.

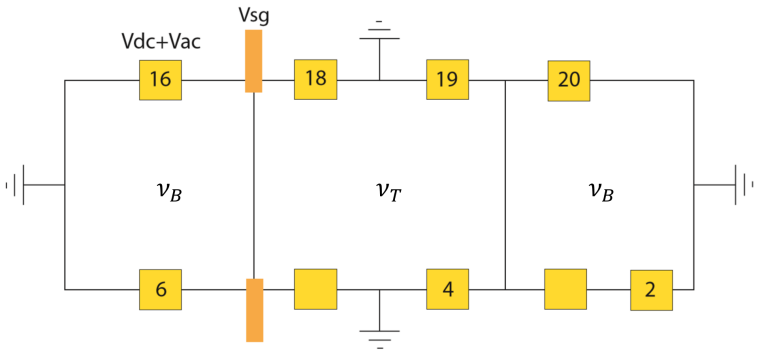

Figure 6.7: **Schematic representation of the valley splitter sample in the spin wave emission configuration.** The filling factors are fixed at $\nu_T = 1$ and $\nu_B = -2$. Two MZIs are formed on both sides of the top gate. A DC bias is applied on ohmic contact 16 and superimposed to an AC lock-in signal. Magnons are emitted from the left pn junction where the transmissions at its ends can be controlled thanks to side gates.

In order to carry out this study, we used the pn junction formed on the left side of the top gate, where the side gates are located (see layout in figure 6.7). As in chapter 3, the sample is set in a MZI configuration, but this time with $\nu_B = -2$ and $\nu_T = 1$. Therefore, two edge states of opposite spin, $|\downarrow, T_L\rangle$ and $|\uparrow, T_L\rangle$, are incoming on the pn junction from the top left ohmic contact 16 (see figure 6.8). From the top right ohmic contact 18, only a single spin down edge state $|\downarrow, T_R\rangle$ is incoming. In the absence of DC bias, the current carried by the spin up state $|\uparrow, T_L\rangle$ is conserved all along the junction due to the large energy cost to flip a spin, and one half of the current directly goes to the bottom left ohmic contact 6. On the other hand mixing between the same spin state is

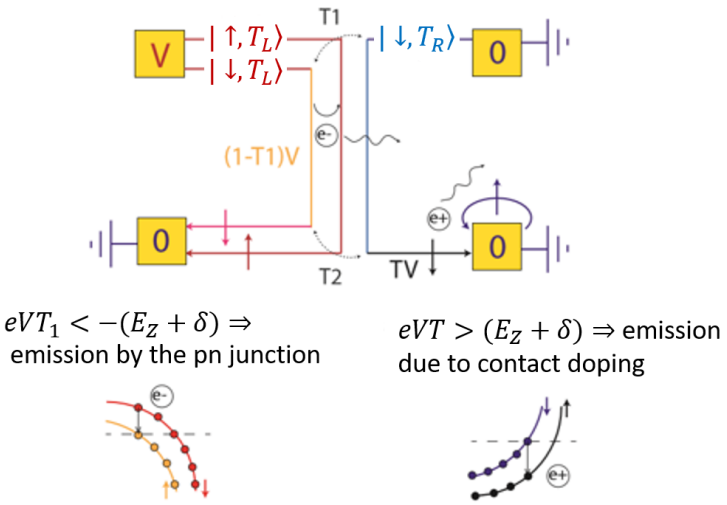

Figure 6.8: Schematic of the spin wave emission mechanism at $\nu_B = -2$ and $\nu_T = 1$. For a negative bias, electrons can relax into the colder edge state along the pn junction (emission site e-) by emitting a spin wave in the insulating bulk. For a positive bias, magnons can be emitted from the site e+ at the ground after the junction. The absorption of the emitted spin wave leads to a non local voltage signal.

allowed at the two ends of the pn junction where the graphene physical edge can provide the large momentum transfer necessary to go from one valley to another : the two ends of the pn junction act as beam splitters. Along the junction the two spin down states form co-propagating interfacial states which are split again at the bottom end of the pn junction, generating a MZI. As detailed in chapter 3, by tuning the bias applied on the top and bottom side gates, we can control the transmission T_1 at the entrance of the MZI and T_2 at its output. For the study of magnon generation thanks to a pn junction, a DC voltage V_{DC} and a lock-in AC excitation V_{AC} are applied on ohmic contact 16, such that the left pn junction is biased.

The emission mechanism of the pn junction is described in figure 6.8. After the first beam splitter of transmission T_1, the bias of the inner edge state in the $\nu = -2$ region is $V = (1 - T_1)V_{DC}$, whereas the outer edge state is at the potential V_{DC}. Emission of spin waves occurs for negative bias when the potential imbalance between the inner and outer edge states on the p-side exceeds the Zeeman energy, giving rise to the following condition : $|eT_1V_{DC}| > (E_Z + \delta)$. For positive bias, emission occurs after the pn junction at the ground due to contact doping in the $\nu_T = 1$ region, when $eTV_{DC} > E_Z + \delta$ where T is the global transmission through the pn junction.

In figure 6.9a, we show, for three different values of V_{sg1}, the non local voltage due to spin wave absorption on contact 20, from which the net voltage V_{nl} is computed and shown in figure 6.9b. For positive and negative DC voltages V_{DC}, the emission threshold changes with the bias applied on the upper side gate V_{sg1}, as indicated by the vertical dashed line in figure 6.9a (for $V_{DC} > 0$). The voltage V_{sg1} modulates the transmission T_1 (and therefore T), thus the dependence of the threshold value on V_{sg1} could be explained

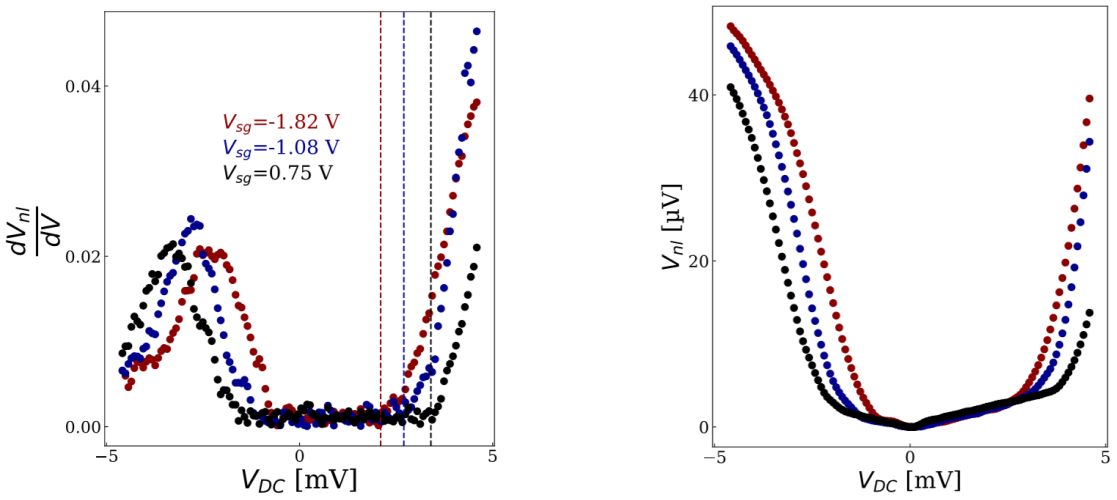

(a) (b)

Figure 6.9: **Spin waves emission across a pn junction.** (**a**) Non local voltage signal on contact 20 as a function of DC bias for different voltage applied on the upper side gate. Spin waves are detected, at positive bias when $eTV_{dc} > E_Z + \delta$ and at negative bias when $eT_1V_{dc} < -(E_Z + \delta)$, the transmission coefficients are modulated with the side gate. The emission threshold for positive bias is shown with the dashed line. (**b**) Computed non local voltage V_{nl} due to spin waves absorption as a function of DC bias.

within our model, however further and more quantitative investigations are needed.

To summarize, thanks to this new method, one may control the magnon emission via a biased pn junction, without using the natural doping of ohmic contacts. This could be really useful when using samples with highly doped contact leads, for instance to study the effect of magnons in the fractional quantum Hall regime.

6.2.2 Effect of spin waves on MZI

In the valley splitter sample at $\nu = 1$, we can achieve as Wei et al. [83] a controlled emission of magnons by applying a DC bias on a ohmic contact, but also thanks to new method that we developed based on a biased pn junction. Interestingly, we can set our sample in a configuration in which a magnon source is in the vicinity of a pn junction tuned in the MZI regime. This enables us to directly investigate the effect of magnons on the coherence, by measuring the visibility of Aharanov-Bohm oscillations as function of the magnon emission. First, I will detail how we coherently detect magnons thanks to a MZI, and in particular the correlations that we observed between the magnon emission and the visibility. In a second part, is exposed a study dealing with a direct measurement of the magnon effect on the MZI phase. In what follows, we used magnons emitted thanks to the contact doping, an analogue study was carried out with magnons generated thanks to a biased pn junction and is presented in appendix A.5.

Coherent detection of magnons with a MZI

For this study, we want to use a MZI as a quantum sensor to measure the decoherence induced by magnons. Therefore, we need to have on the same sample a MZI and a magnon source. To do so, the filling factors were tuned at $\nu_B = 1$ and $\nu_T = -2$, generating a MZI, as depicted in figure 6.10.a, along the top gate border with side gates. The dephasing ϕ imposed between the two paths of the interferometer corresponds to the Aharanov-Bohm phase, which can be tuned linearly thanks to the magnetic field B. On the other hand, a DC bias is applied on contact 16 in order to generate magnons.

In figure 6.10.b, we show the non local voltage signal, dV_{18}/dV, measured in 18 due to a lock-in excitation in 16, dV, as a function of DC bias applied in 16, $V_{DC,nl}$. Due to the chirality of the quantum Hall states, no current should flow from contact 16 to 18. Indeed, experimentally, at $V_{DC,nl} = 0$, we observed a zero non local voltage. When the DC bias is decreased, this non local voltage dV_{18}/dV is zero up to a negative threshold value $\sim -1mV$, where a clear signal appears. For positive voltage, a threshold is also present around the same absolute value $\sim 1mV$, even though the increase in the signal is less pronounced. We interpret this as an effect of magnon absorption on contact 6 at the entrance of the MZI. Indeed, when the DC bias reaches a threshold value, given by $|eV_{DC,nl}| > E_Z + \delta$, spin waves are electrically emitted from contact 16 or the ground following it. The emitted magnons propagate through the $\nu_B = 1$ bulk up to contact 6, where they are absorbed. This leads to a decrease in chemical potential of the lower edge state which enters in the interferometer and is detected in 18. Considering an absorption ε_0 on contact 6 (which is fixed at a chemical potential μ_0), the spin up edge channel incoming on contact 18 is at the potential $\mu_0 - T\varepsilon_0$ (with T the total transmission through the MZI), whereas the non-interfering spin down edge channel (also incoming on 18) stays at the potential μ_0. If one notes μ_{18} the chemical potential of the edge channels leaving contact 18, the current conservation on 18 leads to :

$$\mu_{18} - \mu_0 = -T\varepsilon_0/2 \tag{6.4}$$

In addition, this non local signal dV_{18}/dV, appearing above a threshold value, oscillates with the magnetic field. In the model developed above, these oscillations can easily be interpreted as Aharanov-Bohm oscillations.

In order to investigate the magnon effect on the coherence, we applied an additional lock-in excitation at a different frequency on contact 6 and measured the transmission T_{VI} through the interferometer (via contact 18). In figure 6.10.c, the transmission T_{VI} is plotted as a function of the DC bias applied in 16, $V_{DC,nl}$. Oscillations with the magnetic field, corresponding to interference fringes, are clearly visible. The visibility of the interference is computed over the oscillations and plotted in blue in figure 6.10.d, together with the averaged electric signal due to spin waves absorption (red). While the visibility remains constant at low voltage, it quickly decreases above the threshold of spin waves emission (black dashed lines in figure 6.10.d), $eV_{DC,nl} = E_Z + \delta$, where the absorption signal is detected. The correlation between the visibility decay and the magnon emission leans towards a dephasing effect of magnons. In addition, the slower decay observed for positive DC bias compared to the negative side is consistent with an emission site e+ (for $V_{DC,nl} > 0$) further from the pn junction than the site e- (for $V_{DC,nl} < 0$).

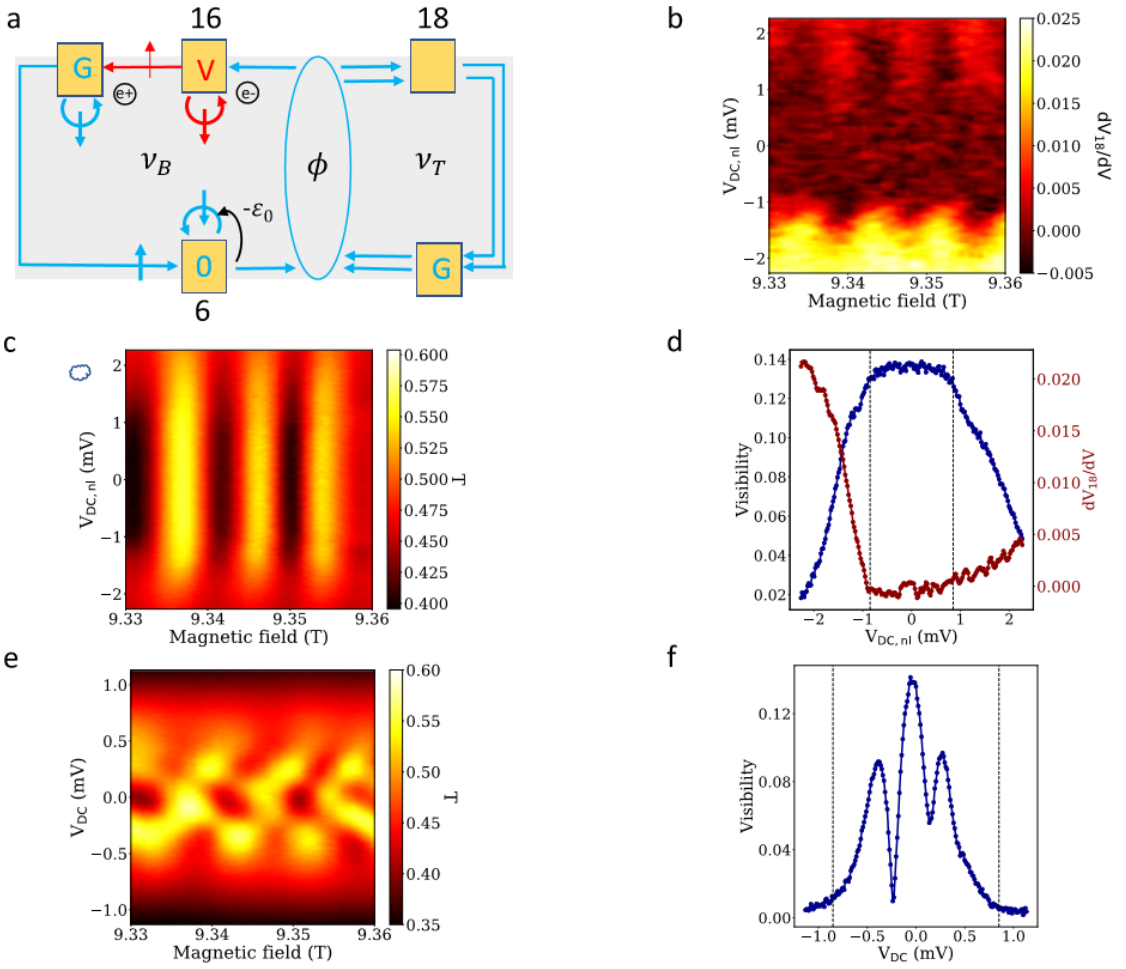

Figure 6.10: **Coherent detection of spin waves with an electronic interferometer.** (**A**) Schematic representation of the device at $\nu_B = 1$ and $\nu_T = -2$. The DC voltage $V_{DC,nl}$, is applied in 16 to emit spin waves on the interferometer without charge current. Spin wave absorption in 6 leads to a reduction of the chemical potential of the lower edge state by $-\varepsilon_0$. (**B**) Non local voltage signal on contact 18, from a lockin excitation applied in 16, as a function of DC bias $V_{DC,nl}$, applied in 16. Spin waves are emitted when $eV_{DC,nl} > E_Z + \delta$. The non local voltage oscillates with the flux ϕ which modulates the interferometer transmission T. (**C**) Interference as a function of $V_{DC,nl}$ in 16. The transmission is measured in 18 from a lockin excitation in 6. (**D**) Visibility (blue curve) and non local voltage signal dV_{18}/dV averaged over the magnetic field span (red curve), as a function of $V_{DC,nl}$ applied in 16. At the emission threshold shown by the vertical dotted lines the non-local voltage is detected and the visibility decreases. (**E**) Interferences as a function of DC bias applied in 6 directly on the interferometer, V_{DC}. (**F**) Visibility as a function of DC bias in 6. The visibility envelope lies within the spin wave emission threshold shown by the vertical dotted lines.

We further investigate the MZI oscillations dependence on local DC bias V_{DC}, i.e. a DC bias directly applied on contact 6. The result is plotted in figure 6.10.e, and present

a characteristic check board pattern. The corresponding visibility, shown in figure 6.10.f, presents a lobe structure, which completely vanishes around $1mV$. Therefore, the visibility envelope lies within the observed energy scale for the magnon emission threshold, indicating that in the case of a local bias another mechanism of decoherence dominates below $1mV$. However, the decoherence effect of magnons could explain the absence of extra side lobes above the threshold energy $\sim 1meV$.

To conclude, the experimentally measured coincidence of the visibility decay and the magnon signal (figure 6.10.d) in the case of a non local DC bias seems to indicate that the coherence in electronic MZIs in graphene is limited by magnons for DC bias above the threshold energy. In the last section, we substantiate this claim thanks to a direct measurement of magnons dephasing effect above the threshold bias.

6.2.3 Aharanov-Bohm phase and magnons

In the previous part, the measurements were achieved at a back gate voltage $V_{BG} = -0.13V$. Strikingly, as shown in figure 6.11.a, when we set the back gate at $V_{BG} = -0.15V$, using the same set up as in figure 6.10.a (with a non local voltage $V_{DC,nl}$ applied in 16), we observed a strong phase shift of the MZI interferences at the threshold voltage for spin wave emission, i.e. $e|V_{DC,nl}| \geq E_Z + \delta$. For each DC bias voltage $V_{DC,nl}$ we computed the phase of the oscillations, taking a zero phase reference at $V_{DC,nl} = 0$; the result is plotted in figure 6.11.b. The phase is almost constant and equal to zero for low non local voltages $|V_{DC,nl}| \leq 1mV$, but above this threshold the phase changes strongly. Indeed, for $V_{DC,nl} < 0$, the phase goes from 0 rad at $V_{DC,nl} \approx -1mV$ to almost -3 rad at $V_{DC,nl} \approx -2mV$. Considering positive DC bias, the dephasing effect is less pronounced, the phase is around -1.5 rad at $V_{DC,nl} \approx 2mV$. This is consistent with an emission site e+ for $V_{DC,nl} > 0$ further away from the pn junction than the site e- for $V_{DC,nl} < 0$. In the phase plot (figure 6.11.b), we added the non local signal in 18, dV_{18}/dV, averaged over the magnetic field range. Interestingly, the resulting signal exhibits the same threshold in $V_{DC,nl}$ as the phase. Indeed, for $|V_{DC,nl}| \leq 1mV$, the dV_{18}/dV is constant and equal to zero, indicating that no magnon is absorbed in 6, explaining the absence of dephasing on this bias span. However, above the threshold a clear non local signal appears, due to the magnon absorption; the signal is stronger for negative than for positive voltages, consistently with the asymmetry in phase.

Naively, one could think that this phase shift originates from a chemical potential increase on the edge channel incoming on the MZI, due to magnon absorption on contact 6. In order to check this, we computed the DC voltage V_{nl} induced on contact 6 (18) at the input (output) of the MZI, resulting from this phenomenon, thanks to the non local signal dV_6/dV (dV_{18}/dV) in 6 (18), via the following formula :

$$V_{nl} = \frac{1}{e}\int_0^{eV_{DC,nl}} \frac{dV_{nl}}{dV}(\epsilon)d\epsilon$$

The resulting DC voltages V_{nl} are plotted in figure 6.11.c, in red for the output bias measured in 18 and in orange for the input bias measured in 6. The amplitude of these DC voltages induced on the MZI by magnon absorption is less than 40μV. Now we look at the MZI response when the DC bias, V_{DC}, is directly applied on the interfering edge states, i.e. on contact 6, to check if such voltage can generate a similar phase shift.

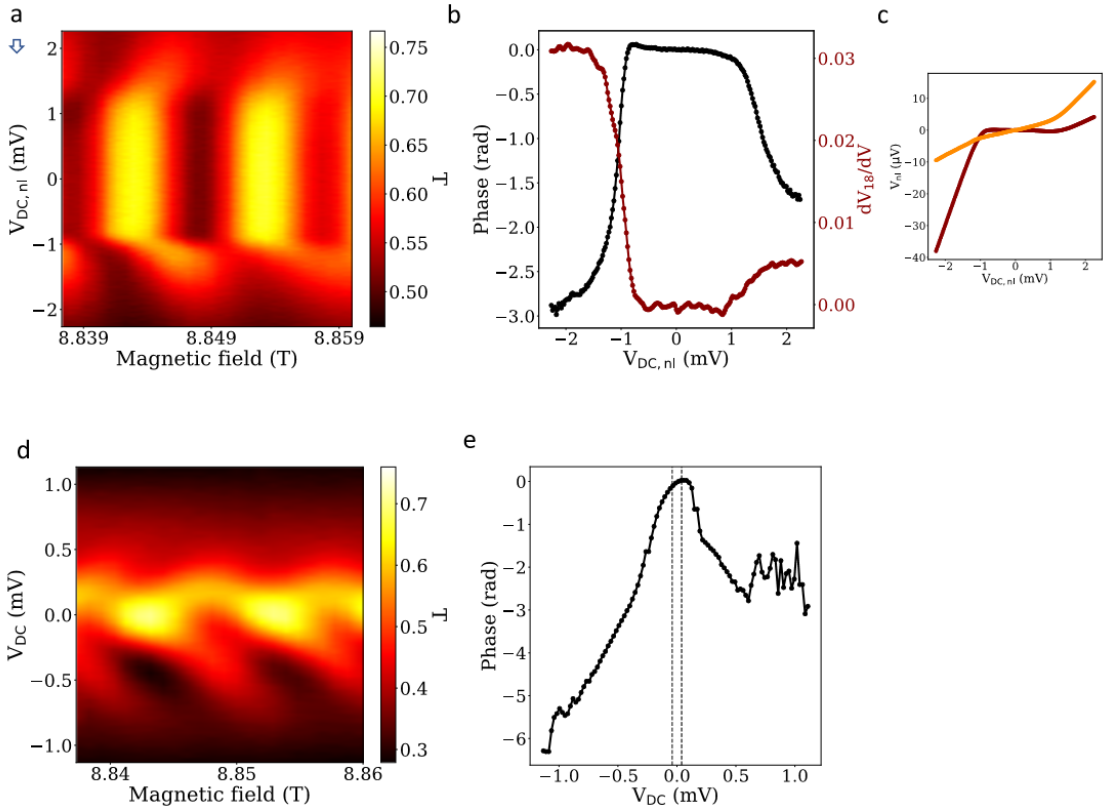

Figure 6.11: **Spin waves induced flux modulation.** (**a**) Interferences as a function of DC bias, $V_{DC,nl}$, applied in 16. (**b**) Phase and averaged non local voltage signal over the oscillations, as a function of DC bias. The phase of the interferences shows a strong modulation at the spin wave emission threshold. (**c**) DC non local voltage V_{nl} induced in contacts 6 (orange) and 18 (red) by the magnons emitted in contact 16, and computed from the non local voltage signals $\frac{dV_{nl}}{dV}$. The DC voltages induced by magnon absorption are small : $V_{nl} < 40\mu V$. (**d**) Interferences as a function of DC bias, V_{DC}, applied on the interferometer arm in 6. (**E**) Phase as a function of the local DC bias in 6. The vertical dotted lines are drawn at $V_{DC} = \pm 40\mu V$.

Figure 6.11.d shows the AB oscillations as a function of local DC bias, V_{DC}, from which the phase, in figure 6.11.e, is extracted. The phase shift at $\pm 40\mu V$ in local DC bias, shown by the vertical dotted lines, corresponds to a few tenth of radiant and thus is negligible compared to the phase shifts observed with the non local bias measurement, where the dephasing can reach π. Therefore, the dephasing induced by magnons is not due to the trivial effect of the chemical potential increase generated by magnon absorption on the input edge channel. We think that it is generated by the itinerant electric dipoles carried by spin waves at $\nu = 1$, modulating the phase of the interference. This assumption needs further studies to support it.

We now look at the MZI response to a DC bias applied in 16, $V_{DC,nl}$, for different values of the back gate voltage to probe the responses at $\nu = 1$, i.e. in the quantum Hall ferromagnet configuration, and at $\nu \leq 1$. In figure 6.12.a, we show the determination of

the filling factor together with the non local voltage signal dV_{18}/dV at zero DC bias. The different back gate voltage values where the MZI response has been studied are indicated by the following symbols : square, triangle, arrow... Note that the back gate voltage values indicated by the cloud and the arrow, also in the quantum Hall ferromagnet, are shown in figure 6.10 and 6.11, respectively; and additional data, for the star symbol, are presented in appendix A.6. With these different measurements, we observed a variety of phase behaviors with $V_{DC,nl}$ depending on the back gate tuning, whose understanding would require further investigations.

To conclude, in this chapter, we have shown that spin waves can be generated on demand in our valley splitter sample at $\nu = 1$ thanks to the local doping around ohmic contacts. In addition, by combining a magnon source and a MZI, we have shown that the decay of the oscillations visibility with the non local DC bias is correlated to the magnon emission, which indicates that it represents the dominant decoherence process in this configuration. Finally, the visibility and the phase signals show a sharp, electrically controlled, variation at the emission threshold, which opens interesting perspectives for detection schemes.

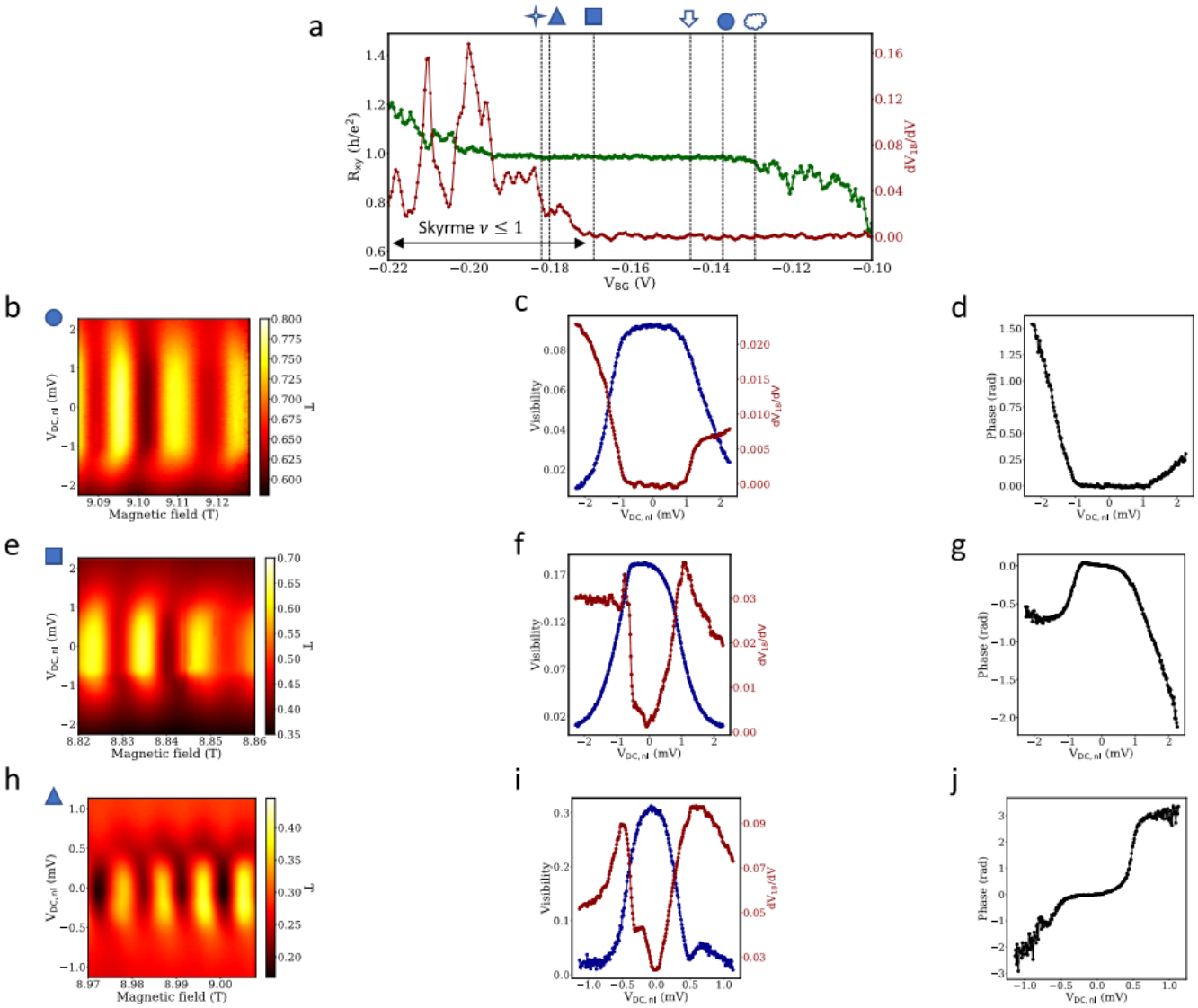

Figure 6.12: **Probing interference dependence on spin waves for different back gate values.** (**a**) Determination of the filling factor ν_B and non local voltage signal measured at zero DC bias. Symbols show the back gate values where the MZI response has been studied. (**b-d**) **Back gate voltage fixed at : $V_B = -0.14V$** (circle symbol, in the QHF phase). In (b), we plot the interferences as a function of DC bias, $V_{DC,nl}$. The corresponding visibility is traced in (c), with the non local voltage signal transmitted through the MZI, as a function of bias. Finally, the phase of the oscillations are represented in (d) as a function of the DC bias. It exhibits a positive variation at the spin wave emission threshold. (**e-g**) **Same study as in (b-d), but at $V_B = -0.17V$** (square symbol in the QHF phase). Here the phase (g) as a function of bias shows a negative variation at the spin wave emission threshold. (**h-j**) **Same study as in (b-d), at $V_B = -0.18V$** (triangular symbol) in the Skyrme ground state. Phase (j) as a function of the DC bias shows a negative variation at the spin wave emission threshold for negative voltages and a positive variation at the spin wave emission threshold for positive voltages.

Conclusion

The development of electron quantum optics, an emerging field based on the reproduction of quantum optics experiments but using electrons, leads to interesting perspectives, in particular for quantum computations. Up to now, the experiments carried out in semi-conducting GaAs/AlGaAs heterostructures exhibited the possibility to encode information in the charge or the spin of an electron, but strong decoherence in these systems implies a great weakness of these quantum states, which survives only below a temperature of 100mK and an electrical bias of $40\mu V$. This fragility makes it difficult to achieve entangled states and limits the development of complex quantum computations. In 2005, the discovery of a novel material, graphene, opened new prospects with on one hand the prediction of a larger phase coherence, and on the other hand the existence, in addition to the spin, of a new degree of freedom, called the valley. The purpose of this PhD thesis is to investigate the possibility to encode information in the valley degree of freedom in graphene, and to study the coherence of the associated valley-polarized electronic quantum states.

For this aim, we used, in the quantum Hall regime, a graphene pn junction, formed thanks to gates deposited on top of a stack composed of a graphene sheet encapsulated between two Boron Nitride (BN) crystals. The first part of the project was to develop the stacking process of crystals, then to design the sample geometry corresponding to our study, and finally to develop and achieve the nano-fabrication of the sample. I participated with M. Jo to the refinement of the stacking set-up and procedures developed by F. Parmentier, giving rise to a reliable stacking procedure. Concerning the sample nano-fabrication, the achievement of good quality ohmic contacts was a real challenge. After long technical developments, we converged to a fabrication process enabling us to obtain ohmic contacts with a low-resistance (of a few hundreds ohms) in a repeatable way. In order to obtain an electrostatic control over the valley polarization, different sample geometries were tested. The final sample is composed of a $1\mu m$ long pn junction, with ohmic contacts on the p and n sides, and local gates (called side gates) — isolated from the other gates by an extra BN — deposited at the intersections between the pn junction and the graphene physical edge.

Thanks to the sample achieved, we studied experimentally the coherent manipulation of the valley polarization of incoming electrons on a pn junction in the quantum Hall regime, with filling factors fixed at $\nu_n = 2$ on the n-side and $\nu_p = -1$ on the p-side. In this configuration, two edge states of opposite spins are incoming on the junction from the n-side, while a spin down edge state is incoming from the p-side. Due to the mixing of the two spin-down edge channels at the intersection between the graphene physical edge and the pn junction, two hybridized interfacial states, with opposite valley polarization,

are formed on each side of the junction. These interfacial states mix again at the bottom end of the pn junction, where it meets again the graphene physical edge. By tuning the voltage applied on the side gates, i.e. by locally tuning the filling factor of the graphene below them, we demonstrated a full control over the valley polarization of the output state when injecting electrons from one of the spin down edge states. In addition, the interface states form a closed loop, and thus the magnetic flux through the area enclosed generates an Aharanov-Bohm phase between the two paths. Associating the electrostatic control of the side gates to a tuning of the Aharanov-Bohm phase via the magnetic field, we showed that it is possible to coherently manipulate the valley of an electronic state almost over the whole Bloch sphere, in a valley representation.

Afterwards, the coherence of the quantum states was investigated thanks to Mach Zehnder interferometry, by measuring the interferences dependence on the chemical potential of incoming electrons and on the temperature of the system. The quantum states formed are exceptionally steady, they persist up to 1.5K and 1mV, in other words at energies 20 times higher than what was observed in GaAs/AlGaAs. Intriguingly, we observed, as in GaAs/AlGaAs MZIs, lobe structures in the evolution of the interference visibility with the DC bias. Different theoretical frameworks were developed in order to model the experimental decoherence observed.

Then, we studied the coherence length, i.e. the distance on which an electron can propagate while keeping its phase coherence, which has never been measured in the quantum Hall regime in graphene. To that end, the interference dependence on the temperature was measured in three pn junctions of different lengths. By doing so, two coherence lengths, corresponding to two different regimes of decoherence, were extracted; in the regime occurring at low temperature, a record value of $374\mu m$ at 20mK was obtained. This long coherence length may be linked to the quantum dots behaviors observed in our system.

Finally, we investigated one of the mechanisms of decoherence in our system, the spin waves, which propagates in the graphene bulk when it is magnetized. In particular, we measured the dephasing induced by the spin waves on Mach Zehnder interference.

During this project, we have shown the possibility to encode information in the valley and to manipulate coherently this degree of freedom in graphene pn junction. This opens interesting new perspectives for a domain that has recently driven a lot of attention : the valleytronics, where the valley degree of freedom would be used to store, manipulate, and read out bits of information. Furthermore, the coherence of the system is exceptional, enabling to envision the achievement of entangled electronic states by using a double Mach Zehnder interferometer geometry. This opens promising prospects for quantum computing, but also for fundamental purposes, with the possibility to demonstrate, for the first time with fermions, the validity of the Copenhagen interpretation of quantum physics within the EPR paradox framework. Another appealing perspective arises when considering the electron flying qubit approach, where, the state of the qubit is "encoded, for example, by the presence or absence of an electron in a wave packet" [22]. In this context, a further development would be the realization of single electron sources in graphene quantum Hall edge channels, thanks to radio frequency pulses, which would also pave the way towards Hong-Ou-Mandel experiments in graphene.

Appendix

A.1 Numerical simulations

This appendix contains a detailed presentation of the models developed and simulations carried out by G. Fleury.

Hereafter, we study numerically the 3-terminal np junction sketched in figures A.1.1(a), A.1.2(a), and A.1.3(a) modeling a valley splitter with disorder (figures A.1.1(a) and A.1.3(a)) or roughness (figure A.1.2(a)) along the physical edge. A graphene rectangular sample of length L and width W is connected to two left and right horizontal leads of width W_h and to one top vertical lead of width L. The Zeeman term that lifts spin degeneracy is not taken into account. We use the spinless scaled tight-binding model of graphene [52] with interatomic distance $\tilde{a} = s_f \tilde{a}_0$ and nearest-neighbor hopping term $t = t_0/s_f$, where $\tilde{a}_0 = 0.142\,\text{nm}$ and $t_0 = 2.8\,\text{eV}$ are respectively the interatomic distance and the hopping term for real graphene while s_f is a scaling parameter. The Hamiltonian of the total system (including the leads) reads :

$$H = -\sum_{\langle i,j \rangle} t e^{i\Phi_{ij}} c_i^\dagger c_j + \sum_i (V_i - \mu) c_i^\dagger c_i + \sum_{i \in \mathcal{B}} V_i^{dis} c_i^\dagger c_i \tag{5}$$

where $c_i^\dagger$ and c_i are respectively the creation and annihilation operators of an electron at site $\mathbf{r}_i = (x_i, y_i)$, the sum $\sum_{\langle i,j \rangle}$ is restricted to nearest neighbors, and $\Phi_{ij} = (e/\hbar) \int_{\mathbf{r}_j}^{\mathbf{r}_i} \mathbf{A}.d\mathbf{r}$ is the Peierls phase accounting for the presence of the perpendicular magnetic field $\mathbf{B} = \nabla \times \mathbf{A}$ applied everywhere. Note that technically, the expression of Φ_{ij} as a function of the spatial coordinates x_i and y_j depends on the choice of the electromagnetic gauge. In practice, the Landau gauge $\mathbf{A}(x,y) = -By \binom{1}{0}$ is chosen in the horizontal leads while a rotated gauge $\mathbf{A}(x,y) = Bx \binom{0}{1}$ is chosen in the vertical lead so as to guarantee that the expression of the Peierls phase is invariant by translation along the lead axis in all leads [77]. Inside the sample, we choose a gauge which interpolates smoothly between the two aforementioned gauges in order to avoid spurious reflections at the interface between the leads and the scattering region (this requires $W \gg W_h$). The second term on the right-hand side of equation (5) mimics a np junction induced experimentally by the top/bottom gates and the side gate. μ is a constant potential applied everywhere and $V_i = V(\mathbf{r}_i)$ defined by

$$V(\mathbf{r}_i) = \frac{V_g}{2} \left[1 + \tanh\left(\frac{2(x_i - c(y_i))}{l} \right) \right], \tag{6}$$

interpolates from 0 in the left part ($x \ll 0$) to V_g in the right part ($x \gg 0$), over a characteristic length l. The position $c(y_i) = x_1 + \frac{x_0 - x_1}{2} [1 + \tanh[(2(y_i - L_{sg} + W/2)/l]]$

of the np interface varies from x_1 (when it intercepts the sample boundary) to x_0 (deep inside the sample). Here L_{sg} is a parameter corresponding to the length of the side gate and the site of coordinates $(0, 0)$ is taken at the center of the sample. When $x_0 = x_1$, the np junction is translationally invariant (see figures A.1.1(a) and A.1.2(a)) and the system models the valley splitter in the vicinity of the graphene physical edge. If $x_0 \neq x_1$, the np junction is twisted (see figure A.1.3(a)) and the modeled valley splitter includes the whole region from the physical edge to the end of the side gate. Finally, the last term in equation (5) is a disordered potential applied only on the outermost sites at the bottom boundary edge $\mathcal{B}$ inside the sample (and not in the leads). V_i^{dis} are random numbers uniformly distributed in $[-V_{dis}/2, V_{dis}/2]$.

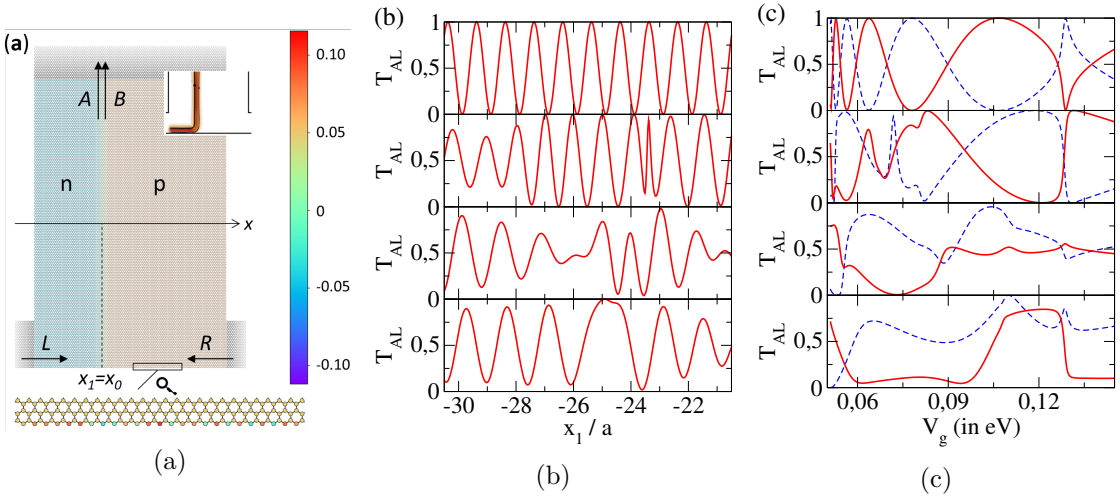

(a) (b) (c)

Figure A.1.1: (**a**) Sketch of the translationally invariant np junction connected to 3 terminals. Two (spin-degenerate and) valley polarized edge states L and R coming from the left and the right lead respectively are scattered into two (spin-degenerate and) valley-degenerate states A and B at the np interface. The color scale shows the value of the potential on each site (in eV). The zoom-in to the boxed region at the bottom boundary highlights the disordered zigzag edge. The top right inset shows a 2D plot of the local current in the system, coming from the left lead. (**b**) Transmission T_{AL} as a function of the position $x_1 = x_0$ of the np interface. Data are shown for one given disorder configuration but different disorder amplitudes ($V_{dis} = 0$, 0.25, 0.5, and 1 eV from top to bottom). (**c**) Same as (b) but T_{AL} is plotted as a function of the amplitude V_g of the np step at fixed $x_1 = x_0 = -50\,\text{nm}$ (red lines) and fixed $x_1 = x_0 = -50\,\text{nm} + a/2 \approx -49\,\text{nm}$ (blue dashed lines) (upon remaining in the regime $(\nu_N, \nu_P) = (2, -2)$). In all panels, $B = 10\,\text{T}$, $\mu = 0.05\,\text{eV}$, $s_f = 8$, $l = 10\,\text{nm} \approx 5a$, $W = 300\,\text{nm}$. In (a), $L = 200\,\text{nm}$ and $W_h = 50\,\text{nm}$ while in (b) and (c), $L = 280\,\text{nm}$ and $W_h = 70\,\text{nm}$. In (b), $V_g = 0.11\,\text{eV}$.

In the following, we consider samples with zigzag edges along the x (horizontal) axis. Perfect edges are considered in figures A.1.1 and A.1.3 while in figure A.1.2, roughness is added along the bottom physical edge. We fix the scaling factor to $s_f = 8$ and take $B = 10\,\text{T}$, $\mu = 0.05\,\text{eV}$ and V_g between roughly $0.05\,\text{eV}$ and $0.15\,\text{eV}$ (the zero of energy being taken at the Dirac point at zero field). With this choice of parameters, the filling factors are respectively $\nu_N = 2$ and $\nu_P = -2$ in the left (N) and in the right (P)

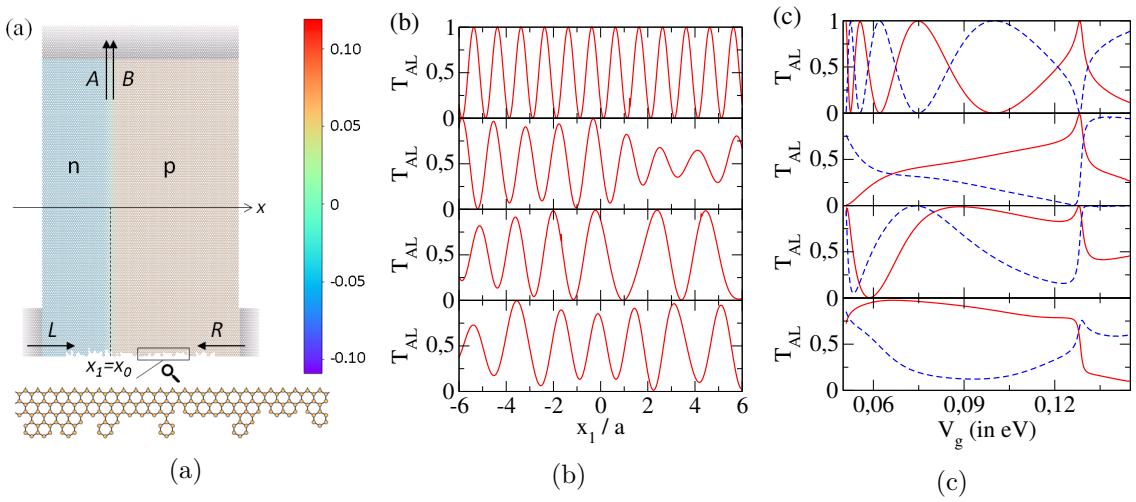

(a) (b) (c)

Figure A.1.2: Same as figure A.1.1 by adding roughness at the zigzag bottom boundary (but no on-site disordered potential *i.e.* $V_{dis} = 0$). Near the np interface (and not in the leads), the y-position of the bottom boundary at x is taken as the maximum value between y_{min} (*i.e.* the y-position of the bottom boundary in the leads) and a random number drawn from a gaussian probability with standard deviation σ_r and center y_{min}. (**a**) Sketch of a sample with edge roughness ($\sigma_r = 2a$). (**b**) Transmission T_{AL} as a function of the position $x_1 = x_0$ of the np interface, for various roughness depths ($\sigma_r = 0$, a, $2a$, and $3a$ from top to bottom). (**c**) Same as (b) but T_{AL} is plotted as a function of the amplitude V_g of the np step at fixed $x_1 = x_0 = 0\,\text{nm}$ (red lines) and $x_1 = x_0 = a/2 \approx 1\,\text{nm}$ (blue dashed lines). All other parameters are the same as in figure A.1.1.

parts, upon restoring the twofold spin degeneracy. We note L the (spin-degenerate) edge state coming from the left lead, and R the one coming from the right lead. Along the np interface, a pair of valley-degenerate (and spin-degenerate) channels, denoted by A and B, co-propagate. Note that within our non-interacting model, A and B are superimposed on each other. Using the KWANT software [31], we compute the transmission probabilities T_{AL} and T_{BL} for a (spinless) electron at zero energy to be scattered from the state L to the state A or B. Obviously, $T_{AL} + T_{BL} = 1$. In the main paper, T_{AL} and T_{BL} are called reflection and transmission probabilities of the beam splitter.

In panels (b) of figure A.1.1, A.1.2 and A.1.3, the transmission T_{AL} is plotted as function of the position x_1 of the np interface for a translationally invariant np junction with disorder (figure A.1.1(b)) or roughness (figure A.1.2(b)) along the bottom edge, and for a twisted np junction with a disordered bottom edge (figure A.1.3(b)). When the bottom zigzag edge is clean ($V_{dis} = 0$) and perfect (no roughness), data are perfectly fitted by $T_{AL}(x_1) = [1 + \cos(\frac{2\pi x_1}{\lambda_1} + \varphi_1)]/2$ where φ_1 is an adjustable phase and the period λ_1 equals $\lambda_1 = 3a$ for the twisted junction (top panel of figure A.1.3(b)) and $\lambda_1 = a$ for the translationally invariant one (top panel of figure A.1.1(b) and of figure A.1.2(b)), $a = s_f\sqrt{3} \times 0.142\,\text{nm}$ being the lattice spacing of the scaled model (fits are not shown). This oscillating behavior of the beam splitter transmission is a signature of the rotation of the valley isospin of the interface states induced by a shift of the position x_1 of the np interface [80]. Note that when the clean translationally invariant np junction is tuned

to the symmetric point (so that the states A and B are perfectly centered around the np interface), $T_{AL} = 0$ [resp. 1] when the np interface position $x_1 = x_0$ intercepts an inner [resp. outer] carbon atom of the zigzag boundary (*i.e.* $x_0 = x_1 \equiv 0\,_{[a]}$ [resp. $a/2\,_{[a]}$] in our geometry). This is not perfectly the case in the top panels of figures A.1.1(b) and A.1.2(b) because the chosen parameters $\mu = 0.05\,\text{eV}$ and $V_g = 0.11\,\text{eV}$ correspond to a np junction which is slightly asymmetric (and the above phase φ_1 depend on those parameters). Moreover, when disorder or roughness is added along the bottom zigzag edge (bottom panels of figures A.1.1(b), A.1.2(b) and A.1.3(b)), the periodic pattern of $T_{AL}(x_1)$ is lost but the transmission keeps oscillating between minimal and maximal values close to 0 and 1. Changing the disorder or edge configuration leads to plots of T_{AL} which are quantitatively different but qualitatively similar. This illustrates the fact that the transmission pattern $T_{AL}(x_1)$ is a fingerprint of the local edge configuration in the vicinity of the region where the np interface and the physical bottom edge intersect.

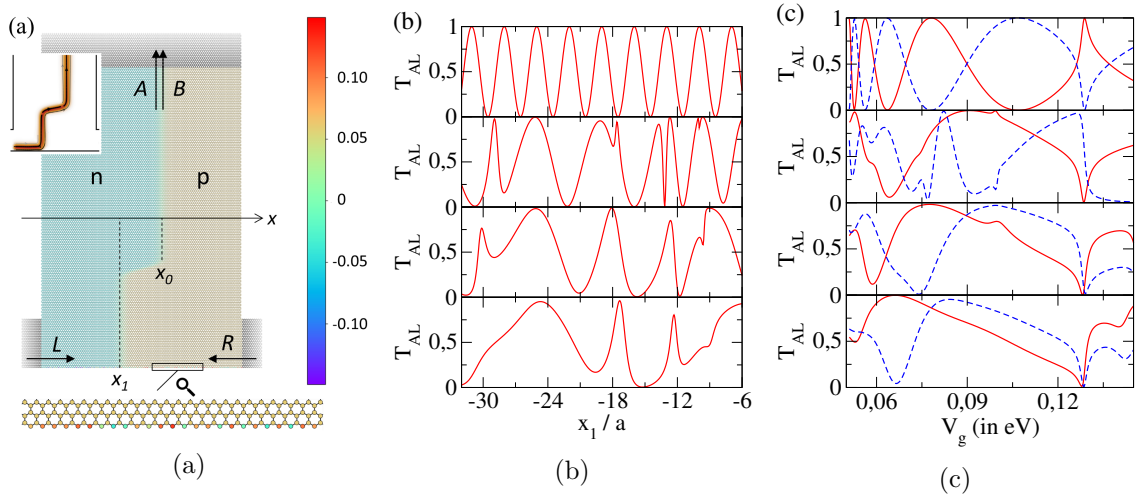

(a) (b) (c)

Figure A.1.3: Same as figure A.1.1 for a twisted np junction (**a**). The transmission T_{AL} is plotted as a function of the position x_1 of the bottom np interface at fixed $x_0 = 50\,\text{nm}$ (**b**) and as a function of V_g (**c**) at fixed $x_0 = 30\,\text{nm}$, $x_1 = -30\,\text{nm}$ (red lines) and at fixed $x_0 = 30\,\text{nm}$, $x_1 = -30\,\text{nm} + 3a/2 \approx -27\,\text{nm}$ (blue dashed lines), for different disorder amplitudes ($V_{dis} = 0$, 0.25, 0.5, and 1 eV from top to bottom). All other parameters are the same as in figure A.1.1 with additionally $L_{sg} = 100\,\text{nm}$. Note that T_{AL} is independent of (finite) L_{sg} as long as $L_{sg} \gg 2l_B$ (l_B being the magnetic length).

Besides, when the positions x_0 and x_1 of the np interface are fixed, we find that the transmission T_{AL} plotted as a function of the height V_g of the np potential step also oscillates between 0 and 1 in an apparent erratic way (figures A.1.1(c), A.1.2(c) and A.1.3(c)). We interpret these oscillations as follows. When V_g is varied (so as to remain in the regime $(\nu_N, \nu_P) = (2, -2)$), the position of the (superimposed) interface states A and B is shifted along x and their valley isospin rotate, which results in a variation of T_{AL}. Experimentally, x_0, x_1, and V_g are varied simultaneously by tuning the gate voltages. A more advanced theoretical description should account for the mixed quantum-electrostatic problem [6] to extract the model parameters from the experimental configurations. This is left for future works.

As a side comment, let us add that all data shown in figures A.1.1, A.1.2, and A.1.3 have been obtained with a characteristic length $l = 10\,\mathrm{nm} \approx 5a$ for the np step (a being defined here for the scaled model, see above). We have reproduced (up to a shift along the $x-$axis) the oscillations of period a and $3a$ shown in the top panels of figures A.1.1(b), A.1.2(b), and A.1.3(b) for different values of l ranging from $l = 2\,\mathrm{nm} \approx a$ to $l = 25\,\mathrm{nm} \approx 12.7a$ (data not shown). The latter value is still much smaller than in experiments, yet numerical instabilities occurring for large l as well as finite-size effects hinder further numerical investigations. We expect the oscillations of period a of $T_{AL}(x_1)$ (corresponding to the translationally invariant junction) to be robust for large l since even a smooth np interface is predicted to induce intervalley scattering near a physical zigzag edge [2]. On the contrary, we expect the oscillations of period $3a$ of $T_{AL}(x_1)$ (corresponding to the twisted junction) to be modified as l becomes large enough not to induce intervalley scattering in the (bulk) region where the np interface changes direction.

A.2 Current conservation

We check experimentally that the injected current is equal to the sum of the reflected and transmitted current through the pn junction with the side gates (device described in the main text, see in figure A.2.1.A). In the n region the Landau-level filling factor is $\nu_n = 1$ and one spin-down channel circulates counterclockwise, while in the p region $\nu_p = -2$ and two channels of the opposite spin ($\uparrow$, $\downarrow$) circulates clockwise. As shown in figure A.2.1.B, transmitted current in red is in phase opposition with the reflected current (in blue). Total current (in black) is conserved.

Note that the AB periodicity of B=12mT (figure A.2.1.B) is two times smaller than described in chapter 3. In the main text, (ν_n, ν_p)=(-1,+2) while here (ν_n, ν_p)=(+1,-2). (ν_n, ν_p)=(-1,+2) is reached with top gate voltage V_{TG}=2.54V and back gate voltage V_{BG}=-0.59V leading to a voltage difference $\Delta V_{G,1}$=3.13V. (ν_n, ν_p)=(+1,-2) is reached with top gate voltage V_{TG}=-2.16V and back gate voltage V_{BG}=0.13V leading to a voltage difference $\Delta V_{G,2}$=2.29V. Ratio of these potential differences for the two opposite chirality is $\frac{\Delta V_{G,1}}{\Delta V_{G,2}}$ =1.37, which leads to a sharper potential profile for (ν_n, ν_p)=(-1,+2) than (ν_n, ν_p)=(+1,-2) and a reduced distance between edge states.

Figure A.2.1.C shows transmitted and reflected current for the test sample without side gates at (ν_n, ν_p)=(+2,-2) (test sample). Total current (in black) is conserved. The AB periodicity is larger, in figure A.2.1.D, mostly because the total length of the interferometer, L=1μm, is smaller, due to the absence of side gates.

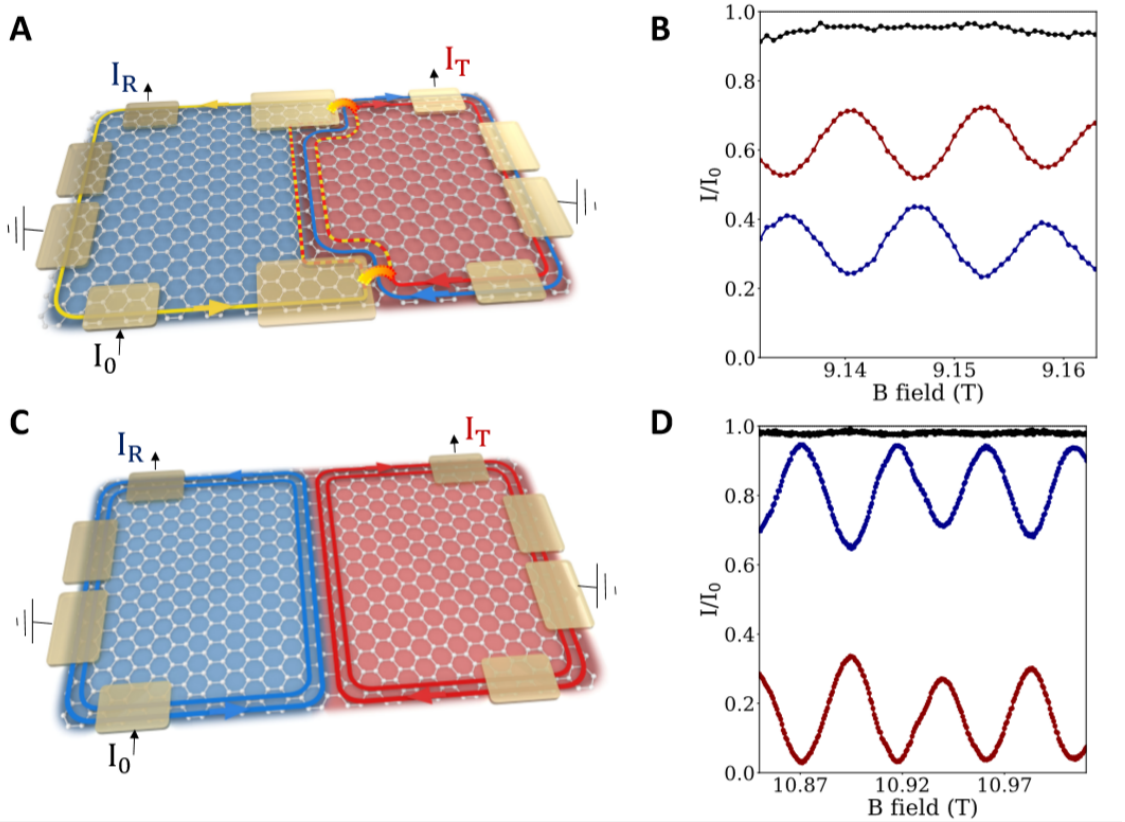

Figure A.2.1: **Current conservation in two interferometers.** (**A**) Schematics representation of an interferometer with side gates (yellow). A current I_0 is injected on the n side (blue) at filling factor $\nu_n = 1$. After its transfer through the pn junction, we measure the reflected, I_R, and transmitted, I_T, current with two ohmic contacs (grey). Additional ohmic contacts are used as ground sinks. (**B**) Transmitted (red) and reflected (blue) current normalized by the injected current I_0, as a function of magnetic field B. These current oscillate with opposite phase and their sum (black) is conserved. (**C**) Schematics representation of an interferometer without side gate. A current I_0 is injected on the n side (blue) at filling factor $\nu_n = 2$. (**D**) Transmitted (red) and reflected (blue) current normalized by the injected current I_0, as a function of magnetic field B. These currents oscillate with opposite phase and their sum (black) is conserved.

A.3 Admittance between capacitively coupled edge channels

In what follows, is presented P. Roulleau computation of the admittance between capacitively coupled edge channels. We note V_D the potential of non-interfering detector edge state (also noted ⓓ), and U_2 the potential of the interfering $|\downarrow, \overrightarrow{\omega}\rangle$ edge state (also noted ②). We introduce the admittance between $|\uparrow, T_R\rangle$ and $|\downarrow, \overrightarrow{\omega}\rangle$: $G_{2,D} = \frac{dI_2(\omega)}{dV_D(\omega)}$. We call $\psi_\alpha(\mathbf{r}; E)$ an incident state from the contact α at energy E. The charge distribution can be described by the Fermi field :

$$\hat{\Psi}(\mathbf{r}, t) = \sum_\alpha \int \frac{dE}{\sqrt{h\nu_{\alpha,E}}} e^{-iEt/\hbar} \psi_\alpha(\mathbf{r}; E) \hat{a}_\gamma(E) \tag{7}$$

The charge density in the PN junction at point $\mathbf{r}$ and time t is given by :

$$\hat{\rho}(\mathbf{r}, t) = e\hat{\Psi}^\dagger(\mathbf{r}, t)\hat{\Psi}(\mathbf{r}, t) \tag{8}$$

After Fourier transforming and quantum averaging we get $\rho(\mathbf{r}, \omega)$ where :

$$\rho(\mathbf{r}, \omega) = \sum_{\alpha,\beta} \int \frac{dE}{\sqrt{h\nu_{\alpha,E} h\nu_{\alpha,E+\hbar\omega}}} \psi^*_\alpha(\mathbf{r}; E)\psi_\beta(\mathbf{r}; E + \hbar\omega)\langle \hat{a}^\dagger_\alpha(E)\hat{a}_\alpha(E + \hbar\omega)\rangle \tag{9}$$

This averaged charge density can be split into an equilibrium part $\rho_0(\mathbf{r}, \omega)$ and a fluctuating one: $\rho(\mathbf{r}, \omega)$=$\rho_0(\mathbf{r}, \omega)$+$\delta\rho_\alpha(\mathbf{r}, \omega)$. $\delta\rho_\alpha(\mathbf{r}, \omega)$ resulting from voltage fluctuations $V_\alpha(\omega)$, it is natural to write $\langle \hat{a}^\dagger_\alpha(E)\hat{a}_\alpha(E + \hbar\omega)\rangle$ as the sum of two terms:

$$\langle \hat{a}^\dagger_\alpha(E)\hat{a}_\alpha(E + \hbar\omega)\rangle = \delta(\hbar\omega)f(E) + \frac{e}{h} V_{\alpha,\omega} F_\alpha(E, \omega) \tag{10}$$

$V_{\alpha,\omega}$ is the Fourier component at frequency ω of V_α(t) and $F_\alpha(E, \omega)$ is defined as $F_\alpha(E, \omega)$=$\frac{f_\alpha(E) - f_\alpha(E+\hbar\omega)}{\hbar\omega}$.

In the following we will assume that the first valley splitter is tuned to 1/2. Scattering states of the PN junction that interfere can be written :

$$\psi_2(\mathbf{r}; E) = \frac{1}{\sqrt{2}} e^{ik_E x + \varphi_2} \tag{11}$$

with φ_2 the accumulated phase along the arm length while the detector state which is fully transmitted is $\psi_D(\mathbf{r}; E) = e^{ik_E x + \varphi_D}$. The fluctuating charge into one edge state is obtained by integrating the charge density over the arm length :

$$Q_2(\omega) = \int_0^L \delta\rho_2(x, \omega) dx \tag{12}$$

For the interfering edge state, we get :

$$Q_2(\omega) = \frac{e^2}{2h} \int dE \frac{i}{\omega} (1 - e^{i\omega\tau}) V_{2,\omega} F_2(E, \omega) \tag{13}$$

For the detector edge state :

$$Q_D(\omega) = \frac{e^2}{h}\int dE \frac{i}{\omega}(1-e^{i\omega\tau})V_{D,\omega}F_D(E,\omega) \tag{14}$$

The limit h$\omega \ll$ k$_B$T leads to the simplification $\int F_D(E,\omega)dE \sim$1. Here, the detector edge state is the only source of thermal dephasing noise. Therefore, we have :

$$\begin{cases} Q_D(\omega) = \frac{e^2}{h}\frac{i}{\omega}(1-e^{i\omega\tau})V_D(\omega) \\ Q_2(\omega) = 0 \end{cases} \tag{15}$$

If we now consider interaction, excess injected charge will in turn induce screening charge proportional to the internal potential U$_\alpha(\omega)$. This leads to :

$$\begin{cases} Q_D(\omega) = \frac{e^2}{h}\frac{i}{\omega}(1-e^{i\omega\tau})(V_D(\omega)-U_D(\omega)) \\ Q_2(\omega) = \frac{e^2}{h}\frac{i}{\omega}(1-e^{i\omega\tau})(-U_2(\omega)) \end{cases} \tag{16}$$

Since $Q_D(\omega) = -Q_2(\omega) = C(U_D(\omega) - U_2(\omega))$ we finally obtain :

$$G_{2,D} = \frac{G_Q(1-e^{i\omega\tau})}{2 + iG_Q(1-e^{i\omega\tau})/\omega C} \tag{17}$$

We want to relate U$_2(\omega)$ to V$_D(\omega)$:

$$U_2(\omega) = -\frac{CV_D(\omega)}{2C + \frac{i}{\omega}\frac{e^2}{h}(1-e^{i\omega\tau})} \tag{18}$$

This leads to :

$$S_{22} = |\frac{C}{2C + \frac{i}{\omega}\frac{e^2}{h}(1-e^{i\omega\tau})}|^2 S_{V_D,V_D} \tag{19}$$

Finally, using the fact that T/T$_\varphi$=$\langle\varphi^2\rangle$/2 we get :

$$\frac{1}{T_\varphi} = \frac{4k_BT}{\hbar}\tau I(\gamma) = \frac{4k_BT}{\hbar}\frac{R_QC}{\gamma}I(\gamma) \tag{20}$$

With : $\begin{cases} \gamma = C/(G_Q\tau) \\ I(\gamma) = \int_0^\infty \frac{sin^2(x)\gamma^2}{sin^2(x)+2\gamma sin(2x)+4\gamma^2x^2}dx. \end{cases}$

A.4 Propagation and absorption of spin waves in the hole states

In section 6.2.1, we studied the spin wave emission from an ohmic contact using the natural local doping around it. In the latter experiment, the whole sample, below and outside of the top gate, was tuned to $\nu = 1$. By applying a DC bias and a lock-in signal on contact 2 (see figure A.4.1) we could detect a clear magnon absorption signal in contact 20 but also in 18 and 19 which are below the top gate. In this appendix, we investigate the magnon signal observed using a similar configuration (shown in figure A.4.1) : a magnon signal is emitted from contact 2 from a region at filling factor $\nu_B = 1$, and we measure the non local signal induced in contacts 18, 19, and 20. However, the top gate is now fixed at filling factor $\nu_T = -1$, enabling us to check if we can detect a magnon signal in the hole states, i.e. with a negative filling factor, via contacts 18 and 19.

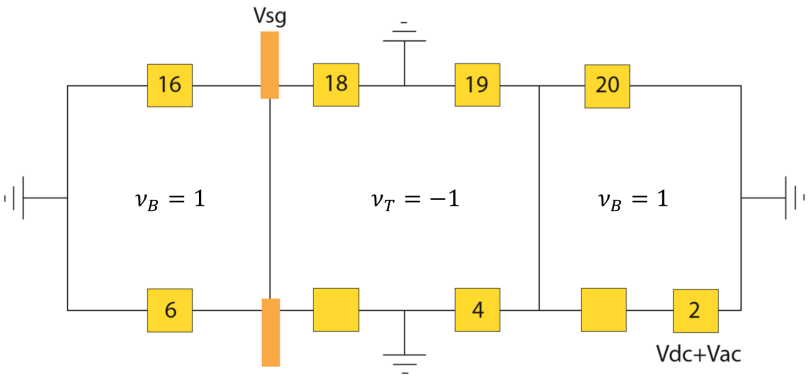

Figure A.4.1: **Schematic representation of the valley splitter sample $\nu_T = -1$ and $\nu_B = 1$.** Two pn junctions are formed on both sides of the top gate. A DC bias is applied on ohmic contact 2 and superimposed to an AC lock-in signal, this enables to generate magnons thanks to the contact doping. The non-local signals, resulting from magnons absorption are measured in contacts 18, 19, and 20.

In figure A.4.2.A, we show the determination of the filling factors by two point resistance measurement as a function of top gate such that $\nu_B = 1$ ($V_B = -0.1V$) and only ν_T is changed. The region situated in between the dotted red lines corresponds to the top gate voltage range where $\nu_T = -1$ is well defined, whereas the region before the blue dotted line corresponds to a well defined $\nu_T = -2$. Note that the chirality below the top gate is reversed compared to the rest of the sample.

Non local voltage on contact 20 which remains at $\nu_B = 1$, shown in figure A.4.2.B, is constant on the top gate voltage span, and the values are consistent with the measurement at $\nu_T = \nu_B = 1$. Figure A.4.2.C and A.4.2.D show respectively the non local voltage measured in 19 and in 18, only weak signals are visible on these color maps. Our interpretation is that at $\nu = -1$ the local doping of the metallic contact is not effective, therefore there is no absorption of magnons in the central region at $\nu_T = -1$, which

implies:

$$\begin{cases} \mu_{19} = \mu_0 \\ \mu_{18} = \mu_0 \end{cases} \tag{21}$$

Another interpretation would be that magnons are simply stoped at the pn junction. However, it has been shown by Wei et al. [83], using a similar configuration, that magnons generated from a $\nu = 1$ region can travel through a $\nu = -1$ region below a top gate, and be detected on the other side in again a $\nu = 1$ region. In their experiment, they did not have contacts below the top gate, so they could not check the absorption in the hole states.

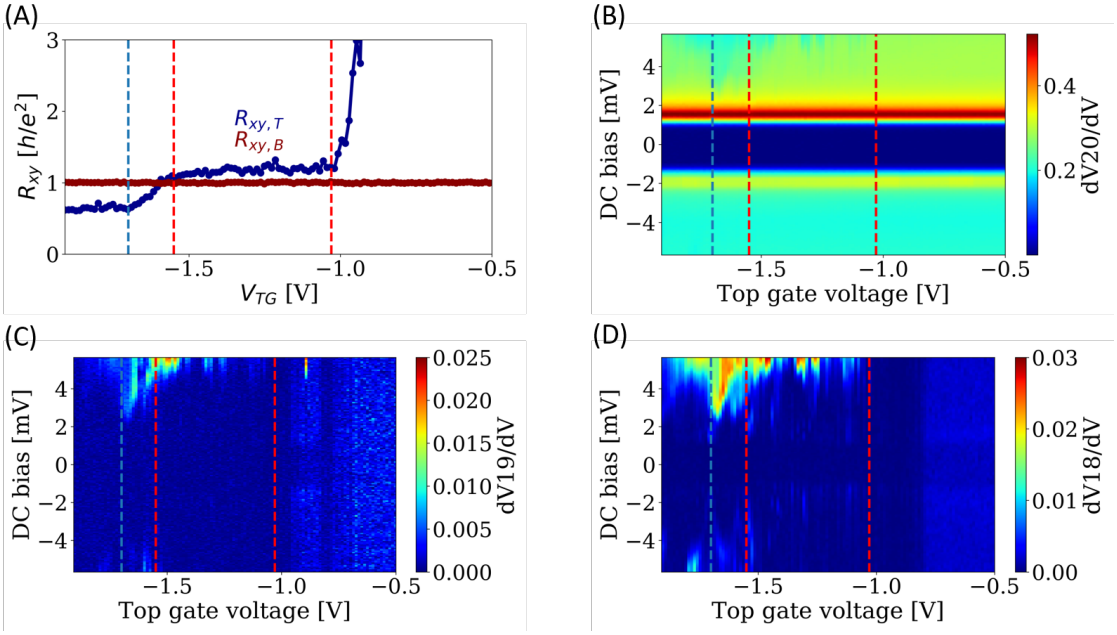

Figure A.4.2: **Propagation of spin waves in the hole states.** The DC bias is applied on contact 2. (**A**) Determination of the filling factors ν_T and $\nu_B = 1$ by two points measurement. (**B**) Non local voltage in 20 as a function of DC bias. Contact 20 is not below the top gate. (**C**) Non local voltage in 19 as a function of DC bias. (**D**) Non local voltage in 18 as a function of DC bias.

At $\nu_T = -2$, similarly there is a weak signal in 18 and 19. Interestingly, the small non-local signal, observed at $\nu_T = -1$ and $\nu_T = -2$, is bigger in 18 than in 19, maybe because it is due to absorption along the left pn junction at $\nu_T = -2$ and at contact 6 at $\nu_T = -1$.

Some signal is observed at $\nu_T = 0$, figure A.4.2.D. But, because the detection contact is in the $\nu_T = 0$ region, this non local voltage signal is not understood.

A.5 Decoherence induced by magnons emitted from a pn junction

In the last section of chapter 6, we studied the decoherence induced by magnons generated thanks to a DC bias applied on an ohmic contact, using a pn junction in the MZI regime as a quantum sensor. Interestingly, we developed a new technique to emit spin waves not based on local doping. Indeed, as detailed in section 6.2.1, by applying a bias on a pn junction, with on the p-side $\nu_p = -2$ and on the n-side $\nu_n = 1$, one can control the spin wave emission. In this appendix, I will present a study of the decoherence induced by magnons produced thanks to this new technique. We followed a similar approach than in section 6.2.2 based on a MZI playing the role of a quantum sensor.

The set up used for this experiment is described in figure A.5.1. The filling factors are fixed at $\nu_T = 1$ under the top gate and $\nu_B = -2$ outside the top gate. This generates two pn junctions at the two borders of the top gate, and thus 2 two MZIs : the right one is used as a magnon emitter, whereas the left one is the quantum sensor MZI. The DC bias used to generate spin wave is applied on contact 2 with a lock-in excitation for the electric detection. Another lock-in excitation is applied in 18 to measure the usual transmission of the MZI in 6.

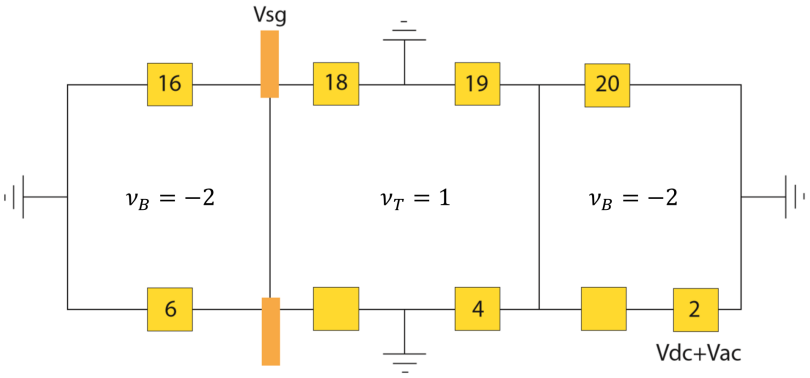

Figure A.5.1: **Schematic representation of the valley splitter sample in the spin wave emission configuration.** The filling factors are fixed at $\nu_T = 1$ and $\nu_B = -2$. Two MZIs are formed on both sides of the top gate. A DC bias is applied on ohmic contact 2 and superimposed to an AC lock-in signal. Magnons are emitted from the right pn junction, and we measure the effect on the coherence of the MZI formed at the left pn junction.

At the threshold voltage for spin waves emission, a strong phase shift of the MZI interferences can be observed, as shown in figure A.5.2.a. Both the extracted visibility in figure A.5.2.b and the phase in figure A.5.2.c exhibit a threshold voltage. Note that the threshold voltages are different at positive and negative bias due to the spin wave emission mechanism of the pn junction which is different depending on the DC bias (V_{DC}) sign. Indeed, as described in section 6.2.1 :

- for $V_{DC} < 0$, the emission takes place along the pn junction
- for $V_{DC} > 0$, the emission takes place at the ohmic contact after the pn junction

From the averaged non local voltage signals presented in figure A.5.2.b, we compute the DC non local voltage felt by the interferometer due to spin waves absorption:

$$V_{nl} = \int_0^{V_{DC,nl}} \frac{dV_{nl}}{dV} dV_{DC,nl}$$

The computed V_{nl} for contacts 18 (red) and 6 (orange) are shown in figure A.5.2.d. The amplitudes of these non local voltages are less than 15μV. Now we look at the MZI response when the DC bias, V_{DC}, is directly applied on the interfering edge states, on contact 18, to check if such voltage can generate similar phase shift. Figure A.5.2.e shows the AB oscillations as a function of DC bias, V_{DC}, from which the visibility figure A.5.2.f and the phase figure A.5.2.g are extracted. The phase shift at ± 15 μV in DC bias, shown by the vertical dotted lines, is negligible compared to the non local bias measurement.

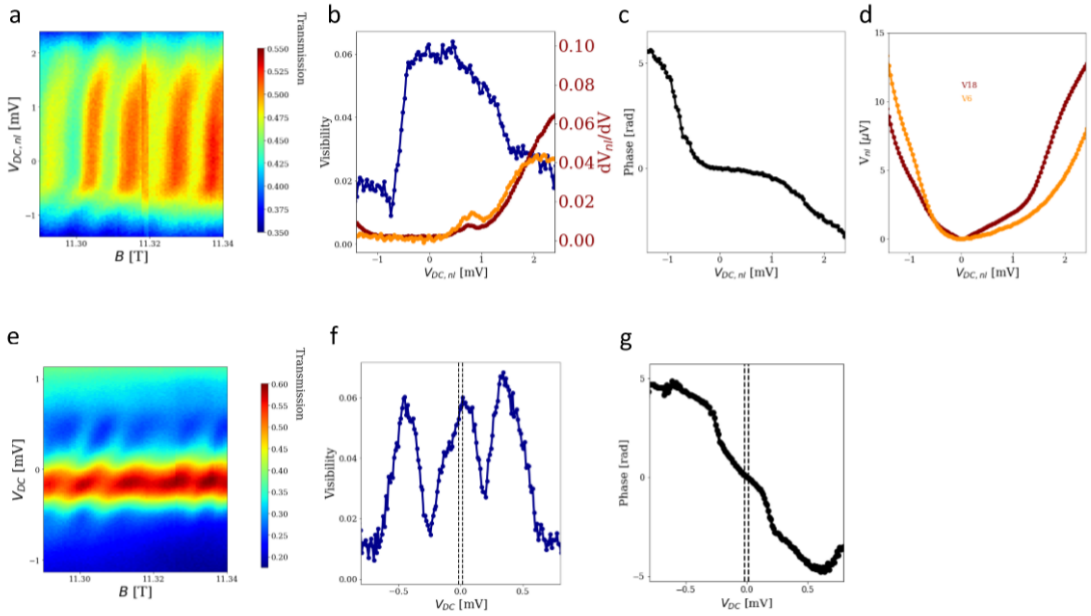

Figure A.5.2: **Coherent detection of spin waves emitted by a pn junction.** (**a**) Interferences as a function of DC bias, $V_{DC,nl}$, applied on a edge state decoupled from the interferometer by ground sinks. (**b**) Visibility and non local voltage signal (red in 18 and orange in 6) due to the bias $V_{DC,nl}$. (**c**) The phase of the interferences show a strong modulation at the spin wave emission threshold. (**d**) DC non local voltage (red in 18 and orange in 6), V_{nl}, transmitted in the MZI, computed from the non local voltage signals $\frac{dV_{nl}}{dV}$. The DC non local voltage are less than $V_{nl} < 15\mu$V. (**e**) Interferences as a function of DC bias, V_{DC}, applied directly on the interferometer arm. (**f**) Visibility as a function of bias. The vertical dotted lines are drawn at $V_{DC} = \pm 15\mu$V. (**g**) Phase as a function of bias. The vertical dotted lines are drawn at $V_{DC} = \pm 15\mu$V.

A.6 Complementary data for back gate points in $\nu \leq 1$ region

In figure A.6.1, we provide additional data concerning the measurement presented in the last section of chapter 6 (see figure 6.12.h) taken at a back gate voltage $V_B = -0.18V$. This data set corresponds to the triangular symbol (in figure 6.12.a) in the Skyrme ground set (filling factor $\nu \leq 1$).

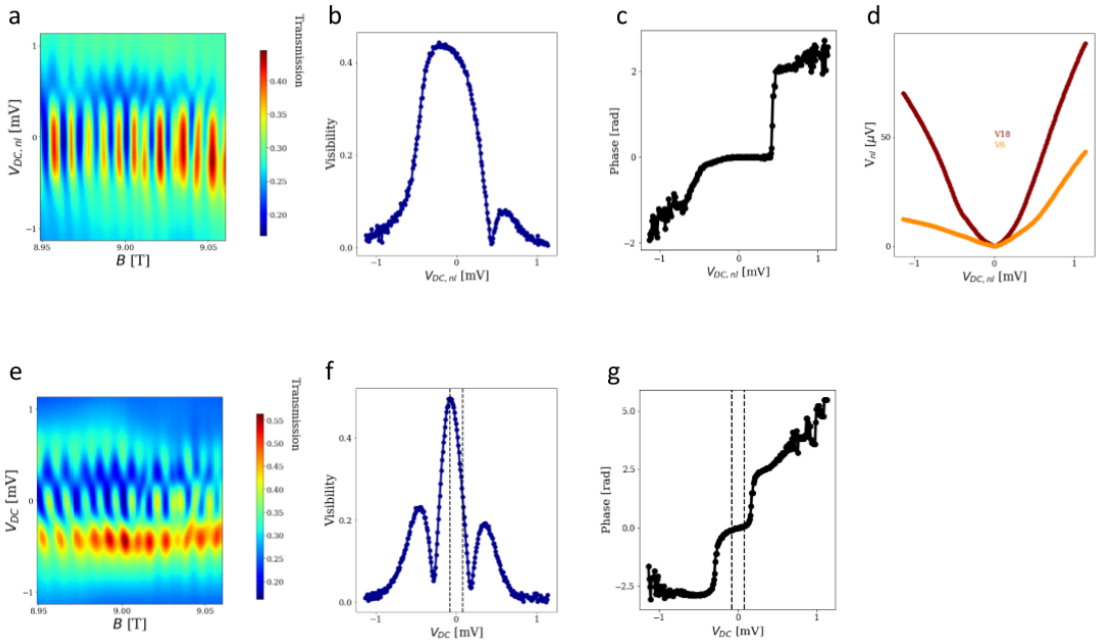

Figure A.6.1: **Data for the triangular symbol (see figure 6.12).** The filling factor are $\nu_B = 1$ and $\nu_T = -2$ ($V_B = -0.18$V, triangular symbol). (**a**) AB oscillations as a function of DC bias applied on contact 16. (**b**) Visibility as a function of bias. (**c**) Phase as a function of bias. (**d**) Non local voltage transmitted in the MZI. The non local voltages are less than $V_{nl} < 80\mu$V in the range where the interferences are visiblible. (**e**) AB oscillations as a function of bias applied in 6 directly on the interferometer arm. (**f**) Visibility as a function of bias. The vertical dotted lines are drawn at $V_{DC} = \pm 80\mu$V. (**g**) Phase as a function of bias. The vertical dotted lines are drawn at $V_{DC} = \pm 80\mu$V.

In figure A.6.2, we plot additional data corresponding to another back gate point in the Skyrme ground state, $V_B = -0.182V$, noted by the star symbol in figure 6.12.a.

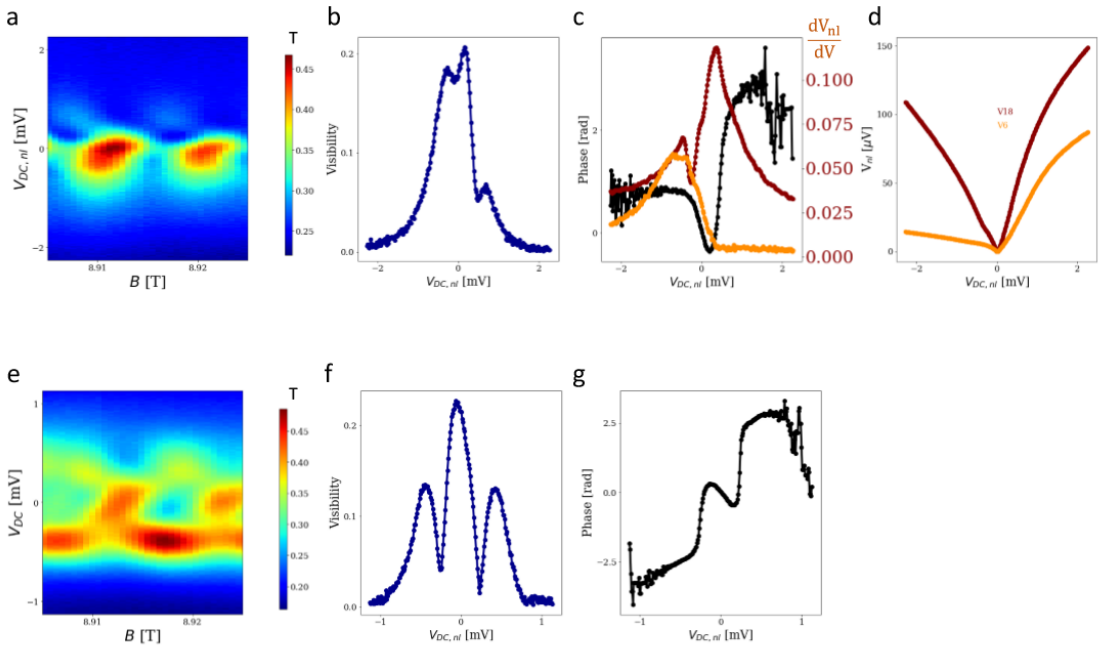

Figure A.6.2: **Data for the star symbol (see figure 6.12).** The filling factor are $\nu_B = 1$ and $\nu_T = -2$ ($V_B = -0.182$V, star symbol). (**a**) AB oscillations as a function of DC bias applied on contact 16. (**b**) Visibility as a function of bias. (**c**) Phase and non local voltage signals as a function of bias. (**d**) Non local voltage transmitted in the MZI. The non local voltages are less than $V_{nl} < 150\mu$V. (**e**) AB oscillations as a function of bias applied in 6 directly on the interferometer arm. (**f**) Visibility as a function of bias. (**g**) Phase as a function of bias.

Résumé

Le développement de la mécanique quantique au début du XXe siècle a eu des implications dans de nombreux domaines de la physique classique, et en particulier en optique. La différence principale apparaît lorsque l'on considère des interférences : en optique classique on étudie des interférences en amplitude de champ électrique, alors qu'en mécanique quantique on considère des interférences en amplitude de probabilité. Dans la plupart des cas, il n'y a aucune différence entre ces deux approches. L'observation expérimentale d'effets relevant de la mécanique quantique en optique constitue en fait un champ de recherche entier, appelé l'optique quantique. Au début des années 60, le développement de ce domaine a conduit à d'impressionnants résultats sur le plan fondamental, et, en particulier, à la résolution de l'une des controverses majeures de la physique du XXe siècle : le paradoxe d'Einstein-Podolsky-Rosen (paradoxe EPR). Selon le paradoxe EPR, la théorie de la mécanique quantique n'est pas complète et ne prend pas en compte certains "éléments de la réalité"; cela a conduit au développement d'une théorie à variables cachées pour décrire la réalité du monde quantique. L'une des expériences essentielles de l'optique quantique est l'expérience menée par Alain Aspect [7] en 1982 démontrant une violation des inégalités de Bell, contredisant ainsi l'existence de variables cachées.

L'optique quantique électronique est un domaine émergent, dont le but est de reproduire des expériences d'optique quantique mais en remplaçant les photons par des électrons. Pour ce faire, les physiciens ont utilisé des systèmes particuliers, nommé gaz électronique bi-dimensionnel (2DEG), constitués d'électrons confinés dans un plan. Un 2DEG peut être formé à la surface de l'Hélium liquide, ou à l'interface d'hétérostructures semi-conductrices comme le très répandu GaAs/AlGaAs. A très basse température (typiquement en-dessous de $100mK$ dans les hétérostructures de GaAs/AlGaAs), un analogue de la fibre optique pour les électrons est obtenu grâce aux canaux de bord chiraux, formés en régime Hall quantique apparaissant lorsqu'un fort champ magnétique est appliqué perpendiculairement au 2DEG. Cela permet de guider les électrons jusqu'à l'équivalent électronique de la lame semi-réfléchissante, grâce auquel il est possible de recréer des expériences d'optique quantique. En utilisant ces techniques, une équipe a pu réaliser pour la première fois en 2003 une version électronique de l'interféromètre de Mach Zehnder (MZ) [37].

Cette expérience pionière a ouvert la voie à la génération d'états intriqués grâce à une structure de double MZ, comme proposé par Samuelsson et al. [74]. Les états électroniques intriqués sont d'une importance primordiale aussi bien pour des raisons théoriques que pratiques. En effet, d'un point de vue théorique, cette expérience de double MZ pourrait permettre de démontrer une violation des inégalités de Bell comme dans l'expérience

d'Alain Aspect, mais cette fois-ci avec des électrons à la place des photons, ce qui fondamentalement est important, les électrons étant des fermions, alors que les photons sont des bosons. D'un autre côté, la formation d'états électroniques intriqués est essentielle dans l'optique d'une informatique quantique basée sur des qubits volants. L'approche des qubits volants a été développée en optique quantique électronique par analogie avec les qubits composés d'un photon unique manipulés en optique quantique. L'état du qubit volant est encodé dans la trajectoire de l'électron, et une superposition de deux trajectoires peut être obtenue en utilisant l'équivalent électronique de la lame semi-réfléchissante (par exemple un point de contact quantique), formant ainsi une porte d'Hadamard. Dans ce cadre, la géométrie de double Mach Zehnder permettant de générer des états intriqués est une brique essentielle pour la réalisation de portes quantiques à plusieurs qubits.

Malheureusement, la cohérence dans les hétérostructures de GaAs/AlGaAs est fragile, et la présence d'une forte décohérence a empêché l'observation expérimentale d'une violation des inégalités de Bell [60]. D'autre part, la fragilité de la cohérence rend difficile de concevoir des calculs quantiques, via des agencements complexes de portes quantiques dans ces hétérostructures semi-conductrices. La solution à ces problèmes pourrait provenir d'un matériau novateur aux propriétés extraordinaires, isolé pour la première fois en 2004 [65] par une équipe de l'université de Manchester : le fameux graphène. Le graphène est un cristal parfaitement bi-dimensionnel composé d'atomes de Carbone arrangés selon un réseau en nid d'abeille. Chaque atome de Carbone possède quatre électrons de Valence : trois formant des liaisons co-valentes avec d'autres atomes de Carbone, et un additionnel au-dessus du plan du cristal. L'ensemble de ces électrons supplémentaires forme un 2DEG à la surface de la couche de graphène, et, comme dans les hétérostructures de GaAs/AlGaAs, l'application d'un champ magnétique perpendiculaire donne naissance à l'effet Hall quantique et à des canaux de bords chiraux. En 2015, Morikawa et al. [58] ont réalisé le premier interféromètre de Mach Zehnder électronique dans le graphène en utilisant une jonction pn en régime Hall quantique, ce qui a ouvert la voie à l'étude détaillée menée par la suite dans le groupe de Yacoby au sein de l'université d'Harvard en 2017 [84].

L'une des propiétés marquantes du graphène est l'existence d'un degré de liberté aditionnel, la vallée, qui s'ajoute au spin, créant ainsi une quadruple dégénérescence en spin et en vallée. Cette dégénérescence est levée en présence d'un champ magnétique perpendiculaire intense, générant des canaux de bords chiraux, polarisés en spin et en vallée. Récemment, la possibilité d'encoder de l'information dans le degré de liberté de vallée au sein de matériaux bi-dimensionnels, présentant une brisure de leur symétrie d'inversion spatiale, a généré beaucoup d'intérêt [10] [75], car cela pourrait engendrer une nouvelle forme d'électronique : la valléetronique. La valléetronique dans le graphène mono-couche a été moins étudiée expérimentallement [30] à cause de la difficulté de manipuler l'isospin de vallée par des moyens électrostatiques; l'inversion de symétrie ne peut pas être brisée par de simples grilles, créant des potentiels changeant doucement sur l'échelle de la distance atomique. Ouvrir cette possibilité est intéressant, car cette difficulté assure la solidité de l'isospin de vallée, ce qui est l'un des principaux avantages de la valléetronique dans le graphène monocouche. Finallement, concernant l'informatique quantique, cela ouvre des perspectives intéressantes, comme la réalisation d'un nouveau type de qubit

volant, où l'information ne serait plus encodé dans la trajectoire, mais dans l'isospin de vallée.

Durant ma thèse, le but principal était de démontrer que, l'isospin de vallée peut être électriquement contrôlé dans le graphène mono-couche, grâce à un interféromètre de Mach Zehnder électronique avec des transmissions contrôlables. Dans ce but, j'ai employé comme Wei et al. [84] une jonction pn comme interféromètre de MZ, le mélange se produisant aux deux extrémités de la jonction pn, jouant le rôle des lames semi-réfléchissantes. Dans leur expérience, ils ne peuvent directement contrôler les trasmissions des deux lames semi-réfléchissantes, ce qui est nécessaire à l'obtention d'un état en sortie avec une polarisation de vallée contrôlée. Afin de surmonter cette difficulté, nous avons ajouté des grilles locales aux extrémités de la jonction pour pouvoir contrôler les transmissions, et ainsi obtenir un contrôle complet de la polarisation en vallée de l'état de sortie. Par la suite, un autre but important de mon travail a été l'étude de la solidité de la cohérence de ces états polarisés en vallée, car cela est un point essentiel à la réalisation de calculs quantiques en utilisant un qubit volant de vallée.

Dans la suite, est exposé un résumé de la structure de ce manuscrit de thèse. Le **chapitre 1** présente brièvement ce qu'est l'optique quantique électronique, ainsi que quelques expériences clefs sur l'interférométrie de MZ et la génération d'états intriqués dans les hétérostuctures semi-conductrices de GaAs/AlGaAs. Dans un deuxième temps, j'ai essayé de résumer brièvement les propriétés essentielles du graphène, et de montrer en quoi ce matériau constituait un bon candidat pour mener des expériences d'optique quantique électronique.

Dans le **chapitre 2**, je présente la géométrie que nous avons élaborée pour notre échantillon, ainsi que la procédure de fabrication développée. L'échantillon est composé d'une mono-couche de graphène fabriquée au laboratoire, encapsulée entre deux cristaux de nitrure de bore (BN). A l'aide de techniques conventionnelles de nano-lithographie, nous avons réalisé des grilles, ainsi que des contacts métalliques sur l'échantillon de graphène encapsulé. Comme visible dans la représentation schématique de l'échantillon, présentée dans la figure A.6.3, l'élément de base de l'expérience est une jonction pn, créée par effet de grille, étudiée en régime Hall quantique. Dans ce régime, apparaissant en présence d'un champ magnétique intense appliqué perpendiculairement à l'échantillon, des canaux de conductions chiraux contre-propageants se forment dans les régions n et p; ces canaux se rejoignent à la jonction pn pour former deux canaux co-propageants cette fois se propageant le long de l'interface. Il a été démontré dans de précédentes études [58][84][56] qu'un tel système se comporte comme un interféromètre de Mach Zehnder, avec des points de mélange localisés aux deux points d'intersection de la jonction pn avec le bord physique du graphène. Pour autant, dans ces études aucun contrôle de la transmission en ces deux points n'était obtenu, ce qui s'avère nécessaire pour démontrer la complète équivalence du système avec un interféromètre de Mach Zehnder; d'autre part, contrôler la transmission aux niveaux des deux points de mélange permet de contrôler la polarisation en vallée des excitations électroniques se propageant le long de la jonction. Afin d'obtenir un tel contrôle, nous avons ajouté dans notre échantillon deux grilles latérales aux extrémités de la jonction pn, nous permettant de contrôler localement

le dopage aux points d'intersection de la jonction pn avec le bord physique du graphène. Des contacts ohmiques sont placés respectivement dans la région dopée n et dans celle dopée p. Le principe de notre expérience est d'injecter un courant sur le contact ohmique en haut à droite de la jonction, et de mesurer l'intensité du courant transmise via le contact ohmique en bas à gauche.

Dans la fin de ce chapitre, est détaillé le montage expérimental de mesure, qui a été entièrement développé et installé durant ma thèse, le cryostat étant arrivé quelques mois après moi.

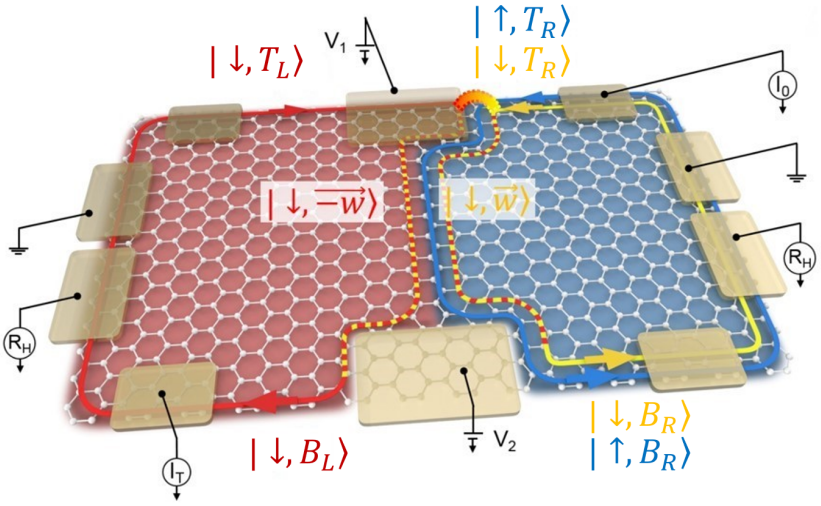

Figure A.6.3: Représentation schématique d'une jonction pn. La région dopée n est représentée en bleu, la région dopée p en rouge. Les électrons sont injectés depuis le contact ohmique en haut à droite (définissant un courant injecté I_0), et un courant transmis I_T est mesuré sur le contact ohmique en bas à gauche. Des contacts ohmiques enterrés permettent de mesurer simultanément le facteur de remplissage par une mesure deux points de la résistance de Hall de chaque côté de la jonction pn (notée R_H sur la figure).

Dans le **chapitre 3** est décrit l'expérience centrale de ma thèse, dans laquelle on a démontré que, grâce à la géométrie de notre échantillon, on a un contrôle électrostatique complet de la polarisation en vallée de l'état de sortie.

La première étape pour ce faire a été de démontrer que, grâce aux grilles latérales, on pouvait contrôler la transmission aux deux points de mélange. La modulation expérimentalement obtenue des transmissions T_1 et T_2, correspondant respectivement aux points de mélange en haut et en bas de la jonction pn, est présentée dans la figure A.6.4. On observe que par la modulation de la tension de grille, on peut aller d'une configuration sans mélange $T_{1,2} \approx 0$ à une transmission presque totale $T_{1,2} \approx 0.9$.

Dans un deuxième temps, on a étudié quantitativement l'évolution des oscillations Aharanov-Bohm dans la configuration de Mach Zehnder en fonction de la transmission T_1 avec $T_2 \approx 0.5$. L'évolution de la visibilité des interférences en fonction de T_1 est présentée dans la figure A.6.5. Ces mesures expérimentales présentent une très bonne adéquation avec la dépendance théorique de la visibilité attendue dans un interféromètre

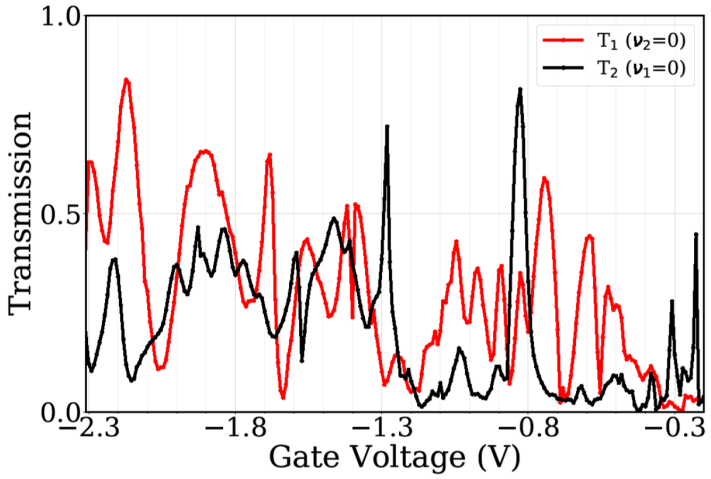

Figure A.6.4: Mesure de la transmission en fonction des tensions sur les grilles latérales. En rouge T_1 en fonction de V_1 pour un facteur de remplissage $\nu_1 \leq -1$ et $\nu_2 = 0$ à $B = 9.23$ T. En noir T_2 en fonction de V_2 pour $\nu_1 = 0$, $\nu_2 \leq -1$ à $B = 8.96$ T.

de Mach Zehnder; ainsi ces résultats confirment que, dans le graphène, la jonction pn en régime Hall quantique se comporte comme un interféromètre de Mach Zehnder. D'autre part, on a pu montrer que le contrôle des transmissions T_1 et T_2 associé à la phase Aharanov-Bohm permettait d'obtenir une maîtrise complète de la polarisation en vallée de l'excitation électronique en sortie du système.

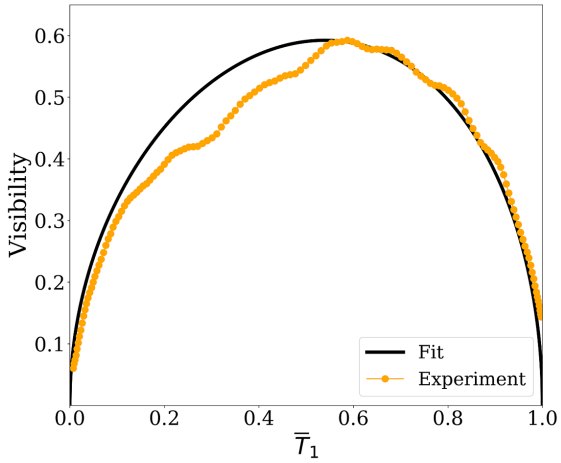

Figure A.6.5: Points oranges : Visibilité mesurée expérimentalement en fonction de la transmission normalisée $\bar{T}_1$ avec T_2=0.5. Ligne noire : Visibilité calculée via la formule $V = 2z\sqrt{\bar{T}_1(1-\bar{T}_1)}$ avec $z = 0.59$.

Ensuite, dans le **chapitre 4**, est présentée l'étude expérimentale des énergies caractéristiques de la cohérence de ces états polarisés en vallée. Dans ce but, on a étudié, la dépendance des interférences de Mach Zehnder en fonction de l'énergie des électrons inci-

dents : premièrement par l'application d'une tension DC sur un canal de bord en entrée de l'interféromètre de Mach Zehnder; deuxièmement en augmentant la température de l'ensemble du système.

Dans le cas de l'application d'une tension DC, on a observé, comme visible dans la figure A.6.6a, une disparition des oscillations autour de $V_{DC} \approx 0.8mV$, ainsi que l'apparition d'un déphasage de π autour de $V_{DC} \approx 0.25mV$. De manière plus quantitative, la visibilité extraite de cette mesure présente une structure de lobe avec un lobe central entouré de deux lobes latéraux. Ces résultats sont similaires à ceux obtenus dans les hétérostructures semi-conductrices de GaAs/AlGaAs. Pour autant, les échelles d'énergie sont complètement différentes ; dans les expériences utilisant du GaAs/AlGaAs, les oscillations disparaissent autour de $V_{DC} \approx 40\mu V$, soit des énergies vingt fois plus faibles.

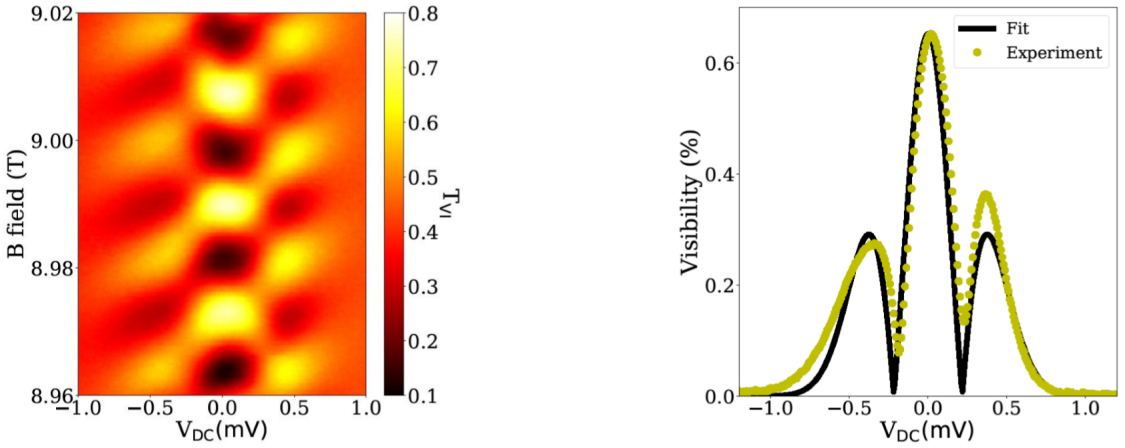

(a) (b)

Figure A.6.6: (**a**) Transmission T_{VI} en fonction du bias DC V_{DC} et du champ magnétique à $\nu_n = +2$,$\nu_p = -1$. (**b**) Visibilité mesurée (points jaunes) en fonction de V_{DC}. Visibilité calculée (ligne noire) en considérant des fluctuations gaussiennes de la phase.

L'évolution expérimentale de la visibilité des oscillations avec la température est tracée dans la figure A.6.7. On observe une température seuil autour de 400mK au-delà de laquelle la visibilité décroit de manière exponentielle. Dans les hétérostructures de GaAs/AlGaAs une même décroissance exponentielle avait été observée, mais pas de température seuil. D'autre part, une fois encore les échelles d'énergies sont complètement différentes. En effet, dans le graphène les oscillations persistent jusqu'à 1.5K, alors que dans les hétérostructures de GaAs/AlGaAs elles disparaissent autour de 100mK.

Le **Chapitre 5** est centré sur la détermination expérimentale de la longueur de cohérence grâce à notre échantillon, ce qui n'a encore jamais été fait dans le graphène en régime Hall quantique. La longueur de cohérence est une longueur caractéristique de la cohérence quantique d'un système, elle représente la distance de propagation sur laquelle une excitation perd sa cohérence de phase à cause de l'échange d'informations. Pour la mesurer, il est nécessaire de mesurer la dépendance en température des interférences dans au moins trois interféromètres présentant des longueurs différentes. De manière remarquable, nous avons pu réaliser cette mesure en utilisant un seul échantillon. Les

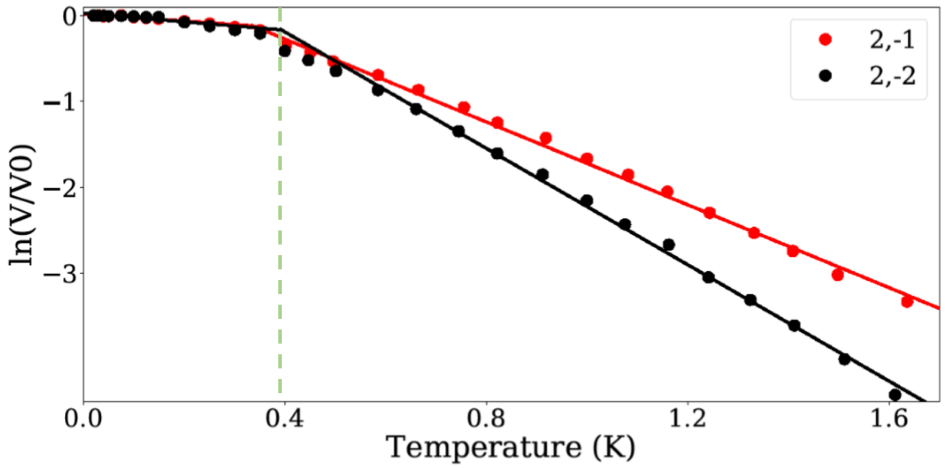

Figure A.6.7: Dépendance en température en échelle logarithmique de la visibilité des oscillations Aharanov-Bohm, dans les configurations suivantes : (ν_n=+2,ν_p=-1) en rouge et (ν_n=+2,ν_p=-2) en noir.

dépendances expérimentales de la visibilité avec la température pour les trois différentes tailles de MZ sont présentées dans la figure A.6.8.a. On observe que plus la taille de l'interféromètre est grande plus la décroissance est rapide. D'autre part, la température seuil, présente dans les trois échantillons, diminue avec la longueur de la jonction, comme visible dans la figure A.6.8.b. Pour finir, l'évolution de la pente dans le régime à haute température et dans le régime à basse température de la figure A.6.8.a est linéaire avec la taille de l'interféromètre (voir figure A.6.8.c). Cela nous a permis d'extraire une longueur de cohérence de $l_\varphi = 1.2\mu m$ à 1K pour le régime à haute température, et de $l_\varphi = 0.37mm$ à 20mK pour le régime à basse température.

Finalement, dans le **chapitre 6**, est exposée l'étude des ondes de spin (ou magnons), ainsi que leur effet sur la cohérence du système. Les magnons correspondent à des excitations magnétiques se propageant à travers un système magnétique, et ils pourraient être une source importante de décohérence en régime Hall quantique lorsque le coeur du graphène est ferromagnétique. En étudiant l'effet des magnons sur les interférences, on a effectivement pu démontrer que la cohérence est limitée en tension DC au-delà de 1mV par l'existence de ces excitations collectives, pour autant la structure de lobe ne peut être expliquée par ce mécanisme puisqu'elle apparait en-deça de 1mV.

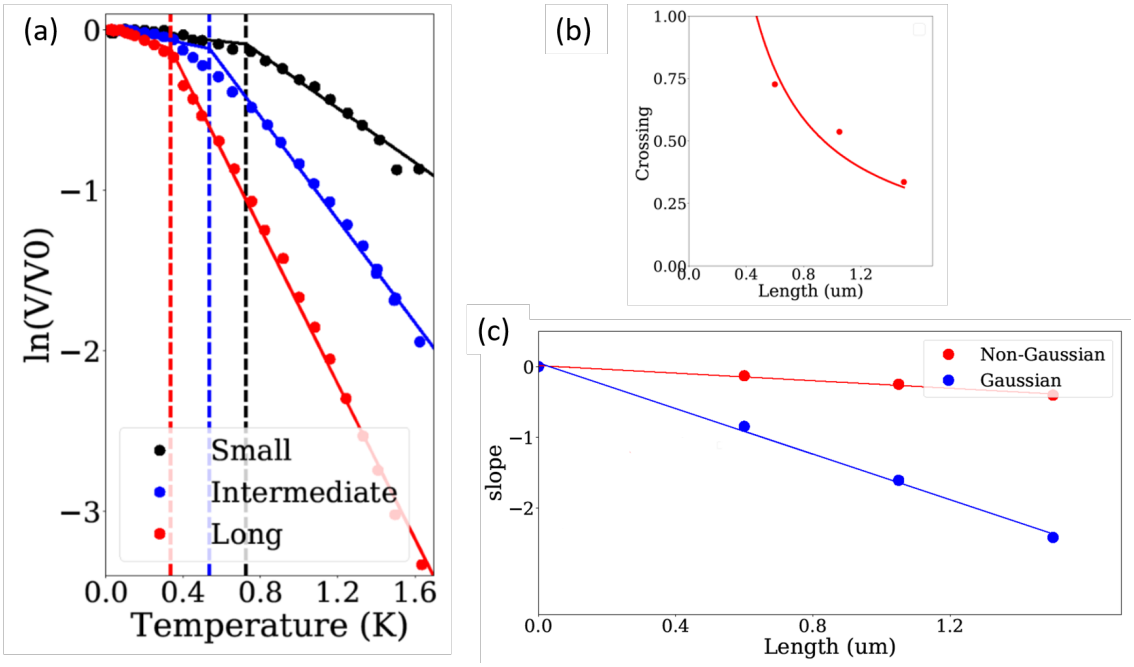

Figure A.6.8: (**a**) Dépendance en température en échelle logarithmique de la visibilité pour les trois différentes tailles d'interféromètre. (**b**) Température seuil en fonction de la longueur de l'interféromètre (points rouges). Dépendance sur la longueur attendue théoriquement (ligne rouge). (**c**) Pente $\ln(V/V_0)/T$ en fonction de la longueur du bras de l'interféromètre dans le régime à haute température (points bleus), ainsi que dans le régime à basse température (points rouges).

Bibliography

[1] DA Abanin and LS Levitov. Quantized transport in graphene pn junctions in a magnetic field. *Science*, 317(5838):641–643, 2007.

[2] AR Akhmerov, JH Bardarson, Adam Rycerz, and CWJ Beenakker. Theory of the valley-valve effect in graphene nanoribbons. *Physical Review B*, 77(20):205416, 2008.

[3] Jason Alicea and Matthew PA Fisher. Graphene integer quantum hall effect in the ferromagnetic and paramagnetic regimes. *Physical Review B*, 74(7):075422, 2006.

[4] C Altimiras, H Le Sueur, U Gennser, A Cavanna, D Mailly, and F Pierre. Non-equilibrium edge-channel spectroscopy in the integer quantum hall regime. *Nature Physics*, 6(1):34–39, 2010.

[5] F Amet, JR Williams, K Watanabe, T Taniguchi, and D Goldhaber-Gordon. Selective equilibration of spin-polarized quantum hall edge states in graphene. *Physical review letters*, 112(19):196601, 2014.

[6] Pacome Armagnat, A Lacerda-Santos, Benoit Rossignol, Christoph Groth, and Xavier Waintal. The self-consistent quantum-electrostatic problem in strongly non-linear regime. *arXiv preprint arXiv:1905.01271*, 2019.

[7] Alain Aspect, Jean Dalibard, and Gérard Roger. Experimental test of bell's inequalities using time-varying analyzers. *Physical review letters*, 49(25):1804, 1982.

[8] SE Barrett, G Dabbagh, LN Pfeiffer, KW West, and R Tycko. Optically pumped nmr evidence for finite-size skyrmions in gaas quantum wells near landau level filling $\nu = 1$. *Physical review letters*, 74(25):5112, 1995.

[9] Christopher Bäuerle, D Christian Glattli, Tristan Meunier, Fabien Portier, Patrice Roche, Preden Roulleau, Shintaro Takada, and Xavier Waintal. Coherent control of single electrons: a review of current progress. *Reports on Progress in Physics*, 81(5):056503, 2018.

[10] CWJ Beenakker. Colloquium: Andreev reflection and klein tunneling in graphene. *Reviews of Modern Physics*, 80(4):1337, 2008.

[11] E Bieri, M Weiss, O Göktas, M Hauser, C Schönenberger, and S Oberholzer. Finite-bias visibility dependence in an electronic mach-zehnder interferometer. *Physical Review B*, 79(24):245324, 2009.

[12] P Blake, EW Hill, AH Castro Neto, KS Novoselov, D Jiang, R Yang, TJ Booth, and AK Geim. Making graphene visible. *Applied physics letters*, 91(6):063124, 2007.

[13] Erwann Bocquillon, Vincent Freulon, J-M Berroir, Pascal Degiovanni, Bernard Plaçais, A Cavanna, Yong Jin, and Gwendal Fève. Coherence and indistinguishability of single electrons emitted by independent sources. *Science*, 339(6123):1054–1057, 2013.

[14] Kirill I Bolotin, K J Sikes, Zd Jiang, M Klima, G Fudenberg, J Hone, Ph Kim, and HL Stormer. Ultrahigh electron mobility in suspended graphene. *Solid state communications*, 146(9-10):351–355, 2008.

[15] Marvin E Cage, Ronald F Dziuba, and Bruce F Field. A test of the quantum hall effect as a resistance standard. *IEEE transactions on instrumentation and measurement*, (2):301–303, 1985.

[16] Cory R Dean, Andrea F Young, Pet Cadden-Zimansky, L Wang, H Ren, Kenji Watanabe, T Taniguchi, P Kim, J Hone, and KL Shepard. Multicomponent fractional quantum hall effect in graphene. *Nature Physics*, 7(9):693–696, 2011.

[17] Cory R Dean, Andrea F Young, Inanc Meric, Chris Lee, Lei Wang, Sebastian Sorgenfrei, Kenji Watanabe, Takashi Taniguchi, Phillip Kim, Kenneth L Shepard, et al. Boron nitride substrates for high-quality graphene electronics. *Nature nanotechnology*, 5(10):722–726, 2010.

[18] Régis Decker, Yang Wang, Victor W Brar, William Regan, Hsin-Zon Tsai, Qiong Wu, William Gannett, Alex Zettl, and Michael F Crommie. Local electronic properties of graphene on a bn substrate via scanning tunneling microscopy. *Nano letters*, 11(6):2291–2295, 2011.

[19] Xu Du, Ivan Skachko, Fabian Duerr, Adina Luican, and Eva Y Andrei. Fractional quantum hall effect and insulating phase of dirac electrons in graphene. *Nature*, 462(7270):192–195, 2009.

[20] J Dubois, T Jullien, Ch Grenier, P Degiovanni, P Roulleau, and DC Glattli. Integer and fractional charge lorentzian voltage pulses analyzed in the framework of photon-assisted shot noise. *Physical Review B*, 88(8):085301, 2013.

[21] J Dubois, T Jullien, F Portier, P Roche, A Cavanna, Y Jin, W Wegscheider, P Roulleau, and DC Glattli. Minimal-excitation states for electron quantum optics using levitons. *Nature*, 502(7473):659–663, 2013.

[22] H Duprez, E Sivre, A Anthore, A Aassime, A Cavanna, A Ouerghi, U Gennser, and F Pierre. Macroscopic electron quantum coherence in a solid-state circuit. *Physical Review X*, 9(2):021030, 2019.

[23] D Ferraro, B Roussel, Ch Cabart, E Thibierge, G Fève, Ch Grenier, and P Degiovanni. Real-time decoherence of landau and levitov quasiparticles in quantum hall edge channels. *Physical review letters*, 113(16):166403, 2014.

[24] Gwendal Fève, Adrien Mahé, J-M Berroir, Takis Kontos, Bernard Plaçais, DC Glattli, A Cavanna, Bernard Etienne, and Yong Jin. An on-demand coherent single-electron source. *Science*, 316(5828):1169–1172, 2007.

[25] Andre K Geim and Irina V Grigorieva. Van der waals heterostructures. *Nature*, 499(7459):419–425, 2013.

[26] Andre K Geim and Konstantin S Novoselov. The rise of graphene. In *Nanoscience and technology: a collection of reviews from nature journals*, pages 11–19. World Scientific, 2010.

[27] Fereshte Ghahari, Yue Zhao, Paul Cadden-Zimansky, Kirill Bolotin, and Philip Kim. Measurement of the $\nu = 1/3$ fractional quantum hall energy gap in suspended graphene. *Physical Review Letters*, 106(4):046801, 2011.

[28] D Christian Glattli and Preden S Roulleau. Levitons for electron quantum optics. *physica status solidi (b)*, 254(3):1600650, 2017.

[29] MO Goerbig. Electronic properties of graphene in a strong magnetic field. *Reviews of Modern Physics*, 83(4):1193, 2011.

[30] RV Gorbachev, JCW Song, GL Yu, AV Kretinin, F Withers, Y Cao, A Mishchenko, IV Grigorieva, KS Novoselov, LS Levitov, et al. Detecting topological currents in graphene superlattices. *Science*, 346(6208):448–451, 2014.

[31] Christoph W Groth, Michael Wimmer, Anton R Akhmerov, and Xavier Waintal. Kwant: a software package for quantum transport. *New Journal of Physics*, 16(6):063065, 2014.

[32] Dorri Halbertal, Moshe Ben Shalom, Aviram Uri, Kousik Bagani, Alexander Y Meltzer, Ido Marcus, Yuri Myasoedov, John Birkbeck, Leonid S Levitov, Andre K Geim, et al. Imaging resonant dissipation from individual atomic defects in graphene. *Science*, 358(6368):1303–1306, 2017.

[33] Clevin Handschin, Péter Makk, Peter Rickhaus, Romain Maurand, Kenji Watanabe, Takashi Taniguchi, Klaus Richter, Ming-Hao Liu, and Christian Schonenberger. Giant valley-isospin conductance oscillations in ballistic graphene. *Nano letters*, 17(9):5389–5393, 2017.

[34] AE Hansen, A Kristensen, S Pedersen, CB Sørensen, and PE Lindelof. Mesoscopic decoherence in aharonov-bohm rings. *Physical Review B*, 64(4):045327, 2001.

[35] Thomas Ihn. *Semiconductor Nanostructures: Quantum states and electronic transport*. Oxford University Press, 2010.

[36] DA Ivanov, HW Lee, and LS Levitov. Coherent states of alternating current. *Physical Review B*, 56(11):6839, 1997.

[37] Yang Ji, Yunchul Chung, D Sprinzak, M Heiblum, D Mahalu, and Hadas Shtrikman. An electronic mach–zehnder interferometer. *Nature*, 422(6930):415–418, 2003.

[38] Zhigang Jiang, Yuanbo Zhang, HL Stormer, and Ph Kim. Quantum hall states near the charge-neutral dirac point in graphene. *Physical review letters*, 99(10):106802, 2007.

[39] Long Ju, Zhiwen Shi, Nityan Nair, Yinchuan Lv, Chenhao Jin, Jairo Velasco Jr, Claudia Ojeda-Aristizabal, Hans A Bechtel, Michael C Martin, Alex Zettl, et al. Topological valley transport at bilayer graphene domain walls. *Nature*, 520(7549):650–655, 2015.

[40] MI Katsnelson, KS Novoselov, and AK Geim. Chiral tunnelling and the klein paradox in graphene. *Nature physics*, 2(9):620–625, 2006.

[41] J Keeling, I Klich, and LS Levitov. Minimal excitation states of electrons in one-dimensional wires. *Physical review letters*, 97(11):116403, 2006.

[42] Maxim Kharitonov. Phase diagram for the $\nu = 0$ quantum hall state in monolayer graphene. *Physical Review B*, 85(15):155439, 2012.

[43] K v Klitzing, Gerhard Dorda, and Michael Pepper. New method for high-accuracy determination of the fine-structure constant based on quantized hall resistance. *Physical Review Letters*, 45(6):494, 1980.

[44] Angelika Knothe and Thierry Jolicoeur. Edge structure of graphene monolayers in the $\nu = 0$ quantum hall state. *Physical Review B*, 92(16):165110, 2015.

[45] R Kraft, IV Krainov, V Gall, AP Dmitriev, R Krupke, IV Gornyi, and R Danneau. Valley subband splitting in bilayer graphene quantum point contacts. *Physical review letters*, 121(25):257703, 2018.

[46] N Kumada, H Kamata, and T Fujisawa. Edge magnetoplasmon transport in gated and ungated quantum hall systems. *Physical Review B*, 84(4):045314, 2011.

[47] N Kumada, FD Parmentier, H Hibino, DC Glattli, and P Roulleau. Shot noise generated by graphene p–n junctions in the quantum hall effect regime. *Nature communications*, 6:8068, 2015.

[48] Norio Kumada, P Roulleau, B Roche, M Hashisaka, H Hibino, I Petković, and DC Glattli. Resonant edge magnetoplasmons and their decay in graphene. *Physical review letters*, 113(26):266601, 2014.

[49] Leonid S Levitov, Hyunwoo Lee, and Gordey B Lesovik. Electron counting statistics and coherent states of electric current. *Journal of Mathematical Physics*, 37(10):4845–4866, 1996.

[50] Ivan P Levkivskyi and Eugene V Sukhorukov. Dephasing in the electronic mach-zehnder interferometer at filling factor $\nu = 2$. *Physical Review B*, 78(4):045322, 2008.

[51] LV Litvin, Andreas Helzel, H-P Tranitz, Werner Wegscheider, and Christoph Strunk. Edge-channel interference controlled by landau level filling. *Physical Review B*, 78(7):075303, 2008.

[52] Ming-Hao Liu, Peter Rickhaus, Péter Makk, Endre Tóvári, Romain Maurand, Fedor Tkatschenko, Markus Weiss, Christian Schönenberger, Klaus Richter, et al. Scalable tight-binding model for graphene. *Physical review letters*, 114(3):036601, 2015.

[53] Timm Lohmann, Klaus von Klitzing, and Jurgen H Smet. Four-terminal magneto-transport in graphene pn junctions created by spatially selective doping. *Nano letters*, 9(5):1973–1979, 2009.

[54] Wen Long, Qing-feng Sun, and Jian Wang. Disorder-induced enhancement of transport through graphene p- n junctions. *Physical review letters*, 101(16):166806, 2008.

[55] Kin Fai Mak, Kathryn L McGill, Jiwoong Park, and Paul L McEuen. The valley hall effect in mos2 transistors. *Science*, 344(6191):1489–1492, 2014.

[56] Péter Makk, Clevin Handschin, Endre Tóvári, Kenji Watanabe, Takashi Taniguchi, Klaus Richter, Ming-Hao Liu, Christian Schönenberger, et al. Coexistence of classical snake states and aharonov-bohm oscillations along graphene p- n junctions. *Physical Review B*, 98(3):035413, 2018.

[57] Scott M Mills, Anna Gura, Kenji Watanabe, Takashi Taniguchi, Matthew Dawber, Dmitri V Averin, and Xu Du. Dirac fermion quantum hall antidot in graphene. *Physical Review B*, 100(24):245130, 2019.

[58] Sei Morikawa, Satoru Masubuchi, Rai Moriya, Kenji Watanabe, Takashi Taniguchi, and Tomoki Machida. Edge-channel interferometer at the graphene quantum hall pn junction. *Applied Physics Letters*, 106(18):183101, 2015.

[59] I Neder, M Heiblum, Y Levinson, D Mahalu, and V Umansky. Unexpected behavior in a two-path electron interferometer. *Physical Review Letters*, 96(1):016804, 2006.

[60] I Neder, M Heiblum, D Mahalu, and V Umansky. Entanglement, dephasing, and phase recovery via cross-correlation measurements of electrons. *Physical review letters*, 98(3):036803, 2007.

[61] Izhar Neder, Florian Marquardt, Moty Heiblum, Diana Mahalu, and Vladimir Umansky. Controlled dephasing of electrons by non-gaussian shot noise. *Nature Physics*, 3(8):534–537, 2007.

[62] Izhar Neder, Nissim Ofek, Y Chung, M Heiblum, D Mahalu, and V Umansky. Interference between two indistinguishable electrons from independent sources. *Nature*, 448(7151):333–337, 2007.

[63] Kentaro Nomura and Allan H MacDonald. Quantum hall ferromagnetism in graphene. *Physical review letters*, 96(25):256602, 2006.

[64] Konstantin S Novoselov, Z Jiang, Y Zhang, SV Morozov, Horst L Stormer, U Zeitler, JC Maan, GS Boebinger, Philip Kim, and Andre K Geim. Room-temperature quantum hall effect in graphene. *Science*, 315(5817):1379–1379, 2007.

[65] Kostya S Novoselov, Andre K Geim, Sergei V Morozov, D Jiang, Y_ Zhang, Sergey V Dubonos, Irina V Grigorieva, and Alexandr A Firsov. Electric field effect in atomically thin carbon films. *science*, 306(5696):666–669, 2004.

[66] Kostya S Novoselov, Andre K Geim, SVb Morozov, Da Jiang, Michail I Katsnelson, IVa Grigorieva, SVb Dubonos, Firsov, and AA. Two-dimensional gas of massless dirac fermions in graphene. *nature*, 438(7065):197–200, 2005.

[67] Kostya S Novoselov, D Jiang, F Schedin, TJ Booth, VV Khotkevich, SV Morozov, and Andre K Geim. Two-dimensional atomic crystals. *Proceedings of the National Academy of Sciences*, 102(30):10451–10453, 2005.

[68] Filippo Pizzocchero, Lene Gammelgaard, Bjarke S Jessen, José M Caridad, Lei Wang, James Hone, Peter Bøggild, and Timothy J Booth. The hot pick-up technique for batch assembly of van der waals heterostructures. *Nature communications*, 7(1):1–10, 2016.

[69] Rebeca Ribeiro-Palau, Shaowen Chen, Yihang Zeng, Kenji Watanabe, Takashi Taniguchi, James Hone, and Cory R Dean. High-quality electrostatically defined hall bars in monolayer graphene. *Nano letters*, 19(4):2583–2587, 2019.

[70] P Roulleau, F Portier, P Roche, A Cavanna, G Faini, U Gennser, and D Mailly. Noise dephasing in edge states of the integer quantum hall regime. *Physical review letters*, 101(18):186803, 2008.

[71] Preden Roulleau. *Etude de la cohérence quantique dans le régime d'effet Hall quantique entier*. PhD thesis, Paris 6, 2008.

[72] Preden Roulleau, F Portier, DC Glattli, P Roche, A Cavanna, G Faini, U Gennser, and D Mailly. Finite bias visibility of the electronic mach-zehnder interferometer. *Physical Review B*, 76(16):161309, 2007.

[73] Preden Roulleau, F Portier, P Roche, A Cavanna, G Faini, U Gennser, and D Mailly. Direct measurement of the coherence length of edge states in the integer quantum hall regime. *Physical Review Letters*, 100(12):126802, 2008.

[74] P Samuelsson, Evgeny V Sukhorukov, and Markus Büttiker. Two-particle aharonov-bohm effect and entanglement in the electronic hanbury brown–twiss setup. *Physical review letters*, 92(2):026805, 2004.

[75] John R Schaibley, Hongyi Yu, Genevieve Clark, Pasqual Rivera, Jason S Ross, Kyle L Seyler, Wang Yao, and Xiaodong Xu. Valleytronics in 2d materials. *Nature Reviews Materials*, 1(11):1–15, 2016.

[76] Georg Seelig and Markus Büttiker. Charge-fluctuation-induced dephasing in a gated mesoscopic interferometer. *Physical Review B*, 64(24):245313, 2001.

[77] Oleksii Shevtsov, Pierre Carmier, Cyril Petitjean, Christoph Groth, David Carpentier, and Xavier Waintal. Graphene-based heterojunction between two topological insulators. *Physical Review X*, 2(3):031004, 2012.

[78] Yuya Shimazaki, Michihisa Yamamoto, Ivan V Borzenets, Kenji Watanabe, Takashi Taniguchi, and Seigo Tarucha. Generation and detection of pure valley current by electrically induced berry curvature in bilayer graphene. *Nature Physics*, 11(12):1032–1036, 2015.

[79] N Stander, B Huard, and D Goldhaber-Gordon. Evidence for klein tunneling in graphene p- n junctions. *Physical review letters*, 102(2):026807, 2009.

[80] Luka Trifunovic and Piet W Brouwer. Valley isospin of interface states in a graphene p n junction in the quantum hall regime. *Physical Review B*, 99(20):205431, 2019.

[81] BJ Van Wees, H Van Houten, CWJ Beenakker, J Gr Williamson, LP Kouwenhoven, D Van der Marel, and CT Foxon. Quantized conductance of point contacts in a two-dimensional electron gas. *Physical Review Letters*, 60(9):848, 1988.

[82] Lei Wang, I Meric, PY Huang, Q Gao, Y Gao, H Tran, T Taniguchi, Kenji Watanabe, LM Campos, DA Muller, et al. One-dimensional electrical contact to a two-dimensional material. *Science*, 342(6158):614–617, 2013.

[83] Di S Wei, Toeno van der Sar, Seung Hwan Lee, Kenji Watanabe, Takashi Taniguchi, Bertrand I Halperin, and Amir Yacoby. Electrical generation and detection of spin waves in a quantum hall ferromagnet. *Science*, 362(6411):229–233, 2018.

[84] Di S Wei, Toeno van der Sar, Javier D Sanchez-Yamagishi, Kenji Watanabe, Takashi Taniguchi, Pablo Jarillo-Herrero, Bertrand I Halperin, and Amir Yacoby. Mach-zehnder interferometry using spin-and valley-polarized quantum hall edge states in graphene. *Science advances*, 3(8):e1700600, 2017.

[85] JR Williams, L DiCarlo, and CM Marcus. Quantum hall effect in a gate-controlled pn junction of graphene. *Science*, 317(5838):638–641, 2007.

[86] Kun Yang, S Das Sarma, and Allan H MacDonald. Collective modes and skyrmion excitations in graphene s u (4) quantum hall ferromagnets. *Physical Review B*, 74(7):075423, 2006.

[87] Matthew Yankowitz, Shaowen Chen, Hryhoriy Polshyn, Yuxuan Zhang, K Watanabe, T Taniguchi, David Graf, Andrea F Young, and Cory R Dean. Tuning superconductivity in twisted bilayer graphene. *Science*, 363(6431):1059–1064, 2019.

[88] AF Young, JD Sanchez-Yamagishi, B Hunt, SH Choi, K Watanabe, T Taniguchi, RC Ashoori, and P Jarillo-Herrero. Tunable symmetry breaking and helical edge transport in a graphene quantum spin hall state. *Nature*, 505(7484):528–532, 2014.

[89] Andrea F Young, Cory R Dean, Lei Wang, Hechen Ren, Paul Cadden-Zimansky, Kenji Watanabe, Takashi Taniguchi, James Hone, Kenneth L Shepard, and Philip Kim. Spin and valley quantum hall ferromagnetism in graphene. *Nature Physics*, 8(7):550–556, 2012.

[90] Y Zhang, Z Jiang, JP Small, MS Purewal, Y-W Tan, M Fazlollahi, JD Chudow, JA Jaszczak, HL Stormer, and P Kim. Landau-level splitting in graphene in high magnetic fields. *Physical review letters*, 96(13):136806, 2006.

[91] Yuanbo Zhang, Yan-Wen Tan, Horst L Stormer, and Philip Kim. Experimental observation of the quantum hall effect and berry's phase in graphene. *nature*, 438(7065):201–204, 2005.

[92] NB Zhitenev, RJ Haug, K v Klitzing, and K Eberl. Experimental determination of the dispersion of edge magnetoplasmons confined in edge channels. *Physical Review B*, 49(11):7809, 1994.

[93] H Zhou, H Polshyn, T Taniguchi, K Watanabe, and AF Young. Solids of quantum hall skyrmions in graphene. *Nature Physics*, 16(2):154–158, 2020.

[94] Katrin Zimmermann, Anna Jordan, Frédéric Gay, Kenji Watanabe, Takashi Taniguchi, Zheng Han, Vincent Bouchiat, Hermann Sellier, and Benjamin Sacépé. Tunable transmission of quantum hall edge channels with full degeneracy lifting in split-gated graphene devices. *Nature communications*, 8(1):1–7, 2017.

université PARIS-SACLAY | ÉCOLE DOCTORALE Physique en l'Île-de-France (PIF)

Titre : Interférométrie de Mach Zehnder et manipulation cohérente de la vallée dans une jonction pn dans une monocouche de graphène

Mots clés : Interféromètre de Mach Zehnder, graphène, vallée-tronique, optique quantique électronique

Résumé : L'optique quantique électronique, i.e. la réalisation de l'analogue électronique d'expériences d'optique quantique, constitue un champ de recherche récent, en plein développement, et offrant des perspectives intéressantes pour l'informatique quantique. Dans ce cadre, l'un des enjeux est la réalisation de bits quantiques en utilisant des états électroniques, ainsi que la formation d'états électroniques intriqués, éléments de bases pour réaliser des calculs quantiques plus élaborés. Les expériences menées jusqu'à présent dans des hétérostructures semi-conductrices de GaAs/AlGaAs ont mis en évidence la possibilité d'encoder l'information dans la charge ou le spin d'un électron, mais la décohérence importante de ces systèmes induit une grande fragilité de ces états quantiques, qui ne peuvent exister qu'en-dessous de 100mK et pour des tensions résiduelles inférieures à $40\mu V$. Cette fragilité rend difficile la fabrication d'états intriqués, et est limitante pour le développement de calculs quantiques complexes.

En 2005, la découverte d'un matériau novateur, le graphène, a ouvert de nouvelles perspectives avec la prédiction d'une cohérence de phase plus grande, et, d'autre part, l'existence en plus du spin d'un nouveau degré de liberté, la vallée, donnant accès à de nouvelles possibilités pour encoder l'information. Dans un premier temps, ce travail de thèse porte sur la manipulation cohérente de la vallée, nécessaire à la réalisation d'un bit quantique de vallée dans le graphène. Pour cela est utilisée, en régime Hall quantique, une jonction pn, formée à l'aide de grilles déposées sur un échantillon de graphène encapsulé dans du nitrure de Bohr. Afin d'obtenir un contrôle électrostatique sur la polarisation en vallée des électrons incidents, des grilles locales ont été déposées, à l'intersection de la jonction pn avec le bord physique du graphène. En alliant ce contrôle électrostatique à celui de la phase Aharanov-Bohm, il nous est possible de manipuler de manière cohérente la vallée d'un électron sur l'ensemble de la sphère de Bloch représentant la polarisation en vallée.

Dans la suite, la cohérence des états quantiques formés est étudiée grâce à un interféromètre de Mach Zehnder, via l'observation de la dépendance des interférences en fonction de la tension appliquée sur les électrons incidents, et de la température du système. Les états quantiques obtenus sont exceptionnellement résistants, ils persistent au-delà de 1.5K et de 1mV, soit à des énergies près de 20 fois supérieures à celles observées dans le GaAs/AlGaAs.

Puis, ce manuscrit décrit l'étude de la longueur de cohérence, correspondant à la distance sur laquelle un électron peut se propager en gardant sa cohérence de phase, ce qui n'avait encore jamais été mesuré dans le graphène. Pour ce faire, la dépendance des interférences vis-à-vis de la température a été mesurée sur trois jonctions pn de longueurs différentes. Une longueur de cohérence a ainsi été extraite pour les deux régimes de décohérence observés ; dont une record, pour le régime à basses températures, de plus de $374\mu m$ à 20mK.

Pour finir, est investigué un des mécanismes causant la décohérence dans le système : les ondes de spin, se propageant lorsque le cœur du graphène est magnétique.

Ainsi, au cours de ce projet, nous avons mis en évidence la possibilité d'encoder de l'information dans la vallée, ouvrant la voie vers un nouveau domaine : la vallée-tronique. D'autre part, la cohérence du système est exceptionnelle, permettant d'envisager la réalisation d'états intriqués grâce à une géométrie de double Mach Zehnder. Cela offre des perspectives prometteuses du point de vue de l'informatique quantique, mais aussi d'un point de vue fondamental avec la possibilité de démontrer pour la première fois, avec des fermions, la validité des prédictions de l'interprétation de Copenhague de la physique quantique dans le cadre du paradoxe EPR.

Université Paris-Saclay
Espace Technologique / Immeuble Discovery
Route de l'Orme aux Merisiers RD 128 / 91190 Saint-Aubin, France

université PARIS-SACLAY | ÉCOLE DOCTORALE Physique en l'Île-de-France (PIF)

Title : Mach Zehnder interferometry and coherent manipulation of the valley in a graphene pn junction

Keywords : Mach Zehnder interferometry, graphene, valleytronics, electron quantum optics

Abstract : Electron quantum optics, i.e. the realization of the electronic analogue of quantum optics experiments, represents a developing and recent research field, offering interesting perspectives for quantum computing. In this context, one of the main stakes is the achievement of quantum bits using electronic states, as well as the creation of entangled electronic states, which are the building blocks to achieve complex quantum computations. Up to now, the experiments carried out in semi-conducting GaAs/AlGaAs heterostructures exhibited the possibility to encode information in the charge or the spin of an electron, but strong decoherence in these systems implies a great weakness of these quantum states, which survives only below temperatures of 100mK and electrical biases of $40\mu V$. This fragility makes it difficult to achieve entangled states and limits the development of complex quantum computations.

In 2005, the discovery of a novel material, graphene, opened new prospects with on one hand the prediction of a larger phase coherence, and on the other hand the existence, in addition to the spin, of a new degree of freedom, named the valley, giving access to new possibilities to encode information. In a first part, this PhD work deals with the coherent manipulation of the valley, which is necessary to achieve a valley quantum bit in graphene. For this aim, we used, in the quantum Hall regime, a graphene pn junction, formed thanks to gates deposited on top of a stack composed of a graphene sheet encapsulated in Boron nitride crystals. In order to obtain an electrostatic control of the valley polarization of incoming electrons, we deposited local gates at the intersections between the pn junction and the graphene physical edge. Associating this electrostatic control to a tuning of the Aharanov-Bohm phase, we can coherently manipulate the valley of an electron over the whole states described by a valley Bloch sphere.

In what follows, the coherence of the quantum states is investigated thanks to Mach Zehnder interferometry, by measuring the interferences dependence on the chemical potential of incoming electrons and on the temperature of the system. The quantum states formed are exceptionally steady, they persist up to 1.5K and 1mV, in other words at energies 20 times higher than what was observed in GaAs/AlGaAs.

Then, the manuscript describes the study of the coherence length, i.e. the distance on which an electron can propagate while keeping its phase coherence, which has never been measured in the quantum Hall regime in graphene. To that end, the interferences dependence on the temperature was measured in three pn junctions of different lengths. By doing so, two coherence lengths, corresponding to two different regimes of decoherence, were extracted; in the regime occurring at low temperature, a record value of $374\mu m$ at 20mK was obtained.

Finally, we investigated one of the mechanisms of decoherence in our system: spin waves, propagating in the graphene bulk when it is magnetized.

During this project, we have shown the possibility to encode information in the valley and to manipulate coherently this degree of freedom, paving the way towards a new domain: the valleytronics. Furthermore, the coherence of the system is exceptional, enabling to envision the achievement of entangled electronic states by using a double Mach Zehnder interferometer geometry. This opens promising prospects for quantum computing, but also for fundamental purposes, with the possibility to demonstrate, for the first time with fermions, the validity of the Copenhagen interpretation of quantum physics within the EPR paradox framework.

Université Paris-Saclay
Espace Technologique / Immeuble Discovery
Route de l'Orme aux Merisiers RD 128 / 91190 Saint-Aubin, France